

LASER SURFACE MODIFICATION OF BIOMEDICAL ALLOYS

A thesis submitted for the degree of
Doctor of Philosophy
by

EVANS CHIKARAKARA
(B.ENG.)

School of Mechanical and Manufacturing Engineering
Faculty of Engineering and Computing
Dublin City University

January 2012

Supervisors
Dr Sumsun Naher
Dr Dermot Brabazon

Preface

This thesis describes original work which has not previously been submitted for a degree in Dublin City University or at any other University. The investigations were carried out in the School of Mechanical and Manufacturing Engineering, Dublin City University, during the period November 2008 to November 2011, under the supervision of Dr Sumsun Naher and Dr Dermot Brabazon. This work has been disseminated through the following publications.

Journal Articles:

- **E. Chikarakara**, S. Naher and D. Brabazon, High Speed Laser Surface Modification of Ti-6Al-4V, Accepted for publication, *Surface and Coatings Technology*, 03/01/2012.
- **E. Chikarakara**, S. Naher and D. Brabazon, Analysis of Microstructural Changes during Pulsed CO₂ Laser Surface Processing of AISI 316L Stainless Steel, *Advanced Materials Research*, **264-265**, 1401-1408, 2011.
- **E. Chikarakara**, S. Naher and D. Brabazon, Process Mapping of Laser Surface Modification of AISI 316L Stainless Steel for Biomedical Applications, *Applied Physics A: Materials Science & Processing*, **101**, 367-371, 2010.
- **E. Chikarakara**, S. Aqida, D. Brabazon, S. Naher, J. A. Picas, M. Punset and A. Forn, Surface Modification of HVOF Thermal Sprayed WC-CoCr Coatings by Laser Treatment, *International Journal of Material Forming*, **3**, 801 – 804, 2010.

International Conference Papers:

- **E. Chikarakara**, S. Naher and D. Brabazon, Tribological Analysis of High Speed Laser Surface Modified Ti-6Al-4V, *11th International Conference on Laser Ablation*, Mexico, November 14 – 18, 2011.
- **E. Chikarakara**, A. Betts, S. Naher and D. Brabazon, Effects of High Speed Laser Surface Modification on Microstructure and Corrosion Characteristics of Ti-6Al-4V, *25th International Conference on Surface Modification Technologies*, Sweden, June 20 – 22, 2011.

- **E. Chikarakara**, M. Punset, J.A. Picas, D. Brabazon and S. Naher, Characterisation of Laser Modified WC-CoCr Coatings, *The 14th International ESAFORM conference on material Forming, Queens University, Northern Ireland, April 27-29, 2011, AIP Conference Proceedings, Volume 1353, pp. 1087-1092 (2011).*
- **E. Chikarakara**, S. Aqida, D. Brabazon, S. Naher, J.A. Picas, M. Punset and A. Forn, Surface Modification of HVOF Thermal Sprayed WC-CoCr Coatings by Laser Treatment, *The 13th International ESAFORM Conference on Material Forming, University of Brescia, Italy, April 7-9, 2010.*
- **E. Chikarakara**, S. Naher and D. Brabazon, Process Mapping of Laser surface modification of AISI 316L Stainless Steel, *10th International Conference on Laser Ablation*, Singapore, November 23 – 27, 2009.
- **E. Chikarakara**, S. Naher and D. Brabazon, Analysis of Microstructural Changes During Pulsed CO₂ Laser Surface Processing of AISI 316L Stainless Steel, *Proceedings of the International Conference on Advances in Materials and Processing Technologies (AMPT)*, Kuala Lumpur, Malaysia, October 26 – 29, 2009.

Seminars and Posters:

- **E. Chikarakara**, S. Naher and D. Brabazon, High Speed Laser Surface Modification of Ti-6Al-4V for Biomedical Applications, *Faculty Research Day, Dublin City University, May 12, 2011. Awarded 3rd prize for the oral presentation.*
- **E. Chikarakara**, S. Naher and D. Brabazon, Laser Surface Modification of Ti-6Al-4V alloy for biomedical applications, *Surface science of biologically important interfaces (SBII 12)*, Ulster University, October 27, 2010.
- **E. Chikarakara**, S. Naher and D. Brabazon, Process Mapping of Laser Surface Modification of AISI 316L Stainless Steel for Biomedical Applications, *Faculty Research Day, Dublin City University, May 12, 2010. Awarded 1st prize for poster presentation.*
- **E. Chikarakara**, S. Naher and D. Brabazon, Overview of Pulsed Laser Surface Melting of AISI 316L Stainless Steel for Biomedical Applications, *Symposium for Mechanical Engineering Research and Practice*, Dublin City University, May 28, 2009.

Declaration

I hereby certify that this material, which I now submit for assessment on the programme of study leading to the award of Doctor of Philosophy is entirely my own work, that I have exercised reasonable care to ensure that the work is original, and does not to the best of my knowledge breach any law of copyright, and has not been taken from the work of others save and to the extent that such work has been cited and acknowledged within the text of my work.

Signed:
(Evans Chikarakara)
ID No. 54781457
Date: 30 January 2012

To Mom

For making my life feel like a vacation

Acknowledgements

First and foremost, I would like to sincerely thank my supervisors, Dr Sumsun Naher and Dr Dermot Brabazon for their support throughout the project. I want to especially thank them for, their encouragements, advice, ever-inspiring expertise, sourcing out collaborations and funding of conference expenses. I am truly grateful for everything they have done to help me get to where I am now.

Special thanks to the late Martin Johnson for his support with the CO₂ laser - may his soul Rest In Peace. Thanks to Michael May, Barry O'Connell, Alan Meehan and Liam Domican for the technical support throughout the study. I would also like to extend my thanks to DCU's mechanical workshop technicians Jim Barry, Cian Merne and Eoin Tuohy for the manufacturing and machining of the parts and materials required for the project.

I am also grateful to all the collaborations I had in the process and would like to thank Anthony Betts from Dublin Institute of Technology for the support in corrosion testing. Many thanks go to Laura Grehan (Athlone Institute of Technology), Tanya Levinstone and John Lau (Royal College of Surgeons) for their assistance in biocompatibility experimental work. Special thanks go to Syarifah Nur Aqida Syed Ahmad and David Moore, who were part of the laser processing group, for the regular exchange of ideas that helped with the progress of this work.

I would like to also thank the DCU's Office of Vice-President of Research (OVRP) and the School of Mechanical and Manufacturing Engineering for funding the project.

Finally, thank you to my family and friends. If it wasn't for you, I'd be way closer to insanity, ndinotenda.

Abstract

This study investigated the effects of high speed laser surface modification on 316L stainless steel and Ti-6Al-4V for biomedical implants application. Laser processing was carried out in an inert argon environment using a 1.5 kW CO₂ laser. Parameters investigated in this work included irradiance, residence time, pulse width and sample pre-treatments. Surface topology, microstructure and melt pool depth were characterised using the scanning electron microscope. White light interferometry and stylus profilometry were used to determine the surface roughness. X-ray diffractometry was used to investigate the crystallinity and phase transformation induced by the laser treatment. Micro-hardness was measured using a Vickers micro-hardness indentation apparatus. Wear behaviour was investigated using a pin on disk apparatus. Corrosion behaviour was evaluated using a potentiostat and an electrochemical cell set-up simulating human body conditions. Biocompatibility of the samples was investigated in vitro by monitoring NIH/3T3 fibroblast and MC3T3-E1 osteoblast cell growth via MTT and Hoechst DNA assays.

A strong correlation between irradiance, residence time, depth of processing and roughness was established in 316L. High depth of altered microstructure and increased roughness were linked to higher levels of both irradiance and residence times. At fixed energy density, increase in residence time resulted in growth of the melt pool. In the melted region, a uniform composition in microstructure with fewer impurities was observed. In Ti-6Al-4V alloy, laser treatment resulted in crack-free layers, twenty to fifty microns thick. With increase in both irradiance and residence time, surface roughness was found to decrease while melt pool depth increased. A martensite structure formed on the laser treated region producing acicular α Ti nested within the aged β Ti matrix. The β Ti phase volume fraction was reduced by up to 19%. Microhardness increased up to 760 HV_{0.05} which represented a 67% increase compared to the bulk material. A homogenous chemical composition of the alloying elements was achieved in laser modified regions. Much lower levels of wear were noted in laser treated samples compared to untreated samples. Stable passive polarisation behaviour and reduction in corrosion rates was noted in treated samples ranging between 86 and 239 nm yr⁻¹ compared to 108 nm yr⁻¹ for untreated samples and 309 nm yr⁻¹ for grit blast samples. Direct contact assays showed that laser treated samples had improved cytotoxicity properties compared to their untreated counterparts.

Contents

CONTENTS.....	VIII
CHAPTER 1 INTRODUCTION.....	1-1
1.1 OVERVIEW	1-1
1.2 STATEMENT OF INVESTIGATION	1-3
1.3 THESIS OUTLINE	1-4
CHAPTER 2 LITERATURE REVIEW.....	2-5
2.1 HIP REPLACEMENT PROSTHESIS.....	2-5
2.1.1 Femoral head.....	2-6
2.1.2 Femoral stem.....	2-7
2.2 CONVENTIONAL BIOMATERIALS USED IN HIP REPLACEMENTS.....	2-7
2.3 METALLIC BIOMATERIALS.....	2-9
2.3.1 316L stainless steel.....	2-10
2.3.2 Ti-6Al-4V.....	2-14
2.4 SURFACE ENGINEERING.....	2-19
2.5 CORROSION.....	2-20
2.6 WETTABILITY CHARACTERISTICS.....	2-22
2.7 BIOCOMPATIBILITY.....	2-25
2.8 LASER SURFACE MODIFICATION.....	2-27
2.8.1 Laser Glazing.....	2-27
2.8.2 Laser Surface Alloying.....	2-30
2.8.3 Laser Surface Cladding.....	2-32
2.8.4 Laser Shock Hardening.....	2-33
2.8.5 Laser Surface Melting.....	2-34
2.9 PARAMETERS AFFECTING LASER SURFACE MODIFICATION.....	2-35
2.9.1 Material Properties.....	2-35
2.9.2 Laser Operating Modes.....	2-38
2.9.3 Laser Power and Irradiance.....	2-39
2.9.4 Sample Speed and Residence Time.....	2-41
2.9.5 Overlap percentage.....	2-41
2.9.6 Pulse Energy density.....	2-42
2.10 EFFECTS OF LASER SURFACE MELTING ON STAINLESS STEEL PROPERTIES.....	2-42
2.11 EFFECTS OF LASER SURFACE MELTING ON Ti-6Al-4V PROPERTIES.....	2-44
2.11.1 Microstructure.....	2-45
2.11.2 Melt Profile.....	2-46
2.11.3 Roughness.....	2-47
2.11.4 Hardness.....	2-48

2.11.5 Wear Properties	2-49
2.11.6 Corrosion Resistance	2-50
2.11.7 Interfacial and Biocompatibility Properties	2-51
2.12 STUDY FOCUS AND OBJECTIVES	2-52
CHAPTER 3 MATERIALS AND METHODS	3-55
3.1 SAMPLE PREPARATION.....	3-55
3.1.1 Surface Pre-treatments.....	3-56
3.2 LASER INSTRUMENTATION AND EXPERIMENTAL SET-UP	3-57
3.2.1 Laser Processing of Cylindrical Work-pieces	3-59
3.2.2 Laser Processing of Planar Work-pieces	3-60
3.3 METALLOGRAPHY	3-60
3.3.1 Sectioning of the Work-piece.....	3-60
3.3.2 Mounting of the Sectioned Sample.....	3-60
3.3.3 Grinding and Polishing of the Mounted Sample	3-61
3.3.4 Etching	3-61
3.4 DESIGN OF EXPERIMENTS (DOE)	3-62
3.4.1 316L Stainless Steel.....	3-63
3.4.2 Ti-6Al-4V	3-66
3.5 MICROSTRUCTURAL ANALYSIS.....	3-67
3.6 MELT POOL PROFILE MEASUREMENT	3-68
3.7 ROUGHNESS MEASUREMENTS.....	3-68
3.8 MICRO-HARDNESS MEASUREMENTS	3-69
3.9 XRD ANALYSIS.....	3-69
3.10 CHEMICAL COMPOSITION ANALYSIS	3-70
3.11 WEAR TESTING	3-71
3.11.1 Reasons for parameter choice	3-73
3.11.2 Wear Testing Procedure	3-73
3.12 CORROSION TESTING.....	3-73
3.12.1 Corrosion Testing Procedure.....	3-76
3.13 CONTACT ANGLE ANALYSIS.....	3-77
3.14 BIOCOMPATIBILITY ANALYSIS	3-78
3.14.1 Cell Attachment and Proliferation	3-78
3.14.2 Cytotoxicity	3-79
CHAPTER 4 : 316L STAINLESS STEEL RESULTS & DISCUSSIONS	4-84
4.1 DESIGN OF EXPERIMENTS 1	4-84
4.1.1 Morphology and Microstructure Analysis.....	4-84
4.1.2 Melt Pool Size Analysis.....	4-88
4.1.3 Roughness Analysis.....	4-90
4.2 DESIGN OF EXPERIMENTS 2	4-92

4.2.1 Microstructure Analysis	4-92
4.2.2 Effects of pre-treatments and residence time on meltpool depth	4-94
4.2.3 Microhardness	4-95
4.2.4 EDS Analysis	4-96
4.3 SUMMARY	4-98
CHAPTER 5 RESULTS: TI-6AL-4V	5-99
5.1. METALLOGRAPHY	5-99
5.1.1 Surface Topography	5-99
5.1.2 Cross-sectional microstructure	5-101
5.2 MELTPOOL PROFILE	5-105
5.3 ROUGHNESS	5-108
5.4 MICROHARDNESS	5-111
5.5 PHASE AND CHEMICAL COMPOSITION CHARACTERISATION	5-114
5.5.1 X-ray diffraction	5-114
5.5.2 Topographic chemical composition analysis.....	5-119
5.5.3 Cross-sectional chemical composition analysis.....	5-122
5.6 WEAR RESISTANCE.....	5-123
5.6.1 Wear Track Micrographs	5-124
5.6.2 Effects of Laser Processing Parameters on Specific Wear rate	5-127
5.7 CORROSION RESISTANCE	5-130
5.8 SURFACE WETTABILITY	5-135
5.8.1 Contact Angles of Unpolished Samples.....	5-136
5.8.2 Contact Angle of Polished Samples.....	5-140
5.9 BIOCOMPATIBILITY	5-141
5.9.1 Cell Attachment and Metabolic Activity	5-141
5.9.2 Cytotoxicity	5-145
CHAPTER 6 DISCUSSION: TI-AL-4V	6-147
6.1 METALLOGRAPHY ANALYSIS.....	6-147
6.1.1 Surface Melting and Morphological Features	6-147
6.1.2 Cross-sectional microstructure	6-149
6.2 MELTPOOL DEPTH ANALYSIS.....	6-151
6.3 ROUGHNESS ANALYSIS.....	6-152
6.4 MICROHARDNESS	6-154
6.5 PHASE TRANSFORMATION AND CHEMICAL ANALYSIS	6-155
6.5.1 X-ray Diffraction Analysis.....	6-155
6.5.2 Chemical Composition	6-157
6.6 WEAR RESISTANCE.....	6-158
6.7 CORROSION RESISTANCE	6-160
6.8 SURFACE WETTABILITY ANALYSIS	6-162

6.8.1 Effects of roughness on contact angle.....	6-162
6.9 BIOCOMPATIBILITY.....	6-164
CHAPTER 7 CONCLUSIONS.....	7-166
7.1 316 STAINLESS STEEL.....	7-166
7.2 Ti-6Al-4V.....	7-167
7.3 FUTURE WORK.....	7-169
REFERENCES.....	7-170
APPENDICES.....	I
A. MATERIAL CERTIFICATES FROM THE SUPPLIERS.....	I
316L stainless steel produced by Acciaierie.....	I
Ti-6Al-4V supplied by Supper Alloys.....	II
B. LINEAR STAGE DISPLACEMENT OF LASER STAGE.....	X
C. PRELIMINARY DOE FOR 316L.....	XII
Design of experiments.....	XII
Preliminary DOE Results.....	XIII
D. RECOMMENDED CUT-OFF LENGTHS FOR ROUGHNESS MEASUREMENTS.....	XX
E. CALCULATION OF LOAD FOR PIN ON DISK WEAR TESTING.....	XXI
F. ADDITIONAL RESULTS FOR 316L STAINLESS STEEL DOE.....	XXIII
Effects of pre-treatments on roughness.....	XXIII
G. MELTPOOL DATA.....	XXV
H. ROUGHNESS DATA.....	XXVI
I. ENERGY DISPERSIVE X-RAY SPECTROSCOPY RAW DATA.....	XXVII
Cross-sectional Analysis.....	XXVIII
J. ABLATION EFFECTS.....	XXXV
K. RAW DATA MATERIAL PROPERTIES MEASURED FOR Ti-6Al-4V.....	XXXVI

List of Figures

FIGURE 1-1: METALLIC IMPLANTS THAT CAN BE IMPROVED VIA LASER SURFACE MODIFICATION [13, 14].	1-2
FIGURE 2-1: HIP ANATOMY WITH PROSTHETIC IMPLANT INSERTED [24].	2-5
FIGURE 2-2: A TYPICAL FEMORAL COMPONENT OF A THR INDICATING NECESSARY REQUIREMENTS.	2-6
FIGURE 2-3: PROPERTIES OF AN IDEAL HARD TISSUE REPLACEMENT BIOMATERIAL [2]	2-10
FIGURE 2-4: 316L STAINLESS STEEL MICROSTRUCTURE CONTAINING LOW CARBON CONTENT [45].	2-11
FIGURE 2-5: THE IRON-CARBON BINARY PHASE DIAGRAM [47].	2-12
FIGURE 2-6: METALLIC MATERIALS USED IN IMPLANTS AND THEIR SUSCEPTIBILITY TO CORROSION [57].	2-15
FIGURE 2-7: THE TITANIUM-ALUMINIUM BINARY PHASE DIAGRAM [68, 69].	2-17
FIGURE 2-8: CONTACT ANGLE (Θ) OF A LIQUID (L) ON A SOLID (S). Γ_{LV} , IS THE INTERFACIAL ENERGY OF LIQUID-VAPOUR INTERFACE; Γ_{SL} , IS THE INTERFACIAL ENERGY OF THE SOLID-LIQUID INTERFACE; AND Γ_{SV} , IS THE INTERFACIAL ENERGY OF THE SOLID-VAPOUR INTERFACE [94].	2-23
FIGURE 2-9: SUPER HYDROPHILIC AND SUPER HYDROPHOBIC CONTACT ANGLES [95].	2-24
FIGURE 2-10: CLASSIFICATION OF DIFFERENT LASER PROCESSING TECHNIQUES [80].	2-27
FIGURE 2-11: COMPARISON OF PERCEIVED GLAZING PROCESS PARAMETERS IN LITERATURE [97, 99].	2-28
FIGURE 2-12: ABSORPTION OF LASER RADIATION WAVELENGTH BY METALS [160].	2-36
FIGURE 2-13: EFFECTS OF ANGLE OF INCIDENCE AND ROUGHNESS ON LASER REFLECTIVITY [162].	2-37
FIGURE 2-14: EFFECT OF OXIDE THICKNESS ON ABSORPTION OF A CO ₂ LASER IRRADIATION [162].	2-38
FIGURE 2-15: GEOMETRY AND INTENSITY OF THE GAUSSIAN LASER BEAM [172].	2-40
FIGURE 2-16: LASER BEAM MODES ILLUSTRATING (A) TEM ₀₀ AND (B) TEM ₀₁ MODES [97].	2-40
FIGURE 2-17: SCHEMATIC DIAGRAM REPRESENTING 50% SPOT OVERLAP.	2-41
FIGURE 2-18: VARIATIONS OF TREATED ZONE WIDTH AND DEPTH WITH INCREASING PULSE ENERGY FOR FIXED VALUES OF PULSE WIDTH (5 MS), FREQUENCY (30 HZ) AND SCAN RATE [163].	2-47
FIGURE 3-1: ILLUSTRATION OF THE Ti-6Al-4V WORK-PIECE, SPECIMEN AND SAMPLE, AS USED IN THIS THESIS.	3-56
FIGURE 3-2: ROFIN CO ₂ LASER SYSTEM AND GAS PUMPING UNIT, SHOWING THE PROCESSING OF A CYLINDRICAL SAMPLE 10 MM IN DIAMETER.	3-58
FIGURE 3-3: SCHEMATIC OF THE LASER PROCESSING SET-UP FOR A CYLINDRICAL SAMPLE.	3-59
FIGURE 3-4: SCHEMATIC OF THE (A) CROSS SECTIONAL SIDE VIEW OF THE EQUIPMENT AND (B) THE PLANAR VIEW OF THE RASTER SCAN PATH FOR THE LASER TREATMENT PROCESS.	3-60
FIGURE 3-5: CARL-ZEISS EVO-LS15 SEM AND ITS COMPONENTS (A) EXTERIOR AND (B) INTERIOR.	3-67
FIGURE 3-6: SAMPLING AND EVALUATION LENGTHS OF A MEASURED SURFACE PROFILE.	3-68
FIGURE 3-7: SCHEMATIC AND IMAGE OF XRD SET-UP [47].	3-69
FIGURE 3-8: (A) SCHEMATIC DEPICTION OF THE VARIATION OF INTERACTION VOLUME SHAPE WITH AVERAGE SAMPLE ATOMIC NUMBER (Z) AND ELECTRON BEAM ACCELERATING VOLTAGE (E ₀); AND (B) CHART FOR CALCULATING X-RAY SPATIAL RESOLUTION FROM THE ACCELERATING VOLTAGE [225].	3-71
FIGURE 3-9: SCHEMATIC OF THE (A) PIN ON DISC APPARATUS USED AND (B) TYPICAL WEAR TRACK	3-72
FIGURE 3-10: SCHEMATIC DIAGRAM OF POLARISATION CELL USED IN THE EXPERIMENTS [228].	3-74
FIGURE 3-11: SCHEMATIC OF INSTRUMENTATION SETUP FOR ELECTROCHEMICAL POLARISATION EXPERIMENTS.	3-75

FIGURE 3-12: FTA 200 ANGSTROM SESSILE DROP MEASURING MACHINE [229].	3-77
FIGURE 3-13: HAEMOCYTOMETER VIEWED AT 200X MAGNIFICATION [230]	3-81
FIGURE 4-1: MICROSTRUCTURE OF AS-RECEIVED 316L STAINLESS STEEL (A) MORPHOLOGY STRUCTURE, AND THE CROSS-SECTIONAL MICROSTRUCTURE OBTAINED VIA (B) SECONDARY ELECTRON (SE) DETECTOR AND (C) BACK SCATTER ELECTRON (BSE) DETECTOR.	4-84
FIGURE 4-2: EFFECTS OF ENERGY DENSITY ON SURFACE MELTING.	4-85
FIGURE 4-3: BACK SCATTER SEM IMAGES OF TRANSVERSE CROSS SECTIONAL MICROSTRUCTURE CORRESPONDING TO PROCESSED SURFACE SHOWN IN FIGURE 4-2 (A), (B) AND (C).	4-85
FIGURE 4-4: GRAIN STRUCTURE RE-ORIENTATION IN SAMPLES LASER TREATED AT ENERGY DENSITIES GREATER THAN 9 J/MM ² .	4-86
FIGURE 4-5: (A) MICROSTRUCTURE VARIATION IN SAMPLES TREATED AT 20.96 J/MM ² AND CLOSE UP VIEW OF SPECIFIC REGIONS (B), (C) AND (D).	4-87
FIGURE 4-6: EFFECTS OF RESIDENCE TIME AND IRRADIANCE AND ON MELT POOL DEPTH.	4-88
FIGURE 4-7: BACKSCATTER SEM CROSS SECTION MICROGRAPHS OF SAMPLES PROCESSED USING THE SAME ENERGY DENSITY (13.1 J/MM ²) WITH: (A) LOW IRRADIANCE (79 kW/MM ²) AND HIGH RESIDENCE TIME (167 μs); (B) HIGH IRRADIANCE (157 kW/MM ²) AND LOW RESIDENCE TIME (83 μs).	4-89
FIGURE 4-8: RELATIONSHIP BETWEEN AVERAGE SURFACE ROUGHNESS AND IRRADIANCE AT VARYING RESIDENCE TIMES.	4-90
FIGURE 4-9: SAMPLE TREATED AT LOW IRRADIANCE (79 kW/MM ²) AND HIGH RESIDENCE TIME (167 MS) ILLUSTRATING EFFECTS OF HIGH DENSITIES ON SURFACE ROUGHNESS.	4-91
FIGURE 4-10: RELATIONSHIP BETWEEN AVERAGE SURFACE ROUGHNESS AND ENERGY DENSITY FOR LASER PROCESSING OF 316L WITH DOE 1.	4-91
FIGURE 4-11: INFLUENCE OF LOW ENERGY DENSITY 5 J/MM ² ON MELTING OF SURFACE (A) SURFACE TOPOLOGY AND (B) CROSS SECTIONAL MICROSTRUCTURE	4-92
FIGURE 4-12: INFLUENCE OF HIGH ENERGY DENSITY 25 J/MM ² ON MELTING OF SURFACE (A) SURFACE TOPOLOGY AND (B) CROSS SECTIONAL MICROSTRUCTURE	4-92
FIGURE 4-13: EFFECTS OF PROCESSING PARAMETERS AT A FIXED ENERGY DENSITY (10.48 J/MM ²): (A) HIGH IRRADIANCE (157 kW/MM ²) AND LOW RESIDENCE TIME (67 μs); (B) LOW IRRADIANCE (62.9 kW/MM ²) AND HIGH RESIDENCE TIME (167 μs).	4-93
FIGURE 4-14: (A) AND (B) BSE MICROGRAPHS OF TRANSVERSE CROSS SECTIONAL MICROSTRUCTURE CORRESPONDING TO PROCESSED SURFACE SHOWN IN FIGURE 4-13 (A) AND (B) RESPECTIVELY.	4-94
FIGURE 4-15: EFFECTS OF PRE-TREATMENTS AND RESIDENCE TIME ON MELTPOOL DEPTH.	4-95
FIGURE 4-16: EFFECTS OF LASER PROCESSING ON 316L HARDNESS COMPARED TO AS RECEIVED MATERIAL HARDNESS.	4-96
FIGURE 4-17: MICROGRAPH AND EDS SPECTRUM OF THE BULK 316L MATERIAL.	4-97
FIGURE 4-18: MICROGRAPH AND EDS SPECTRUM OF THE LASER MELTED 316L STAINLESS STEEL.	4-97
FIGURE 5-1: SEM MICROGRAPHS SHOWING THE PLANE VIEW OF (A) AS-RECEIVED AND (B) GRIT BLASTED Ti-6Al-4V	5-99
FIGURE 5-2: BACK SCATTER DETECTOR (BSE) SURFACE MORPHOLOGY IMAGES OF LASER SURFACE MODIFIED Ti-6Al-4V AT A CONSTANT RESIDENCE TIME OF 1.08 MS AND THREE LEVELS OF IRRADIANCE (A) 15.72, (B) 20.4 AND (C) 26.7 kW/MM ² .	5-100

FIGURE 5-3: BACK SCATTER DETECTOR (BSE) SURFACE MORPHOLOGY IMAGES OF LASER SURFACE MODIFIED Ti-6Al-4V AT A CONSTANT RESIDENCE TIME OF 1.44 MS AND THREE LEVELS OF IRRADIANCE (A) 15.72, (B) 20.4 AND (C) 26.7 kW/MM ²	5-100
FIGURE 5-4: BACK SCATTER DETECTOR (BSE) SURFACE MORPHOLOGY IMAGES OF LASER SURFACE MODIFIED Ti-6Al-4V AT A CONSTANT RESIDENCE TIME OF 2.16 MS AND THREE LEVELS OF IRRADIANCE (A) 15.72, (B) 20.4 AND (C) 26.7 kW/MM ²	5-100
FIGURE 5-5: GRAIN DISTRIBUTION ON THE SURFACE OF A SAMPLE LASER MELTED AT AN IRRADIANCE OF 26 kW/MM ² AND A RESIDENCE TIME OF 2.16 MS, IMAGED IN BSE MODE.....	5-101
FIGURE 5-6: CROSS-SECTIONAL MICROGRAPHS OF THE AS-RECEIVED Ti-6Al-4V OBTAINED VIA (A) OPTICAL MICROSCOPY AND (B) BSE.	5-102
FIGURE 5-7: CROSS SECTIONAL BSE MICROGRAPH OF LASER MODIFIED Ti-6Al-4V, OBTAINED VIA (A) OPTICAL MICROSCOPY AND (B) BSE.....	5-102
FIGURE 5-8: BACK SCATTER DETECTOR (BSE) SURFACE MORPHOLOGY IMAGES OF LASER SURFACE MODIFIED Ti-6Al-4V AT A CONSTANT LEVEL OF IRRADIANCE 15.72 kW/MM ² AND THREE LEVELS OF IRRADIANCE OF RESIDENCE TIME OF (A) 1.08 (B) 1.44 AND (C) 2.16 MS.	5-104
FIGURE 5-9: BACK SCATTER DETECTOR (BSE) SURFACE MORPHOLOGY IMAGES OF LASER SURFACE MODIFIED Ti-6Al-4V AT A CONSTANT LEVEL OF IRRADIANCE 20.4 kW/MM ² AND THREE LEVELS OF IRRADIANCE OF RESIDENCE TIME OF (A) 1.08 (B) 1.44 AND (C) 2.16 MS.	5-104
FIGURE 5-10: BACK SCATTER DETECTOR (BSE) SURFACE MORPHOLOGY IMAGES OF LASER SURFACE MODIFIED Ti-6Al-4V AT A CONSTANT LEVEL OF IRRADIANCE 26.72 kW/MM ² AND THREE LEVELS OF IRRADIANCE OF RESIDENCE TIME OF (A) 1.08 (B) 1.44 AND (C) 2.16 MS.	5-104
FIGURE 5-11: EFFECTS OF LASER IRRADIANCE AND RESIDENCE TIME ON MELTPOOL DEPTH FOR THE Ti-6Al-4V SAMPLES.	5-105
FIGURE 5-12: EFFECTS OF LASER IRRADIANCE AND RESIDENCE TIME ON MELTPOOL DEPTH FOR THE Ti-6Al-4V SAMPLES.	5-106
FIGURE 5-13: A GRAPH OF THE ACTUAL MELTPOOL DEPTH VERSUS THE PREDICTED VALUES.....	5-107
FIGURE 5-14: EFFECTS OF IRRADIANCE AND RESIDENCE TIME ON AVERAGE ROUGHNESS OF THE Ti-6Al-4V SAMPLES....	5-108
FIGURE 5-15: EFFECTS OF IRRADIANCE AND RESIDENCE TIME ON AVERAGE ROUGHNESS OF THE Ti-6Al-4V SAMPLES....	5-109
FIGURE 5-16: A GRAPH OF THE ACTUAL ROUGHNESS VERSUS THE PREDICTED VALUES.	5-110
FIGURE 5-17: EFFECTS OF IRRADIANCE AND RESIDENCE TIME ON MICROHARNESS.	5-111
FIGURE 5-18: A GRAPH OF THE ACTUAL MICROHARDNESS VERSUS THE PREDICTED VALUES.	5-112
FIGURE 5-19: MICROHARDNESS OF LASER SURFACE MODIFIED Ti-6Al-4V WITH RESPECT TO DEPTH FROM THE SURFACE FOR SAMPLE 9.....	5-113
FIGURE 5-20: X-RAY DIFFRACTION PATTERN OF UNTREATED Ti-6Al-4V.	5-114
FIGURE 5-21: XRD PATTERN OF UNTREATED AND LSM SAMPLES.	5-116
FIGURE 5-22: EFFECTS OF IRRADIANCE AND RESIDENCE TIME ON THE <i>β</i> -Ti PHASE.....	5-117
FIGURE 5-23: A GRAPH OF THE ACTUAL <i>β</i> -Ti VOLUME FRACTION VERSUS THE PREDICTED VALUES.....	5-118
FIGURE 5-24: EDS ANALYSIS OF THE Ti-6Al-4V TOPOGRAPHIC SURFACE (A) AREA SCAN AND (B) POINT ANALYSIS.	5-119
FIGURE 5-25: ELEMENTAL COMPOSITION USING DIFFERENT SCAN METHODS AND PROCESSING TIMES.	5-119

FIGURE 5-26: GRID SCAN MICROGRAPHS OF (A) UNTREATED AND (B) GRIT BLASTED Ti-6Al-4V.....	5-120
FIGURE 5-27: EDS SPECTRUM OF UNTREATED Ti-6Al-4V.....	5-121
FIGURE 5-28: EDS SPECTRUM OF GRIT BLASTED Ti-6Al-4V.....	5-121
FIGURE 5-29: EDS SPECTRUM OF LSM Ti-6Al-4V.....	5-121
FIGURE 5-30: TYPICAL EDS ANALYSES OF THE CROSS-SECTIONAL MICROSTRUCTURE PERPENDICULAR TO THE DIRECTION OF THE BEAM	5-122
FIGURE 5-31: EDS ANALYSIS OF TITANIUM COMPOSITION DISTRIBUTION IN SAMPLES 3, 6 AND 9.	5-122
FIGURE 5-32: EDS ANALYSIS OF ALUMINIUM COMPOSITION DISTRIBUTION IN SAMPLES 3, 6 AND 9	5-123
FIGURE 5-33: RELATIONSHIP OF WEAR TRACK AND DISTANCE TRAVELLED BY THE PIN.	5-124
FIGURE 5-34: 3D WEAR TRACK PROFILE OF (A) UNTREATED Ti-6Al-4V TESTED FOR 150 M, (B) LSM Ti-6Al-4V TESTED FOR 150 M AND (A) LSM Ti-6Al-4V TESTED FOR 20 M	5-124
FIGURE 5-35: MICROGRAPHS OF UNTREATED Ti-6Al-4V AT VARIOUS MAGNIFICATIONS, SAMPLES TESTED FOR 20 M...	5-125
FIGURE 5-36: MICROGRAPHS OF LSM 3 (26.72kW/MM ² AND 2.16 MS) AT VARIOUS MAGNIFICATIONS, SAMPLES TESTED FOR 20 M.....	5-125
FIGURE 5-37: MICROGRAPHS OF UNTREATED Ti-6Al-4V AT VARIOUS MAGNIFICATIONS, SAMPLES TESTED FOR 150 M.	5-126
FIGURE 5-38: MICROGRAPHS OF LSM 3 (26.72 kW/MM ² AND 2.16 MS) AT VARIOUS MAGNIFICATIONS, SAMPLES TESTED FOR 150 M.....	5-126
FIGURE 5-39: SPECIFIC WEAR RATES OF Ti-6Al-4V AT TWO SLIDING DISTANCES OF 20 AND 150 M.....	5-127
FIGURE 5-40: RELATIONSHIP OF SPECIFIC WEAR RATE AND MELT-POOL DEPTH FOR SAMPLES TESTED FOR 150 M.	5-127
FIGURE 5-41: EFFECTS OF LASER PROCESSING PARAMETERS ON SPECIFIC WEAR RATE OVER 20 M SLIDING DISTANCE.	5-128
FIGURE 5-42: ACTUAL SPECIFIC WEAR RATE VALUES VERSUS THE PREDICTED RESPONSE VALUES.....	5-129
FIGURE 5-43: OCP VARIATION WITH TIME OF IMMERSION FOR AS-RECEIVED, GRIT BLASTED AND LSM 3,6 AND 9 SAMPLES DURING IMMERSION IN 0.9 % NaCl AT 37°C.	5-130
FIGURE 5-44: OCP VARIATION WITH TIME OF IMMERSION FOR AS-RECEIVED, GRIT BLASTED AND LSM 1,4 AND 7 SAMPLES DURING IMMERSION IN 0.9 % NaCl AT 37°C.	5-131
FIGURE 5-45: OCP VARIATION WITH TIME OF IMMERSION FOR AS-RECEIVED, GRIT BLASTED AND LSM 2,5 AND 8 SAMPLES DURING IMMERSION IN 0.9 % NaCl AT 37°C.	5-131
FIGURE 5-46: POLARISATION CURVES OF AS-RECEIVED, GRIT BLASTED, LSM 4 AND LSM 7 Ti-6Al-4V SAMPLES IN 0.9% NaCl AT 37°C.....	5-132
FIGURE 5-47: POTENTIODYNAMIC POLARISATION CURVES OF AN UNTREATED AND LASER TREATED Ti-6Al-4V	5-133
FIGURE 5-48: LOCALISED CORROSION OF (A) AS-RECEIVED Ti-6Al-4V, (B) LSM 8 AND (C) MAGNIFIED VIEW OF SUB-SECTION FROM (B).	5-134
FIGURE 5-49: TYPICAL CONTACT ANGLES OF (A) POLISHED AND (B) GRIT BLASTED Ti-6Al-4V.	5-135
FIGURE 5-50: IMAGES OF CONTACT ANGLES ON LASER SURFACE MODIFIED Ti-6Al-4V AT A CONSTANT IRRADIANCE OF 15.72kW/MM ² AND THREE LEVELS OF RESIDENCE TIME (A) 1.08, 1.44 AND 2.16MS.....	5-136
FIGURE 5-51: IMAGES OF CONTACT ANGLES ON LASER SURFACE MODIFIED Ti-6Al-4V AT A CONSTANT IRRADIANCE OF 20.43kW/MM ² AND THREE LEVELS OF RESIDENCE TIME (A) 1.08, 1.44 AND 2.16MS.....	5-136
FIGURE 5-52: IMAGES OF CONTACT ANGLES ON LASER SURFACE MODIFIED Ti-6Al-4V AT A CONSTANT IRRADIANCE OF 26.72kW/MM ² AND THREE LEVELS OF RESIDENCE TIME (A) 1.08, 1.44 AND 2.16MS.....	5-136

FIGURE 5-53: EFFECTS OF IRRADIANCE AND RESIDENCE TIME ON CONTACT ANGLE.	5-137
FIGURE 5-54: CONTOUR PLOT HIGHLIGHTING THE EFFECTS OF IRRADIANCE AND RESIDENCE TIME ON MEASURED CONTACT ANGLES.	5-137
FIGURE 5-55: A GRAPH OF THE ACTUAL CONTACT ANGLES OF UNPOLISHED LASER TREATED SAMPLES VERSUS THE PREDICTED VALUES.	5-139
FIGURE 5-56: RELATIONSHIP BETWEEN ENERGY DENSITY AND CONTACT ANGLES.	5-139
FIGURE 5-57: EFFECTS OF CONTACT ANGLE IRRADIANCE AND RESIDENCE TIME ON CONTACT ANGLES OF POLISHED SAMPLES	5-140
FIGURE 5-58: CELLULAR ATTACHMENT AT 2 HOURS SHOWN AS A PERCENTAGE OF THE NUMBER OF CELLS ORIGINALLY SEEDED.	5-142
FIGURE 5-59: RELATIONSHIP BETWEEN CONTACT ANGLE OF UNPOLISHED LSM SAMPLES AND CELL ATTACHMENT	5-142
FIGURE 5-60: EFFECTS OF ROUGHNESS ON CELL ATTACHMENT	5-143
FIGURE 5-61: METABOLIC ACTIVITY AT 24 HR, 96 HR, AND 7 DAYS * ($P<0.05$).	5-143
FIGURE 5-62: METABOLIC ACTIVITY SHOWN AS PERCENT REDUCTION.	5-144
FIGURE 5-63: CELL NUMBER AS MEASURED ON DAY 3 AND DAY 7 * ($P<0.1$).	5-144
FIGURE 5-64: EFFECT OF Ti-6Al-4V SAMPLES IN DIRECT CONTACT WITH NIH/3T3 FIBROBLASTS FOR 24 HR USING THE MTT CELL VIABILITY ASSAY AS A MEASURE OF TOXICITY.	5-145
FIGURE 5-65: EFFECT OF VARIOUS CONCENTRATIONS OF Ti-6Al-4V SAMPLE EXTRACT IN CONTACT WITH NIH/3T3 FIBROBLASTS FOR 24 HR USING THE MTT CELL VIABILITY ASSAY AS A MEASURE OF TOXICITY.	5-146
FIGURE 5-66: SCHEMATIC OF THE LASER MELTED POOL PERPENDICULAR TO THE DIRECTION OF LASER BEAM MOVEMENT [97].	6-147
FIGURE 5-67: IRRADIANCE OF THE TEM MODE AS A FUNCTION OF DISTANCE ACROSS THE LASER BEAM [234].	6-148
FIGURE 5-68: (A) CROSS SECTIONAL BSE MICROGRAPH OF LASER MODIFIED Ti-6Al-4V, (B) LASER MODIFIED LAYER AND (C) SUBSTRATE MICROSTRUCTURE.	6-149
FIGURE 5-69: EFFECTS OF ENERGY DENSITY ON MELTPOOL DEPTH.	6-152
FIGURE 5-70: RELATIONSHIP BETWEEN ENERGY DENSITY AND ROUGHNESS.	6-153
FIGURE 5-71: BSE MICROSTRUCTURAL IMAGES OF (A) UNTREATED AND (B) LASER TREATED Ti-6Al-4V; AND (C) X-RAY DIFFRACTION PATTERN OF UNTREATED AND LASER TREATED Ti-6Al-4V.	6-155
FIGURE 5-72: EFFECTS OF ENERGY DENSITY ON THE VOLUME FRACTION OF THE β -Ti PHASE.	6-156
FIGURE 5-73: EFFECTS OF ENERGY DENSITY ON SPECIFIC WEAR RATE.	6-158
FIGURE 5-74: POLARISATION CURVES OF AS-RECEIVED, LSM 7 AND LSM 8 Ti-6Al-4V IN 0.9% NaCl AT 37°C.	6-160
FIGURE 5-75: RELATIONSHIP BETWEEN CONTACT ANGLE AND ROUGHNESS OF THE LSM SAMPLES.	6-163
FIGURE 5-76: RELATIONSHIP BETWEEN CONTACT ANGLE AND ROUGHNESS WITHOUT THE OUTLIER.	6-163
FIGURE 5-77: CONTACT ANGLES OF POLISHED AND UNPOLISHED SAMPLES, WHERE AR IS AS-RECEIVED, GB IS GRIT BLASTED AND 1-9 ARE LASER MODIFIED SAMPLES.	6-164

Nomenclature

<i>Symbols/ Acronym</i>	<i>Description</i>	<i>Units</i>
α	Thermal diffusivity	m ² /s
λ	Emission wavelength	μm
ρ	Density	g/cm ³
σ_i	Resistance of the crystal lattice to dislocation	-
σ_y	Yield stress	MPa
τ	Pulse width	s
v	Scan speed	mm/s
γ_{LV}	Interfacial energy of liquid–vapour interface	-
γ_{SL}	Interfacial energy of the solid–liquid interface	-
γ_{SV}	Interfacial energy of the solid–vapour interface	-
<i>2FI</i>	Two factor interaction model (DOE)	-
<i>A</i>	Absorption coefficient	-
<i>BCC</i>	Body-centred cubic crystal structure	-
<i>BSE</i>	Back scatter electrons	-
<i>CW</i>	Continuous mode (laser operation)	-
d	Beam diameter at the lens inlet	mm
d_g	grain diameter	nm
<i>DMSO</i>	Dimethyl sulfoxide	-
D_s	Diameter of the spotsize	mm
E_f	Energy Density	J/mm ²
E_p	Pulse energy	J

<i>Symbols/ Acronym</i>	<i>Description</i>	<i>Units</i>
<i>f</i>	Focal length of the lens	mm
<i>HA</i>	Hydroxyapatite	-
<i>HCP</i>	Hexagonal close packed structure	-
<i>I</i>	Irradiance	W/mm ²
<i>k</i>	Thermal conductivity	W/m-K
<i>k_g</i>	Hardening contribution of the grain boundaries	-
<i>L_p</i>	Length to be laser processed	mm
<i>LSA</i>	Laser surface	-
<i>LSM</i>	Laser surface modification/modified	-
<i>m</i>	Mass of melted material during the residence time	g
<i>MTT</i>	Tretrazolium salt	-
<i>N</i>	Number of laser spots per unit length	-
<i>O</i>	Overlap	%
<i>OCP</i>	Open circuit potential	mV
<i>P</i>	Laser power	W
<i>PBS</i>	Phosphate-buffered saline	-
<i>PE</i>	Polyethylene	-
<i>PM</i>	Pulsed Mode (laser operation)	-
<i>PRF</i>	Pulse repetition frequency	Hz
<i>PTFE</i>	Polytetrafluoroethylene (also known as Teflon)	-
<i>Q</i>	Heat energy	J
<i>r</i>	Radius of spherical section of melt pool	m

<i>Symbols/ Acronym</i>	<i>Description</i>	<i>Units</i>
<i>R</i>	Residence Time	s
<i>Ra</i>	Mean surface roughness	μm
<i>r_b</i>	Radius of the beam spot	m
<i>SE</i>	Secondary electrons	-
<i>SEM</i>	Standard error of mean	-
<i>SCE</i>	Saturated calomel electrode	-
<i>t</i>	Time	s
<i>t₁</i>	Heating time	s
<i>t₀</i>	Time necessary for heat to diffuse over a distance equal to the laser beam radius on the work-piece surface	s
<i>T₀</i>	Ambient temperature	K
<i>TEM</i>	Transverse mode of the laser beam (Transverse Electro-Magnetic)	-
<i>THR</i>	Total Hip Replacements	-
<i>TiN</i>	Titanium nitride	-
<i>UHMWPE</i>	Ultra-high molecular weight polyethylene	-
<i>w_o</i>	Initial beam radius at focus	mm
<i>w_z</i>	Beam radius along the propagation line	mm
<i>z</i>	Distance to focus below the surface of work-piece	mm
<i>z₀</i>	Distance over which heat can diffuse during the laser beam interaction time.	mm
<i>XRD</i>	X-ray diffraction	-

Chapter 1

Introduction

1.1 Overview

Average life expectancy of humans in the developed world has seen a huge increase due to ever improving availability of medical facilities. Human joints, especially in aged persons, are prone to degenerative and inflammatory diseases that result in pain and stiffness of joints [1]. Approximately 90% of the population over the age of 40 suffer some degree of degenerative joint disease [2]. One in four hundred people receive hip replacement surgeries in Ireland and more than 250,000 hip replacements surgeries occur annually in the USA [3-5]. The demand of total hip arthroplasty is estimated to grow to 572,000 in USA alone by the year 2030 [3]. Approximately 10 to 20% of hip replacement surgeries that occur are replacements of failed implants [6]. Operation success rate has significantly increased but the lifespan of the implant after operation is still lower than required. Typical implant life times of ten years are common leading to the same patient having to go through the same procedure several times in their life [5, 6]. This presents a low quality of life and proves to be costly for both the patient and the state [7]. Developing affordable and improved lifelong biomaterial and manufacturing technology remains a challenge for material engineers; which is the present focus of this study.

The most common reasons for revision of hip replacement, according to the Canadian Joint Replacement Registry (CJRR) in 2004, were loosening of implants, osteolysis, implant wear and infection [8]. Causes of implant failure are interrelated; loosening of implants is mainly due to infection of surrounding tissue which is caused by release of ions and accumulation of tiny particles due to wear and corrosion of the implant [6, 9]. The interaction between the implant material and surrounding physiological environment is of high importance. Unsatisfactory interaction may lead to either failure of the implant to function as it was intended, or have an adverse effect on the patient resulting in the rejection of the implant by the surrounding tissue, or both [10].

To combat the mechanical degradation leading to early removal of the implant, thus extending the life of the implant, laser surface modification was investigated, as presented in this thesis, to improve the microstructure, tribological, wear, corrosion and biocompatibility properties of 316L stainless steel and Ti-6Al-4V. In this context, the

work was mainly focused on high speed laser processing for application on the femoral stem and the prosthetic hip bearing head. For biomedical implants different properties are required at different locations of the implant which needs to be manufactured at reasonably high manufacturing rates. This is the case for the three parts of a typical hip replacement, namely, the femoral stem, the femoral head and the acetabular cup. All three components require different properties in order to have a good functional prosthesis [11].

Manufacturing of implants involves a range of factors that are governed by regulatory requirements, patient needs, durability cost, dimensions and weight of implants. The current manufacturing techniques for hip implants do not allow for custom designing for specific patient needs with a rapid turnaround; instead surgeons are forced to adapt existing designs to fit the patients' requirements [12]. An imperative need exists for functionally graded hip implants representing a better balance of properties via novel high speed laser processing techniques. Even though the work presented mainly focuses on hip replacements, the processing technique can be applied to a wide range of biomedical implants where improved wear and corrosion resistance are necessary. Figure 1-1 highlights different implants in which this technology could be applied.

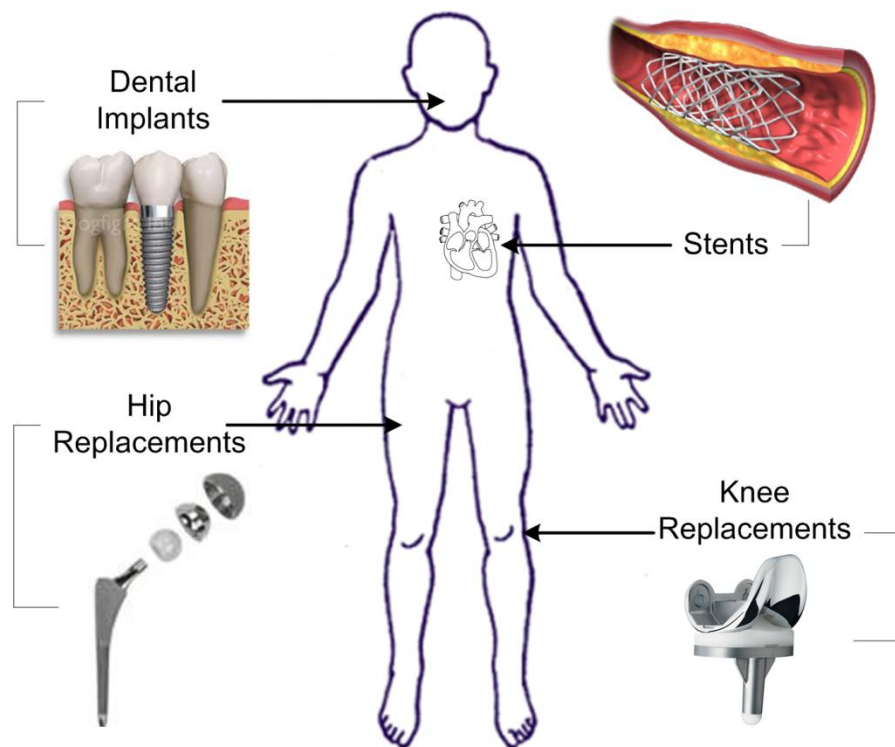


Figure 1-1: Metallic implants that can be improved via laser surface modification [13, 14].

1.2 Statement of Investigation

Laser surface modification plays a dual role: minimizing the release of metal ions by making the surface harder, wear and corrosive resistant, as well as making the surface more bioactive and stimulating bone growth due to improvement in wettability and lower local surface energies [15]. The aim of this study was to provide for improved performance characteristics of biomedical implants thus improving the quality of life of their recipients. This study investigated the effects of high speed laser surface modification of two common biomedical alloys i.e. 316L Stainless Steel and Ti-6Al-4V. The objective was to improve the hardness, wear resistance, corrosion behaviour, and bio-compatibility, by transforming the surface microstructure through high speed laser treatment.

Laser melting of material to improve their scope of application has widely been investigated for several applications including aerospace, automotive parts and tooling. Although this process has been applied to industrial engineering components and alloys, very few investigations have been carried out for biomedical implants. The focus of this study is on biomedical implants, particularly hip replacements. Previous studies on laser processing of biomedical alloys have concentrated on combinations of lower irradiances and higher residence times than are currently possible with newer laser systems [16-20]. Previous work has demonstrated that higher irradiances and lower residence times provide enhanced microstructure and corrosion properties [18, 19, 21]. Most studies of laser modification of biomedical alloys presented in the literature are based on low speed laser processing and use of alloying elements (e.g. laser nitriding) to improve the material properties.

The present study is not limited to the aforementioned processing parameters. The work presented in this thesis provides new insights into the laser surface modification of biomedical alloys. The thesis explores the results of both tried and tested methods as well as marshalling enhanced techniques for modifying biomedical alloys. The current work is separated from other studies due to extensive study of:

- | | |
|---|---|
| i. High speed laser treatment | vi. Hip replacement application |
| ii. High power densities | vii. Pulsed laser treatment |
| iii. Extremely low exposure times | viii. Unalloyed laser treatment |
| iv. Use of cylindrical samples | ix. Creation of crack free surfaces |
| v. Micrometre laser spot size resulting in high power densities | x. Characterisation including biological interactions |

1.3 Thesis Outline

The thesis has been laid out in a progressive manner that initially introduces the reader to the problem at hand. Background knowledge relating to the subject is then presented, followed by the material and methods used in the work. The results from the study are the elucidated followed by discussions and conclusions. The contents of each chapter are highlighted below:

Chapter 2 – The aim of the chapter is to introduce the reader to the several subjects the thesis encompasses. The chapter reviews the necessary background theory of hip replacements, surface engineering, biomaterial and the reasons behind the choice of material and processes used in this research. Chapter 2 also reveals previous work carried out in this field, highlighting the short-comings that need improvements and further study. The chapter focuses on the various laser surface modification techniques implemented in literature. The chapter also elucidates a survey of processing parameters previously implemented and their effects on surface properties.

Chapter 3 – The chapter aims on revealing the materials and methods used, and allow for experimental repeatability by readers. The chapter outlines the material preparation, procedures and design of experiments implemented in this research.

Chapter 4 – The chapter disseminates results obtained from laser surface melting of 316L stainless steel. The results are split into two sections Design of Experiments 1 and 2. Each section analyses the resulting microstructure, meltpool profile, roughness, hardness and chemical composition induced by laser surface modification.

Chapter 5 – Results obtained from laser surface melting of Ti-6Al-4V are elucidated in this chapter. The main focus of this research study was on Ti-6Al-4V; therefore each section thoroughly investigates the effects of laser surface melting on microstructure, melt profile, roughness, hardness, phase transformation, chemical composition, wear, corrosion, wettability, cell attachment and cytotoxicity.

Chapter 6 – The chapter discusses the findings of Ti-6Al-4V results presented in chapter 5.

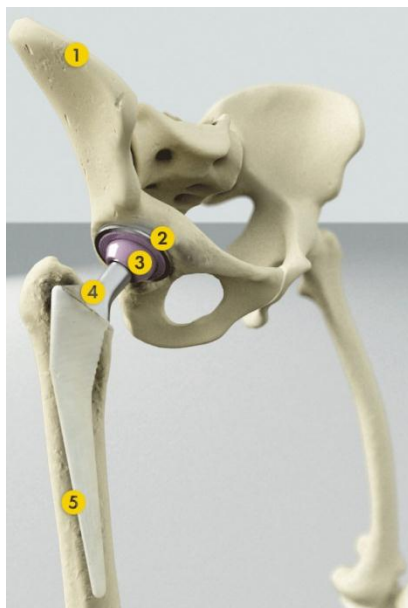
Chapter 7 – This chapter presents an overall discussion of the study and concludes by highlighting the most important findings and recommendations for future research work.

Chapter 2

Literature Review

2.1 Hip Replacement Prosthesis

Total hip replacement (THR) is one of the most commonly performed orthopaedic procedures and has been shown to improve functional status and relieve the pain often associated with osteoarthritis, rheumatoid arthritis and traumatic arthritis [7, 22, 23]. Figure 2-1 highlights the anatomy of a hip with a typical prosthetic inserted.



1. Pelvis
2. Acetabulum with uncemented prosthesis
3. Prosthetic femoral head
4. Neck of femoral prosthesis
5. Femoral prosthesis within the femur

Figure 2-1: Hip anatomy with prosthetic implant inserted [24].

The hip replacement prosthesis is made up of two main parts, the femoral and acetabular components. Earlier hip replacements were made of single-piece femoral and acetabular components. Current implant models have adapted the modular design that has a separate femoral head. Having separate components allow surgeons to adjust for variable leg sizes/offset and also gives them material choice options. The modern acetabular component also has two components the metal shell and inner liner which can be made of either metal or polymer. Surface modification in this research targets the metallic femoral head and stem component, see Figure 2-2. Each region of the femoral component has different functions and thus different material properties requirements.

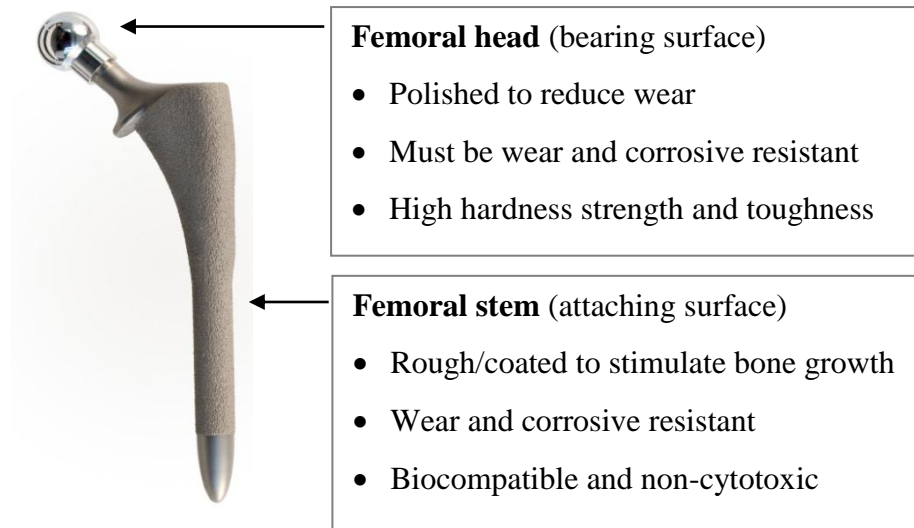


Figure 2-2: A typical femoral component of a THR indicating necessary requirements.

2.1.1 Femoral head

Femoral head is the part of the femoral component that interfaces with the acetabular cup. The modern femoral head has increased in diameter compared to previous designs, typically >38 mm, to increase stability and reduce risks of dislocation [25, 26]. The femoral head is typically made of metal. The main requirements of the femoral head component include: extremely low roughness, high hardness, high wear and corrosion resistant, and non-cytotoxic of released ions/debris.

The femoral head has to have extremely low average roughness (Ra), typically less than 26 nm [27, 28]. Low roughness in bearing surfaces is necessary as it reduces the wear rate of the surface. High hardness also plays a part in increasing the surfaces wear resistance subsequently minimising metal ion release. Aseptic loosening usually occurs when wear particles form at the bearing surfaces of the implant due to friction at the joint, which induces biological responses and causes osteolysis. These wear particles are composed of microscopic grains of bearing material. Wear resistance of the modified layer will be assessed to highlight effects of laser melting. Another crucial property is that the metal ions released should be non-toxic. Cytotoxicity of released metallic ions can affect the surrounding tissue thus leading to the loosening of the implant. Other necessary properties crucial in bearing surfaces include: good fracture toughness, yield strength and density. These properties are not the focus of this study since conventional biomedical alloys used in this research meet the minimum requirements and these properties are insignificant contributing factors to the majority of implant removals.

2.1.2 Femoral stem

The femoral stem is part of the prosthesis that fits into the femur (thigh bone). Bone is firstly removed from the femur and shaped to fit the dimensions of the stem. The fixation can either be cemented or cementless. Cementless implants are used in younger, more active, patients while cemented implants are used for older patients where there will be less post-operative activity or in cases of reduced bone density. Cemented fixations commonly use acrylic cements while cement-less fixations are held in place by friction and aid of surface coatings that simulate bone-to-implant bonding. The stem is made of metallic alloys mainly titanium based, cobalt chrome alloys and 316L stainless steel [29].

The main requirements for femoral stems include: excellent osseointegration, high wear and corrosion resistance. Osseointegration refers to the direct structural and functional connection between living bone and the surface of a load-bearing artificial implant without intervening connective tissue. The implant material has to permit bone cells to attach and proliferate on the surface without imposing cytotoxic risks. This required that the laser treated surface be tested for its ability to permit cells to attach and proliferate. Wear accelerated by corrosion also plays a part in the mechanical degradation. This type of corrosive degradation can progress little by little for many years on the surface of material attaching to the surrounding tissue [13]. Thus, the factors inducing corrosion in implants should be examined to improve corrosion resistance of femoral bearing surfaces. Other properties necessary in femoral stem requirements include: low elastic modulus (close to bone in order to prevent stress shielding), high strength, good fatigue resistance and good fracture toughness.

2.2 Conventional Biomaterials Used in Hip Replacements

The three main types of material currently being used in hip replacement components are ceramics, polymers and metals [30, 31]. Applications of non-metallic biomaterial in load bearing systems are limited to some extent due to their inferior mechanical properties such as lower fracture toughness in the case of ceramics and lower strength in the case of polymers.

Ceramics are used in bearing surfaces primarily due to their superior wear resistance that reduces metal ion release compared to metal alternatives. Ceramics also possess high hardness, good biocompatibility, excellent corrosion resistance properties and are less difficult to process compared to other material types. The most popular biomedical ceramics are alumina (Al_2O_3) and zirconia (ZrO_2) [31, 32]. Alumina is the most

common orthopaedic ceramic, usually used in femoral heads in hip replacements and wear plates for knee replacements [33]. The main concern related to ceramic implants is the limited lifetime due to their inferior fracture toughness and mechanical integrity brought about by their brittle nature [31]. This has been evidenced in 2001, by the recall of thousands of ceramic femoral heads by their manufacturer -St. Gobain Desmarquest [34]. Salts like hydroxyapatite (HA) can be crystallised from calcium phosphate and since the mineral phase of bone and teeth closely resemble HA, it has high biocompatibility properties. The properties and use of HA as a biomaterial are well established and documented [35]. The major drawback of this HA is its poor mechanical properties. Its fracture toughness (K_{IC}) is less than $1.2 \text{ MPa m}^{0.5}$. On the other hand, the fracture toughness of human bone ranges from 2 to $12 \text{ MPa m}^{0.5}$. Therefore, the application of HA is limited to low load bearing applications, coatings, or porous implants [36].

Polymers are used as bone biomaterial due to their high corrosion resistance and biocompatibility properties. The use of these polymers in total hip replacements is restricted due to their insufficient mechanical properties [33]. The most common polymers used in orthopaedics include polytetrafluoroethylene (PTFE), polyethylene (PE), ultra-high molecular weight polyethylene (UHMWPE) and acrylic. PTFE polymers were largely used as acetabular cups in THR until a discovery of their poor wear resistance and distortion characteristics. PTFE acetabular cups have since been discontinued. PE has widely been used on metallic bearing surfaces in knee and hip total joint replacement. However, polyethylene cups created debris due to wear of interfacial adhesion between tissues and the implant. This debris is attacked by the immune system causing bone loss. Studies have revealed that although polyethylene is biologically inert as a whole, microscopic particles released due to wear have a toxic effect that may lead to osteolysis if realised in large amounts. This may also lead to loosening of the implant. Osteolysis is mainly triggered by polyethylene wear particles in the size range of $0.2 \pm 0.1 \text{ mm}$ which are phagocytosed by macrophages leading to the release of inflammatory mediators, or cytokines, which act upon other cells and also lead to bone resorption [31, 37, 38]. Since their discovery, polymers made of lactic acid became more popular in the medical field due to their high stable structure leading to biodegradability.

The aforementioned concerns with ceramics and polymers have renewed an interest in metal-on-metal bearing surfaces on implants, particularly on large contact areas [39, 40]. Tipper *et al.* revealed that metal wear particles isolated were an order of magnitude

smaller than polyethylene particles. Up to 100-fold more particles were produced per unit volume of wear compared to polyethylene [41]. Lower wear rates are critical in extending the life of the implant; especially in orthopaedics since most of the revision surgeries are now due to wear and loosening of the implants. The primary focus was on metals for this study due to:

- i. Concerns with ceramics and polymers, primarily reduced lifetime in ceramics and high ion release in polymers.
- ii. Metals can be used in both the femoral head and stem.
- iii. The most successful material combinations for total artificial hip joint replacements have been ultra-high molecular weight polyethylene (UHMWPE) sliding against metallic counterfaces.
- iv. Laser surface modification of metallic alloys is less complicated and highly repeatable compared to laser surface modification of polymers or ceramics.
- v. Surface modification of metals produce more significant microstructural changes compared to those seen for polymer and ceramic materials.

2.3 Metallic Biomaterials

Some of the desirable properties required in hip replacement include, high biocompatibility, excellent mechanical properties like hardness, static and fatigue strength, thermal conductivity, low friction and mechanical shock resistance. Metallic implants all share these properties making them the most used material type for joint replacements [29, 32]. Metals also provide high X-ray imaging visibility which is crucial during inspection. Tribological properties like wear and corrosion resistance also play a crucial part in joint replacement. The major drawback in metallic implants is that electrochemical reactions take place on metallic surfaces in the human body. Metals are known to corrode in contact with body fluid environments. Most cells cannot metabolise the corroded particles therefore giving rise to harmful infection to the body. Improved tribological properties reduce toxic ions from being released in vivo. Contamination of ions released from joint replacements is still a major issue that needs to be resolved for metallic biomaterials.

When designing biomedical implants two main categories of properties should be taken into consideration; surface properties that affect bio integration and also the bulk properties that meet the mechanical requirements. Figure 2-3 shows properties of an ideal hard tissue replacement biomaterial. It is considerably difficult to obtain a material that can achieve both mechanical and biological property requirements.

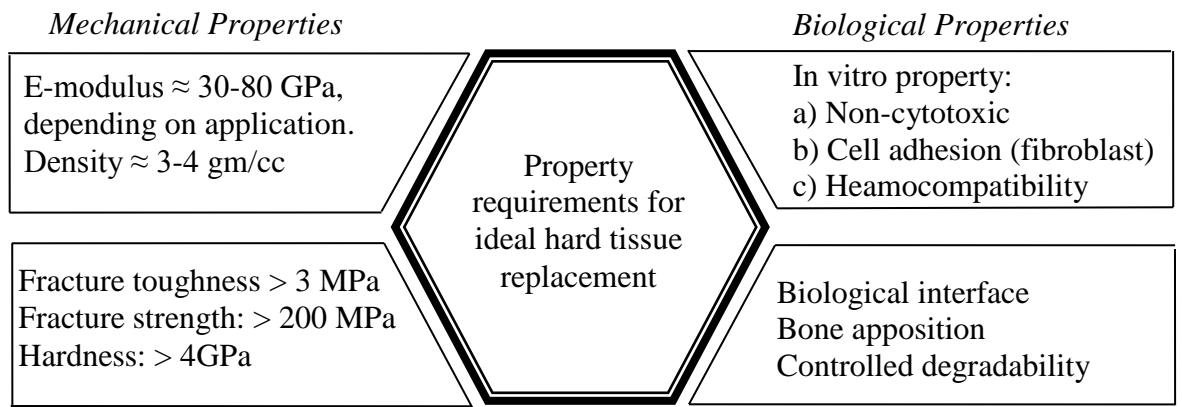


Figure 2-3: Properties of an ideal hard tissue replacement biomaterial [2]

The three most dominant metals used in joint replacements are AISI 316L stainless steel, cobalt-chrome alloys (Co-Cr) and titanium alloys (Ti-6Al-4V) [29, 31]. A comparison of properties of 316L stainless steel, Co-Cr, Ti-6Al-4V alloys and cortical bone are listed in Table 2-1. There has also been recent interest in magnesium to be used as an orthopaedic biomaterial due to its light weight and mechanical properties which are similar to natural bone structure [42]. Magnesium was not examined in this work. One drawback of magnesium is its biodegradability nature which makes it impractical in load bearing systems. Co based alloys were also not studied in this work. One problem that has occurred with Co based alloys is their release of toxic ions which recently instigated a recall of the DePuy ASR ® hip replacements [43].

Table 2-1: A comparison of the properties of orthopaedic metals to cortical bone [2, 29]

	<i>316L SS</i>	<i>Co-Cr-Mo</i>	<i>Ti-6Al-4V</i>	<i>Cortical bone</i>
<i>Modulus of elasticity (GPa)</i>	190	240	110	10 – 16
<i>Bending strength (MPa)</i>	485	825	900	120
<i>Hardness (GPa)</i>	235	430	325	-
<i>Ductility</i>	40	10	12	0 - 2

2.3.1 316L stainless steel

Type 302 was the first stainless steel to be used for implant fabrication but was later replaced by 316 stainless steel which contains a small percentage of molybdenum for improved corrosion resistance. In 1950, 316 stainless steel was further improved by reducing the carbon content to a maximum of 0.03 % from 0.08 % to reduce the risk of intergranular corrosion attacks [32]. This became known as 316L stainless steel, where the “L” stands for low carbon content. Additional molybdenum also enhances corrosion pitting in vivo. 316L stainless steel has become the most popular stainless steel used for

biomedical implants due to its improved corrosion resistance properties. The American Society of Testing Materials (ASTM) also recommends this type of steel in implant fabrication [32]. Nickel content in 316L is set at maximum of 17 to 20%. This composition is suitable for stabilising the austenitic phase at room temperature and also enhance the corrosion resistance. However, large ratios of Ni: Cr concentrations were also found to impose allergic infections to the host body [44]. The minimum amount required for maintaining the austenitic phase is 10% Ni. Small amounts of silicon are present in the steel composition. Silicon increases the hardness of ferrite, oxidation resistance and is an effective deoxidizer. Even with the detailed compositions, it should be noted that 316L steel may corrode under certain circumstances in a highly stressed and oxygen depleted region. It is therefore crucial to modify the surface of the metal to improve the wear resistance, corrosion resistance and fatigue strength of 316L steel [32].

Figure 2-4 shows the microstructure of 316L stainless steel containing about 0.1 % C by weight, alloyed with iron. The steel has two major constituents, which are ferrite and pearlite. The light coloured region of the microstructure is the ferrite. The dark regions are the pearlite and the grain boundaries between the ferrite grains are visibly clear. Pearlite is made up from a fine mixture of ferrite and iron carbide, which can be seen as a "wormy" texture [45]. Pearlite is hard and it gives the steel strength. The ferrite is soft and it gives the steel ductility and toughness. If the amount of carbon in the steel is increased, this increases the amount of pearlite in the steel. This has the effect of increasing the strength, but it also decreases the ductility and toughness [46].

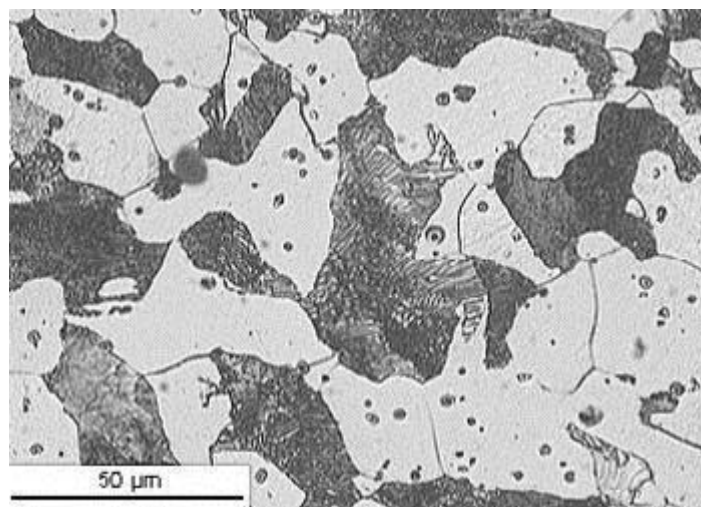


Figure 2-4: 316L stainless steel microstructure containing low carbon content [45].

Small spots within the ferrite grains, visible in Figure 2-4, are inclusions or impurities such as oxides and sulphides. The properties of the steel depend upon the microstructure. Decreasing the size of the grains improves the strength and decreasing the amount of pearlite, increases the ductility and the toughness of the steel [45].

Phase diagram: Some mechanical properties of 316L stainless steel are a function of its microstructures, and consequently, its thermal history. Phase diagrams are crucial in understanding the melting and crystallisation of the alloy. Phases in an alloy can be described as homogeneous portions that have uniform physical and chemical characteristics [47]. In the case of 316L a binary alloy (Iron-Carbon) phase diagram is used to describe the characteristic phase transformations. Figure 2-5 show the iron rich portion of the Fe-C phase diagram. Only 0.02% C is present in 316L stainless steel therefore only the area along the left vertical axis is considered.

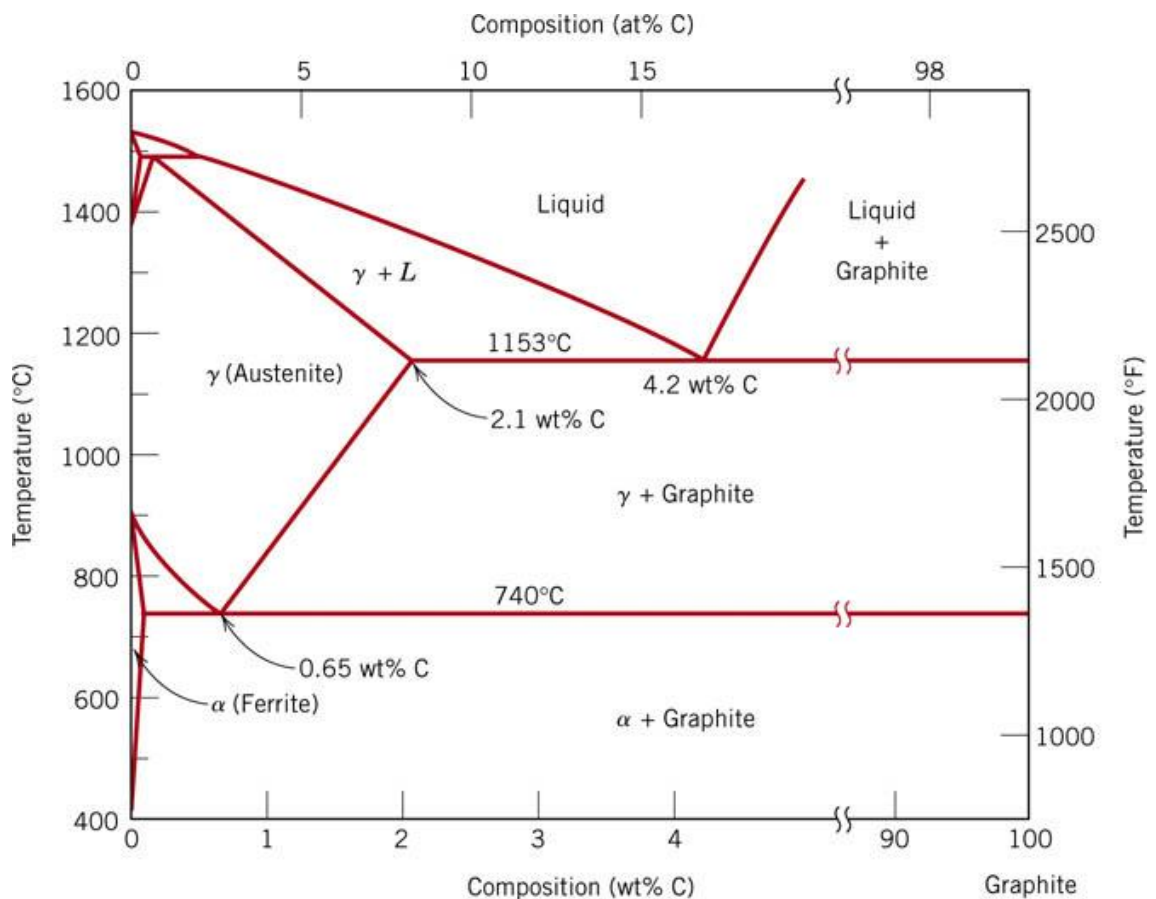


Figure 2-5: The iron-carbon binary phase diagram [47].

There are two crystal structure transformations that occur in iron before melting. Stable ferrite (α iron) with a BCC crystal structure exists at room temperature. At approximately 912 °C, a polymorphic transformation occurs; ferrite becomes an FCC austenite (γ iron). At 1394 °C, the austenite reverts to a BCC ferrite (δ iron) structure.

The structure is similar to that of α iron except that it is stable at high temperatures. When alloyed just with carbon the austenite phase is known to be unstable at temperatures below 727 °C. Addition of alloying elements, i.e. in 316L stainless steel, stabilised the structure at lower temperatures. Melting finally occurs at approximately 1538 °C. In iron alloys like 316L SS, carbon is an interstitial impurity which forms solid solutions with α and δ ferrites as well as the austenite. Carbon in iron alloys significantly influences the mechanical properties of ferrite regardless of the small weight percentage (0.2%). The ferrite phases are known to be relatively soft. Mechanically, cementite is very hard and brittle, steels with the presence of cementite increase in strength.

It should be noted that addition of other alloying elements (Cr, Ni, Ti, etc.) brings about changes in the Fe-C phase diagram. Alloying elements alter the temperature of the eutectoid reaction and the relative fraction of pearlite and the pro-eutectoid phase that form. The phase transformation shown in Figure 2-5 assumes extremely slow cooling rates. Heat treatment for improved hardness properties is extremely difficult at such low cooling rates. Laser melting on the other hand can produce extremely high cooling rates, 10^6 K/s can be easily achieved. Utilising such high cooling rates to low carbon steels can render them amenable to heat treatment. High quenching prevents low temperature phase transformations from occurring by only providing a narrow window of time in which the reaction is both thermodynamically favourable and kinetically accessible. This can allow for reduced crystallinity thereby increasing the mechanical properties like hardness and wear resistance. Introducing a martensite structure radically improves the steels hardness, this is achieved by rapidly cooling it through the eutectoid point at which the austenite is unstable.

Ion Release: The presence of nickel and chromium in 316L brings about ion release which is dangerous for the human body. 316L tends to release Ni ions that provoke allergies in some patients [48]. It has been proven that metal ion releases alter cellular protein and energy production therefore causing functional deficiencies in the macrophage's ability to direct inflammatory response [49]. To reduce the nickel and chromium release some biomedical implant manufactures coat the stainless steel with polyamides but these coatings present sites for platelet adhesion and the polymer is degraded by wear. It is also possible to oxidise the stainless steel by means of ion implantation which has shown better results compared to polyamides coating. However, the oxygen is incorporated to a very low depth from the stainless steel surface because of the low solubility and difficulty of this chemical reaction with the chromium. This

provokes a slight decrease of the ion release [48]. Recent reports have found that oxide formation plays a crucial role in ion release of metallic implants. Oxide films formed on metallic implants protect the surface from ion release [50, 51]. Hanawa noted that low concentrations of dissolved oxygen, the presence of inorganic ions, and the presence of protein cells, accelerate the metal ion release. Formation and regeneration of the oxide directly control the release rate.

Heat Treatability: Alloying provides the basis for the heat treatability of steel. While iron is the balance element in steel, carbon is the most important alloying element in terms of its strengthening effect on iron. The main challenge of laser modifying stainless steel for increased hardness is a well-known characteristic that the stainless steel does not harden through conventional heat treatment. Since CO₂ laser irradiation can be considered as a heat source, hypothetically, the same factors affecting heat treatability may also apply. However the study of CO₂ irradiation is still carried out since the exposure time and corresponding melt cooling rate is extremely rapid. One of the pre-requisites for hardening through heat treatment is sufficient carbon and alloy content, since diffusion rate is based on the differential of concentration. If there is sufficient carbon then the steel can be directly hardened through heat treatment, typically more than 0.25% C [52, 53], otherwise the surface of the work-piece has to be carbon enriched using some diffusion hardening treatment techniques. The carburising process occurs by exposing the work-piece to a carbon rich atmosphere at an elevated temperature thus allowing diffusion to transfer the carbon atoms into the steel [46].

2.3.2 Ti-6Al-4V

Titanium and its alloys have been used as implant material for various medical applications for more than 30 years. Titanium and its alloys are favourable to orthopaedic implants due to their high specific strength and fatigue resistance, excellent biocompatibility properties, and good corrosion resistance [54-56]. Titanium and its alloys are considered the most corrosion resistant of the implant metals presently employed, see Figure 2-6. The most widely used titanium alloy is the $\alpha+\beta$ alloy, Ti-6Al-4V, because of its high strength and low content of interstitial elements. A relatively new $\alpha+\beta$ alloy, Ti-13Nb-13Zr, uses niobium as β -phase stabiliser, and exhibits an interesting low elastic modulus [12].

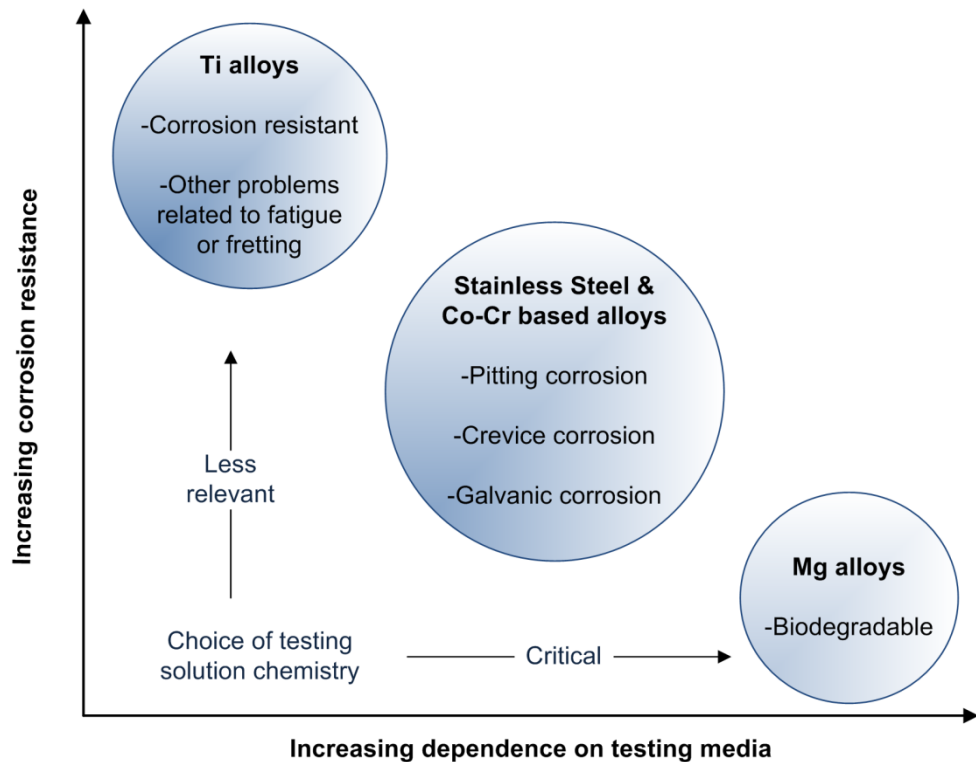


Figure 2-6: Metallic materials used in implants and their susceptibility to corrosion [57].

The interaction between titanium and body tissues, which allow osseointegration in contact with bone, is greatly advantageous over other metallic biomaterials. High biocompatibility and corrosion resistance is mainly credited to the ability of titanium to develop an oxide layer in contact with body fluids. Several authors have demonstrated the high biocompatibility properties of titanium and its alloys [31, 58, 59]. Another advantage of titanium is the non-ferromagnetic properties that allow for safe examination with magnetic resonance imaging thus making them useful as long term implants. Importantly the lower Young's modulus of titanium alloys compared to steel and Co-Cr alloys more closely matches that of bone thus reducing the effects of stress shielding.

A disadvantage of Ti-6Al-4V use arises from the wear and corrosion related release of harmful products including aluminium which is related to neurotoxin effects and vanadium which is cytotoxic [60, 61]. Release of vanadium ions by the way of passive dissolution or another process involving wear can cause discoloration of the surrounding tissue or an inflammatory reaction causing pain and even leading to loosening owing to osteolysis [62]. Corrosion fatigue triggered by body fluids is another factor limiting use of titanium for biomedical implants [63]. Titanium's corrosive resistance properties are credited to a tenacious oxide layer that forms on the surface of the metal. Improving the corrosion properties can be done by thickening the oxide,

nitriding and laser remelting. Ti-Al-V alloys exhibit very good corrosion resistance, but are subject to fretting and wear. Particles of the alloy have been found in surrounding tissue; rather than precipitated corrosion products due to uniform or localised corrosion [10, 64-66].

A common way of fabricating coatings on Ti substrate is plasma spraying of hydroxyapatite (HA). However, the long term stability of the plasma spray coated HA is currently limited due to occasional failure at the interface between coatings and substrate. In addition, the formation of amorphous calcium phosphate phase reduces the crystallinity and changes the chemical composition in the coatings. Modification of microstructure or composition of the alloy through conventional nitriding techniques has already been explored and is known to improve hardness of the material [67]. However, this process requires high treatment temperatures and extensive hours of processing. Ion implementation is another alternative process. Only a few micrometres of microstructure can be altered by this process and long processing times are required even for relatively small specimen sizes thus detracting from this option. Oxide thickening and nitriding methods have resulted in hard and brittle surface which cracks and flakes off easily when force is applied. These drawbacks bring about interest in using laser surface modification techniques as an alternative to achieve the improved tribological properties.

Phase diagram: Like most alloys, Ti-6Al-4V mechanical properties of depend on its microstructures, and consequently, its thermal history. To show the changes in microstructure with temperature variation a Titanium-Aluminum phase diagram is used, see Figure 2-7. The binary phase diagram shows the expected phases at equilibrium for different combinations of aluminium content In the Ti-Al phase diagram there are two allotropic forms of solid titanium: HCP α Ti which is stable at room temperature and up to 882 °C and BCC β Ti which is stable from 882 °C to the melting temperature. In Ti-6Al-4V, the alloying elements aluminum and vanadium are alpha and beta phase stabilisers, respectively. Aluminium is the only common metal that raises the beta transus temperature. The metal is miscible in both alpha and beta phase. Vanadium is a beta stabiliser that is completely miscible with β Ti. Only 6% Al is present in Ti-6Al-4V therefore Ti_3Al and other phases are not taken into account. It should be noted that the phase transformation shown in Figure 2-7 is only for slow cooling rates. Laser melting on the other hand can produce extremely high cooling rates therefore the phase diagram does not full highlight the resulting phases.

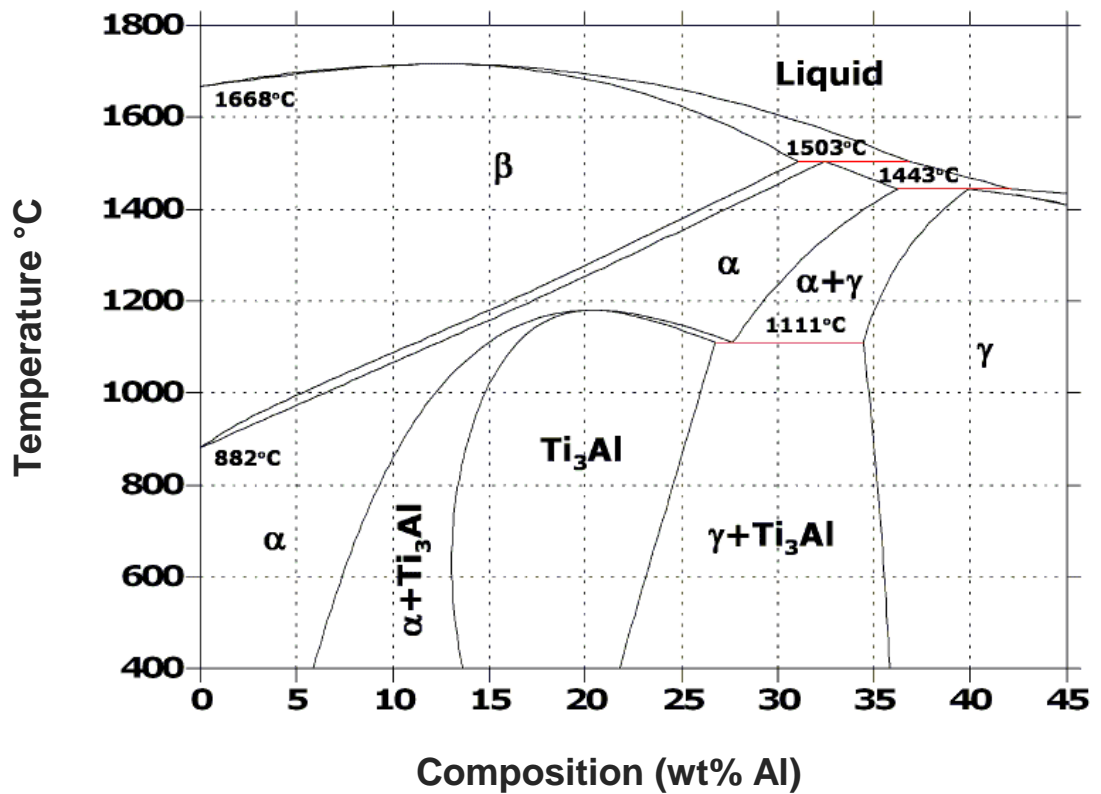


Figure 2-7: The titanium-aluminium binary phase diagram [68, 69].

Selection of Ti-6Al-4V: Titanium alloys usually have three microstructure categories: α , $\alpha+\beta$ and β alloys. Ti-6Al-4V falls under the $\alpha+\beta$ category and is mostly widely used due to the range of microstructural features that can be achieved via thermo mechanical and heat treatments [70, 71]. The α phase is a low temperature phase with a hexagonal closed packed (HCP) structure and the β phase is a high temperature phase with a body centred cubic (BCC) structure. Heating effects such as occur in weldments, casting and laser remelting, of the first eleven alloys listed in Table 2-2, generally result in properties (e.g. wear and corrosion) which are similar to the untreated counterparts. This is because these alloys contain so little alloy content and second phase that metallurgical instability and thermal effects are not significant [72]. Ti-6Al-4V was specifically chosen out of the remaining alloys due to its laser heat treatability and well known biocompatibility properties.

Table 2-2: Various commercial titanium alloys [72].

<i>Common Alloy Designation</i>	<i>Nominal Composition, wt%</i>	<i>ASTM Grade</i>	<i>Alloy Type</i>
Grade 1	unalloyed titanium	1	α
Grade 2	unalloyed titanium	2	α
Grade 3	unalloyed titanium	3	α
Grade 4	unalloyed titanium	4	α
Ti-Pd	Ti-0.15Pd	07-Nov	α
Ti-0.05-Pd	Ti-0.05Pd	16/17	α
Ti-Ru	Ti-0.1Ru	26/27	α
Grade 12	Ti-0.3Mo-0.8Ni	12	near α
Ti-3-2.5	Ti-3Al-2.5V	9	near α
Ti-3-2.5-Pd	Ti-3Al-2.5V-0.05Pd	18	near α
Ti-3-2.5-Ru	Ti-3Al-2.5V-0.1Ru	28	near α
Ti-6-4	Ti-6Al-4V	5	$\alpha+\beta$
Ti-6-4-ELI	Ti-6Al-4V(0.13% O max)	23	$\alpha+\beta$
Ti-6-4-Ru	Ti-6Al-4V-0.1Ru (0.13% O max)	29	$\alpha+\beta$
Ti-5-2.5	Ti-5Al-2Sn	-	α
Ti-8-1-1	Ti-8Al-1VMo	-	near α
Ti-6-2-4-2	Ti-6Al-2Sn-4Zr-2Mo	-	near α
Ti-550	Ti-4Al-2Sn-4Mo-0.5Si	-	$\alpha+\beta$
SP-700	Ti-4.5Al-3V-2Fe-2Mo	-	$\alpha+\beta$
Ti-6-6-2	Ti-6Al-6V-2Sn-0.6Fe-0.6Cu	-	$\alpha+\beta$
Ti-6-2-4-6	Ti-6Al-2Sn-4Zr-6Mo	-	$\alpha+\beta$
Ti-6-22-22	Ti-6Al-2Sn-2Zr-2Cr-2Mo-0.15Si	-	$\alpha+\beta$
Ti-10-2-3	Ti-10V-2Fe-3Al	-	near β
Ti-15-3-3-3	Ti-15V-3Sn-3Cr-3Al	-	β
Beta-21S	Ti-15Mo-2.7Nb-3Al-0.2Si	21	β
Ti-3-8-6-44 (Ti Beta-C™)	Ti-3Al-8V-6Cr-4Zr-4Mo	19	β
Ti-13-11-3	Ti-3Al-13V-11Cr	-	β

Conventionally pure metals solidify at a single temperature. Alloys on the other hand solidify over a temperature range during which they are in the semi-solid state. Solidification, from the liquid, proceeds from nucleation to solid growth to a fully solidified metal. All industrially important alloys, when solidified from a molten state under certain conditions, form dendrites. The size, shape, and orientation of the dendrites help determine the mechanical and tribological properties of the metal. Solidification in alloys is important in laser surface modification as the nature in which the melt pool solidifies influences the resultant alloy's properties.

The first stage of solidification is nucleation. Spontaneous nucleation, known as homogeneous nucleation, may occur when an alloy is cooled rapidly to a temperature well below its equilibrium freezing temperature. Due to the moderate cooling rates experienced in most metal solidification processes, a large enough under-cooling for homogeneous nucleation does not normally occur. Instead, solidification commonly

commences by heterogeneous nucleation in which preferential nucleation sites are irregularities such as cracks on mould walls and solid impurities in the molten metal [73, 74]. However laser surface modification involves a beam of radiation that is focused and has short duration energy input. This establishes a steep thermal gradient between the liquid pool and the relatively cold substrate underneath, which acts as a heat sink. The thermal gradient of great magnitude coupled with the conduction mode of heat transfer can establish a cooling rate as high as 10^{11} K/s. Owing to this high cooling rate (almost always $>10^3$ K/s), the surface freezes with a non-equilibrium microstructure [36, 75]. The rapid cooling rates achieved through laser surface engineering also open up the possibility of amorphisation, which is known for many metals to have improved wear and corrosion properties.

In general, laser surface melting which induces extremely high cooling rates, due to low volume melt pools and rapid workpiece movement results in a finer grain size and a larger number of grains per unit volume. This is desirable within the solidified metal as the larger grain boundary surface area effectively blocks the slip of crystal structure defects, resulting in better mechanical and tribological properties. An empirical relationship between grain size and yield stress (σ_y) was formalised mathematically by Hall and Petch [76], see Equation (1)

$$\sigma_y = \sigma_i + k_g d_g^{-0.5} \quad (1)$$

where σ_i represents the overall resistance of the crystal lattice to dislocation movement (constant for a particular metal), k measures the relative hardening contribution of the grain boundaries (constant for given metal), and d_g is the grain diameter.

2.4 Surface Engineering

Biomedical implants not only rely on their bulk material properties but also on surface characteristics. For example, wear activities that occur depend on the implants surface properties, contact area and the environment in which they operate. Enhancement of the surface characteristics increases lifespan of the implant. Surface engineering techniques are suitable for biomedical implants as only the surface is hardened thus the inner substrate remains softer for improved fatigue results. Most commonly practised conventional surface engineering techniques like galvanising, diffusion coating and nitriding have several disadvantages including [77-80]:

- i. Long processing time,
- ii. High energy and material consumption,

- iii. Poor precision and flexibility,
- iv. Lack in scope of automation,
- v. Requirement of complex heat treatment schedules, and
- vi. Easy deformation of work-piece being treated.

Another popular technique, thermal spray coating, has drawbacks mainly due to limited bond strength between the coating and substrate and the subsequent lifetime of coating [31]. These issues arise mainly due to low coating density, non-uniform coating thickness and mismatch of coefficient of thermal expansion [81]. Surface engineering methods based on application of electron, ion and laser beams are free from such limitations. Laser treatment is more advantageous compared to electron and ion beam based processing because electron and ion beams cause the [80]:

- i. Rapid deceleration of high energy electrons generates X-rays which is a possible health hazard, and
- ii. Requirement of an expensive ionisation chamber delivery system and ultra-high vacuum level

Laser treatment can be free of the aforementioned short-comings. Laser surface modification provides precise control over the morphology of processed area and has the ability to process complex parts and specific areas of the component without affecting the bulk material. Due to the need of high irradiance and low residence times, only high power lasers (typically Nd:YAG and CO₂) can be used for metallic surface modification [82].

2.5 Corrosion

Corrosion of human body metallic implants is critical because it can adversely affect biocompatibility and mechanical integrity [83]. The question “Does laser surface modification of this biomedical alloy have an effect on its corrosion properties?” is one that material engineers need to ask when considering the use of this process with a specific alloy for use within the human body. A brief background is discussed in this section covering the effects of corrosion and methods used to assess rates of corrosion.

The human body is a harsh environment for implants due to its high oxygen concentration, saline electrolyte conditions of pH 7.15 to 7.35 (it decreases down to 5.2 during an inflammation reaction [84]) and a temperature of about 37 °C. Chloride solutions are known to be aggressive and corrosive to metals, however, ionic composition and protein concentration in body fluids complicate the nascent

understanding of biomedical corrosion even further. Variations in alloy compositions can lead to subtle differences in mechanical, physical, or electrochemical properties. However, these differences are minor compared with the potential variability caused by differences in fabrication methodology, heat treatment, cold working, and surface finishing, where surface treatments are particularly important for corrosion and wear properties [10].

The typical types of corrosion that occur in metallic implants are pitting, crevice, galvanic, intergranular, stress-corrosion cracking, corrosion fatigue, and fretting corrosion. Surface modification of implants, is considered to be the best solution to combat corrosion and to enhance the life span of the implants and longevity of the human beings. Tribocorrosion studies are gaining importance in relation to toxicity because of the influence of friction or fretting on the local depassivation and release of metallic ions [85]. To replicate the real environment as closely as possible, implants should be tested *in vivo* in animal experimentation; but the possibility of monitoring electrochemical processes is limited and very complex [57]. *In vitro*, titanium has been proved to have high stability and corrosion resistance [54, 86, 87]. However, there are studies that still show metal release and corrosion *in vivo*, thus requiring surface modification of the implant material [88, 89].

To accelerate corrosion processes, electrochemical tests are used to directly amplify the impact of corrosion processes. This is possible since electrochemical tests use some fundamental model of the electrode kinetics associated with corrosion processes to quantify corrosion rates. To maintain reproducibility and minimize variables, simulated body fluids that contain some combination of amino acids, proteins and ions at the proper temperature and pH are often used, simply due to the complexity and often non-well controlled nature of the *in vivo* system, and the inherent difficulty of reproducing that system in the laboratory. This approach is known to yield significant results compared to *in vivo* testing [10]. There are two types of methods used in electrochemical testing. These are polarisation and electrochemical impedance spectroscopy (EIS). Polarisation measures susceptibility to localized corrosion for corrosion resistant materials. EIS can be used to follow actively corroding systems like degradable surfaces. Electrochemical corrosion testing also allows for monitoring of the release of toxic ions in the body, which is another major issue long before failure occurs [57].

It is worth noting that, body fluid consists of inorganic ions (Na^+ , Cl^- , Ca^{2+} , H_2PO_4^- *etc.*), therefore the simulated body fluids (SBF) need to be carefully considered. The concentration of oxygen depends on the part of body: in the intercellular fluid and

arterial blood, it is $1/80$ and $1/4$ respectively. It is two thirds of these values under ambient conditions. The kind of cell in the surrounding tissue depends on the part of body and varies as time proceeds after implantation. In corrosion testing metallic biomaterials are typically evaluated in saline, phosphate buffer saline solution, simulated body fluid containing only inorganic ions, and medium with and without the addition of serum [13]. Because the type of cells used changes the environment and secrete various chemical that have an effect on the corrosion processes, using the appropriate SBF is therefore important.

Pitting corrosion: is a localized form of corrosion by which cavities or "holes" are produced in the material. Pitting is considered to be more dangerous than uniform corrosion damage because it is more difficult to detect, predict and design against. Pitting corrosion of the laser treated material can be compared to the untreated by calculating the corrosion rate derived from potentiodynamic polarisation studies. Potentiodynamic polarization is a technique where the potential of the electrode is varied at a selected rate by application of a current through the electrolyte. Polarization methods involve changing the potential of the working electrode and monitoring the current which is produced as a function of time or potential. The three main polarisation methods are anodic, cathodic and cyclic polarisation.

- i. *Anodic*: involves changing the potential in the anode causing the working electrode to become the anode and causing electrons to be withdrawn from it
- ii. *Cathodic*: the working electrode becomes more negative and electrons are added to the surface
- iii. *Cyclic*: both anodic and cathodic polarisations are performed in a cyclic manner.

2.6 Wettability Characteristics

Events leading to integration of the implant into the bone, which in turn determine the performance of the device, take place largely at the tissue-implant interface [90]. The ability to promote bone cell anchorage, attachment, spreading and growth is a key factor for a successful biomaterial in orthopaedics. It is important that the interface between the implant and host tissues do not induce any deleterious effects such as chronic inflammatory response or formation of unusual tissue. It is therefore crucial to design biomaterials used in implants with the best surface properties that can encourage ideal bio-integration. The wetting of a surface to a liquid and the spreading of the liquid are very important aspects in surface engineering for biomedical implants.

Wettability is the ability of the liquid to spread on a solid surface. Surface energy and wetting characteristics can be used as a measure for biocompatibility [91, 92]. Wetting measurements are only sensitive to the upper 0.5 nm or so of the surface. Measuring surface energies at the interface is crucial for biomedical implants as these energies drive important processes such as adsorption and adhesion. When a drop is placed on a solid surface under gravity, it has a tendency to spread. Once the cohesion (internal forces) of the liquid, the gravity forces and the capillary forces (related to the surface tension) are in thermodynamic balance, the equilibrium state is reached and the specific contact angle, θ , between the solid surface and the liquid can be measured. The triple interface formed between solid, liquid and gas will move in response to the forces arising from the three interfacial tensions until an equilibrium position is established [93]. Contact angle, θ , is the angle between the solid surface and the tangent of the liquid surface, see Figure 2-8. Spreading of the liquid over a solid depends on the components of the interfacial tension and is given by Young's Equation (2).

$$\gamma^{sv} = \gamma^{sl} + \gamma^{lv} \cos\theta \quad (2)$$

where γ are the surface tension coefficients of solid, gas and liquid interfaces. This theoretical relation is true for smooth and homogeneous solid surface; it does not have practical application for rough surfaces.

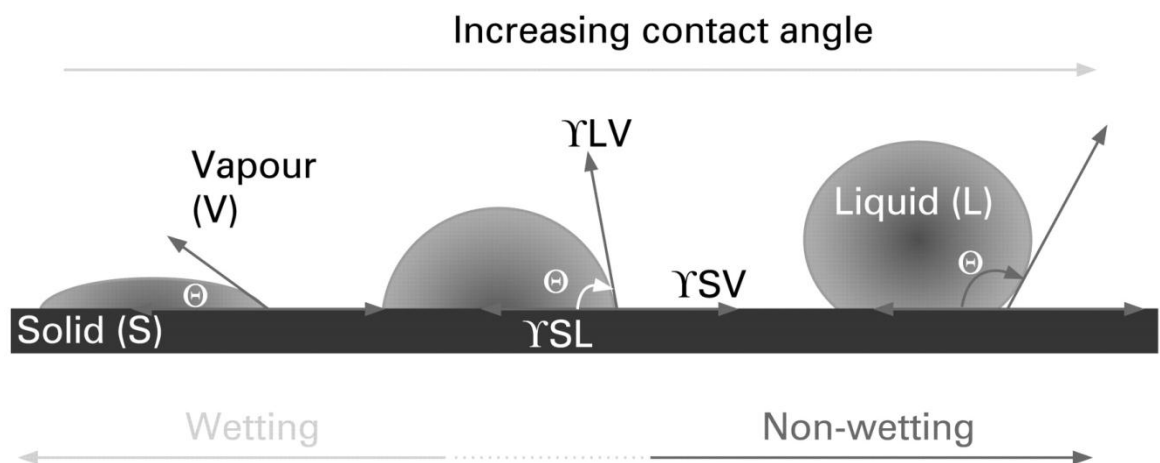


Figure 2-8: Contact angle (θ) of a liquid (L) on a solid (S). γ_{LV} , is the interfacial energy of liquid–vapour interface; γ_{SL} , is the interfacial energy of the solid–liquid interface; and γ_{SV} , is the interfacial energy of the solid–vapour interface [94].

The present techniques used to alter a material's wettability characteristics are often complex and difficult to control. Lasers offer high control capability and flexibility.

There are numerous publications demonstrating the practicability of employing lasers for surface wettability modification [15, 90, 92].

Hydrophilic surfaces have good affinity for water and therefore have strong adhesive forces, high surface energies and low contact angles. On the other hand *hydrophobic* surfaces are made up of non-polar groups and have large contact angles. Figure 2-9 demonstrates hydrophilic and hydrophobic surfaces. Measurements of contact angle are thus used to gain qualitative information about the chemical nature of the surface. Wetting can be determined from the equilibrium contact angle. If $\theta < 90^\circ$, the liquid is said to wet the solid and a zero contact angle is known as complete or perfect wetting.



Figure 2-9: Super hydrophilic and super hydrophobic contact angles [95].

2.7 Biocompatibility

Biocompatibility is the fundamental requirement for choosing a metallic implant material; the material has to exhibit nontoxic properties to the surrounding biological system. Hip implant biocompatibility problems are most often caused by toxins that leach out of the implant material into the surrounding tissues and body fluids. The main cause of osteolysis in hip replacements is the release of ions due to metal on metal wear in bearing surfaces. To identify and quantitate specific leachable moieties, analytical extraction studies are carried out. Extracts are obtained from the material and prepared under exaggerated conditions of time and temperature in order to allow a margin of safety over normal physiological conditions.

The tissue culture assays examine the toxicity or irritancy potential of materials at a cellular level through the use of isolated cells *in vitro*. The most important factor in testing toxicity is the dose of chemicals delivered to each individual cell [31]. There are three ways of performing the cytotoxicity test, namely: direct contact, agar diffusion and elution methods. With all three assays the outcome is measured by observing changes in the morphology of the cells. The main difference between the assays is the way the cells are exposed to the material being tested.

Direct contact: - This assay involves placing a piece of test material directly onto growing culture medium. The cells are incubated at normal body conditions and subsequently stained with a cytochemical stain such as haematoxylin blue. Dead cells lose their adherence to the culture plate while live cells adhere and are stained by the cyto-chemical stain. Therefore toxicity is evaluated by the absence of stained cells on the specimen. A disadvantage of this assay is that it is suited for low density materials.

Agar diffusion: - This method involves placing a contact thickness of agar over the culture cells. The test material is then placed on top of the agar layer and subsequently incubated at normal body conditions. The agar mixture usually contains a dye that allows for visualisation of the live healthy cells while dead cells cannot absorb the dye and therefore remains colourless allowing for toxicity evaluation. Agar diffusion is also suitable for high density materials.

Elution: This method uses extracting media and extraction conditions to test material according to actual conditions or to exaggerated conditions. An extract of material is usually prepared using sodium chloride or serum free culture medium. The extract is placed on a prepared layer of cells and the toxicity is evaluated after incubation at normal body conditions. Live and dead cells are distinguished by using histochemical or

vital stains thus evaluating the toxicity levels. Table 2-3 lists the advantages and disadvantages of these cell culture methods [96].

Table 2-3: Advantages and disadvantages of the cell culture methods [96].

	<i>Advantages</i>	<i>Diadvantages</i>
<i>Direct contact</i>	<p>Eliminate extraction preparation zone of diffusion.</p> <p>Target cell contact material.</p> <p>Can extend exposure time by adding fresh media.</p>	<p>Cellular trauma if material moves</p> <p>Cellular trauma with dense material</p> <p>Decreased cell population with highly soluble toxicants</p>
<i>Agar diffusion</i>	<p>Eliminate extraction preparation zone of diffusion.</p> <p>Better concentration gradient of toxicant.</p> <p>Can test one side of a material independent of material density.</p>	<p>Require flat surfaces</p> <p>Solubility of toxicants in agar</p> <p>Risk of thermal shock when preparing agars overlay</p> <p>Limited exposure time</p> <p>Risk of absorbing water from agar</p>
<i>Elusion</i>	<p>Separation extraction from testing</p> <p>Extended exposure time.</p> <p>Choice of extract condition.</p> <p>Choice of solvents.</p>	<p>Additional time and steps</p>

2.8 Laser Surface Modification

Laser material processing can be divided into three major classes, namely heating, melting and vaporisation. These three classes are determined by power density (irradiance) and exposure/interaction time (residence time) as shown by the chart in Figure 2-10. Within these classes there are various processes that can be achieved through careful selection of the irradiance and residence time.

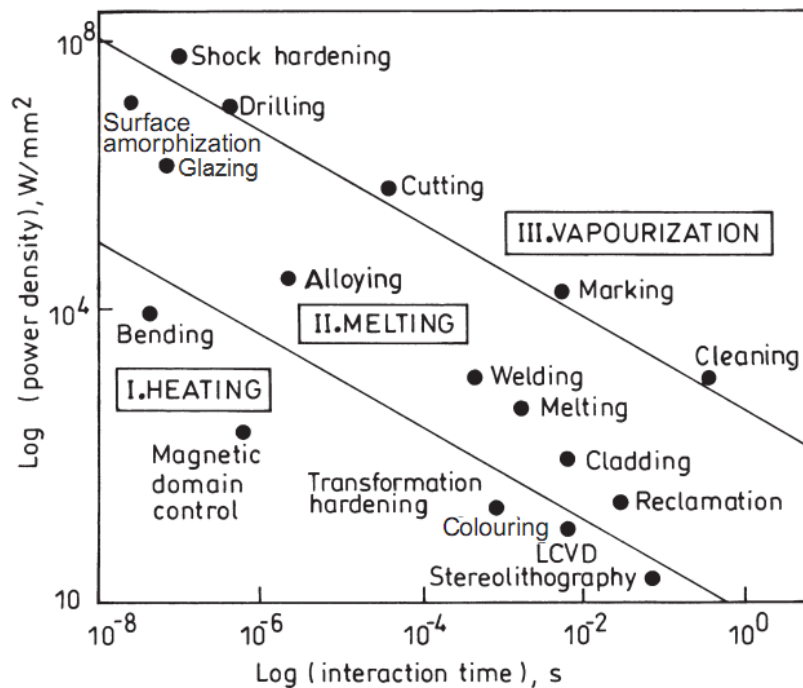


Figure 2-10: Classification of different laser processing techniques [80].

This study focuses on the high power density melting regime which requires substantial amount of energy to be induced at a very short period of time to trigger microstructure and phase transformation. High laser power levels and reliability are crucial, thus making CO₂ and Nd–YAG lasers the only practical solutions for this type of process [80]. Since the focus of this study was within the melting regime, some of the processes within this class i.e. glazing, alloying and cladding will be discussed in more detail.

2.8.1 Laser Glazing

To date it is well known that decreasing grain sizes into the nanoscale increases strength, hardness and tribological properties of both metals and ceramics [2]. An amorphous structure has no grains and is known to increase hardness and surface properties through elimination of crystalline anisotropy and inter-crystalline defects [80]. The term ‘glazing’ refers to the process of being able to make ‘glassy’, to make a solid without any crystalline structure [97]. Laser glazing occurs when a beam of

sufficient intensity, to create a molten state, is scanned rapidly across a solid. Extremely rapid cooling caused by conduction of heat into the bulk material and shallow processed area result in major microstructural alteration i.e. freezing of the atoms in a random state before they can form crystals. These microstructural changes enable laser glazing to produce higher compressive strength, hardness, wear and corrosion resistance properties [98].

However, laser glazing and the parameters required to produce such a state of processing is difficult to distinguish as various authors throughout literature define the process differently [97, 99-102]. With the various formats of irradiance and exposure time figures presented in literature, it is very difficult to predict a priori the precise conditions which promote the formation of glazed surfaces [80, 97, 99, 103]. Figure 2-11 highlights some of the irradiance versus irradiance time graphs as published by different authors.

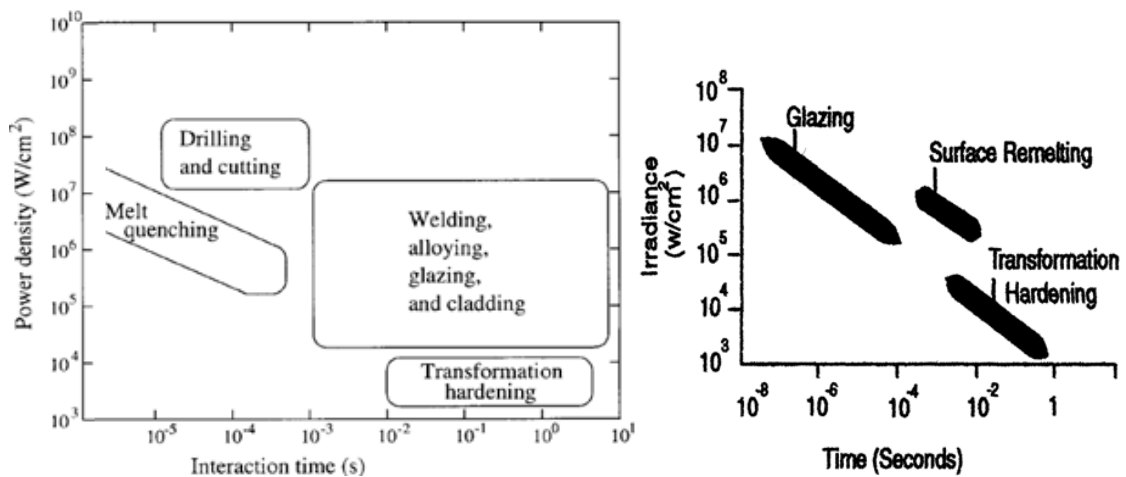


Figure 2-11: Comparison of perceived glazing process parameters in literature [97, 99].

Mahank defined the glazing as a melting process used for surface modification in which a thin layer of substrate or coating is melted to remove surface roughness or porosity [99]. The author associated the process with a combination of irradiance ranging between 2.5 – 7000 kW/cm² and beam interaction time between 0.001 – 10 s. DiMelfi *et al.* [104] used laser glazing to reduce the friction coefficient of rail steel with treatments producing up to 100 μm deep glazed surfaces. In their study, a pulsed 1.6 kW Nd:YAG laser with a 1.06 μm wavelength and 0.2 mm spot size was used. The 1.06 μm wavelength was particularly used because it eliminates the need for an absorptive coating for rail steel. Two beam shapes were exploited, circular and elliptical, with an average of 1 kW power being used for each pass. Nitrogen was used as an assist gas during their experiments. The laser glazing treatment used on the steel produced micro

hardness values of up to 1072 HV, 257% higher than the typical untreated steel. Static friction experiments proved that a reduction in friction coefficient of approximately 40% occurred which corresponded with a calculated reduction in the crack propagation rate of 79%. A drawback noted from DiMelfi's study was that the X-ray diffraction scans showed full crystallinity of the glazed layer, therefore the study was inconclusive regarding the nature of the glazed layer [104]. In this respect, it can be seen that the term laser glazing used in the literature does not generally correspond with the production of amorphous material but rather represents a process which uses high power density and low surface interaction times.

Laser glazing typically occurs with a partially focused beam incident on a sample moving at high speed, for example, with the sample on a rotating turntable. Speeds of several meters per second can be readily achieved. Cases in which such glass structures have been confirmed in metals are often of a eutectic composition, such as for the Fe-C-Si-B and Pd-Cu-Si alloys. However not all eutectic alloys will produce glassy structures. Pre-treatment to homogenise the microstructure prior to the glazing pass have been used to achieve glassy structures [97]. Most of the confirmed laser glazing cases that highlight the presence of amorphous structure are for ceramics [100, 101, 105]. Ceramics are known to radically reduce in grain size by applying appropriate heat treatment regimes therefore validating the possibility of achieving a glazed surface [31]. Laser glazing also has the potential to seal heat checks formed on the surface of alloys and relax surface stresses [106].

Due to the vague definition of laser glazing process in literature, the process parameters used in this research can be termed as being within the glazing range. If laser glazing is defined by the processing maps given in [80, 97, 99] then the processing parameters used in this study are within the glazing umbrella. However, for clarification purposes the process used in this study is defined as being laser melting or laser surface modification.

Amorphisation of the metal surface was not sought as a primary goal in this study mainly due to the following:

- i. Readily amorphised alloys require compositions, that allow rapid quenching, that are not present in biomedical alloys [107-111]. Including these elements would change the biocompatibility properties thus making the material usable within the body.
- ii. Uncertainty of laser glazing in titanium alloys [110]. Laser glazing of titanium alloys is mentioned in two publications Malakondaiah *et al.* [112] and Ready *et*

al. [97]. However, as discussed in DiMelfi's study [104], Malakondaiah *et al.* did not prove the amorphous structure by means of XRD or otherwise. Ready *et al.* [97], refers to creation of α martensite as laser glazing. The process of creating α martensite was achieved in this study and several other [17, 113, 114] and has been proven to be a crystalline structure.

- iii. Metallic glasses are known to be brittle therefore limiting their performance in load bearing applications like hip replacement application [115].
- iv. The area of laser surface modification of biomedical alloy already presents a significant large scope for optimisation and investigation.

2.8.2 Laser Surface Alloying

Laser surface alloying (LSA) is a surface modification technique which utilises high power density available from focused laser sources to melt, externally added, alloying elements and the underlying substrate [116, 117]. The process is similar to laser melting except that extraneous alloying elements are added to the melt pool, thus changing the chemical composition of the surface. The bulk of research carried out on surface modification of titanium alloys have been focused on laser alloying. There are two main ways used to deposit the alloying element namely: co-deposition and pre-deposition. Co-deposition involves direct deposition of the alloying element during laser irradiation. The alloying element is deposited mainly in the form of gas [118, 119], powder [120, 121] or wire [122]. Co-deposition of the alloying element is considered the most attractive as it involves a single step processing. This method also offers the significant advantage of real time control, over pre-deposition where the alloying element is deposited prior to laser irradiation. Gas deposition has been the main technique used for laser alloying of biomedical alloys. In previous studies laser nitriding of titanium alloys has been thoroughly studied [123-127]. The attractiveness of LSA as compared to alternative coating techniques is mainly due to rapid quenching from liquid phase which allows formation of extended solid solutions and novel metastable phases with superior mechanical and chemical properties.

Up to 500 μm thicknesses of titanium nitride (TiN) layers have been reported, with increased hardness as well as erosion and wear resistance [128]. Laser nitriding of titanium alloys is typically conducted with either Nd:YAG or CO_2 continuous lasers operating at power densities between 10^8 and 10^{11} W/m^2 with typical cooling rates of between 10^3 and 10^5 K/s [124, 129]. The type of gas is also known to affect the resulting surface roughness, nitrogen gas results in higher average surface roughness

compared to a mixture of nitrogen and argon. Considerable roughness is desired in the stem of biomedical hip implants because it improves the bone bonding capabilities [130]. The thickness of the processed region greatly depends on nitrogen pressure intensity. Smooth processing is attributed to nitrogen pressures above atmospheric pressure, however, an increase in nitrogen pressure also results in reduced thickness due to the cooling effect imposed by the higher pressures. Continuous wave laser processing of energy density, beam diameter, scanning velocity and nitrogen pressure of 5×10^4 W/cm², 3 mm, 6 mm/s and 0.4 MPa respectively, easily forms a fine titanium nitride (TiN) compound [131].

TiN is extremely hard and is known to be used to improve the substrate's surface properties. It hardens and protect surfaces, its non-toxic properties allow for it to be used for medical implants as it meets the FDA requirements [132]. To produce the TiN, experiments have to be conducted in a nitrogen atmosphere. Ageing treatments increase hardness and distribute the TiN uniformly on the treated areas [113]. In laser nitriding, up to five fold increases in hardness have been reported on Ti-6Al-4V alloy surface compared to substrates of approximately 350 HV [113, 124, 133, 134]. TiN coatings are most popular for corrosion resistance in machine tooling, with lifetime improvement being increased by a factor of three or more [132, 135]. Formation of α -Ti was observed in the heat affected zone (HAZ) with hardness values averaging 450 HV.

Jiang *et al.* also investigated the hardness and wear resistance of laser treated Ti-6Al-4V alloy with a 3.3 kW continuous laser [136]. The authors reported an increase in both parameters and related improvements to laser beam scanning rate. A lower beam scan speed resulted in laser surface alloyed composite coating having a higher volume fraction of TiN reinforcement due to the longer gaseous nitrogen and liquid interaction time. Gyorgy *et al.* found the presence of TiN in Ti-6Al-4V alloys treated using a pulsed Nd:YAG laser in a controlled nitrogen atmosphere [137]. The process of laser nitriding can be achieved through the use of either pure nitrogen or a mixture with argon or helium. The best wear resistance properties were observed by laser melting in pure nitrogen followed by a mixture with argon. Pulsed laser systems allow for high repetition rates to be achieved subsequently improving the depth of the processed layer [138]. Improved cavitation erosion resistance was also observed and compared to untreated samples [139].

The main problems still associated with this process are the formation of cracks due to high cooling rates and lack of reproducibility. Cracks have been associated with the laser scanning speed and nitrogen gas parameters [139]. Investigations carried out by

Mridha *et al.* demonstrated a reduction in number of cracks as the laser scanning speed increased [140]. The study also established that nitriding in dilute gas environments nitrogen-helium and nitrogen-argon produced a significant reduction of cracks. The surface hardness after glazing was dependent on the nitrogen concentration in the mixture and was seen to increase with increasing nitrogen content. Formation of less dendritic TiN was cited as a contributing factor to lower crack formation. Preheat treatment through laser glazing under argon prior to nitriding produced a more uniform depth of treatment and reduced cracking effects [127]. In addition to production of cracks, laser alloying also introduces foreign alloying elements therefore achieving homogeneity and repeatability is very difficult. Homogeneity and repeatability are crucial in achieving a quality implant and therefore crucial in the biomedical industry.

2.8.3 Laser Surface Cladding

Laser surface cladding (LSC) is a melting process where there is fusion of a substrate material with a material of different metallurgical properties. Laser cladding is similar to laser surface alloying except the dilution by the substrate is kept at a minimum. Normally, processes involving less than 10% dilution are referred to as cladding while those with dilutions exceeding 10% are termed as alloying [117]. The cladding process offers optimum bonding, great flexibility, low distortion, and low thermal load on the work piece together with little need for post cladding treatment [97]. Ni-based alloys are the most commonly used material for cladding titanium and its alloys. Ni-based alloys are often used due to their good high temperature wear and corrosion resistance properties and they are easier to bond to the substrate than other materials [141-143]. However, nickel based alloys do not offer good biocompatibility properties due to the toxicity of nickel within body environments [44].

High hardness coating up to 1000 HV with excellent wear resistance and very low load sensitivity properties can be obtained by laser cladding [144]. One of the early works on improvements of wear and oxidation properties of titanium was carried out by Hirose *et al.* [145]. They investigated the effects of laser cladding aluminides on CpTi. More work on cladding of titanium has been carried out by Guo *et al.* [146] and Pu *et al.* [147]. Cracking was found in all the laser modified specimens, this raised a cause of concern for this laser treatment. Hardness levels up to 600 HV have been achieved through the formation of TiC, TiB and TiB₂ via laser cladding [148]. Recently studies on the cladding of Ti-6Al-4V by cobalt to improve corrosion resistance were carried out by Majumdar *et al.* [149]. A significant improvement in microhardness was achieved at the interfacial region. Uniform corrosion resistance increases along the graded

interfaces were noted, but the pitting corrosion resistance marginally deteriorated. In this case, the direct laser clad Co layer showed a better biocompatibility than that of as-received Ti-6Al-4V sample.

The main drawback of cladding is that it often produces uncontrollable cracks, which result from the very high cooling rate of the melted pool. The process also has poor reproducibility. This is due to the complexity in dissolving the material uniformly in the melted pool. In an effort to achieve improved coating composition laser cladding uses a lower power density, around 10^2 kW/mm² compared to 10^3 to 10^4 kW/mm² for laser surface melting. This lower power density not only reduces the relative extent of distortion, but also ensures a closer control of the dilution. Laser cladding is also costly compared to other laser processing techniques [97, 117].

2.8.4 Laser Shock Hardening

There are other laser processing techniques that modify the surface structure like laser shock hardening (LSH). The principle of LSH is to use a high intensity laser and suitable overlays to generate high pressure shock waves on the surface of the treated material. When a material is irradiated with a Q switched pulse laser, operated at power density greater than 0.1 GW/cm², a shock wave can be generated on the surface. Surface of the treated material can be coated with a black paint before LSH as a laser energy absorbing layer. The workpiece is usually covered with a transparent layer (for example water or glass). When the laser beam strikes the coated sample, the black paint, due to absorption of laser beam energy, is heated and instantaneously vaporized. The vapour absorbs the remaining laser beam radiation and produces plasma. The rapidly expanding plasma creates a high surface pressure, which propagates into material as a shock wave. The shock wave can induce compressive residual stress that penetrates beneath the surface and strengthens the surface of the treated material. This effect may induce microstructural changes, cause a high increase in dislocation density, influence roughness surface of the material as well as introduce a compressive residual stresses into the treated surface of the material [150, 151]. The effects of such a process would not greatly influence the crucial wear and corrosion properties needed in a biomedical implant. Although LSH improves the wear and corrosion properties, the improvements are insignificant compared to other laser surface modification techniques. It is because of this reason that LSH was not implemented in this study.

2.8.5 Laser Surface Melting

The process used in this research can be best described as laser surface melting. In this process the alloy surface is laser melted and rapidly re-solidified without any direct addition of other material elements to modify the chemical composition of the surface. Vaporization is avoided during this laser treatment and the molten pool solidifies rapidly. There is a sequence of events which initiate when the laser beam contacts the surface. Firstly, the near surface region rapidly reaches the melting point and then a liquid/solid interface starts to move through the alloy. Diffusion of elements follows within this liquid phase. At this point the laser pulse is nearly terminated while the surface has remained below the vaporization temperature. At this stage the maximum melt depth has been attained, inter-diffusion continues, the re-solidified interface velocity is momentarily zero. The interface then rapidly moves back to the surface from the region of maximum melt depth. Inter-diffusion continues in the liquid, but the re-solidified metal behind the liquid/solid interface cools so rapidly that solid state diffusion is negligible compared to that expected from an equilibrium phase diagram. Finally, re-solidification is completed and a surface modified layer has been created. Due to the relatively small depth of the melted zone (10 to 1000 micrometres), very high quench rates are achieved, in the range of 10^3 to 10^6 K/s, resulting in non-equilibrium martensitic microstructure [152]. The re-solidified alloy has a titanium oxide film on the surface, which confers good hardness, wear and corrosion resistance. Due to the extremely high thermal gradients, residual stresses can develop which may result in distortion of the work-piece. These effects can be overcome by applying a low powered surface heating procedure following the laser melting process [152].

The advantages of laser melting in surface modification of biomedical implants include:

- i. No foreign material is used that might cause early or stress forced failure.
- ii. Elimination of alien species eliminates the complex material dispensing procedure therefore allowing for homogenous surface treatment.
- iii. Less parameters are used, therefore, compared to other laser surface modification techniques, the results are repeatability which is crucial in biomedical industries.
- iv. Less material and energy are required compared to other laser modification techniques resulting in a cheaper process.
- v. Superior corrosion properties result compared to nitriding or cladding [17, 153].
- vi. Superior biocompatibility can result due to elimination of foreign elements.
- vii. Crack-free modification easily created compared to laser nitriding and cladding.

2.9 Parameters Affecting Laser Surface Modification

The main process variables in the laser surface modification operation are: laser power, beam diameter, beam configuration, work-piece velocity, substrate condition (roughness, temperature and absorptivity), alloy composition and thermophysical properties of the work-piece [80]. In order to obtain the required properties it is crucial that the selected interaction time and power density allow the material to undergo the desired degree of heating and phase transition. Power density (irradiance) input largely determines the maximum temperature attained. Duration of interaction (residence time) largely determines the reaction among the phases and the cooling rates. Interfacial properties are also strongly attributed to the temperature encountered during treatment [36]. The control of these laser processing parameters in this study is important to achieve repeatability and optimum microstructure changes on the surface. It should be noted that the parameter selection process is complex. For instance, it would be more convenient to quantify different laser processing using a singular parameter like energy density (J/mm^2) determined from power density multiplied by time. However, this would not define the true outcome of each individual processing parameter as it is the specific combination of power and time (rather than their product) which determines the resulting thermal and material effect.

2.9.1 Material Properties

To achieve any level of hardening in alloys, certain types of microstructure are favourable. For example, in steel microstructures a fine pearlitic structure and small grain sizes typically provide optimal conditions for laser processing [154-156]. If the structure was made up of coarse graphite with large grains of ferrous alloys it would not respond as well to laser hardening, preventing the complete transformation from the austenitic phase to the martensitic phase. The final hardness of the steel is directly related to the quantity of residual austenite or martensite formed during laser hardening. Steel alloys can be heat treated down to greater depths than plain carbon steel due to their lower thermal conductivity. Research to date suggests that laser treating is the best method at inducing the formation of retained martensite due to the extremely low quenching times [157]. Laser hardening has also been found to produce surface residual compressive stresses which can minimise crack growth leading to higher fatigue limits and better wear resistance. Ti-6Al-4V is preferred over other titanium alloys due to its laser treatability characteristic [70, 71].

Metals are known to reflect the infrared irradiation of the CO₂ laser at its 10.6 μm wavelength. Surface modification techniques such as sandblasting, machining, etching, anodising and coating are known to improve the absorption of metals [80]. Absorption of the CO₂ laser beam greatly affects the thermal cycles and peak temperature therefore all heat transfer calculations on laser material processing require knowledge of the beam's absorptivity. The absorption of infrared radiation by metals largely depends on conductive absorption by free electrons and therefore the absorptivity can be calculated from the knowledge of the electrical resistivity of the substrate. Arata *et al.* demonstrated that the absorptivity of various polished metallic surfaces is a linear function of the square root of the electrical resistivity of the respective metals [158]. Ti-6Al-4V absorption is estimated to be approximately 0.42 or 42% [16].

Metals absorptivity to incident laser irradiation depends on the following parameters:
Wavelength: At shorter wavelength, more energetic photons can be absorbed by a greater number of bound electrons and so the reflectivity falls at shorter wavelengths and absorptivity of the surface increases as shown in Figure 2-12. Generally, laser energy is absorbed by metals better when it is of a short wavelength rather than a long wavelength. The absorptivity of (0.694 μm) ruby lasers, for example is over 15% greater than absorptivity of (10.6 μm) CO₂ lasers for irradiated mechanically polished 321 stainless steel at 294 K [159].

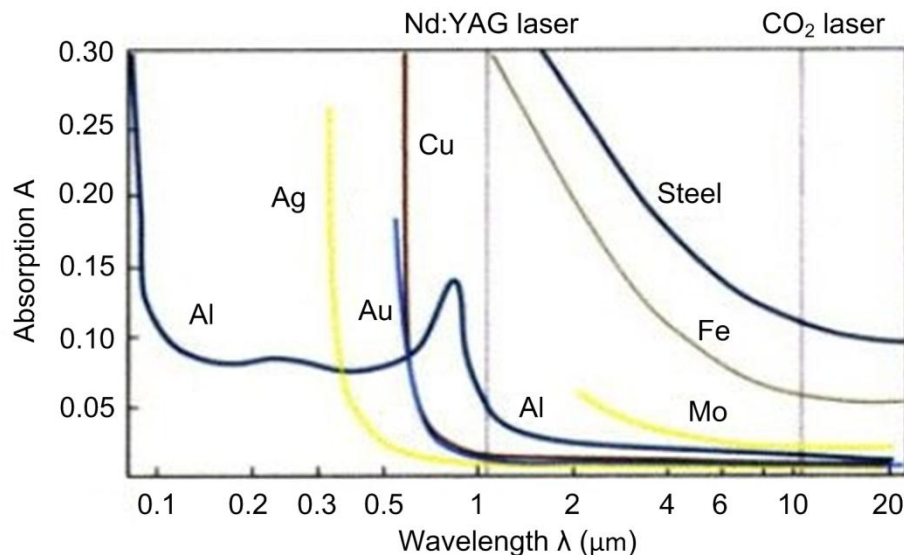


Figure 2-12: Absorption of laser radiation wavelength by metals [160].

Effects of angle of incidence: At certain angles the surface electrons may be constrained from vibrating since to do so would involve leaving the surrounding surface. Thus if the electric vector is in the plane of incidence, the vibration of the electron is inclined to

interfere with the surface and absorption is thus high. There is a particular angle, the “Brewster” angle, at which the angle of reflection is at right angles to the angle of refraction. When this occurs it is impossible for the electric vector in the plane of incident to be refracted [161]. Effects of high angle absorption and multiple reflections due to the angle of incidence are illustrated in Figure 2-13.

Surface roughness: Absorbance of CO₂ irradiation by steel surfaces is known to be dependent on surface roughness [99, 158, 162]. Roughness has a large effect on absorption due to the multiple reflections in the undulations, see Figure 2-13. There may also be some stimulated absorption due to beam interference with sideways reflected beams. Provided the roughness is less than the beam wavelength, the radiation will not suffer these events and hence will perceive the surface as flat [161].

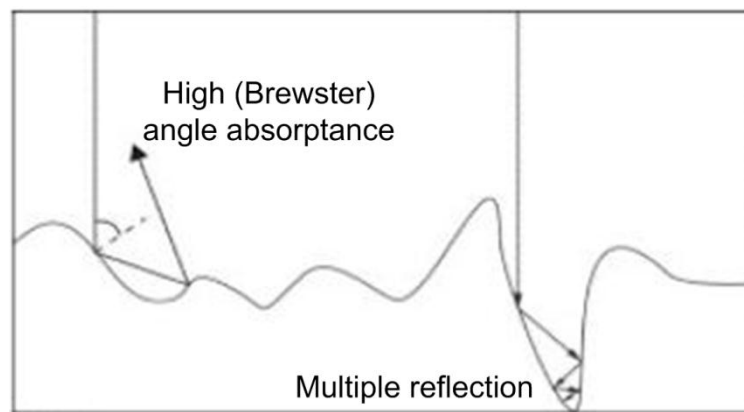


Figure 2-13: Effects of angle of incidence and roughness on laser reflectivity [162].

Temperature: Clean surfaces of all metals and alloys at room temperature are known to be highly reflective to the infrared radiation of CO₂ laser thus causing a problem in the transfer of energy onto the surface of the metal [80]. As the temperature of the structure rises there will be an increase in the phonon population causing more phonon-electron energy exchanges. Thus the electrons are more likely to interact with the structure rather than oscillate and re-radiate. There is thus a fall in the reflectivity and an increase in the absorptivity with a rise in temperature.

Surface Films: The reflectivity is essentially a surface phenomenon and so surface films may have a large effect. The absorption variation for CO₂ radiation by the surface oxide films at different thickness is shown in Figure 2-14.

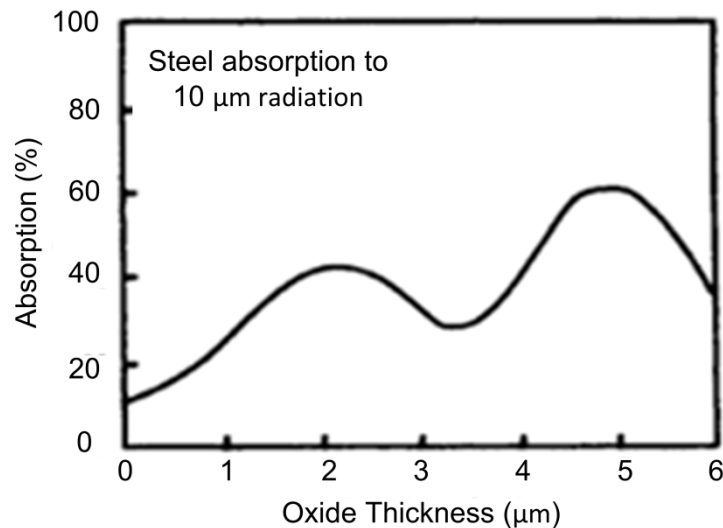


Figure 2-14: Effect of oxide thickness on absorption of a CO₂ laser irradiation [162].

2.9.2 Laser Operating Modes

Both continuous wave (CW) and pulsed mode (PM) lasers may be employed for surface modification. In contrast to the continuous wave operation, a pulsed beam offers several challenges owing to the higher number of operating variables and the complexity of optimising the process parameters. For a given melt profile, surface characteristics and other aspects including economy, the operating parameters such as pulse energy, pulse width, pulsing frequency, scan rate etc. have to be chosen. This calls for an excellent knowledge of the influence of operating parameters on melt profile and an in depth understanding of its effect on structure and properties [163]. Compared with continuous wave lasers, the high peak power of a single pulse produced by a pulsed laser can readily induce higher absorptivity in metals. Short duration times of pulsed lasers mean short heating times which therefore contribute to higher cooling rates, subsequent grain refinement, and the formation of non-equilibrium phases [164]. Since pulsed lasers allow for adjustments of various pulse parameters, they can provide a flexible processing window that can be tailored to suit certain microstructures and materials [164]. CW operation on the other hand can offer higher depths of processing compared to PM as previously seen for example in 316L stainless steel [165].

There have been very few comparative studies examining the effects of laser operational mode on microstructure in the literature. Samant *et al.* studied the use of CW and PM for the surface modification of alumina ceramics [166]. The two processing conditions generated two different grain structures. The grains showed facets for CW mode of laser operation while they were non-faceted for PM mode. The author observed much higher cooling rates for PM (two orders of magnitude) compared to the cooling rates from the

CW laser processing. PM also created deeper melts depths due to higher energy densities being supplied for shorter periods of time, thus melting more material than CW where smaller energy densities were supplied for a longer periods of time. Thus the melt depth was shown to be a function of the input energy and the time for which it was supplied (residence time) without much direct bearing on the under cooling. Under cooling in this case is defined conventionally as being the difference between the melting point of the material and the temperature at which the temperature derivative with respect to time is zero.

2.9.3 Laser Power and Irradiance

The average power of the laser beam, whether it is operating in the continuous mode (CW) or pulsed mode (PM), affects the nature and scale of the resultant structures [167]. The use of pulsed power allows two more variables to be considered, namely, pulse repetition frequency (PRF) and percentage overlap. Penetration of the laser beam is a function of power. However, high power settings result in vaporisation and material ejection [161]. The power density or irradiance of a laser beam is determined by the power of the laser beam used and the diameter of its focal spot (spot size). Also known as the laser intensity, irradiance is given by:

$$I = \frac{P}{\pi w_o^2} \quad (3)$$

where, I is the irradiance (W/mm^2), P is power (W), and w_o is the radius of the spot size. Figure 2-15 illustrates the laser beam profile depending on the focusing. Most of studies in the literature focus the beam either below or above the surface to achieve larger beam diameters than the focused spot size and hence give the power density required [16, 110, 153, 168, 169].

The focused spot size, D , for a Gaussian beam shown in Figure 2-15, can be calculated to a good approximation using Equation (4) [170]:

$$D = 2d = \frac{\lambda f}{\pi w_o} \quad (4)$$

where d is the beam diameter at the lens inlet, f is the focal length of the lens, and $2w_o$ is the spot diameter at the focus, see Figure 2-15.

The optimal diameter of the beam which contains almost 86 % of the total laser power is defined by $1/e^2$ of the peak intensity. A CO_2 laser that functions in TEM_{00} mode produces a Gaussian shaped spot as illustrated in Figure 2-16 (a). Generally, the intensity along with the material properties gives an indication of the expected rise in

temperature in the focal region and consequently indicates the melting intensity of the material [171].

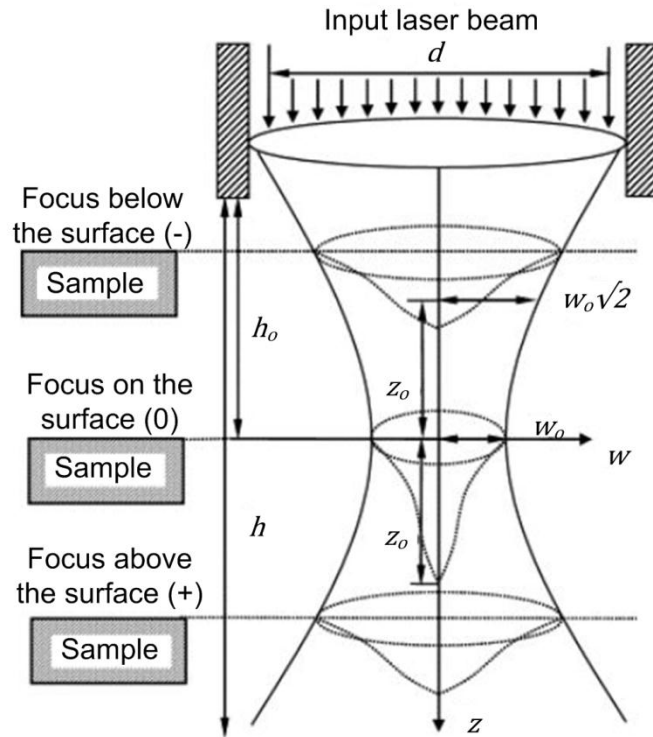


Figure 2-15: Geometry and intensity of the Gaussian laser beam [172].

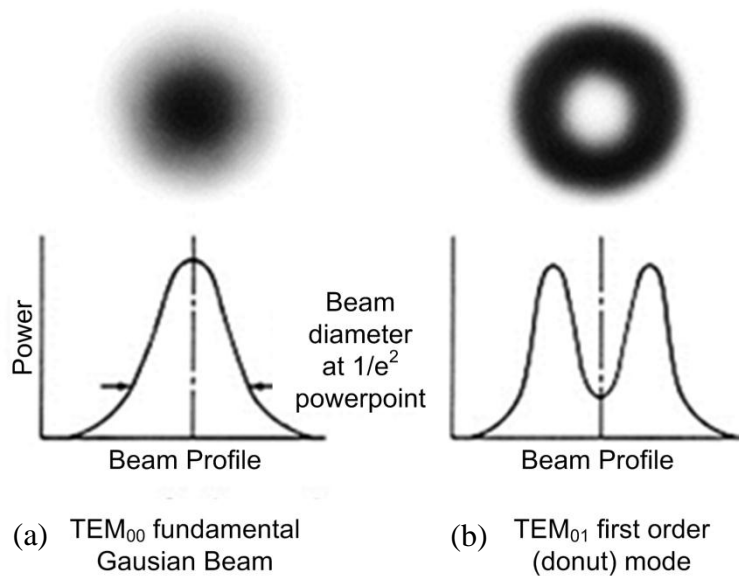


Figure 2-16: Laser beam modes illustrating (a) TEM_{00} and (b) TEM_{01} modes [97].

2.9.4 Sample Speed and Residence Time

The speed of the sample and laser beam spot size is crucial in determining the residence time. Residence time can be defined as the amount of time the laser beam is in contact with material. For pulsed mode, residence time encompasses the duty cycle, tangential speed of the sample and beam diameter. This time is equivalent of exposure time for continuous mode lasers and can be calculated as follows [166]:

$$R = \frac{\tau \times D_s \times PRF}{v} \quad (5)$$

Where R is the residence time (s), τ is the pulse width, D_s is the diameter of the spot size, PRF is the pulse repetition frequency and v is the sample scan speed.

When continuous mode is used the pulse width and repetition frequency are ignored in this calculation since the duty cycle is 100% and duty cycle is given by the product of pulse width and PRF.

2.9.5 Overlap percentage

Overlap is the ratio of the distance between two consecutive laser spots and the diameter of the spot. A homogeneous structure is achieved in pulsed laser beams by using controlled overlap. Overlap percentage is typically calculated as:

$$O = \left(1 - \frac{L_p}{D_s \times (N + 1)}\right) \times 100 \text{ (\%)} \quad (6)$$

where O is the overlap percentage, L_p is the length being processed, D_s is the diameter of the spot size and N is the number of spots within length L_p .

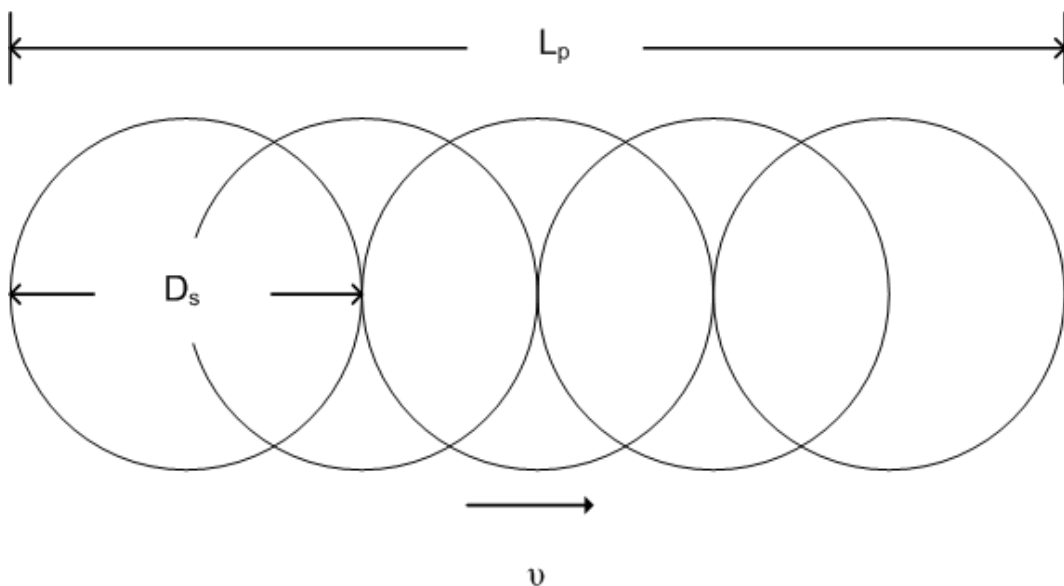


Figure 2-17: Schematic diagram representing 50% spot overlap.

The best results for laser processing of Ti-6Al-4V were found from 50% overlap [152, 173]. Other works found that 30% and 35% overlap produced satisfactory surfaces [174]. Overlapping has a large effect on heat build-up on the workpiece, resulting in preheating before subsequent tracks [175]. It is therefore crucial that the overlap percentage is carefully chosen to address these issues.

2.9.6 Pulse Energy density

Energy density is the power per unit time per unit area delivered by a single laser pulse at the focal spot. Energy density is a more accurate parameter to compare the effect of a laser beam with varying pulse durations. Energy density is the product of irradiance and residence time and can be calculated as follows:

$$E_f = I \times R \quad (7)$$

where, E_f is the energy density (J/mm^2), I is the irradiance (W/mm^2) and R is the residence time (s).

2.10 Effects of Laser Surface Melting on Stainless Steel Properties

Steels that can be heat treated are typically of high carbon content [97]. AISI 316L stainless steel is extremely difficult to heat treat for hardness due to its low carbon content. Carbon enrichment methods have to be implemented before heat treatment operations. Laroudie *et al.* published a study on laser surface alloying of 316L stainless steel to improve the hardness of the 316L steel surface [176]. The process consists of melting the surface of the base alloy with known amounts of pre-deposited materials. In particular, the two routes presented were (i) the formation of iron-chromium carbides by carbon and SiC incorporation, and (ii) the incorporation of submicron particles of TiC and precipitation of titanium carbides. Surface alloying was carried out on polished samples using a 300 W continuous wave Nd:YAG laser with argon as a shielding gas to prevent oxidation. A circular spot of 950 μm in diameter resulting in a maximum power density of 4.11 W/m^2 was implemented in their research. The quality of the coating was noted through high hardness, reduced cracks, and improved homogeneity throughout the sample. SiC alloying micro hardness measurements revealed mean values of between 500 and 600 HV in the melted area and with absence of cracks on the surface. Carbon alloying produced microstructures leading to an average micro hardness of 400 HV. TiC submicron particles alloying produced crack-free, but a heterogeneous surface with a slight increase in micro hardness to about 280 HV. Micro hardness of the surface alloy ranged between 350 HV and 700 HV for Ti + SiC alloying. Laroudie *et al.* thereby

showed that 316L austenitic stainless steel can be hardened by laser surface alloying [176].

The average surface roughness depends on pulse width and pulse period for pulsing mode lasers. Pinkerton and Li obtained rougher surfaces using low pulse periods of 20 ms compared to higher pulse periods of 80 ms [165]. High duty cycles were found to produce rougher surfaces due to longer irradiation times. Pulsing mode was found to produce better roughness properties compared to continuous mode. Average surface roughness R_a of as low as $0.07 \mu\text{m}$ were achieved with a larger spot size of $1.7 \mu\text{m}$ and lower irradiance of 198 W/mm^2 .

Corrosion in 316L can take many forms; the most common identified forms are intergranular, pitting, fretting and crevice corrosion. More than 30 years ago, heterogeneous intergranular distribution of carbon was observed in surgical grade 316 to result in intergranular corrosion due to the formation of chromium carbides. This resulted in a demand for low carbon content alloys in surgical specifications. The introduction of austenitic stainless steel with carbon content, lower than 0.03%, saw a reduction in the risk of corrosion attacks of this form. Pitting is the most common form of corrosion arising from the breakdown of the passivating oxide film, which can be enhanced by the presence of proteins in the tissue fluid and serum [10]. Corrosion products due to fretting on 316L immersed in extracellular tissue fluid were found to be oxides containing chromic chloride and potassium dichromate as well as variable amounts of calcium, chloride, and phosphorous, with nickel and manganese being absent, indicating preferential release of these metal ions into the surrounding solution. These results indicate that for 316L implant surfaces, nickel and manganese are depleted in the oxide film and that the surface oxide composition changes to mostly chromium and iron oxide with a small percentage of molybdenum oxide in the human body. 316L is highly susceptible to crevice corrosion attack as compared to the other implant alloys. Corrosion has been identified on bone plates and screws made of 316L at the interface between the screw heads and the countersink [177]. In cases where there are galvanic couples arising from the combination of dissimilar metals, such as 316L stainless steel and the Co-Cr-M alloy or Ti-6Al-4V alloy, the stainless steel will be attacked (galvanic corrosion) therefore these combinations should be avoided. There continues to be a debate as to whether stress corrosion cracking takes place in 316L in the body. While fractures of this alloy have been found to exhibit the classical stress corrosion cracking appearance, in other cases it has been determined that intergranular corrosion had weakened the device, thus influencing the fracture.

Laser melting of sensitised 316L stainless steel showed significantly increased resistance to pitting. This increase was attributed to the elimination of the more reactive heterogeneous microstructure by laser melting [178]. Studies on retrieved implants show that more than 90% of the failures of 316L stainless steel implants are due to pitting and crevice corrosion attack [179]. Hansen *et al.* [10] suggested that this fact alone deems that a better material be used for even temporary implant devices.

Passivation and pitting-resistance properties were also seen to be enhanced with increase in δ -ferrite content in Laser Surface Modified (LSM) samples [180]. Possibilities of improving intergranular corrosion (IGC) and intergranular stress corrosion cracking (IGSCC) resistance were successfully investigated by melting the surface of nitrogen containing 316L stainless steel using a CW CO₂ laser [181]. The main cause of IGC and IGSCC is formation of M₂₃C₆ carbides along the grains subsequently leading to depletion of chromium adjacent to these carbides, a process referred to as sensitisation. When sensitised microstructure is exposed to corrosive solution IGC and IGCC can occur. By using a CW CO₂ laser, sensitised microstructure can be eliminated. A CO₂ laser at 5 kW with a traverse speed of 20 mm/s was used in the reported work [177]. Depending upon the temperature profiles, cooling rate, and interaction time, continuous M₂₃C₆ carbides present in the sensitized specimen dissolved. At the interface between the heat-affected zone and the unmelted zone, globular particles of M₂₃C₆ were discontinuously distributed. Alloy depletion around these particles was discontinuous, thus failure due to IGC or IGSCC was seen to be less likely [181].

2.11 Effects of Laser Surface Melting on Ti-6Al-4V Properties

Laser surface modification of Ti-6Al-4V has been widely investigated in the literature. The bulk of modification techniques carried out are laser nitriding. This section of the thesis focuses on the technique examined in the authors work and presented later in this thesis, laser surface melting, where an inert gas is used to avoid alloying. Table 2-4 shows the laser processing parameters from the literature for unalloyed laser melting of Ti-6Al-4V.

Table 2-4: Processing parameters previously presented in the literature for the laser surface modification of Ti-6Al-4V.

Ref	Laser				Interpreted parameters	
	Type	Power (W)	Speed (mm/s)	Overlap %	*Irradiance (kW/mm ²)	*Residence Time (ms)
[17]	Diode	600-800	1 - 6	25	0.114	583
[182]	Nd:YAG	150	6 - 16.7	20 - 50	-	-
[168]	Nd:YAG	500 - 1000	2.5 – 4.2	-	2	190
[153]	Excimer	200	16.7	-	.254	59
[16]	Nd:YAG	800-1500	25	15	0.01	140
[163]	Nd:YAG	400	5-25	-	5.6	12

*Highest irradiance/residence time attained

2.11.1 Microstructure

A very common result of irradiation with a scanning beam is single phase microstructure that looks featureless through an optical microscope. This single phase occurs when various constituents in the solid have dissolved with rapid solidification thwarting segregation of the various alloying elements into high and low concentration regions. Laser surface melting typically produces a fine α martensite structure with a layer of various films, TiO, TiO₂ and Ti₂O₃, which have excellent wear and corrosion resistance [20, 183]. The mentioned transformation is the most common in $\alpha+\beta$ titanium alloys during cooling from very high temperatures (>1660 °C). Since the cooling rates of the laser melt pool during solidification is extremely high (10^4 to 10^{10} K/s), complete transformation of $\alpha + \beta$ to acicular α (transformed β) is reasonable. The creation of acicular α -Ti is found to result from these very high cooling rates [16].

As bought/received Ti-6Al-4V (grade 5) consists of a mixture of α and β -Ti. The relative volume fraction of β -Ti is usually lower than that of α -Ti. Laser surface melting is known to lead to an increased volume fraction of acicular α martensite and a decreased volume fraction of the β phase in the microstructure [16, 17]. Reduction in volume fraction of β -Ti following melting is attributed to the stabilisation of acicular martensite in the structure during rapid quenching. This fine, acicular martensite has a hexagonal closed packed structure and possesses a high hardness but relatively low ductility and toughness [184, 185]. Acicular martensite structure enhances the materials wear and corrosion resistance. A decrease in β phase in the microstructure is known to improve corrosion properties since pitting attacks mainly target the β phase [71].

Laser surface melting has a significant effect on grain structure of Ti-6Al-4V. Extreme cooling rates resulting from low residence time reduce the grain size and grain sizes have been found to increase with distance from the surface of the treated zone [97]. Generally the heat affected zone has a large grain structure compared to the melted zone [174]. Singh *et al.* reported grain growth from 65 μm to 89 μm for an increase in laser power from 800 to 1500 W [16]. This grain growth was associated with high temperatures which produced larger melt pools and subsequently a slower cool rate. Some reports have reported defects on laser melted surfaces [182]. Defects, especially cracks have been seen to result from lack of use of an inert assist gas. Ossowska *et al.* in particular used air in their laser melting technique thus producing large cracks on the melted surface [182]. The formation of surface cracks is likely to be due to extensive oxidation of titanium as it is irradiated in atmospheric air [153]. When argon gas has been used at a sufficient flow rate, laser surface melting has been shown to produce crack-free surfaces [17, 153].

2.11.2 Melt Profile

The depth of processing can influence the service life and final application of the component. In coating technology the depth of coating is a very important factor as thicker coatings have a chance to delaminate while thinner coatings have a short lifetime. The same applies for the laser processed surface where an average layer thickness of between 40 μm and 60 μm has been reported to be ideal [2]. Melt pool profile depends on various laser processing parameters including laser spot size, power and scan speed. Variation of scan speed and power has previously been used to analyse their effects on melt layer depth profile. However considering irradiance and residence time solely does not give a complete representation of all factors affecting the melt pool profile. The product of these two parameters (energy density) assists in gaining further understanding of the influences on melt pool depth profile. When the process parameters were analysed individually, treated zone depth and width was found to decrease with increasing scan rate for Ti6Al-4V [136, 163]. This phenomenon was concluded to be a result of a reduced interaction time between the target and the laser beam. In samples treated in pulsed mode the width and depth of the treated zone increased linearly with increasing pulsing frequency. This was attributed to the increased average power deposited with increasing frequency. Kumar found that melt pool width and depth increased with increasing pulse energy [163]. The treated depth increased from 0.15 mm to 0.75 mm and the treated width increased from 0.85 mm to 2.35 mm for an increase in pulse energy from 2 to 12 J, see Figure 2-18. As the pulse

energy increases both the average and peak power increases, increasing the treated zone dimensions.

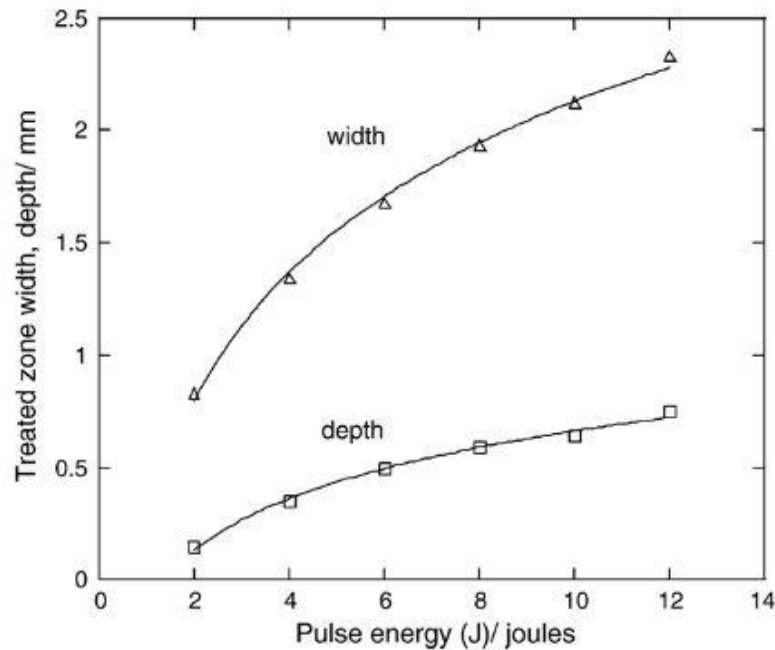


Figure 2-18: Variations of treated zone width and depth with increasing pulse energy for fixed values of pulse width (5 ms), frequency (30 Hz) and scan rate [163].

A mathematical model was developed for the 3-D melt-pool geometry and single-crystalline melt-pool solidification in laser surface melting [186-188]. The models relate power and scan speed to melt-pool depth and width. The model was found to match the effects mentioned earlier. The model was also found to be in good agreement between the predicted and experimentally observed microstructures. Chan *et al.* also created a thermal model to show the effects of conduction and convection on depth and width of the melt-pool [189]. It was found that the physics of the process can change from conduction dominated to convection dominated for large melt pools. This was noted to change the pool geometry dramatically, resulting in up to a 150% increase in the aspect ratio (width/depth) as compared to the case with only pure conduction taken into account. The study done by Chan also highlighted the crucial role of overlap on melt-pool dimensions and the need to consider it as a parameter. The temperature distributions and molten flow within the melt-pool were further detailed by Bamberger [190].

2.11.3 Roughness

Effects of laser surface modification of roughness have received little interest in the literature mainly because many applications require a finishing surface machining

operation before service. Roughness greatly depends on the variation of irradiance and residence time. Very smooth surfaces have been previously reported in the literature [152]. Surface roughness usually arises from the ridges and periodic structure caused by the laser pulsing and the movement of the sample during laser treatment. Laser melting produces smooth flat islands, surrounded by a wave-like micro-relief. Surface rippling or roughness of laser modified Ti-6Al-4V is dependent on the viscosity of the melt. Morton *et al.* concluded that waviness is a function of the convectional flow of the melt surface and also further noted that it is influenced by the percentage overlap [173]. Energy density also plays a crucial role in the resultant roughness. Li *et al.* showed that increased energy density and number of pulses resulted in higher roughness [191]. Roughness has a major effect on cell attachment onto the surface.

2.11.4 Hardness

Hardness can be described as the measure of the resistance of a material to plastic deformation and is dependent on the chemical composition and microstructure of the alloy. Hardenability on the other hand is the depth to which the alloy can be hardened during a heat treatment such as quenching. The microstructure, in this case, is dependent on the severity of quenching. Achieving a rapid cooling rate with laser should produce reduced grain size and improve hardness properties. Hardness has a significant influence on the wear properties of a material a fact which has resulted in a significant amount of research on this point [152, 192].

Singh *et al.* reported an increase in hardness from 254 HV in an untreated sample up to 297 HV from laser modified surfaces [16]. Other reports in literature have recorded micro-hardness improvements up to 510 HV [17, 182]. Typically, hardness reduces with distance from the surface. The heat affected region has lower hardness values compared to the melted region [193]. Investigations by Biswas *et al.* revealed that uniform hardness can be obtained within the melted region. This study showed a 490 HV hardness that was consistent throughout the 350 μm treated region [17]. The hardness then dropped to 260 HV within the untreated bulk alloy. The improvement in micro-hardness of the melt zone was attributed to refinement of microstructure and formation of acicular martensite during rapid quenching. The hardness of laser surface-treated Ti-6Al-4V decreased with increase in laser power [16]. This is in accordance with the well-known Hall-Petch relation that defines the increase in hardness with decreased grain size [116, 194].

Various reports have been published showing the decrease of hardness with increase in scan speed [152, 193, 195]. However, from the literature on laser nitrided samples, the same result cannot be guaranteed as with laser melted samples. Hamad *et al.* extensively studied the effects of laser nitriding on Ti-6Al-4V and noticed a bell shaped relation between hardness and scan speed [125]. Initially as scan speed increased the hardness increased. Conversely, at very high speed, with laser nitriding, the hardness reduced for further increases in scan speed. It is worth noting that laser nitriding tends to have high hardness compared to laser melting in argon [16, 17]. This is due to the formation of the hard TiN alloyed layer on the nitride surface.

2.11.5 Wear Properties

Titanium alloys are known to have poor fretting fatigue resistance and poor tribological properties. Mathematical models have shown that metals with low theoretical tensile and shear strengths exhibit higher coefficients of friction than higher strength materials. Ti-6Al-4V has a hexagonal close packed structure and has relatively low theoretical tensile and shear strength. Consequently, it is expected that it will have high coefficient of friction (μ) values, which is the case for titanium sliding against titanium in air is $\mu = 6$ [196]. Lower strength materials also show greater material transfer to non-material counter-faces, than higher strength materials. The great affinity of titanium for oxygen leads to the formation of oxide which is transferred and adheres to non-metallic materials, such as polymers, resulting in severe adhesive wear. Surface modification is therefore required to increase near surface strength, thereby reducing μ and lowering the tendency for transfer of material and adhesive wear [197].

Yerramareddy and Bahadur were among the first to study both sliding wear and abrasive wear of titanium alloys following laser surface modification [138]. They assessed the wear following surface melting in an argon atmosphere with nitriding and nickel alloying. Sliding wear tests were undertaken using a block-on-ring configuration in dry conditions, with the titanium alloy sliding against a tool steel. The steady state wear rate decreased from $40 \times 10^{-4} \text{ mm}^3/\text{m}$ to $0.8 \times 10^{-4} \text{ mm}^3/\text{N m}$ after Ni alloying, to $0.5 \times 10^{-4} \text{ mm}^3/\text{N m}$ after surface melting, and to the lowest wear rate of $0.3 \times 10^{-4} \text{ mm}^3/\text{N m}$, following laser nitriding. The as-received value of μ was reduced from 0.62 to 0.43 for all the laser treated specimens. The study showed that laser surface melting can be used to enhance the wear properties of Ti-6Al-4V.

Biswas *et al.* [198] and Singh *et al.* [16] laser treated Ti-6Al-4V to improved wear and corrosion properties for bio-implant applications. Generally the wear rate increased with an increase in power. Singh *et al.* attributed the reduction in wear rate of treated

samples to the modifications in microstructure, hardness, grain size and alteration of the electrochemical response of the modified surface.

2.11.6 Corrosion Resistance

Ti-6Al-4V is considered to be highly corrosive resistant. However, corrosion can still occur especially when the passivation layer is damaged by fretting of a loosened implant and/or a change in pH value occurs due to wounds or infection [199]. Gilbert, *et al.* reported that approximately 16% to 35% of 148 retrieved total hip implants showed signs of moderate to severe corrosive attack in the head-neck taper connection [200]. Improvements in corrosion potential and primary potential for pit formation compared to the as-received Ti-6Al-4V have been observed in the literature [17]. Biswas *et al.* [17] and Yue *et al.* [153] reported better corrosion properties in laser melting surfaces compared laser nitrided surfaces. Corrosion potential values for laser surface modified sample shifts significantly towards the nobler direction after treatment. Shifting of the corrosion potential was attributed to formation of acicular martensite and a reduction in β Ti volume phase. Unlike the untreated specimen, LSM samples were not seen to passivate over the current range of 10^{-6} to 10^{-5} A/cm² [16, 17, 153, 168]. Pitting potentials reduced in laser melted samples compared to the untreated samples [16]. Singh *et al.* reported pitting potentials of 2.4 V and <1.8 V in laser treated and untreated samples, respectively [16]. However, when the laser treated samples were polished the pitting potential was greater than 2.4 V and highest corrosion resistance was noted from processing at 800 W.

Re-distribution of alloying elements within the treated titanium alloys improved pitting corrosion resistance. Geetha *et al.* found improved corrosion resistance of laser nitrided samples in a simulated body environment using potentiodynamic polarisation [130]. These results also indicated pitting potential increase by 200 mV for the laser treated surface. Studies carried out using excimer lasers showed significant increase in pitting potential of the Ti alloy when the material was treated in argon gas [18]. Up to a seven-fold reduction in corrosion current was obtained when the material was treated in nitrogen gas. The improvements were credited to the reduction of the solute partitioning effect of detrimental aluminium segregation from α phase [18].

Zaveri *et al.* studied treated Ti-6Al-4V alloy with pulsed-wave Nd:YAG laser under various conditions to obtain a surface oxide layer for improved corrosion resistance [168]. Corrosion resistance studies were carried out in three different simulated bio-fluids (SBFs), namely, NaCl solution, Hank's solution, and Cigada solution. Tafel analysis showed that the laser-treated Ti-6Al-4V were more corrosion resistant than the

bare specimens in any of the above SBFs [168]. Langlade *et al.* used a Nd:YAG laser to study the oxidising Ti-6Al-4V [20]. Stratified layers giving different coloured films were related to oxide thicknesses and oxide compositions. It was noted that titanium oxides may exhibit a solid lubricant effect, while the oxygen dissolved in the titanium matrix had a hardening effect.

The reduced pitting corrosion provided by surface melting is possibly because of partial suppression of β phase formation in the microstructure and the change in morphology from granular to acicular [17, 153]. Yue *et al.* attributed corrosion enhancement to the presence of the transformed Ti martensitic structure in the laser-modified layer [153]. The poor corrosion resistance of untreated Ti-6Al-4V can also be attributed to the local enrichment of aluminium (α stabilizer) and the formation of a galvanic cell between the two different phases α and β . Partitioning of aluminium from α -phase during electrochemical corrosion is the primary mechanism of degradation of the aluminium containing Ti-alloys, whereas, acicular α in laser treated Ti-6Al-4V lacks this partitioning effect [16].

2.11.7 Interfacial and Biocompatibility Properties

Bandyopadhyay *et al.* has shown that the laser processing does not have a negative effect of inherent biocompatibility of the materials used to fabricate the structures [114]. Laser surface modification produces minimal contamination compared to conventional surface modification techniques, thus it can help improve osseointegration [90, 201, 202]. The highest implant stability can be achieved by complete osseointegration of a large implant surface.

Several publications have shown that roughness and wettability produced by laser modification plays a vital role in biocompatibility properties [202-207]. Hao *et al.* showed that improved surface roughness, surface oxygen content and surface energy generated by laser treatment accounted for the better wettability characteristics of the material and enhancement of the adhesion with the biological liquids used. Although surface roughness played a role on the osteoblast response, the authors reported that wettability characteristics were the chief mechanism governing the osteoblast response [207].

An investigation of initial cell spreading and adhesion on longitudinally and transversally oriented micro-grooves produced by the laser irradiation of Ti-6Al-4V surfaces was carried out by J. Chen *et al.* [208]. Samples were polished and laser treated. Human osteosarcoma (HOS) cells, common bone cancer cells, were cultured at periods ranging from 15 minutes to 24 hours with immuno-fluorescence staining of

adhered proteins (actin and vinculin) being used to study the spreading and adhesion of the cells. Enzymatic detachment tests were carried out to quantify the adhesion of cells. Results of the experiment showed that cell spreading and adhesion were enhanced by the longitudinally and transversally oriented micro-grooves. Contact guidance was found to promote cell adhesion due to the increase in interactions between the focal adhesions and the patterned extra-cellular matrix (ECM) proteins on the laser micro-grooved surfaces [208].

Grizon *et al.* found that rougher titanium implants have stronger bone response compared to smoother implants after a long term implantation [407]. A study conducted by Wennerberg *et al.* reported the optimal surface for biomedical implants shows wave structures with an average wavelength of 11.6 μm and height deviations of 1.4 μm [201, 209]. The structure of the surface of titanium implants dictates the success for the subsequent healing process. It is primarily the microscopic structure of the implant surface that is responsible for bone apposition to the implant [201]. Surface treatment of implant material has been proven to influence the attachment of cells [202, 210-213].

2.12 Study Focus and Objectives

The vast majority of laser surface modifications for improved Ti-6Al-4V found in literature are on the topic of laser surface nitriding. Nitriding is an alloying process which has limited applications in bio-implants due to non-homogeneity of the surface properties, crack development on the surface and difficulty in reproducibility. Laser surface melting has a great potential as it does not suffer from the same limitations as alternate processes. For bio-implants, laser surface melting provides (relative to other processes) very low contamination, easy elimination of cracks, and the ability to easily achieve uniform and repeatable surface properties. However, the limited laser melting studies conducted in previous work have mainly focused on low scan speeds and the use of a large spot-size for the laser treatments. These previous works therefore have been restricted to high residence times and low irradiance, which in essence produce lower cooling rates than would be required to achieve finer surface structures with enhanced properties. None of the work reviewed in the literature followed a design of experiments approach so it is difficult to gain a full understanding of the process even within the parameter ranges that have been investigated to date. Studies reviewed in the literature only relate processing parameters to one individual response without cross-relating between multiple measured properties achieved by laser melting. This makes process mapping considerable challenging.

In this work, design of experiments was used to provide a detailed understanding of the effects of processing parameters on resulting surface properties. This work presents a comprehensive study of high speed laser surface melting of commercially available 316L stainless steel and Ti-6Al-4V for biomedical applications. The work in particular investigates the possibility of implementing extremely high irradiance and low residence times in order to improve the alloys' microstructure, tribological and biocompatibility properties. The aims can be summarised as follows:

- i. Implementing design of experiments to study the effects of CO₂ laser processing parameters on surface properties relating to biomedical applications
- ii. Investigate in particular the use of high irradiances and low residence times with a view to producing a surface which has a combination of properties required for biomedical implants, including a surface which is chemically homogenous, has low corrosion potential, low wear, high hardness, high degree of biocompatibility, good melt pool depth, roughness appropriate for various biomedical applications, and a low induced surface stress.
- iii. To provide a laser treatment process to enhance the life time of a currently used biomaterials to avoid the need for new biomaterial development as well as process development.
- iv. Microstructure analysis – study of the resulting topography and cross-sectional microstructures induced by laser treatment.
 - v. Melt pool profile – characterising the melt pool profile induced by laser treatment.
 - vi. Roughness – study of effects of laser process parameters on roughness.
 - vii. Hardness analysis – investigate the effects of laser processing on hardness and resulting hardness distributions within the treated surface.
- viii. X-ray diffraction analysis – phase distribution in treated samples and effects of irradiance and residence time on residual strain/stress.
- ix. Chemical composition analysis – variation in chemical elements within the treated samples.
 - x. Wear – investigating the wear mechanism in laser treated samples and difference compared to untreated samples.
 - xi. Corrosion resistance – study the corrosion behaviour and rates of the untreated and treated samples.
 - xii. Biocompatibility – In this study, screening tests were used to test biocompatibility of the laser treated samples. Since the material being used for this research is

already being used for hip replacement implants the biocompatibility tests were used to evaluate the performance of the laser treated alloys relative to the untreated alloy. In this research the biocompatibility of the material was investigated using analytical chemistry (in vitro) techniques [31].

Chapter 3

Materials and Methods

This chapter covers the materials and methods used in this research. This chapter presents details on the experimental work carried out and necessary information to replicate the work as needed. The majority of methods were similar for both sets of materials i.e. 316L stainless steel and Ti-6Al-4V. The sections in this chapter, therefore, refer to both sets of materials unless otherwise stated.

3.1 Sample Preparation

In order to achieve very low exposure times, high sample speeds needed to be implemented. Previous studies have shown that extreme temperature gradients can be attained by using rotating cylindrical samples at high speeds [97]. For 316L stainless steel, the work-pieces used in this work were cylindrical sections 120 mm long and 10 mm in diameter. The composition of the as-received AISI 316L austenitic stainless steel, is given in Table 3-1. The material was manufactured and supplied by Acciaierie Valbruna Stainless Steel Supplier, Italy (see *Appendix A*).

Table 3-1: Elemental chemical composition of AISI 316L stainless steel (weight %).

Element	Cr	Ni	Mo	Mn	Si	Co	N	S	P	C	Fe
wt%	16.82	10.14	2.03	1.51	0.55	0.08	0.061	0.03	0.03	0.02	Bal.

Cylindrical samples were not used for testing Ti-6Al-4V as this would have made it very difficult to perform the required wear, corrosion, XRD and biocompatibility testing. Flat samples were used for laser surface modification of Ti-6Al-4V; work-pieces were 120 mm long, 20 mm wide and 4 mm thick. The as-received Ti-6Al-4V was previously annealed at 704°C for 2 hours and subsequently ground using a centre-less grinder tool by the supplier, Super Alloys International Limited - Milton Keynes UK (see *Appendix A*). Composition of the as-received alloy is listed in Table 3-2.

Table 3-2: Elemental chemical composition of Ti-6Al-4V (weight %).

Element	C	Si	Fe	O	V	Al	Ti
wt%	0.14	0.01	0.16	0.17	3.97	6.36	Bal.

The terms work-piece, sample and specimen which are used in this thesis are defined as illustrated in Figure 3-1.

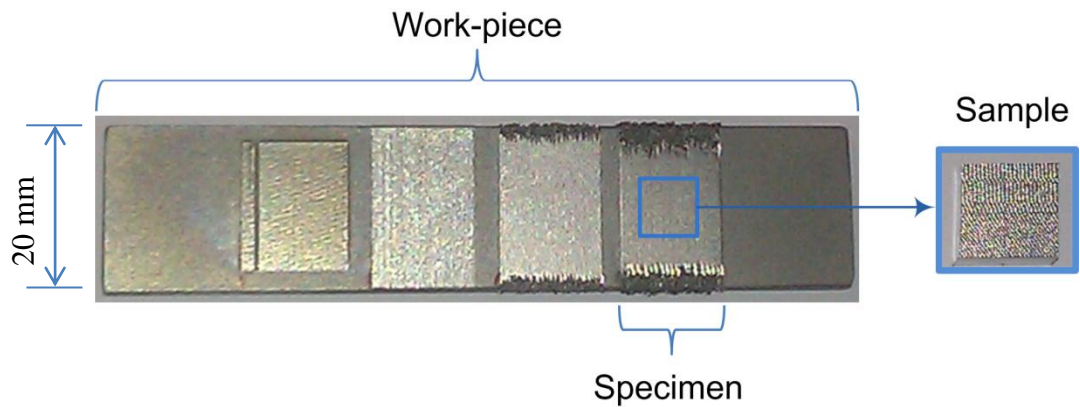


Figure 3-1: Illustration of the Ti-6Al-4V work-piece, specimen and sample, as used in this thesis.

3.1.1 Surface Pre-treatments

316L stainless steel work-pieces were machined and in some cases etched prior to laser treatment, to improve the CO₂ laser wavelength absorption. Chemical etching was carried out by immersing the work-pieces in glyceresia for 10 minutes before laser treatment. Glyceresia is a chemical etchant made up of 10 ml HNO₃, 20-50 ml HCl and 30 ml glycerol. Etchant preparation and application was carried out under fume hood ventilation. Glyceresia reacts with 316L stainless steel, darkening the metal for better 10.6 μm wavelength absorption. Roughening is another well-known technique for improving laser wavelength absorption as explained in section 2.9.1. Roughening of 316L SS samples was achieved by machining the surface using a Computer Numerical Controlled (CNC) turning machine to produce 2.90 ± 0.2 μm average surface roughness. Ti-6Al-4V samples were grit blasted before treatment. Parameters of grit blasting procedure are outlined in Table 3-3.

Table 3-3: Grit blasting parameters used for Ti-6Al-4V samples.

Machinery	Distance	Pressure	Angle	Type of Particles	Shape	Size
Guyson F 1400®	100 mm	8 bar	~45°	Soda lime glass*	Spherical and smooth	106-212 μm

*Chemically inert Honite® Grade 13 [214]

There are two main reasons for grit blasting the samples:

- i. Grit blasting removes surface contaminants from the titanium workpiece. Imperfections on the surface are eliminated when small inert particles are launched at high velocities. Eliminating imperfections is also desirable in laser processing for even surface processing.

- ii. Grit blasting is also known to improve absorption of the CO₂ laser by creating a non-reflective surface [75, 162].

After grit blasting the work-piece still had tightly adhering particles embedded onto the surfaces. These contaminants were composed of insoluble particles loosely attached and held in place by ionic or cohesive forces. These particles needed only be displaced sufficiently to break the attractive forces in order to be removed. All work-pieces were ultrasonically cleaned for 10 minutes in filtered clean de-ionised water. This ultrasonic cleaning is less aggressive cleaning, compared to other chemical cleaning methods, which therefore does not affect the composition of the substrate [215].

3.2 Laser Instrumentation and Experimental Set-up

Laser treatment of the samples was carried out using a, Rofin DC015 slab CO₂ laser. This CO₂ laser system was utilised in this study due to its versatility, high unsaturated gain and mostly high-power output capabilities [161, 216]. The laser has a maximum power output of 1.5 kW in the far infrared region (10.6 μm wavelength). Both pulsing mode and continuous wave laser operation were implemented, depending on the DOE. All experiments were carried out with the laser beam focused on the work-piece surface providing a Gaussian laser spot size of 90 μm. Minimal laser beam spot size was used for high cooling rates during processing. Table 3-4 gives a summary of the CO₂ laser system implemented in this investigation.

Table 3-4: CO₂ laser system specifications used in this work.

Laser system specifications	
Active medium	Carbon Dioxide
Output wavelength	10.6 μm
Peak power capacity	1.5 kW
Operation mode	Pulsed/Continuous
PRF range	2 – 5000 Hz
Pulse width range	26 μs – 125 ms
Laser beam specification	
Spatial mode	TEM ₀₀
Beam quality factor, K	>0.9
Beam propagation parameter, M ²	1.11

Argon was used as an assist gas with three crucial functions in laser surface melting:

- i. Shielding the melt pool thus avoiding oxidation during laser processing
- ii. Preventing small ablated particles from back-spattering into the nozzle and possibly damaging the laser optics
- iii. Aids the cooling process thus allowing for even higher cooling rates

The laser was controlled from the main Rofin laser control unit provided. The main unit facilitates control of laser beam peak power, duty cycle, and pulse repetition frequency. Figure 3-2 shows the CO₂ laser system used in this study.

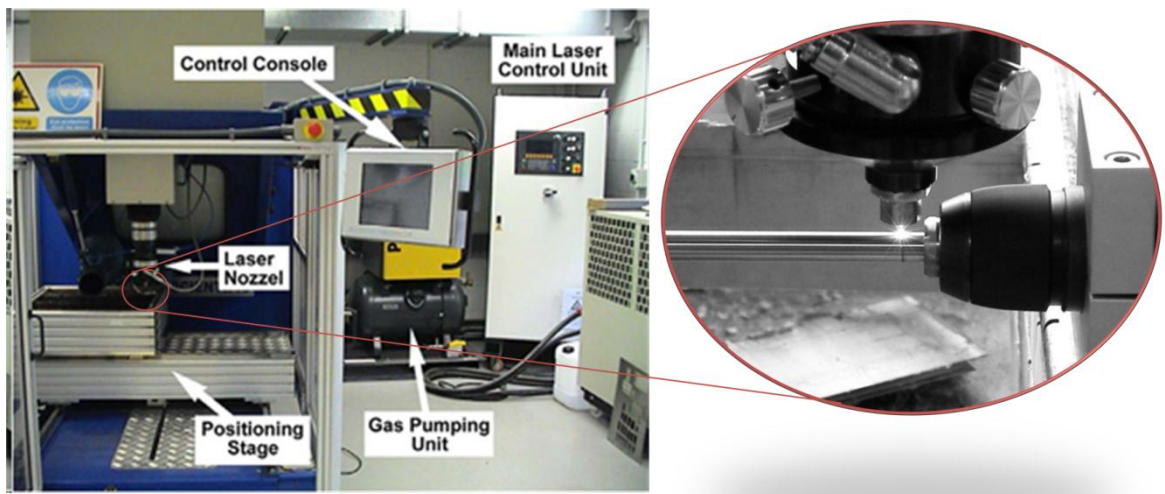


Figure 3-2: Rofin CO₂ laser system and gas pumping unit, showing the processing of a cylindrical sample 10 mm in diameter.

The control console shown in Figure 3-2 was used to position the stage, control the table motion during processing and gas delivery through the nozzle. The laser came equipped with a MTI 0505 Scientific Motion System (positioning stage). This motion system, shown in Figure 3-2, consisted of a machining table that provided XY cutting area of 50 × 50 cm. The motion resolution provided via the optical rotary encoders was 1.25 μm. The XY positioning speed was controllable from 1 to 5000 mm/min, and the acceleration at the beginning of the motion could be as high as 2 m/s². The laser beam was focused onto the moving samples via a 127 mm (5 inch) focal-length lens which was part of the nozzle assembly. The nozzle assembly was guided by vertical linear variable displacement transducers (LVDT) which provided 150 mm of vertical height or focal position adjustment capability [170].

3.2.1 Laser Processing of Cylindrical Work-pieces

Cylindrical work-pieces, 10 mm in diameter, were rotated using a DC motor attached to the positioning stage. The DC motor was capable of reaching speeds up to 2500 rpm. Figure 3-3 shows a schematic of the laser modification process. The laser beam was kept perpendicular to the work-piece during laser irradiation to maximise the absorbance and ensure uniform conditions for processing [99]. Tangential and linear velocities were varied using the control console depending on the pulse repetition frequency being used. The tangential and linear velocities also determined the resultant laser spot overlap. The calculation method used for overlap percentage determination is detailed in section 2.9.5. Specimens of 10 mm length along the bar were processed with different processing parameters according to the DOEs for subsequent characterisation as outlined below.

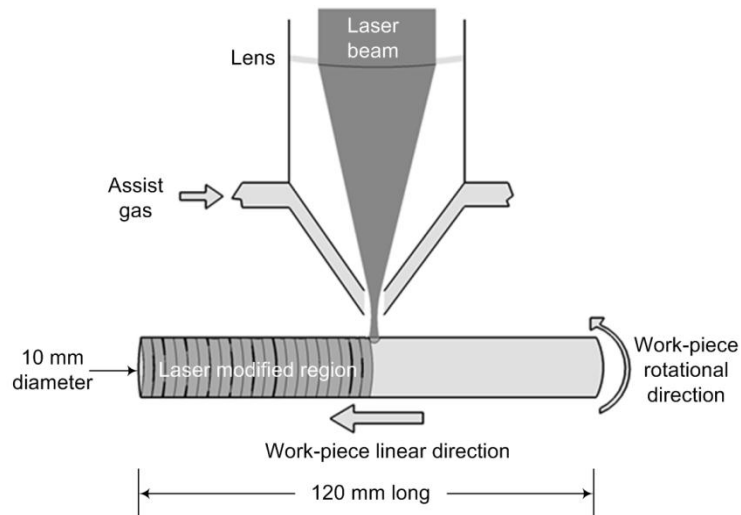


Figure 3-3: Schematic of the laser processing set-up for a cylindrical sample.

Spot diameter (z) on the sample surface could be controlled through setting the sample distance from focal plane of the Gaussian beam. Equation (8) was used to calculate the focus distance, see section 2.9.3 for more details.

$$w(z) = w_0 \left[1 + \left(\frac{\lambda \cdot z}{\pi \cdot w_0^2} \right)^2 \right]^{1/2} \quad (8)$$

where the beam radius along the propagation line, $w(z)$ was 45 μm , initial beam radius at the focus, w_0 was 45 μm , and the wavelength of the CO₂ laser, λ is 10.6 μm . All experiments were conducted with the laser beam focused on the surface of the work-piece.

3.2.2 Laser Processing of Planar Work-pieces

Laser processing of planar samples was performed in a raster scan fashion. Figure 3-4 shows the cross sectional side view of the equipment and the planar view of the raster scan path for the laser treatment process. The starting and ending points for each run were carefully chosen to allow the laser to accelerate to constant velocity before the laser beam interacted with the sample surface; more details on this are available in *Appendix B*. Specimens of 15 mm length along the flat workpiece and 20 mm width across workpiece were processed according to the DOE for subsequent characterisation as outlined below.

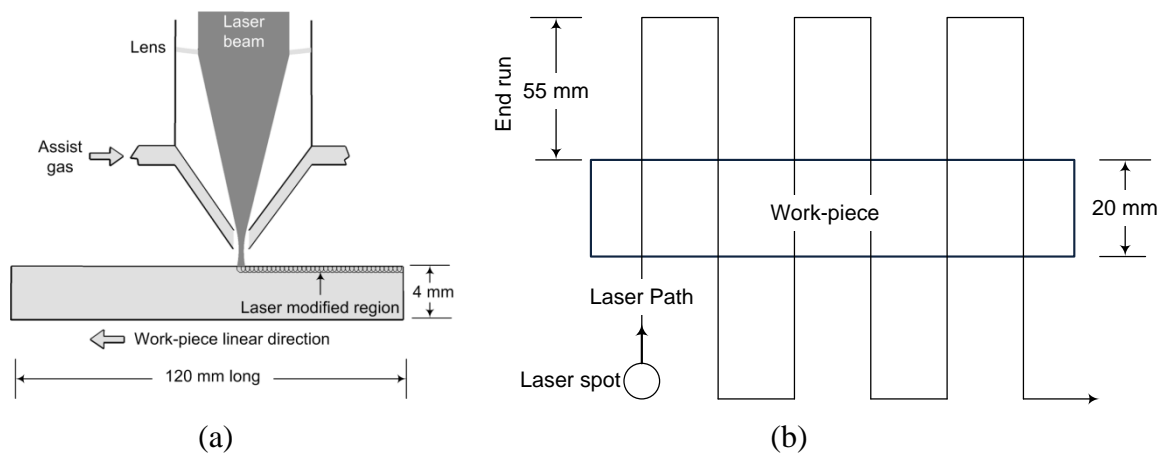


Figure 3-4: Schematic of the (a) cross sectional side view of the equipment and (b) the planar view of the raster scan path for the laser treatment process.

3.3 Metallography

The material microstructure can be thought of as its fingerprint and is directly related to the material properties and performance. In order to study the material microstructure a series of surface preparation techniques have to be done. The necessary surface preparation processes are detailed in the following sections.

3.3.1 Sectioning of the Work-piece

Sectioning was performed using the Delta AbrasiMet[®] abrasive cutter. A SiC cut-off wheel at 3800 rpm, in continuous flowing coolant, was used to avoid deformation and overheating during sectioning.

3.3.2 Mounting of the Sectioned Sample

Samples were encapsulated or mounted to protect the sample material and also to produce a uniform dimensionally stable size for subsequent automatic grinding and

polishing operations. Compression hot mounting was implemented in this study. Bakelite™ thermoset phenolic mounting material was used in a SimpliMet® 2000 mounting press. Thermosetting phenolic mounting material was chosen because once set it remains rigid even when subjected to heat. Curing was carried out at 180 °C for 8 minutes. The encapsulated samples were then cooled for 4 minutes.

3.3.3 Grinding and Polishing of the Mounted Sample

During the metallographic preparation of the treated region, damage can be induced to the sample. Sectioning of the specimen can cause localized cracking. As a result, the plane of evaluation must be at a point beyond this induced damage. This initial step, designed to quickly remove material, is referred to as planar grinding. The samples were ground on successive grades of silicon carbide paper using water to keep the specimen cool and flush away loose particles of metal and abrasive. Final polishing was carried out using a microcloth and alumina or diamond suspension. Both grinding and polishing were done using Buehler Motopol® 2000 automatic grinder/polisher machine. Table 3-5 highlights the grinding and polishing parameter used for both 316L SS and Ti-6Al-4V.

3.3.4 Etching

In order to reveal information such as grain boundaries and phases of the material, the samples were chemically etched. Grinding and polishing produces a highly deformed, thin layer on the surface which is removed chemically during etching. Etchants attack the surface with preference for those sites with the highest energy, leading to surface relief which allows different crystal orientations, grain boundaries, precipitates, phases and defects to be distinguished in reflective light. 316L stainless steel was etched by exposing the surface to be characterised in glyceric acid for approximately 1 minute [217]. The higher HCl content in glyceric acid reduces pitting tendency, attacks σ phase and outlines carbides. Glyceric acid was always used while fresh and discarded when it turned orange in colour. Micro-etching of Ti-6Al-4V was carried out by immersion in Kroll's reagent for one and a half minutes. Composition of the etchant being: 92 ml distilled water H₂O, 6 ml nitric acid HNO₃, and 2ml hydrofluoric acid HF [218].

Table 3-5: Grinding and polishing parameters for 316L SS and Ti-6Al-4V [219]

<i>Process</i>	<i>Surface</i>	<i>Abrasive</i>	<i>Lubri- cation</i>	<i>Time (min)</i>	<i>Base Speed (rpm)</i>	<i>Head speed/ direction</i>	<i>Force (N)</i>
<i>316L SS</i>							
Planar grinding	SiC	240-, 600-1200-grit	H ₂ O	Until Plane	200	120/Comp.*	5
Sample integrity	Ultra Pad	6 um Diamond suspension	-	4	150	120/Comp.	5
	Acetate Silk	1 um Diamond suspension	-	4	150	120/Comp.	5
Final polish	Chemomet	0.0 5 um Alumina suspension	-	2	150	60/Comp.	5
<i>Ti-6Al-4V</i>							
Planar grinding	SiC	320-grit (P400)	H ₂ O	Until Plane	240 - 300	60/ Contra	20
Sample integrity	UltraPol™ PSA Silk Cloth	9 um Diamond suspension	-	10	120 -150	60/ Contra	20
Final polish	MicroCloth® or Veltex cloths	0.0 6 um Alumina suspension	-	10	120 -150	60/ Contra	20

*Comp. = Complementary (platen and specimen holder both rotate in the same direction while contra is in the opposite direction)

3.4 Design of Experiments (DOE)

A DOE approach was taken in this study in order to systematically evaluate the effects of processing parameters on resultant surface properties. Design Expert 8, DOE software, was implemented in this research. The software was supplied by State Ease and has several statistical tools that allow for:

- i. Screening of designs to identify vital factors (processing parameters).
- ii. Discovering the best combination of factors.
- iii. Creating models and response surfaces from the factors.
- iv. Statistical analysis of resulting models.
- v. Graphically displaying the models.

Design Expert® was used for the analysis of variance (ANOVA) to test the adequacy of the developed models. The statistical significance of the model and each term in the regression equation was examined using the sequential F-test, and other adequacy measures (i.e. R², Adj- R², and Pred.R²) to obtain the best fit. From the statistical

models created by Design Expert, the F-values are indications of a factor's influence, higher F-values signify that the factor is of greater influence. Low p-values less than 0.05 indicate that the model is significant. A p-value of 0.05 indicates 95% confidence of the model. The R-squared value is a measure of the amount of variation around the mean explained by the model. The closer it is to 1 the less variance there is around the mean. The adjusted R-squared value is a measure of the amount of variation around the mean adjusted for the number of terms in the model. The adjusted R-squared value should be in reasonable agreement with the predicted R-squared value. The Adeq Precision value measures the signal to noise ratio. A higher ratio is desirable, and for the terms used in this study, a ratio greater than 4 is desirable.

3.4.1 316L Stainless Steel

Three DOEs were implemented for 316L stainless steel, however, only the last two are presented in the results section. The preliminary (screening) DOE is presented in the *Appendix C*. This initial DOE was a full three level factorial design (3^3). This model was chosen as it gave a more comprehensive analysis of all parameter interactions. The results from this pilot run were used to determine the parameters that had the most influence on the surface properties.

Design of Experiments 1

After the initial DOE, the two main parameters that had a pronounced effect on the surface properties were found to be residence time and irradiance. From the pilot DOE it was decided to further investigate the parameters using a 5^2 DOE. This DOE was named DOE 1. Two factors irradiance and residence time were varied for five levels from 78.6 to 235.8 kW/mm² and 49.6 to 165.3 μ s respectively. These parameters correspond to energy densities from 3.93 to 39.3 J/mm². Table 3-6 summarises the parameters used. The following parameters were kept at these specified constant levels throughout the laser treatment:

- i. Cylindrical sample diameter, 10 mm
- ii. Laser beam spot size, 90 μ m
- iii. Assist gas, Argon at 200 kPa
- iv. Overlap, 0%
- v. Surface tangential speed, 272 mm/s
- vi. PRF, 3000 Hz
- vii. Table speed, 46.8 mm/min

Table 3-6: DOE 1 processing parameters for 316L stainless steel.

<i>ID</i>	<i>Peak Power</i>	<i>Duty Cycle</i>	<i>Average Power</i>	<i>Irradiance</i>	<i>Residence Time</i>	<i>Energy Density</i>	<i>Est Temp.</i>
	(W)	%	(kW)	(kW/mm ²)	(μ s)	(J/mm ²)	(°C)
1	500	15	75	78.6	49.6	3.93	483
2	800		120	125.8		6.29	773
3	1000		150	157.2		7.86	967
4	1300		195	204.4		10.22	1260
5	1500		225	235.8		11.79	1450
6	500	20	100	78.6	66.1	5.24	644
7	800		160	125.8		8.38	1031
8	1000		200	157.2		10.48	1289
9	1300		260	204.4		13.62	1676
10	1500		300	235.8		15.72	1933
11	500	25	125	78.6	82.6	6.55	806
12	800		200	125.8		10.48	1289
13	1000		250	157.2		13.10	1611
14	1300		325	204.4		17.03	2094
15	1500		375	235.8		19.65	2417
16	500	30	150	78.6	99.2	7.86	967
17	800		240	125.8		12.58	1547
18	1000		300	157.2		15.72	1933
19	1300		390	204.4		20.43	2513
20	1500		450	235.8		23.58	2900
21	500	50	250	78.6	165.3	13.10	1611
22	800		400	125.8		20.96	2578
23	1000		500	157.2		26.20	3222
24	1300		650	204.4		34.06	4189
25	1500		750	235.8		39.30	4833

The laser beam spotsize was kept constant at the lowest permissible diameter of 90 μ m as lower spotsize would result in higher cooling rates. The cylindrical sample diameter and overlap were kept constant at optimised levels from previous studies that showed smoother surface properties at these levels [102]. The surface tangential speed, PRF and assist gas pressures were derived from the preliminary DOE. Surface temperatures were predicted using Equation 12 [97, 220].

$$T(z,t) = T_0 + \frac{AP}{2k\pi V_b \sqrt{t(t_i + t_0)}} \left[\exp\left\{-\frac{(z+z_0)^2}{4\alpha t}\right\} + \exp\left\{-\frac{(z-z_0)^2}{4\alpha t}\right\} \right] \operatorname{erfc}\left(\frac{z+z_0}{\sqrt{4\alpha t}}\right) \quad (9)$$

where A is the absorption coefficient, P the laser power (W), k the thermal conductivity (W/m·K), V_b the scan speed (m/s), t the residence time (s), t_1 the heating time (s), t_0 the time necessary for heat to diffuse over a distance equal to the laser beam radius on the workpiece surface (s), $t_0 = R_b^2/4\alpha$, α is the thermal diffusivity (m^2/s), z is the coordinate perpendicular to the treated surface, and z_0 is the distance over which heat can diffuse during the laser beam interaction time.

The thermophysical properties and absorption coefficients used in Equation 12 are given in Table 3-7. The majority of the absorbance data presently available considers only polished and roughened alloys rather than the commercially available (unpolished) alloys. Absorption coefficient of 316L stainless steel was set at 0.35 [99]. This absorption coefficient value corresponds to 96.5% reflectivity of highly polished and roughened samples for a CO_2 laser wavelength of 10.6 μm . It should be noted that Equation 12 was created for continuous mode so it is only expected to give an indication of the actual relative changes in temperature between samples but not the absolute values of temperature.

Table 3-7: Thermophysical properties of 316L stainless steel [221].

<i>Density</i>	<i>Specific Heat Capacity</i>	<i>Liquidus Temp.</i>	<i>Thermal conductivity</i>	<i>Thermal Diffusion</i>	<i>Absorption coefficient</i>
7970 kg/m^3	500 $\text{J}/\text{kg } ^\circ\text{C}$	1400 $^\circ\text{C}$	21.4 $\text{W}/^\circ\text{C m}$	$5.37 \times 10^{-6} \text{ m}^2/\text{s}$	0.35

Design of Experiments 2

To more fully comprehend the effects of irradiance, residence time and pre-treatments a new DOE, termed DOE 2, was implemented. The parameters of DOE 2 are summarised in Table 3-8. These parameters were carefully chosen so that they just barely melt the surface. These laser parameters were selected based on the previous DOE experiments and the thermal prediction model. The energy density was set at two levels, pulse width at two levels and three techniques were used for surface pre-treatments. The as-received (non pre-treated) surface was also processed with the DOE 2 parameters for benchmarking purposes. This resulted in 20 experimental conditions/samples being investigated. The machined pre-treatment consisted of machining ridges with an

average roughness of approximately 3 μm . As the overlap was set to 0 % for DOE 2, the residence time was equivalent to the pulse width.

Table 3-8: Laser processing parameters implemented in the fractional DOE.

<i>Run*</i>	<i>Peak Power (W)</i>	<i>Duty Cycle (%)</i>	<i>Irradiance (kW/mm²)</i>	<i>Residence Time (μs)</i>	<i>Energy density (J/mm²)</i>
1	1000	20	157	67	10.48
2	800	25	126	83	10.48
3	400	50	63	167	10.48
4	700	30	110	100	11.00
5	1400	15	220	50	11.00

*Each run was repeated using three surface pre-treatments etched; machined; machined+etched

3.4.2 Ti-6Al-4V

Design of Experiments 1: Planar samples

Experiments with Ti-6Al-4V were conducted with flat samples as opposed to the cylindrical samples used for the 316L processing. A 3² design of experiment was implemented. The two factors chosen were irradiance and residence, each time varied at three levels. The laser was used in continuous mode to irradiate the workpiece at three levels of irradiance: 15.72, 20.43 and 26.72 kW/mm² and three levels of residence time: 1.08, 1.44 and 2.16 ms, see Table 3-9.

Table 3-9: DOE 1 processing parameters for Ti-6Al-4V

<i>ID</i>	<i>Average Power (W)</i>	<i>Sample Speed (mm/s)</i>	<i>Irradiance (kW/mm²)</i>	<i>Residence Time (ms)</i>	<i>Energy Density (J/mm²)</i>
<i>LSM 1</i>	100	41.2	15.72	2.16	34
<i>LSM 2</i>	130		20.44		44
<i>LSM 3</i>	170		26.72		58
<i>LSM 4</i>	100	62.5	15.72	1.44	23
<i>LSM 5</i>	130		20.44		29
<i>LSM 6</i>	170		26.72		38
<i>LSM 7</i>	100	83.3	15.72	1.08	17
<i>LSM 8</i>	130		20.44		22
<i>LSM 9</i>	170		26.72		29

The laser beam was focused on the work-piece surface providing a Gaussian laser spot size of 90 μm . Since a continuous beam was used, pulse frequency and pulse width were not taken into account for residence time calculation, see section 2.9.4 for more

details. Low workpiece velocity compared to 316L samples subsequently resulted in much lower residence times. Due to the continuous nature of the beam the power is expressed as average power as opposed to peak power for Ti-6Al-4V. Irradiation was carried out using a raster scan with a partial overlap of 30% in order to provide for microstructural and compositional homogeneity. Argon at a pressure of 200 kPa was used as an assist gas to avoid oxidation. The laser beam was kept perpendicular to the workpiece during laser irradiation to maximise absorbance and ensure uniform conditions for processing.

3.5 Microstructural Analysis

The influence of the process parameters on the microstructure of the modified surface topology and cross section were studied using optical and scanning electron microscopy (SEM). Microstructure analysis was used to enable characterisation of the following:

- i. Pits and cracks
- ii. Grain structure and sizes
- iii. Gas-, shrinkage-, and interfacial-voids
- iv. Inclusions

A Reichart Me F2 Universal optical microscope was used for bright field examination of polished metallographic specimens. The microscope was equipped with Buehler Omnimet Enterprise, a software driven tool that allows for the quantitative analysis of the sample image. A Carl-Zeiss EVO-LS15 scanning electron microscope, shown in Figure 3-5, integrated with SmartSEM software was used for both morphological and microstructure analysis.

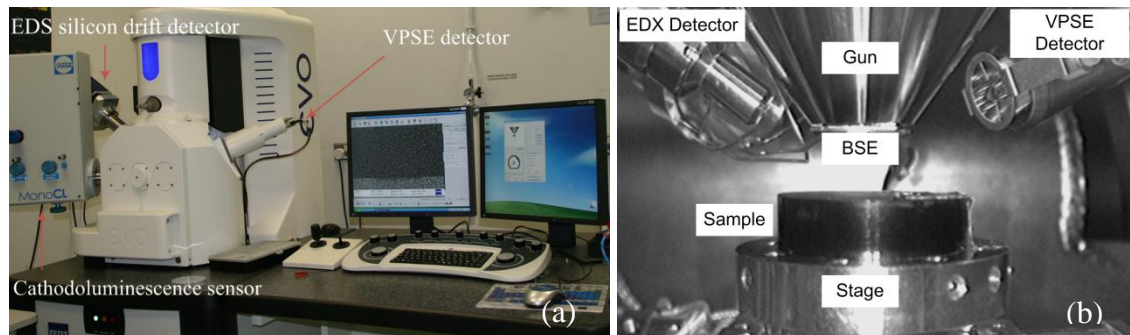


Figure 3-5: Carl-Zeiss EVO-LS15 SEM and its components (a) exterior and (b) interior.

Micrographs obtained from secondary electrons were primarily used for morphological analysis, while the backscatter detector images from the SEM were used to reveal microstructure features. The dependence of the backscatter yield with atomic number formed a basis for differentiating between different phases, thus providing an ideal starting point for further microanalysis. All images were captured at a high accelerating

voltages (20 kV) and high contrast to reveal the grain structure. Cross sectional views were prepared by sectioning the sample perpendicular to the longitudinal axis. The ‘analyse particles’ option in Image J (version 1.45), image analysis open software, was used to determine the grain size. The software uses Fret’s diameter technique, which measures the grain size by the greatest distance between two parallel lines touching opposite sides of the grain [222].

3.6 Melt Pool Profile Measurement

Analysis of the melt pool width and depth was performed from images obtained by the optical microscope and SEM. Average melt pool depth was determined with the software, Image J. An average depth for the laser modified surface was taken from at least ten measurements for statistical analysis.

3.7 Roughness Measurements

Roughness was calculated from a 2D profile. The surface profile was scanned with a stylus profilometer, Civil Instruments TR200, with a stylus tip radius of 2 μm. The surface mean roughness (Ra) measurements were derived from a given evaluation sampling and evaluation length. Figure 3-6 defines the evaluation and sampling lengths.

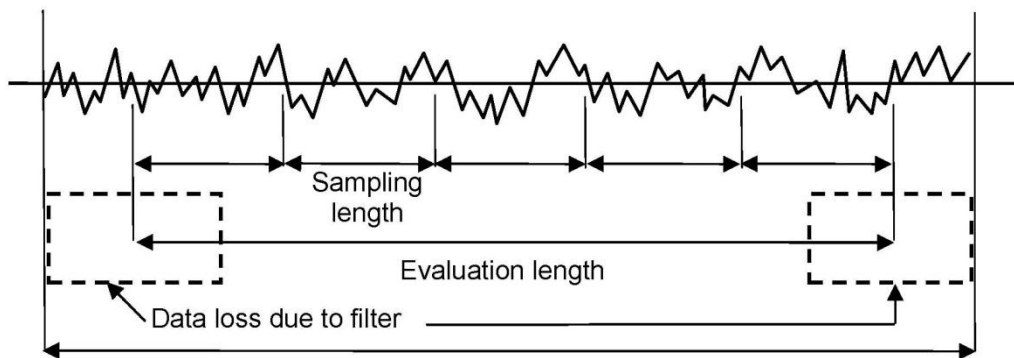


Figure 3-6: Sampling and evaluation lengths of a measured surface profile.

Once the surface profile was measured, waviness was eliminated with a Gaussian filter. The choice for a good cut-off length over which to measure the roughness is important. The cut off is a filter designed to measure only small irregularities with a spacing less than a given value of wavelength. Sampling length is always numerically equal to cut-off and the relationship between the cut off and an evaluation length is given by Equation (10):

$$\lambda_c = \frac{1}{5} \times l_n \quad (10)$$

where λ_c is the cut off length and l_n is the evaluation length

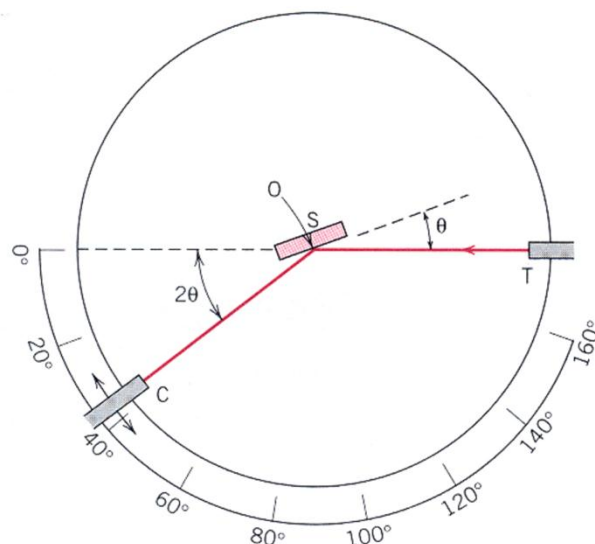
Sampling and evaluation lengths used were 0.8 mm and 4 mm respectively. The roughness was measured according to ISO 4287/4288. A table of the recommended cut-off lengths is shown in *Appendix D*.

3.8 Micro-hardness Measurements

A Leitz mini-load tester was used to perform the microhardness measurements of all samples. Vickers microhardness tests were carried out using a set load of 500 mN and an indentation time of 30 s. The measurements were taken from the cross-sectional surface that had been polished to a finish of 0.05 μm . Vickers microhardness was calculated by measuring the diagonal length (d_1) of square indentations. Five measurements were taken from the middle of the modified layer, unless otherwise stated. Measurements were taken according to the ISO 14577 standard. The indents were kept at least three diameters (indentation diameter) away from a free surface or interface and at least five diameters, of the largest indent, from each other to avoid interference [223].

3.9 XRD Analysis

X-ray diffraction patterns of the samples were recorded using a Bruker D8 XRD system with Cu $K\alpha$ ($\lambda = 1.5405 \text{ \AA}$) radiation. The test set-up is schematically shown in Figure 3-7. Samples were cleaned with acetone and rinsed with deionised water prior to analysis.



T= x-ray source, S = Specimen, C = detector, and O = axis.

Figure 3-7: Schematic and image of XRD set-up [47].

A fixed detector slit size of 0.2 mm wide and 12 mm long was used for all samples. A z scan was used to position samples at correct heights on the z drive prior to XRD measurement. Locked coupled scans were performed at a rate of 5 sec/step, with 0.01 step increments, varying the diffraction angle between 20 and 120°. Each scan took 13 hours and 47 minutes to complete. The diffraction patterns produced were plotted with intensity against 2 theta angles, and used for phase transformation and crystallinity analysis. Ti-6Al-4V is not included in the Joint Committee on Powder Diffraction Standards (JCPDS) database. Therefore, miller indices and phase determination were derived from the hexagonal α -Ti pattern (JCPDS file #44-1294) and the cubic β -Ti pattern (JCPDS file #44-1288). Strain and residual stress calculation induced by laser treatment can be calculated by using the variation in interplanar spacing, derived from shifting of the diffraction peaks, [224].

3.10 Chemical Composition Analysis

Element analysis and chemical characterisation were performed with an energy dispersive x-ray spectrometer (EDS). The Inca X-Act and Microanalysis suit, Oxford Instruments, integrated in the SEM was used, see Figure 3-5. The instrument is capable of analysing composition of sample areas down to 2 μm to be analysed on conductive samples with a relative accuracy of +/- 2%. The volume analysed, in which the primary electrons interact with the sample is generally characterized as pear/onion shaped region as seen in Figure 3-8 (a).

The geometry and volume of this shape is dependent on the average sample atomic number and electron beam accelerating voltage. The accelerating voltage used in the electron column influences both the spatial resolution of the x-ray signal and the efficiency with which characteristic x-rays are excited from the sample atoms. Higher voltages produce higher energy electrons, which penetrate more deeply into the sample and spread more widely than low-energy electrons. The result is degradation in resolution on the one hand, but more efficient excitation on the other. The relationship between the accelerating voltage, density and spatial resolution is given in Figure 3-8 (b). The red dashed line in Figure 3-8 (b) indicates the conditions use for analysis of the Ti-6Al-4V samples in this work.

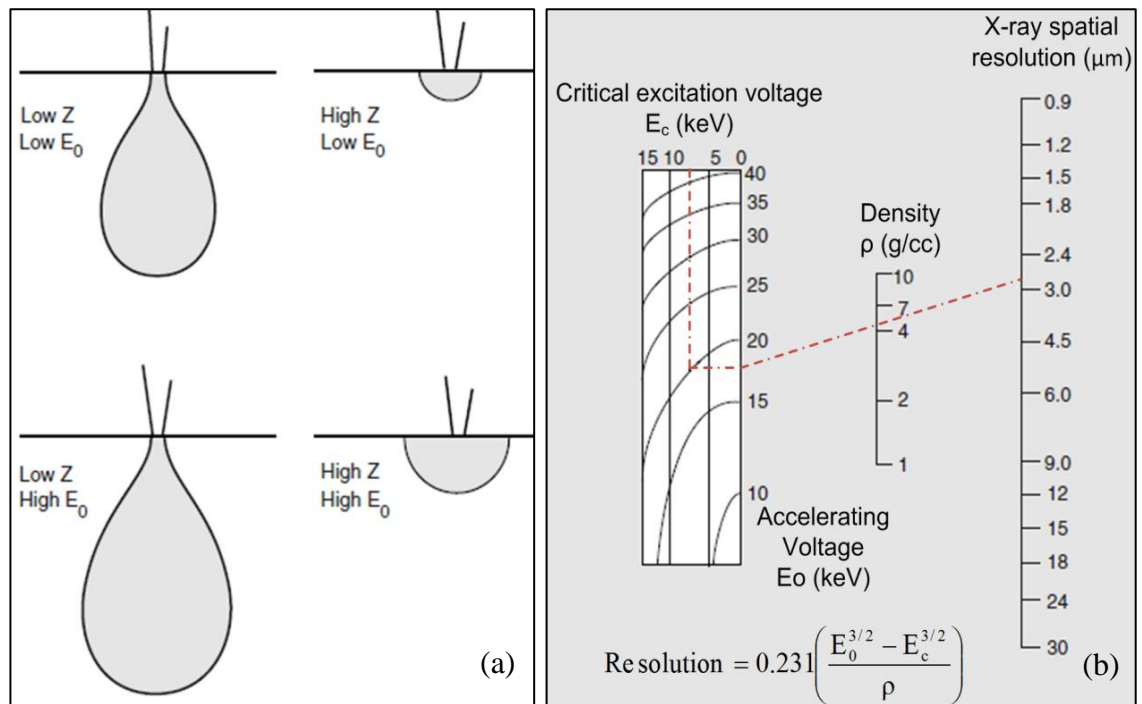


Figure 3-8: (a) Schematic depiction of the variation of interaction volume shape with average sample atomic number (Z) and electron beam accelerating voltage (E₀); and (b) chart for calculating x-ray spatial resolution from the accelerating voltage [225].

3.11 Wear Testing

Tribological evaluation of the modified surface was obtained using a pin on disk tribometer (ball on disc configuration); according to ASTM wear testing standard G-99. The apparatus used a pin pressing against the disk (sample) at a specified load. Amount of wear was determined by measuring appropriate linear dimensions of the wear track of the specimen after the test. The wear track shape was characterised using the SEM and dimension measured using the white light interferometry, Veeco's Wyko NT110 optical profiling system. The continuous recording of wear data was obtained using a LVDT to characterise the formation of the track. The continuous wear depth data alone cannot be used to fully characterise the wear properties due to the complicated effects of wear debris and transfer film present in the contact gap and the low, but significant, vibrations of the mechanism. A schematic of the pin-on-disk wear tester is shown in Figure 3-9. The Ti-6Al-4V samples were polished to within 0.2 μm average roughness to avoid excessive damage of the wear of the testing pin. Wear tests were carried out by sliding a 5 mm commercial zirconia pin against the polished samples at a constant speed of 18.9 mm/s with an applied load of 5 N.

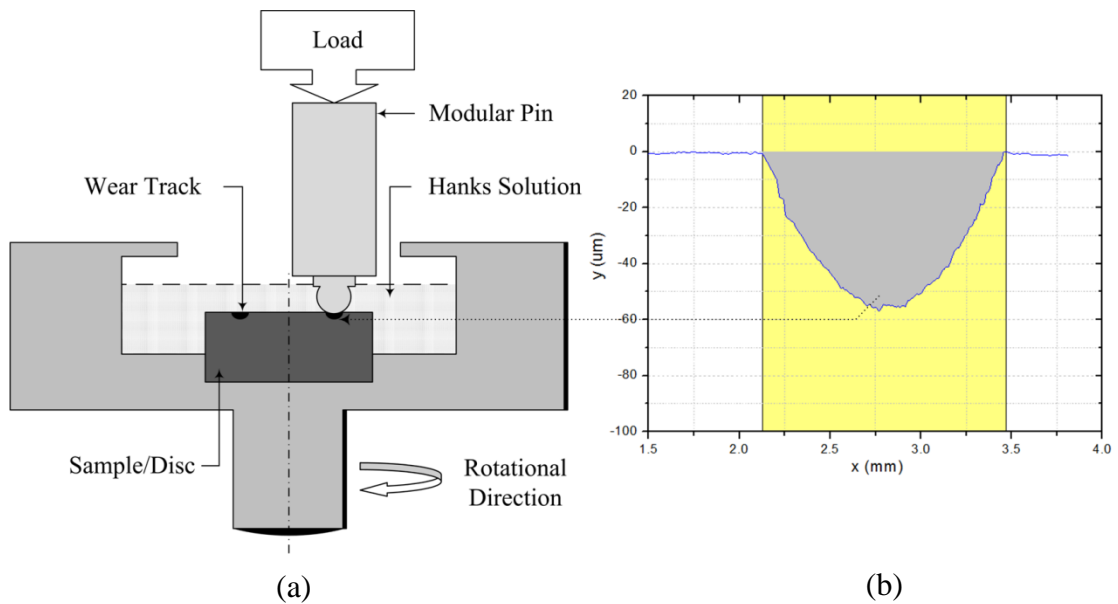


Figure 3-9: Schematic of the (a) pin on disc apparatus used and (b) typical wear track

The full list of testing parameters used for wear testing is shown in Table 3-10. Sliding distance was varied by adjusting the number of revolutions completed by the wear pin. All samples were cleaned with acetone in an ultrasonic bath, and dried prior to testing and measuring.

Table 3-10: Wear testing parameters

Sample/Disc material	Ti-6Al-4V	Applied load	5 N
Pin material	Zirconia (ZrO_2)	Atmosphere	Air
Pin diameter	5 mm	Test solution	Hanks solution
Speed	18.9 mm/s	Temperature	Ambient
Radius of wear track	1.5 mm	Sliding distance	20 and 150 m

Specific wear rate determines the wear behaviour of the Ti-6Al-4V with respect to sliding distance, contact pressure, velocity, temperature and test solution used. The specific wear rate for all samples was calculated using Equation (11). The amount of wear was determined using two methods. The first method evaluated the volume loss by measuring the mass of the sample before and after wear experiments by means of a precision balance (Avery Berkel's FA215DT) with 0.00001 g resolution, via Equation (12). The second method evaluated the volume loss by characterising the worn track dimensions using white light interferometry, via Equation (13). The optical micrographs of the wear track were further evaluated using the SEM.

$$\text{Specific Wear Rate (mm}^3\text{/N} \cdot \text{m)} = \frac{\text{Volume of wear track}}{\text{Total sliding distance} \times \text{Normal load}} \quad (11)$$

$$\text{Volume loss (mm}^3\text{)} = \frac{\text{Mass loss}}{\text{density}} \times 1000 \quad (12)$$

$$\text{Volume of wear track (mm}^3\text{)} = 2\pi \times r_{\text{track}} \times A_{\text{track}} \quad (13)$$

where r is radius of the pin from the central rotation axis of the sample and A is the cross-sectional area of the wear track obtained using the white light interferometer.

3.11.1 Reasons for parameter choice

Zirconia was chosen as it has high strength, hardness (>1200 HV), stability in physiological environments and is widely used as a head and socket material for hip replacements. The Ti-6Al-4V sample rotational speed of 120 rpm was chosen to obtain a linear tangential sample velocity of 18.9 mm/s which is approximately the mean sliding velocity for femoral heads of 28 mm diameter [27, 226]. A 5 N load was chosen for the normal load applied to the pin during testing. The reasoning for choosing 5 N as the load for wear testing is discussed in Appendix E.

3.11.2 Wear Testing Procedure

1. Specimen were cleaned and dried prior to testing and measuring using acetone.
2. The sample dimensions were measured and weighed to the nearest 2.5 μm and 0.00001 g respectively.
3. The disk was then inserted to the holding device, $\pm 1^\circ$ perpendicular to the axis of rotation to maintain the necessary surface conditions.
4. The load (5 N) was added directly onto the pin.
5. The revolution counter was set to zero.
6. The test was then run with the pin in contact with the specimen. The test was not interrupted or restarted until the set number of revolutions was reached for the corresponding test distance.
7. The wear material removal characteristics were investigated using the SEM.
8. The samples were then removed and cleaned.
9. The wear track dimensions and weight were then measured.

3.12 Corrosion Testing

To accelerate the corrosion process, electrochemical tests were used to directly amplify the impact of corrosion processes. This was possible since electrochemical tests use a fundamental model of the electrode kinetics associated with corrosion processes to

quantify corrosion rates [227]. Two types of electrochemical testing were employed. The first method was the corrosion measurement at the free corrosion potential (open circuit potential) in order to follow the active corrosion. The second was polarisation which measured susceptibility to localized corrosion for corrosion resistant materials. Prior to electrochemical testing, specimens were machined into square samples of 10 mm × 10 mm (+/- 1 mm) subsequent to laser treatment. The precise sample dimensions were measured prior to each test to 0.01 mm resolution and these measurements were input into the software before each test. The samples were embedded in epoxy resin exposing 1 cm² of the sample surface to the electrolyte. All samples were ultrasonically cleaned in acetone and rinsed using deionised water. A polarisation test cell with the following inserts was used: test, auxiliary and reference electrodes; luggin capillary; and thermometer, see schematic in Figure 3-10. Potentiodynamic polarisation was carried out using an ACM Gillac® potentiostat scanning unit. The potentiostat was capable of maintaining an electrode potential within 1 mV of a pre-set value. The auxiliary electrode supplied the current to the working electrode (test specimen) in order to polarise it. The potential between the specimen and the reference electrode was monitored in the test.

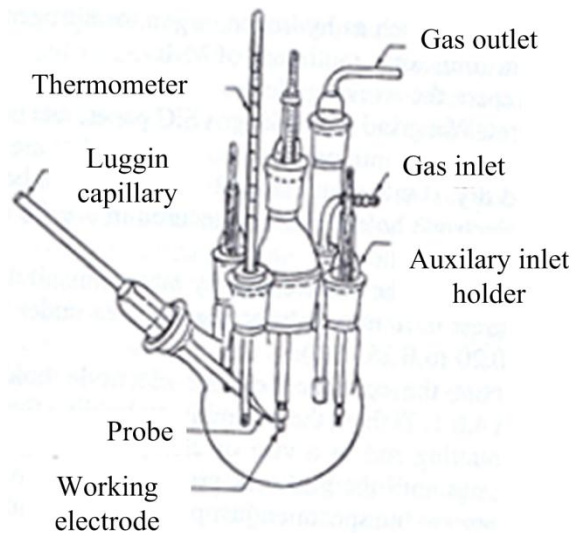


Figure 3-10: Schematic diagram of polarisation cell used in the experiments [228]

Figure 3-11 shows the experimental set-up used to monitor the electrochemical corrosion. A saturated calomel electrode and a platinum electrode were utilised as the reference and auxiliary electrode respectively.

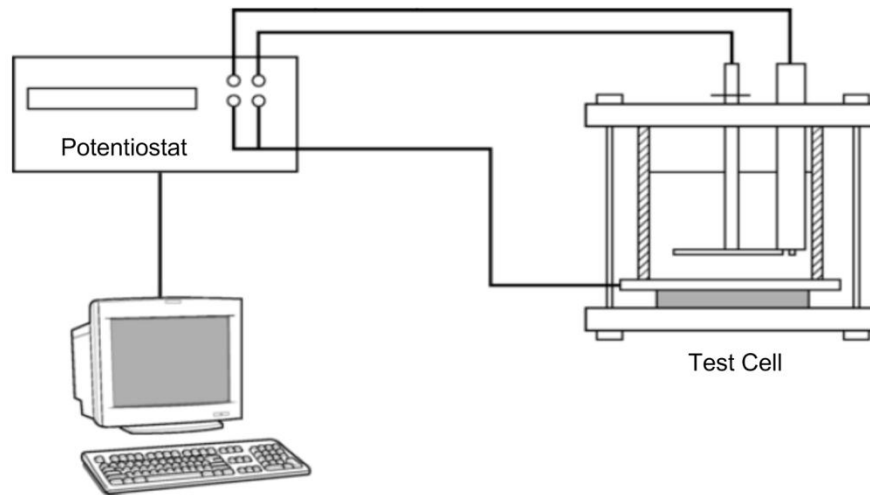


Figure 3-11: Schematic of instrumentation setup for electrochemical polarisation experiments.

To simulate body conditions a 0.9% NaCl and Hank's solution at $37 \pm 1^\circ\text{C}$ was used as the electrolyte; see Table 3-11 for the experimental parameters.

Table 3-11: Corrosion experimental parameters

<i>Tests</i>	1. Open Circuit Potential (OCP) 2. Potentiodynamic scan (PDS) - Tafel analysis
<i>Simulated Body Fluid (SBF)</i>	1. NaCl Solution 2. Hanks Solution Experiments carried out in aerated conditions
<i>pH</i>	7
<i>Temp</i>	37°C
<i>Electrodes</i>	Reference: Saturated Calomel Electrode Counter : platinum
<i>Open circuit voltage sampling time</i>	1 - 2 hours or until the corrosion potential (E_{corr}) changed no more than 2 mV over a 5 min period (OCP)
<i>Potential range</i>	-250 to 3000 mV at 0.5 mV/s
<i>Exposed Area</i>	10 mm^2

Open Circuit Potential (OCP) was measured in aerated conditions in each sample for one hour before potentiodynamic scans were started. After one hour the OCP stabilised and the potentiodynamic scans were started at 250 mV below OCP, at a rate of 0.5 mV s^{-1} . The results were analysed in terms of geometric surface area. Tafel extrapolation analysis was used to determine quantitative assessment of corrosion. Corrosion rate was determined by Equation (14):

$$CR = K \frac{i_{cor}}{\rho} EW \quad (\text{mm/y}) \quad (14)$$

where i_{cor} is the corrosion current density ($\mu\text{A cm}^{-2}$), K is a constant of $3.27 \times 10^{-3} \text{ mm g} (\mu\text{A cm yr})^{-1}$, EW is the equivalent weight ($11.768 \text{ g equiv.}^{-1}$), and ρ is the density (4.42 g/cm^3).

3.12.1 Corrosion Testing Procedure

Sample Preparation

1. The specimens to be used for corrosion testing were marked with a unique designation during preparation.
2. Dimensions of the sample were recorded.
3. Samples were cleaned with acetone and dried before mounting.
4. Silver paste was applied to attach an insulated wire to the opposite of the tested area sample and secured to the sample using tape. A requisite resistivity of less than 1Ω was kept for all samples.
5. Samples were cold mounted using epoxy and allowed to set for at least 6 hours.
6. For comparison purposes the control samples were polished. Grinding was accomplished using 320 grit SiC paper and polishing was conducted using $9 \mu\text{m}$ diamond suspension and followed by $0.06 \mu\text{m}$ alumina solution.
7. The surface structure was analysed under SEM or optical microscopy for existing defects before corrosion testing.

Apparatus Set-up

8. The prepared NaCl/Hank's solution was poured into a clean polarisation cell.
9. The temperature of the solution was raised to $37 \text{ }^\circ\text{C}$ using a controlled water bath.
10. Components of the test cell were placed into the cell. The sample was then mounted on the electrode holder. Degreasing was carried out using acetone and rinsing using distilled water, just before immersion.
11. The working electrode was transferred to the cell and the salt bridge adjusted so that the probe tip was about 2 mm away from the surface of the specimen.

Corrosion Testing

12. Before each polarisation scan was initiated, the corrosion sample was allowed to stabilise in the electrolyte for either 1 hour or until the corrosion potential, E_{corr} , changed by no more than 2 mV over a 5 min period.
13. Cyclic sweep scan was carried out at a sweep rate of 0.5 mV/s -

Post-test

14. Ultrasonic cleaning was carried out in reagent water to remove loose products.
15. Assessment of corrosion damage: microscopical examination for dealloying, exfoliation, cracking or intergranular attack by metallographic examination.
16. Data analysis involved OCP variation with time analysis and comparison of polarisation curves.

3.13 Contact Angle Analysis

The wetting characteristics of the surfaces were evaluated by measuring the contact angle between the surface and deionised water droplets, based on the standard sessile drop test. The contact angles, θ , of deionised water on the untreated and laser treated Ti-6Al-4V was determined in atmospheric conditions using a sessile drop measuring machine (goniometer). FTÅ 200 angstrom equipment was used for this which comprised of a monochrome camera and a motor actuated 10 ml syringe, see Figure 3-12. To avoid contamination, all samples being tested were cleaned with acetone in an ultrasonic bath for 30 mins, rinsed with deionised water several time and allowed to dry for at least 30 minutes. A wait period of 30 seconds was used before each θ measurement was taken. Dedicated software was used to calculate the wetting angles. Three measurements taken at different positions were averaged to get the final contact angle value for each sample. The mean value for the angle from both sides of each drop was used.

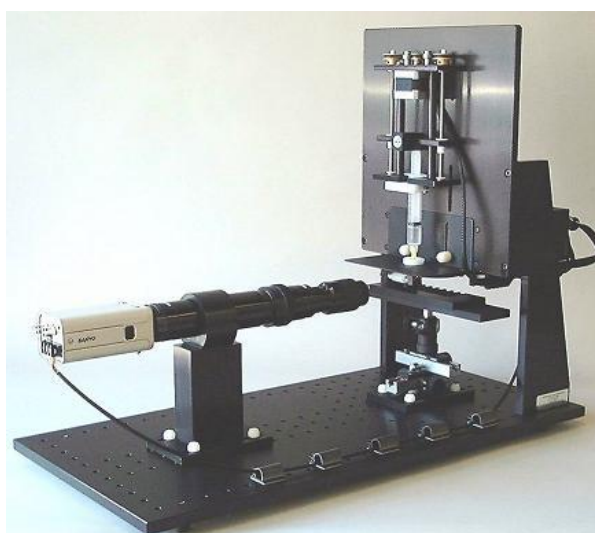


Figure 3-12: FTA 200 angstrom sessile drop measuring machine [229].

3.14 Biocompatibility Analysis

The biocompatibility work carried out in this research is split into two sections: (i) cell attachment and proliferation, and (ii) cytotoxicity analysis. The methods taken for each section are detailed in sections 3.14.1 and 3.14.2 respectively.

3.14.1 Cell Attachment and Proliferation

Cell culture

MC3T3 pre-osteoblastic cells were cultured in T175 flasks (Sarstedt) in standard media (α -MEM media (BioSera) supplemented with 10% fetal bovine serum (BioSera), 2% penicillin/streptomycin (Sigma Aldrich), and 1% L-glutamate (Sigma Aldrich)). Cells were passaged using trypsin-EDTA to detach the cells after several washes with sterile Phosphate Buffered Saline (PBS). The cells were incubated for 3 minutes then media added to deactivate trypsin. The solution was then placed in a centrifuge and processed at 1200 rpm for 5 minutes. The mixture of trypsin and media was then pipetted out and the resulting pellet re-suspended and split among T175 flasks. Media was then added to the flasks and the flasks were placed in incubators at 37° C and 5% CO₂. Media was refreshed every 3 days.

Seeding cells

Media was removed from the flasks and the cells rinsed several times with PBS. Cells were detached from the flasks using trypsin-EDTA solution and then incubated for 3 minutes. Media was added to deactivate the trypsin. The resulting solution was then placed in the centrifuge at 1200 rpm for 5 minutes to separate the cells and the solution. The mixture of trypsin and media was then pipetted out and the pellet re-suspended in 10 ml of media. Cells were then counted using a haemocytometer several times and the average used to calculate the total amount of cells in the solution. The media was again removed and the pellet then re-suspended to yield a cell suspension containing 2.5×10^5 cells per 20 μ l. The titanium samples were warmed in the incubator in 24 well plates and then seeded with 20 μ l of the pre-defined cellular solution on each of the treated surfaces. The samples were incubated for 15 minutes with 1 ml of media at 37°C and 5% CO₂.

Evaluating cell attachment

At 2 hrs, the cells were removed using trypsin-EDTA solution, and digested using papain solution to expose the DNA. Hoechst dye binds to DNA (hence the exposure of DNA required) and fluoresces, resulting in higher levels of fluorescence with higher

amounts of DNA. Cell number was quantified using a Hoechst 33258 DNA assay. Measurements were made using a fluorescence spectrophotometer (Varioskan Flash, Thermo Scientific) (excitation: 355 nm; emission: 460 nm) and readings were converted to cell numbers using a standard curve. Cell attachment was quantified using the results from the Hoechst 33258 DNA assay.

Evaluating metabolic activity

10% alamarBlue® solution (Invitrogen, UK) was made using α -MEM media (BioSera) and alamarBlue® dye. AlamarBlue is a compound that is reduced in cells and this reduction results in a colour change of the solution, thereby indicating the cell metabolic activity. The samples were then removed from the media and placed in 24 well plates with 1 ml of 10% alamarBlue® solution in each well. The samples were then incubated at 37°C and 5% CO₂ for 4 hours. They were then transferred back to 24 well plates with 1 ml of media in each well, and the alamarBlue® solution pipetted out in 100 μ l triplicate on 96 well plates and read with a spectrophotometer at 540 and 620 nm absorbance. This process was repeated at 24 and 96 hours and 7 days to assess cell metabolism.

Evaluating cell number

At 3 days and 7 days, the cells were removed using trypsin-EDTA solution, and digested using papain solution to expose the DNA. Cell number was quantified using a Hoechst 33258 DNA assay. Measurements were made using a fluorescence spectrophotometer (Varioskan Flash, Thermo Scientific) and readings were converted to cell numbers using a standard curve. Cell number was quantified, again using the results from the Hoechst 33258 DNA assay.

Statistical Analysis

One way repeated analysis of variance (ANOVA) followed by Holm-Sidak multiple comparisons were performed on both sets to compare data. T-tests were also used to compare the treated and untreated samples. Error is reported as standard deviation and is represented on figures, and significance noted for cases with probability, $p < 0.05$.

3.14.2 Cytotoxicity

Cytotoxicity tests were performed in accordance with ISO 10993-5 (2009) guidelines and included the direct contact, the indirect contact and elution tests with MTT as an endpoint.

Cell culture

The *in vitro* cytotoxicity assessment of the titanium samples was performed on the mouse embryo fibroblast (NIH/3T3) cell line. All culture and manipulation of cells was performed within a class 11 laminar flow unit in a dedicated cell culture laboratory. To ensure an adequate level of sterility, aseptic technique was strictly adhered to in accordance with ISO 10993 standards. Tissue culture plasticware was utilised at all times while incubators and laminar flow units were periodically cleaned with 70% ethanol to reduce the risk of contamination. In accordance with American Type Culture Collection (ATCC) recommendations for cell type media selection, 200 ml volumes of media, were aseptically prepared in 75 cm² culture flasks. Table 3-12 outlines the preparation of NIH/3T3 complete culture medium. Complete media was stored at 4°C for no more than 14 days. Media was heated to 37°C prior to use.

Cryovials of NIH/3T3 cells were removed from liquid nitrogen (-196°C) storage and disinfected with 70% ethanol. Cells were placed in a 37°C water bath to thaw. Cells were added to 10 ml of pre-warmed medium in sterile 25 ml universals and spun at 1500 rpm for 5 min in a bench top centrifuge (Mistral 1000, MSE Ltd.). Cell pellets were re-suspended in 1 ml of complete medium. Cell suspensions were subsequently pipetted into 25 cm² culture flasks and cultured in a humidified atmosphere of 5% CO₂: 95% air at 37°C until subconfluent.

Table 3-12: Composition of NIH/3T3 complete culture medium.

<i>Constituent</i>	<i>Volume/200 ml</i>
Dulbecco's Modified Eagles Medium (DMEM)	178
Fetal Calf Serum (FCS)	20
Penicillin-Streptomycin	1
Amphotericin B	1

Upon reaching 80% confluency, anchorage dependant cells were detached from the growth substratum. Media was aspirated off, under the laminar flow unit, cells were washed with sterile PBS and 2 ml of 0.25% trypsin-ethylenediamine tetra-acetic acid (EDTA) was added in order to facilitate cell removal. Cell culture flasks were incubated at 37° C for 5 mins. The degree of detachment was then assessed under an inverted light microscope. In order to deactivate the trypsin upon complete cellular detachment, 2 ml fresh media was added. Cell suspensions were aseptically removed to a sterile universal and centrifuged at 1500 rpm for 5 mins. The supernatant was discarded and the cell pellet was re-suspended in 1 ml of complete medium. If required, a cell count was

performed; otherwise the re-suspended cell pellet was split equally between two cell culture flasks and incubated at 37°C in a humidified CO₂ incubator.

A volume of 0.1 ml of cell suspension was transferred to a sterile eppendorf tube along with 0.15 ml PBS and 0.25 ml of 0.45% trypan blue. The suspension was inverted several times to allow for even distribution of cells. 10 µl of cells were loaded onto a Neubauer haemocytometer (previously washed with 70% ethanol) and covered with a glass cover-slip. All viable cells were counted in five 1 mm² squares (see shaded regions in Figure 3-13), viewed under an inverted light microscope at 200x magnification.

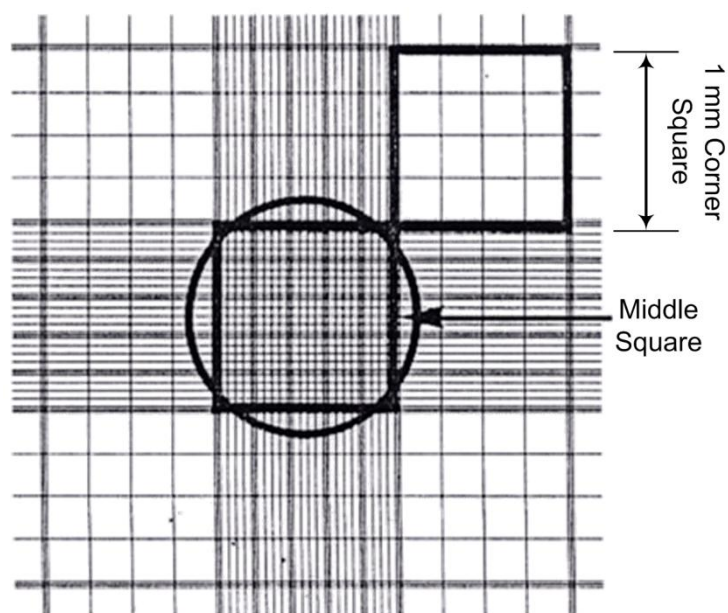


Figure 3-13: Haemocytometer viewed at 200x magnification [230]

The count was repeated three times for accuracy and the number of cells per ml of suspension was calculated, Equation (15).

$$\text{No. of cells/ml} = \frac{\text{Total No. of viable cells counted} \times 10^4 \times \text{dilution factor}}{\text{No. of squares in chamber used}} \quad (15)$$

Cytotoxicity Assessment

Cytotoxic effects on cell growth and viability were determined by the MTT assay. This assay determines the ability of viable cells to convert the soluble tetrazolium salt (MTT) into a purple formazan precipitate which can be quantified spectrophotometrically. The conversion of the tetrazolium ring to the formazan product is maintained by the mitochondrial enzyme succinate dehydrogenase and the cofactors nicotinamide adenine

dinucleotide (NADH) and nicotinamide adenine dinucleotide phosphate (NADPH). The amount of formazan produced is directly proportional to the number of viable cells. Ti-6Al-4V samples tested were insoluble, hence suitable for all three types of cytotoxicity test outlined in ISO 10993-5 (2009).

Prior to biocompatibility testing, the titanium samples were prepared to obtain reproducible and valid samples for testing. The risk of microbial contamination was reduced by briefly submerging the samples in 70% ethanol solution. Removal of residual ethanol was facilitated by evaporation under aseptic conditions and UV – irradiating at 263 nm for 10 mins. Sample eluate was prepared by immersion of samples in culture media for 7 days followed by preparation of serial dilutions. A 1% solution of Triton[®]X-100 was prepared fresh on the day of use by adding 100 µl of Triton[®]X-100 to 9.9 ml of fresh complete medium in a sterile universal. The solution was mixed, shaking by hand, and used immediately.

Direct contact assay (MTT endpoint)/ Agarose overlay

An MTT stock solution (5 mg/ml) was made by dissolving 50 mg MTT salt in 10 ml of sterile PBS. The solution was filtered through a 0.22 µm Polyethersulfone (PES) membrane filter, kept in the dark, refrigerated at <4°C and discarded after 21 days. NIH/3T3 cells were seeded at 500,000 cells ml⁻¹ in 60 mm tissue culture plates and incubated at 37°C until confluent. Sterile laser treated and untreated Ti-6Al-4V samples were placed in the centre of confluent cultures covering approximately 10% of the growth area and incubated for a further 24 h at 37°C. Following careful removal of samples with sterile tweezers, and cell incubation in MTT medium (0.5 mg/ml) for 4 h, morphology and viability was qualitatively assessed under an inverted light microscope and toxicity graded as outlined in Table 3-13 (ISO 10993-5, 2009).

Table 3-13: Reactivity grades for direct and indirect (agarose overlay) contact assays - adapted from ISO 10993-5 (2009).

<i>Grade</i>	<i>Reactivity</i>	<i>Description of reactivity zone</i>
0	None	No detectable zone around or under specimen
1	Slight	Some malformed or degenerated cells under specimen
2	Mild	Zone limited to area under specimen
3	Moderate	Zone extends up to 1.0 cm beyond specimen
4	Severe	Zone extends greater than 1.0 cm beyond specimen but does not involve entire dish/well

For quantitative assessment 4 ml of fresh culture media supplemented with 0.5 mg/ml MTT, was added to each well and incubated for a further 4 h at 37°C. The MTT media was carefully aspirated off and 4 ml of Dimethyl Sulfoxide (DMSO) was added to each well to aid in solubilisation of the crystals. Plates were shaken for 15 s and incubated at room temperature for 10 min prior to recording optical densities at 540 nm, with cell viabilities calculated as a percentage of untreated control cells \pm the standard error of the mean (SEM) using Equation (16):

$$\text{Cell viability (\%)} = \frac{\text{Absorbance}_{540\text{nm}} \text{ of treated cells}}{\text{Absorbance}_{540\text{nm}} \text{ of untreated cells}} \times 100 \quad (16)$$

Elution test (MTT endpoint)

NIH/3T3 cells were seeded at 10,000 cells per 100 μ l of media in 96 well microtitre plates and incubated in a humidified atmosphere of 5% CO₂: 95% air at 37°C until the desired degree of confluency was obtained. Subsequently cultures were exposed to pre-warmed test media containing 100-0% eluate from Ti-6Al-4V samples or 1% Triton[®]X-100 positive control for a further 24 h at 37°C. Following removal of test media cells were washed with 100 μ l of warm sterile PBS. 100 μ l fresh culture media supplemented with 0.5 mg/ml MTT was added to each well and plates were incubated for a further 4 h at 37°C. The MTT media was carefully aspirated off and 100 μ l of DMSO was added to each well to aid in solubilisation of the crystals. Plates were shaken for 15 s and incubated at room temperature for 10 min prior to recording optical densities at 540 nm. Cell viabilities were calculated as a percentage of untreated control cells \pm the standard error of the mean using Equation (15).

Chapter 4 : 316L Stainless Steel

Results & Discussions

4.1 Design of Experiments 1

This DOE was especially designed to study the effects of irradiance and residence time on 316L stainless steel after reviewing of literature and preliminary results, see *Appendix C*.

4.1.1 Morphology and Microstructure Analysis

Figure 4-1 shows SEM images the (a) planar and (b) cross-sectional microstructure prior to laser surface modification. The as-received surface, Figure 4-1 (a), showed an uneven topology with significantly large scratches and cracks. The cross sectional micrographs, Figure 4-1 (b) and (c), clearly show the phases present in 316L stainless steel. Small pores are visible as dark spots on the BSE micrographs. These are likely to be caused by the pull out of inclusions in the steel during grinding and polishing.

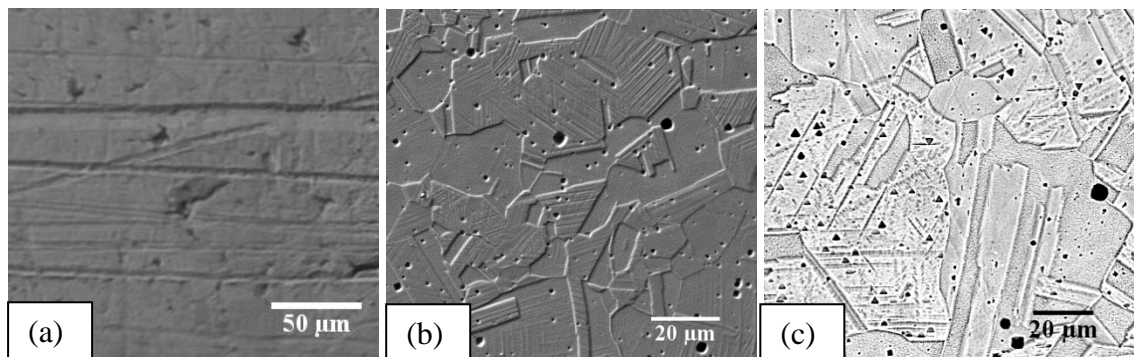


Figure 4-1: Microstructure of as-received 316L stainless steel (a) morphology structure, and the cross-sectional microstructure obtained via (b) secondary electron (SE) detector and (c) back scatter electron (BSE) detector.

To demonstrate the effects of laser processing parameters on the morphology and cross-sectional microstructure three levels of energy density have been selected, 5.24, 10.48 and 20.96 J/mm². These three levels are important as they illustrate three different stages that result from energy density variations. Surface morphology and cross-sectional microstructure of the laser processed 316L stainless steel are presented in Figure 4-2 and Figure 4-3 respectively. Figure 4-2 illustrates the surface melting induced by the laser treatment at increasing energy density from (a) to (c). The surface

temperature directly under the surface was estimated, using Equation (9) to be approximately 1190, 2001 and 3111 K for the samples in Figure 4-2/ Figure 4-3 (a), (b) and (c) respectively.

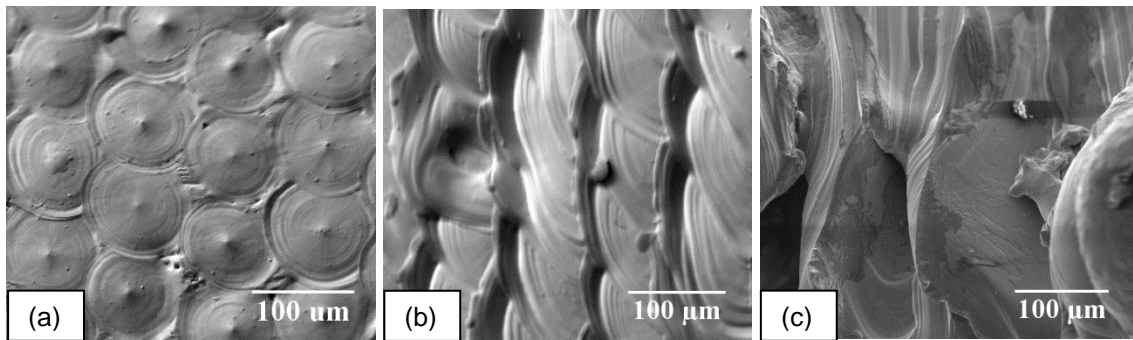


Figure 4-2: Effects of energy density on surface melting
(a) 5.24 J/mm², (b) 10.48 J/mm² and (c) 20.96 J/mm².

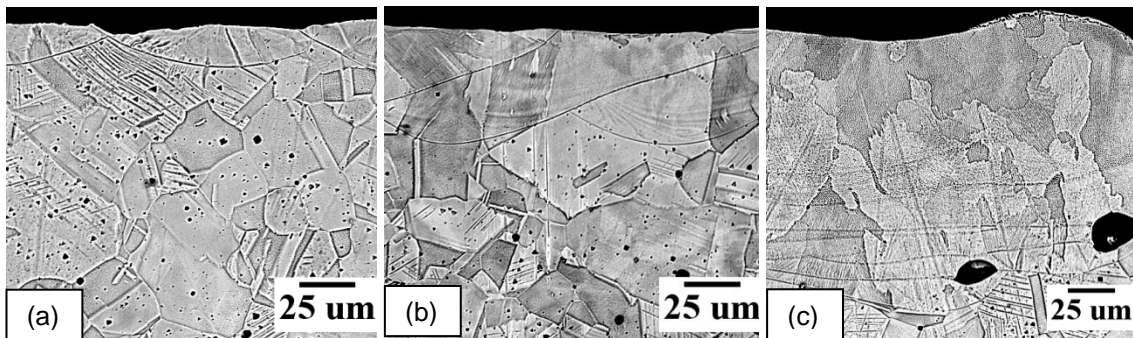


Figure 4-3: Back scatter SEM images of transverse cross sectional microstructure corresponding to processed surface shown in Figure 4-2 (a), (b) and (c).

Sample rotation parameters were set to produce 0% overlapping of the melt pool as represented in Figure 4-2 (a) and Figure 4-3 (a). At 5.24 J/mm², Figure 4-2 (a) and Figure 4-3 (a), laser marking features are visible. The low energy density only produces localized melting effects. This is more evident in Figure 4-3 (a) which shows less than 20 μm depth of processing in the cross sectional microstructure. No significant grain structure changes are visible in Figure 4-3 (a).

At 10.48 J/mm², Figure 4-2 (b) and Figure 4-3 (b) illustrate homogenised melting with increased depth of processing. Using the spot size diameter of 90 μm created on the surface of the material, the work-piece velocity and PRF were adjusted to create an overlap of 0%. However overlapping of the melt pool was visible at energy densities of 10.48 J/mm². This overlapping effect is due to the production of melt pools wider than the original spot size and subsequent flow due to the fast rotation of the specimen. High

sample surface speed (272 mm/s) and the beam's Gaussian profile are believed to also contribute to the overlapping effect. The effects of the Gaussian beam and distribution of power density are explained in detail in section 6.1.1. The grain structure of samples laser treated at 10.48 J/mm^2 changed direction at the substrate laser treated interface. The grain structure re-orientation is clearly highlighted in Figure 4-4. The phenomenon was visible in all samples laser treated at energy densities greater than 9 J/mm^2 . Tangential force produced by the rotation of the sample is attributed to the grain direction re-orientation. Even though the residence time was very low, the cooling rates were still not high enough to significantly impact the grain sizes. There was no significant grain size changes observed in the sample laser treated at 10.48 J/mm^2 . Unchanged grain sizes could possibly be also due to the high carbon content of 316L stainless steel that also restricts hardening of the material through heat treatment.

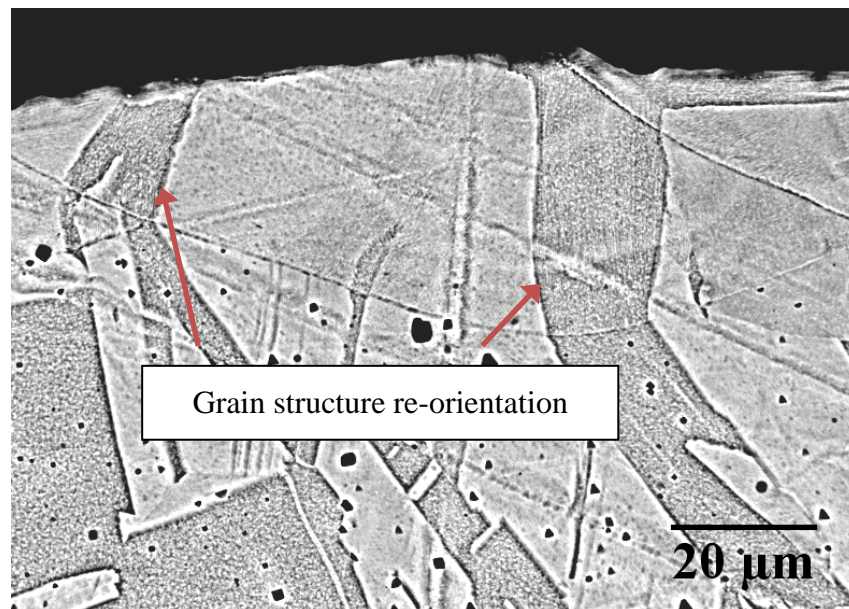


Figure 4-4: Grain structure re-orientation in samples laser treated at energy densities greater than 9 J/mm^2 .

Figure 4-2 (c) and Figure 4-3 (c) depict the surface and cross-section microstructure at an energy density approximately 4 times larger than Figure 4-2 (a) at 20.96 J/mm^2 with surface temperatures approximated at 3111 K. An increased depth of processing is observed, while other regions showed some ablation due this higher irradiance values. Grain size and orientation alteration are also visible. The overlapping boundaries visible at high energy density, 20.96 J/mm^2 , can be seen in Figure 4-2 (c) as layers representing different isotherms. Figure 4-5 shows the variation in microstructure at different points within the laser treated region.

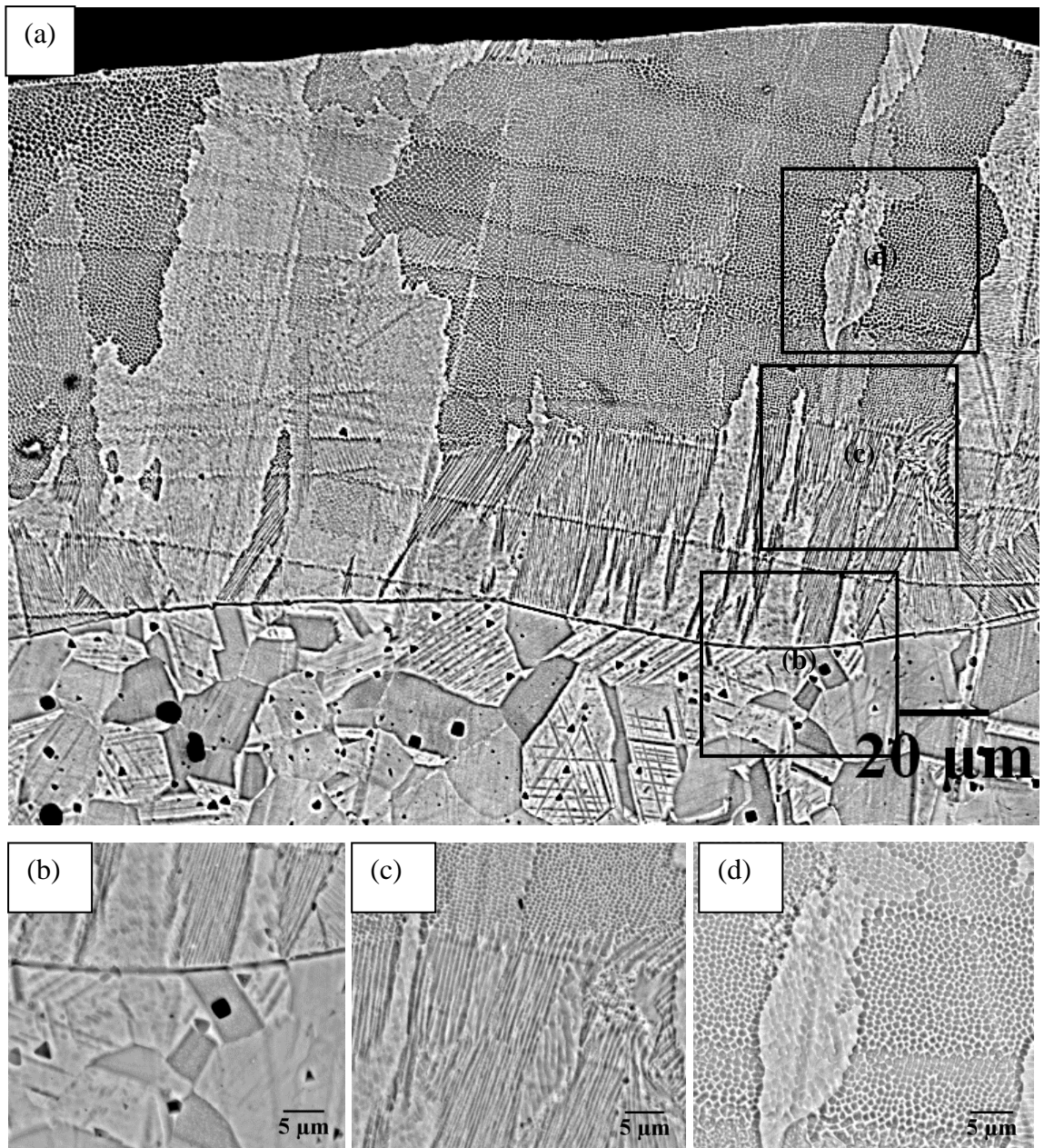


Figure 4-5: (a) Microstructure variation in samples treated at 20.96 J/mm^2 and close up view of specific regions (b), (c) and (d).

Figure 4-5 (b) shows the interface between the untreated and LSM regions highlighting grain structure re-orientation and transition of the grain structure from the typical austenite grain structure into a lamellar structure. The lamellar morphology created at this interface in the LSM region resembles the grain structure after diffusion-less transformation as presented in the ASM Handbook Vol. 9 [231]. These martensitic microstructures are produced by rapid quenching of the austenitic parent phase. The austenitic phase is not retained due to the uninterrupted rapid cooling which prevents austenitic decomposition into ferrite and pearlite via diffusional processes. The substrate

acts as a heat sink thus assisting with achieving the rapid solidification necessary for formation of this structure.

Figure 4-5 (c) shows the transition from lamellar structures to nodular structures. The nodular structure, shown in Figure 4-5 (d), is prevalent near the surface. This structure has not previously been identified in literature. However, it is postulated that the transition is caused by the high cooling rates and thermal gradient induced by a combination of high irradiance and low residence times. Such thermal gradients produce variant phases from the typical austenite structure within the untreated region.

4.1.2 Melt Pool Size Analysis

Figure 4-6 shows the effects of residence time on the depth of processing at irradiance values for the three irradiances 79, 157 and 236 kW/mm². All DOE meltpool depth results are shown in *Appendix F*. Augmentation in melt pool depth is closely linear for increasing residence time for all irradiance values. High residence times result in increased interaction of laser beam and surface of the material thus increasing exposure time and melting pool depth size. Low levels of irradiance (79 kW/mm²) and residence time (50 μs) produced the minimum melt pool depth of 10 μm. The maximum melt pool depth of 95 μm was produced with combination of high levels of both residence time (100 μs) and irradiance (23.6 kW/mm²).

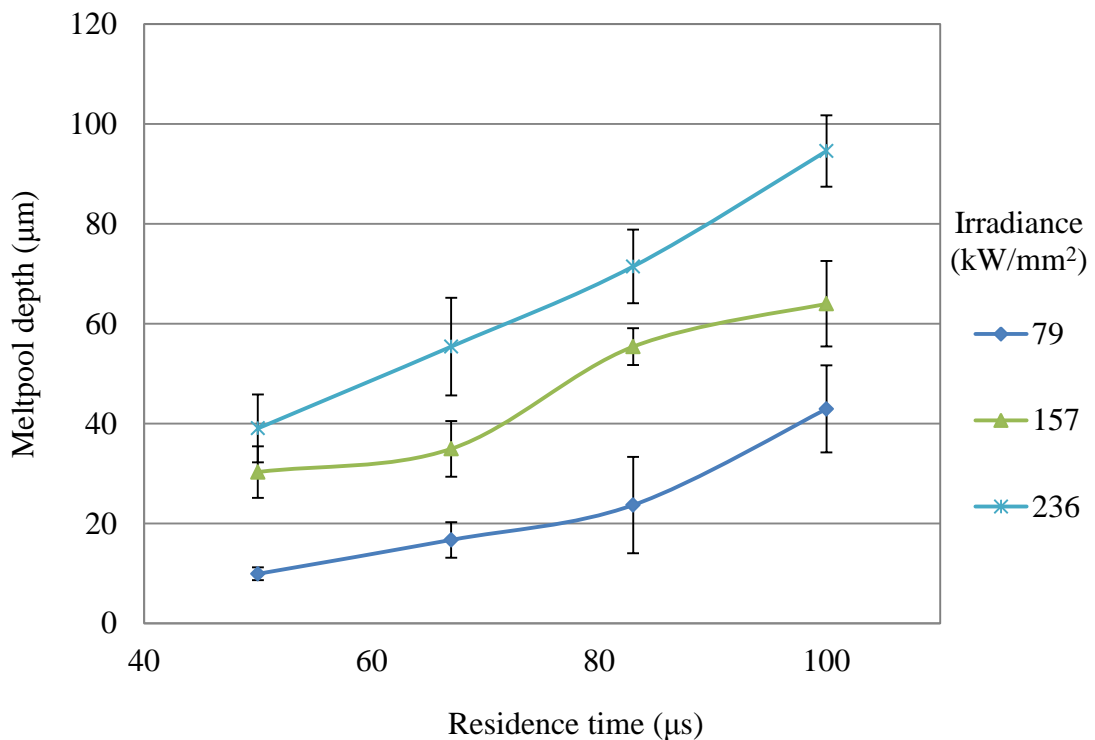


Figure 4-6: Effects of residence time and irradiance and on melt pool depth.

To illustrate the effects of irradiance and residence time on the depth of processing and roughness, energy density was fixed at 13.1 J/mm^2 with two different combinations of irradiance and residence time. The resulting micrographs are shown in Figure 4-7. A combination of low irradiance (79 kW/mm^2) and high residence time ($167 \text{ }\mu\text{s}$) produced a melt pool depth of $115 \text{ }\mu\text{m}$. The depth was approximately double that of a combination of high irradiance (157 kW/mm^2) and low residence time ($83 \text{ }\mu\text{s}$) which produced a depth of $57 \text{ }\mu\text{m}$, see Figure 4-7. An observation of the aforementioned results show that residence time has a greater effect on depth of processing compared to irradiance. The results prove that depth of processing cannot be related to a product value (energy density) of irradiance and residence time. Independent values of both parameters have to be considered in order to understand the output depth of processing. In order to have a microstructure with low grain sizes (improved hardness), very high cooling rates are required. The cooling rates can only be obtained at very low exposure time with extremely high irradiance. Using the minimum permissible residence time from the system of $27 \text{ }\mu\text{s}$, an irradiance of over 1500 W would be required which is over the limit of the laser unit used in the presented research. One way to increase the energy input is to improve the laser absorbance of the stainless steel surface as only 3.5% absorption was estimated using the surface temperature prediction Equation (9) per the literature [99].

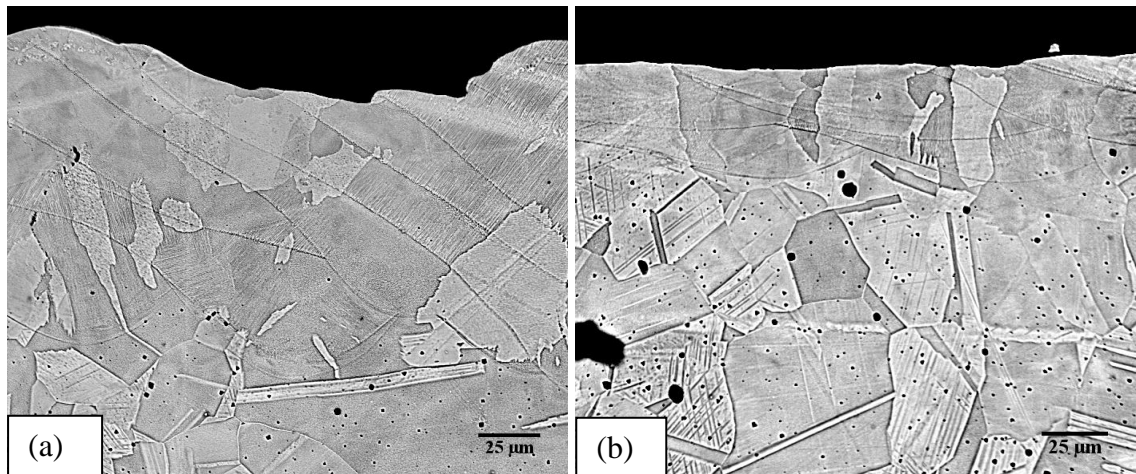


Figure 4-7: Backscatter SEM cross section micrographs of samples processed using the same energy density (13.1 J/mm^2) with: (a) low irradiance (79 kW/mm^2) and high residence time ($167 \text{ }\mu\text{s}$); (b) high irradiance (157 kW/mm^2) and low residence time ($83 \text{ }\mu\text{s}$).

4.1.3 Roughness Analysis

The average roughness of untreated stainless steel was measured to be $1.96 \pm 0.26 \mu\text{m}$. Figure 4-8 illustrates the roughness results obtained at various levels of irradiance and residence times. The roughness increases as the irradiance increases for all given residence times. At low irradiance (79 kW/mm^2), varying residence time does not have a significant effect on roughness. There is no significant increase in roughness at low residence times since no melting occurs at minimum exposure times. At low exposure times the laser beam is in contact with the beam for a very short period of time therefore extremely high laser powers are required to induce melting on the surface. Low exposure times have roughness values comparable to the untreated steel due to the aforementioned effects. The roughness values obtained in this study give a good indication of the melting status of the parameters used in the experiment.

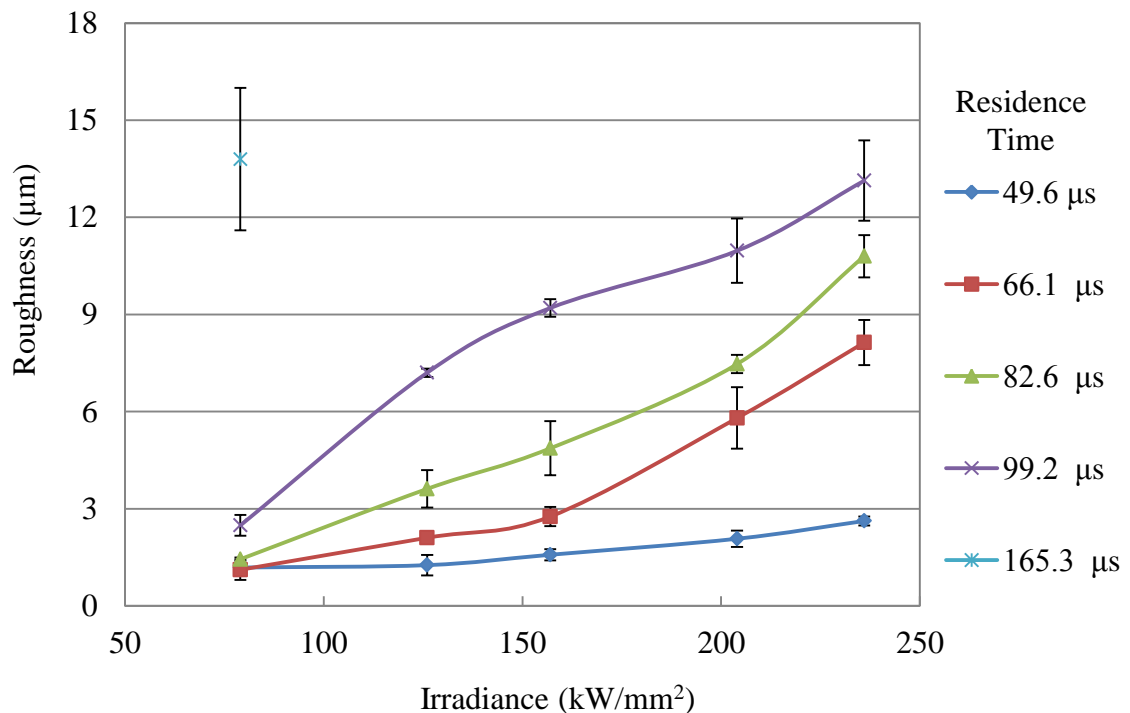


Figure 4-8: Relationship between average surface roughness and irradiance at varying residence times.

An increase in the laser beam residence time results in elevated surface temperatures. The characteristic of such a treatment is increased roughness due to ablation occurring on the surface. The highest residence time implemented in the experiments conducted ($167 \mu\text{s}$) resulted in high roughness. This residence time produced an average roughness of $13.8 \mu\text{m}$ when coupled with the lowest irradiance of 79 kW/mm^2 . At a residence time of $167 \mu\text{s}$, and for irradiances higher than 79 kW/mm^2 the profilometer was unable to

detect resulting high sample roughness due to extensive ablation. Figure 4-9 illustrates the effect of low irradiance and high residence time on the surface roughness.

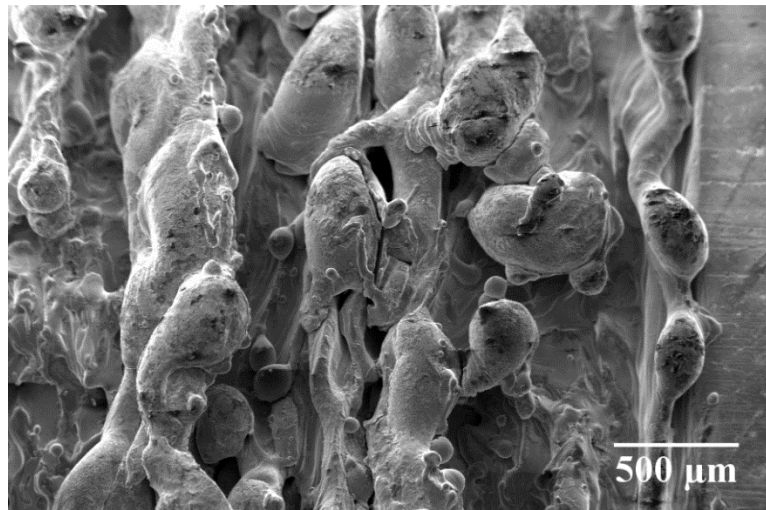


Figure 4-9: Sample treated at low irradiance (79 kW/mm^2) and high residence time (167 μs) illustrating effects of high densities on surface roughness.

Figure 4-9 shows the typical, channel-like, ablation features that are induced at high energy densities. A strong correlation is also visible between roughness and energy density used in the experiment regardless to the residence time; see Figure 4-10. The first three points (bottom left) on the graph were results from samples in which no melting occurred due to the low energy density. A linear increase in roughness is observed with higher energy densities.

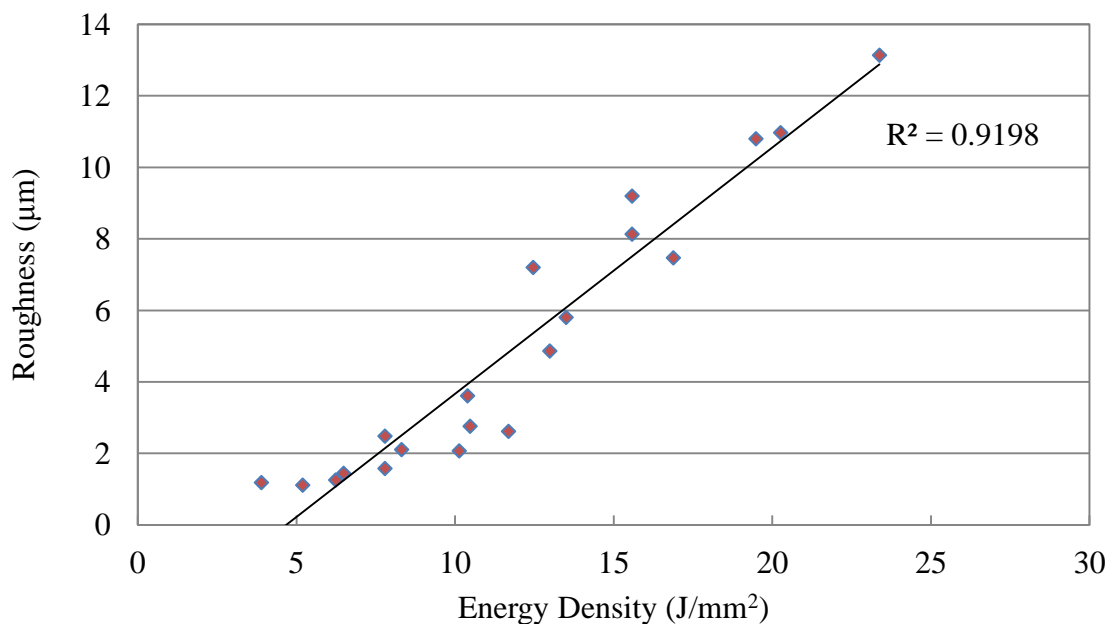


Figure 4-10: Relationship between average surface roughness and energy density for laser processing of 316L with DOE 1.

4.2 Design of Experiments 2

Two energy densities (10.48 and 11 J/mm²) which provided the most homogenous melting of the surface were especially studied in this DOE. While keeping the energy densities at 10.48 and 11 J/mm², irradiance and residence times were varied in order to study their effects. All design points were processed on as-received, machined, etched, and machined+etched work-pieces to study the effects of surface pre-treatments.

4.2.1 Microstructure Analysis

Prior to DOE 2, energy densities ranging between 5 and 25 J/mm² were examined. Figure 4-11 shows the result of processing at 5 J/mm². Figure 4-12 shows the result from processing at 25 J/mm².

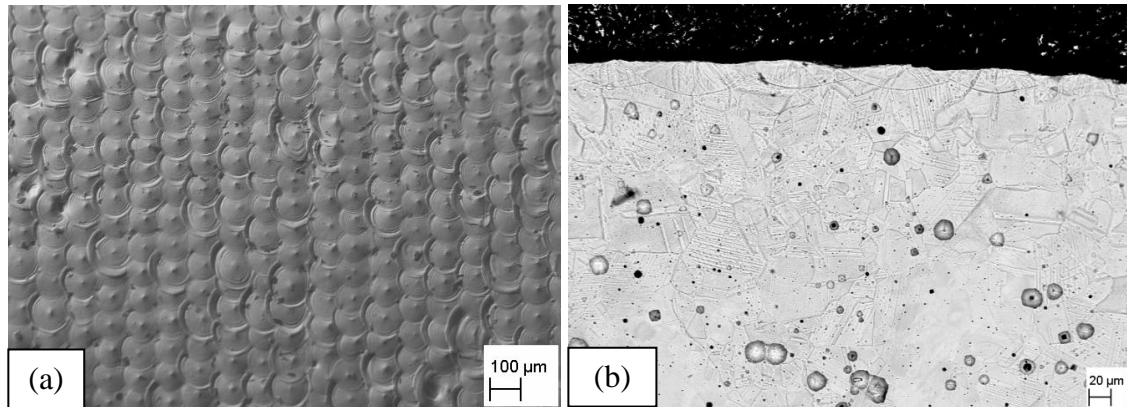


Figure 4-11: Influence of low energy density 5 J/mm² on melting of surface
(a) surface topology and (b) cross sectional microstructure

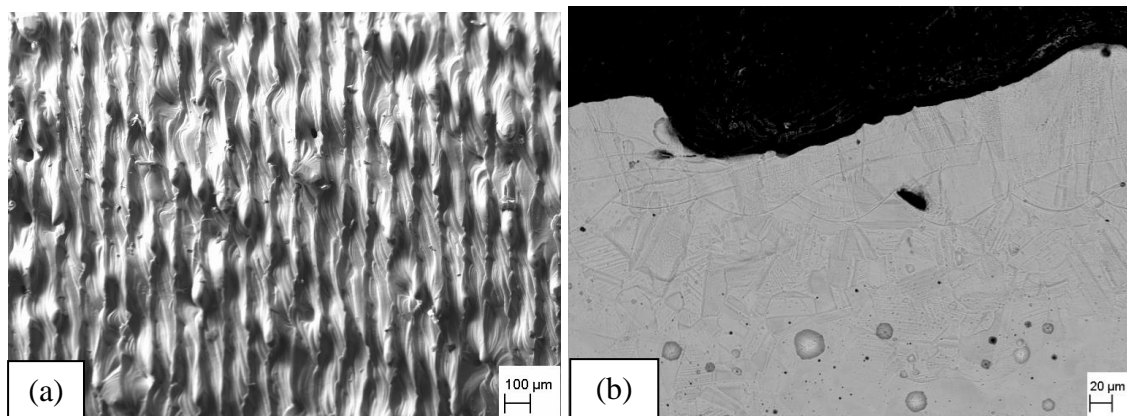


Figure 4-12: Influence of high energy density 25 J/mm² on melting of surface
(a) surface topology and b) cross sectional microstructure

The processing parameters of these results are not within the DOE 2 set of processing parameters, however are included here to illustrate process parameter space boundaries

for the laser processing of 316L. The low energy density in this case resulted in insufficient surface melting. The laser spot shapes produced are attributed to the Gaussian characteristics of the laser beam and very small volumes of surface metal melting. Negligible overlap occurred due to relatively small amount of melting occurring thus the characteristic of the set spot size is visible. There is no significant change in microstructure as can be seen in Figure 4-11 (b).

Increasing the pulse energy to 15 J/mm^2 produced ablation on the surface of the steel as shown in Figure 4-12 (a). The ablation can easily be noticed through the formation of distorted channel-like features on the steel. Figure 4-12 (b) shows the corresponding microstructural effects and material removal on the steel surface. Overlapping of the individual molten volumes is visible and this is attributed to high irradiance producing melting pools larger than the set laser beam surface spot diameter.

The rest of the results in this section correspond to DOE 2 set parameters. The topography of the samples laser modified using an energy density (10.48 J/mm^2) but with different peak powers and residence times are shown in Figure 4-13. Figure 4-13 (a) shows the treated surface at an irradiance of 157.2 kW/mm^2 and $67 \text{ }\mu\text{s}$ residence time. Figure 4-13 (b) shows the surfaces processed at an irradiance and residence time of 62.9 kW/mm^2 and $167 \text{ }\mu\text{s}$ respectively.

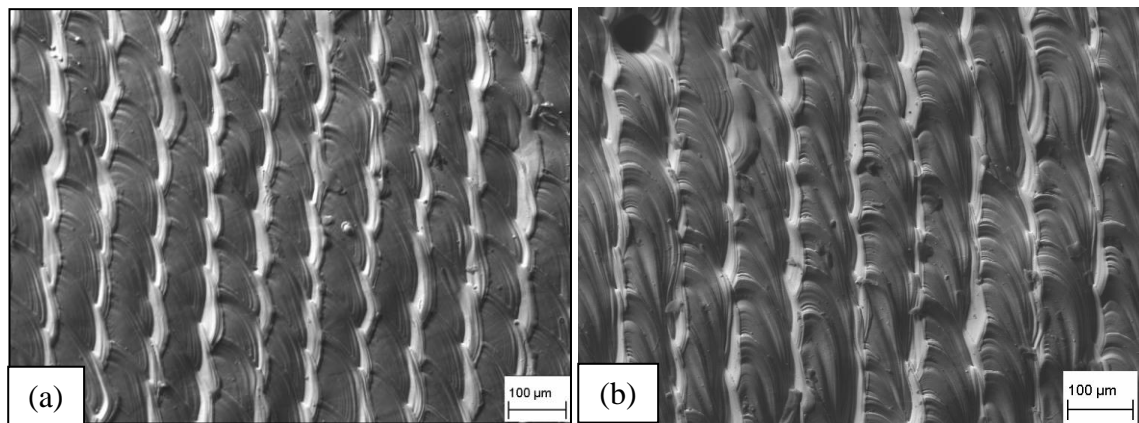


Figure 4-13: Effects of processing parameters at a fixed energy density (10.48 J/mm^2):
(a) high irradiance (157 kW/mm^2) and low residence time ($67 \text{ }\mu\text{s}$);
(b) low irradiance (62.9 kW/mm^2) and high residence time ($167 \text{ }\mu\text{s}$).

Figure 4-14 (a) and (b) shows the cross sectional views corresponding to Figure 4-13 (a) and (b). Lower exposure times produced less surface melting and hence a smoother surface morphology. The morphology exhibited in Figure 4-13 (a) and Figure 4-13 (b) show an enlarged melted phase due to higher exposure times resulting from the higher

pulse width durations. This is evident from the melt pool depth and roughness results shown in Table 4-1.

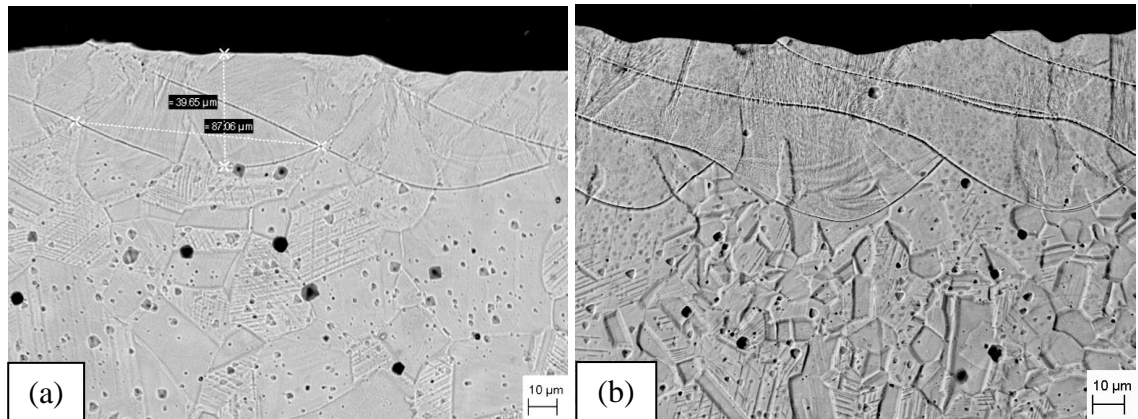


Figure 4-14: (a) and (b) BSE micrographs of transverse cross sectional microstructure corresponding to processed surface shown in Figure 4-13 (a) and (b) respectively.

Glyceresia etchant revealed carbide formation and inclusions within the stainless steel microstructure. The small dark spots visible within the microstructure in Figure 4-14 (a) and (b) resemble carbides and other inclusions in the steel. However these inclusions are nearly eliminated within the laser processed regions. Creation of a chemically uniform and defect free surface is useful as it can lead to increased wear resistant surfaces [45].

Table 4-1: Melt pool depth and roughness measurements from DOE 2 for 316L.

<i>Residence Time</i>	<i>Energy Density</i>	<i>Irradiance</i>	<i>As-received</i>		<i>Machined</i>		<i>Machined and Etched</i>	
			<i>Depth</i>	<i>Ra</i>	<i>Depth</i>	<i>Ra</i>	<i>Depth</i>	<i>Ra</i>
(μs)	(J/mm^2)	(kW/mm^2)	(μm)	(μm)	(μm)	(μm)	(μm)	(μm)
50	11.00	220	38	4.00	48	3.35	43	2.23
67	10.48	157	42	2.14	44	2.40	51	3.35
83	10.48	126	51	2.42	53	2.79	60	2.79
100	11.00	110	59	6.90	77	7.13	84	4.01
167	10.48	62.9	72	3.63	86	3.38	91	3.38

4.2.2 Effects of pre-treatments and residence time on meltpool depth

Figure 4-15 shows the effects of residence time, machining and etching on the modified layer depth. Meltpool depth increased with increased residence time for all sample conditions. A steeper increase was noted between 50 and 100 μs . The small increase in meltpool depth at 160 μs was due to the low irradiance of $62.9 \text{ kW}/\text{mm}^2$ used for the

sample processed at this point. Etched samples did not improve the meltpool depth thus indicating that it had the least impact on improving CO₂ laser absorption of 316L stainless steel. Machined and etched samples showed the highest meltpool depths. Machining of samples had a greater effect on meltpool depth compared to etching. There were no significant effects of pre-treatments on roughness, see *Appendix F*.

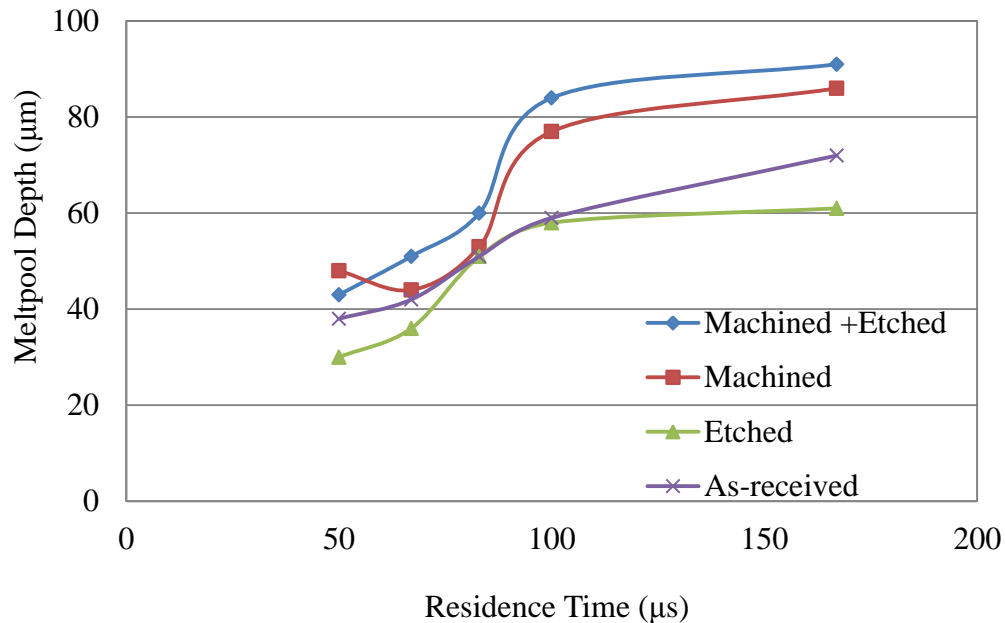


Figure 4-15: Effects of pre-treatments and residence time on meltpool depth.

4.2.3 Microhardness

The average hardness of untreated 316L stainless steel was measured from the sectioned samples to be 250 HV. Figure 4-16 shows the effects of laser surface melting on microhardness. The dotted line represents the hardness of untreated samples. Some samples showed slight increase in hardness. Although a significant increase in hardness was identifiable for specific laser processing conditions, the level of increase was small and for most samples no strong relationship was present from the effects of laser processing parameters on resultant microhardness. In order to have significant increase in hardness within the steel, time is needed for the carbon content to diffuse to allow the transformation from austenite to martensite to occur [97]. When insufficient time is provide due to rapid heating and cooling or when insufficient carbon content is present to aid the driving of the diffusion process, then little hardening effect would be expected to occur. Both of these situations were present in this case due to the rapid laser processing and the low carbon content in 316L material respectively.

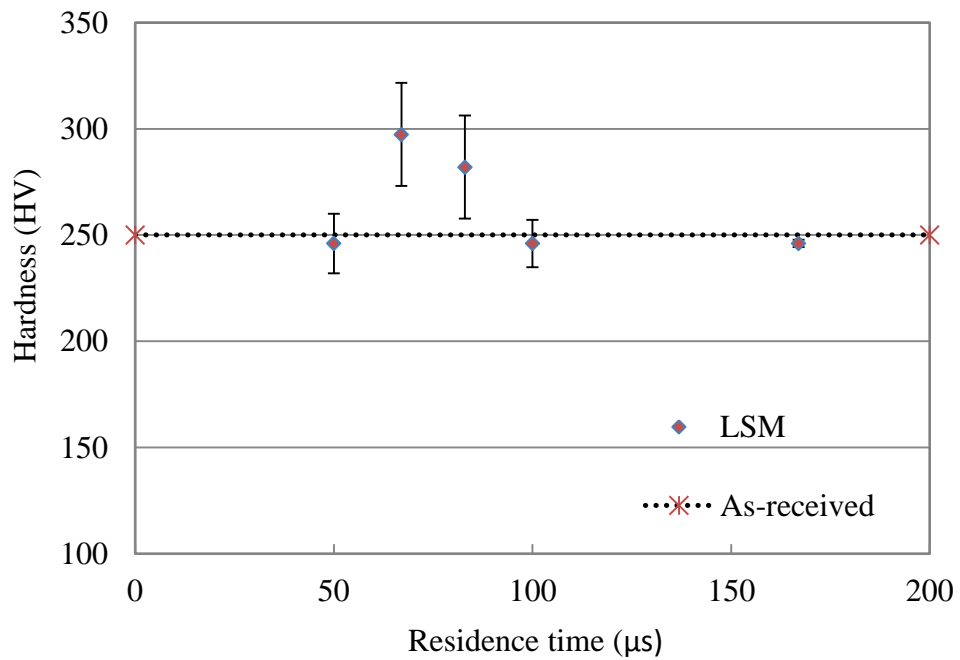


Figure 4-16: Effects of laser processing on 316L hardness compared to as received material hardness.

Due to the aforementioned phenomena, 316L stainless steel was not conducive to laser hardening. Laser surface hardening of 316L could be achieved via extreme quenching methods that induce formation of either a quasi-crystalline or an amorphous structure [232]. An amorphous structure can be achieved on the surface of the material by freezing the molten surface atoms in a random state through extremely rapid quenching techniques. A possible quenching technique that could be implemented to achieve this is by conducting cryogenic laser surface melting. The laser surface melting in this case would be conducted with a cryogenic coolant used to assist in quenching the surface.

4.2.4 EDS Analysis

The chemical composition of untreated and laser treated regions were analysed using energy dispersive x-ray spectroscopy (EDS). Figure 4-17 shows the cross-sectional microstructure highlighting the point of analysis and the corresponding EDS spectrum of the bulk material. Figure 4-18 shows the microstructure, point of analysis, and EDS spectrum of the laser treated region. Table 4-2 shows that there was no significant difference in chemical composition of the various elements constituting 316L stainless steel. Regardless of the high cooling rates implemented in this study the XRD analysis did not show any phase transformation.

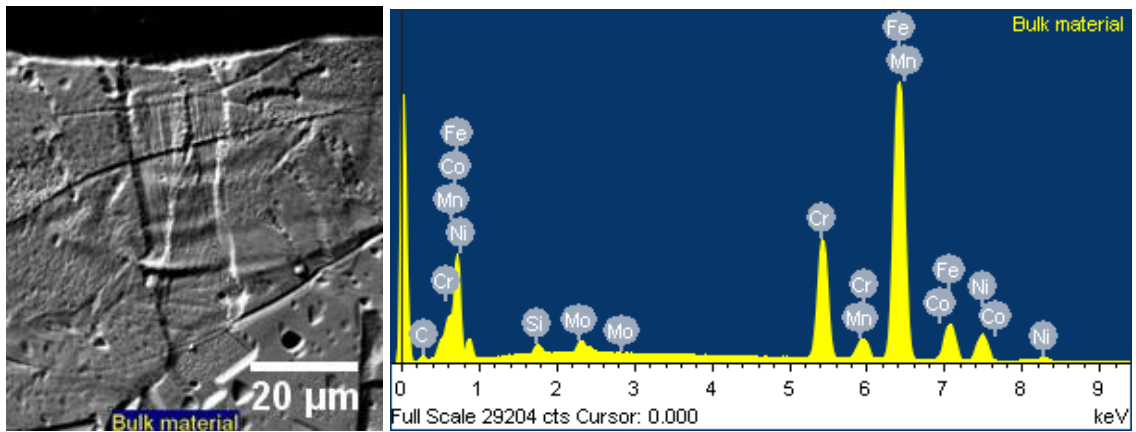


Figure 4-17: Micrograph and EDS spectrum of the bulk 316L material.

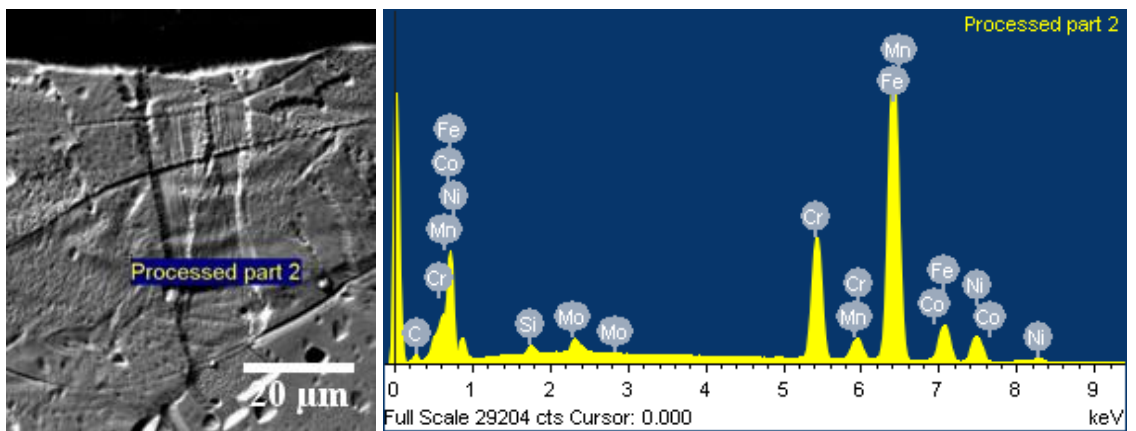


Figure 4-18: Micrograph and EDS spectrum of the laser melted 316L stainless steel.

Table 4-2: Chemical composition of elements in 316L stainless steel measured using the energy dispersive x-ray spectroscopy.

<i>Bulk Material</i>		<i>Laser modified region</i>	
<i>Element (K level)</i>	<i>Weight%</i>	<i>Element (K level)</i>	<i>Weight%</i>
C	3.06	C	4.16
Si	0.69	Si	0.68
Cr	17.10	Cr	16.89
Mn	1.51	Mn	1.58
Fe K	65.43	Fe K	64.47
Co K	0.23	Co K	0.28
Ni K	9.68	Ni K	9.43
Mo L	2.29	Mo L	2.51

4.3 Summary

This chapter presented results for the laser surface modification of 316L stainless steel. In particular, the effects of the laser surface modification processing conditions on melt pool profile, microstructure, roughness, hardness, and chemical composition were presented. It was found the surface could be melted and solidified in a controlled manner by control of the laser processing parameters. Novel microstructures have been obtained which were not previously reported in the literature. Laser surface modification also reduced asperities and eliminated cracks and inclusions within the treated region. An increase in hardness was achieved for some of the laser processing conditions relative to the untreated surface. However, the level of this increase was typically not high and no correlation was evident between the range of processing parameters investigated and the hardness results. Melt pool depths were found to increase for increased residence time and for machined as well as machined and etched surfaces.

Reduced irradiance and higher residence times resulted in lower surface roughness values. While reduced roughness and increased melt pool depths could be seen as beneficial for biomedical implants, other physical properties of the surface also need to be considered, in particular, the levels of hardness. The lack of significant phase transformation and chemical composition changes of the microstructure for the processing parameters investigated would indicate that the possibility of significant improvements of hardness and necessary tribological properties would not be great for this alloy. This indicates that an alternate process that alters the material structure in a different manner would be required if laser surface modification was to be successful for increasing the hardness and life span for 316L hip implants. One possible method of achieving this would be to create an amorphous structure on the surface of this implant material. Amorphous structures are known to have excellent hardness, wear and corrosion properties. Such a structure could potentially be achieved by cryogenic laser surface treatment.

Chapter 5

Results: Ti-6Al-4V

This chapter presents results for high speed laser melted Ti-6Al-4V. The results include microstructure analysis, meltpool profile, roughness, microhardness, phase and chemical composition, wear and corrosion resistance, wettability and biocompatibility properties. Compared to 316L stainless steel results presented in Chapter 4, much more detailed characterisations were carried out on Ti-6Al-4V samples.

5.1. Metallography

The results presented in this section are mainly microscopic analysis of the physical structure of the Ti-6Al-4V before and after laser melting. Surface topography results represent the plan view analysis while the cross-section views were obtain after a transverse sectioning and etching to highlight phase structure.

5.1.1 Surface Topography

Figure 5-1 presents the plan view of the (a) as-received and (b) grit blasted Ti-6Al-4V. There were no visible voids, inclusions, pits or cracks on the surface of as-received samples.

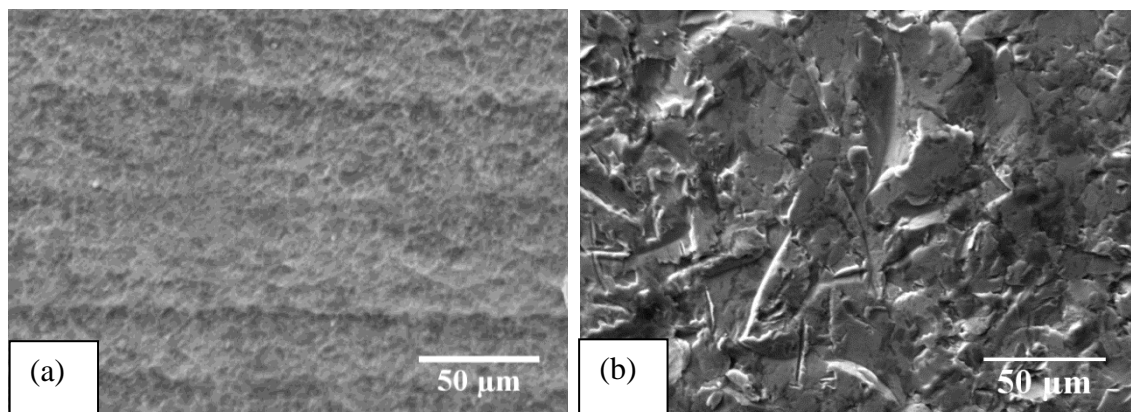


Figure 5-1: SEM micrographs showing the plane view of
(a) as-received and (b) grit blasted Ti-6Al-4V

Figure 5-2 to Figure 5-4 presents the topographical characteristics of the laser melted region, highlighting the repetitive processing tracks created due to rapid solidification.

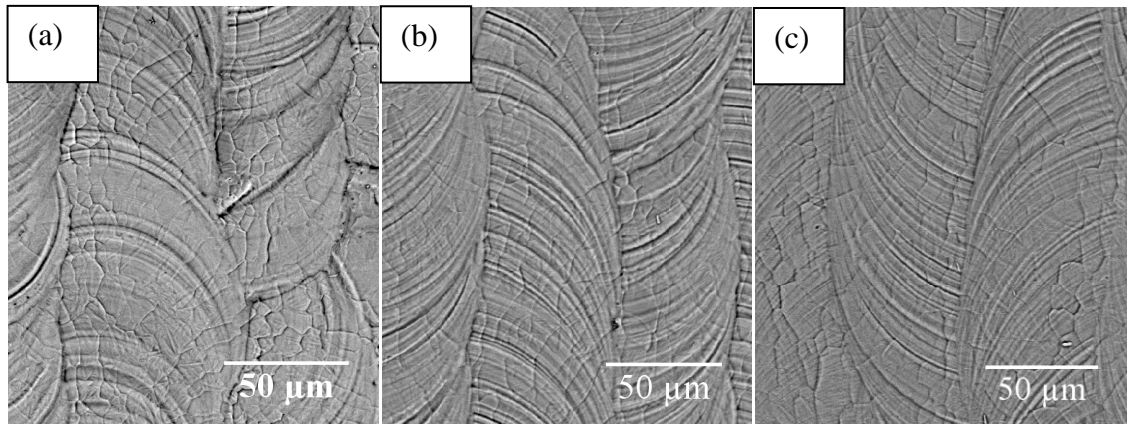


Figure 5-2: Back scatter detector (BSE) surface morphology images of laser surface modified Ti-6Al-4V at a constant residence time of 1.08 ms and three levels of irradiance (a) 15.72, (b) 20.4 and (c) 26.7 kW/mm².

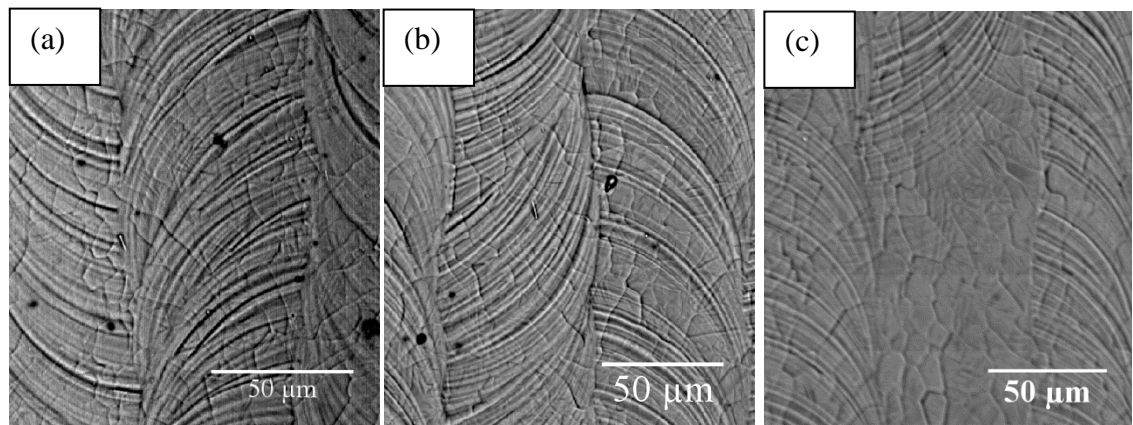


Figure 5-3: Back scatter detector (BSE) surface morphology images of laser surface modified Ti-6Al-4V at a constant residence time of 1.44 ms and three levels of irradiance (a) 15.72, (b) 20.4 and (c) 26.7 kW/mm².

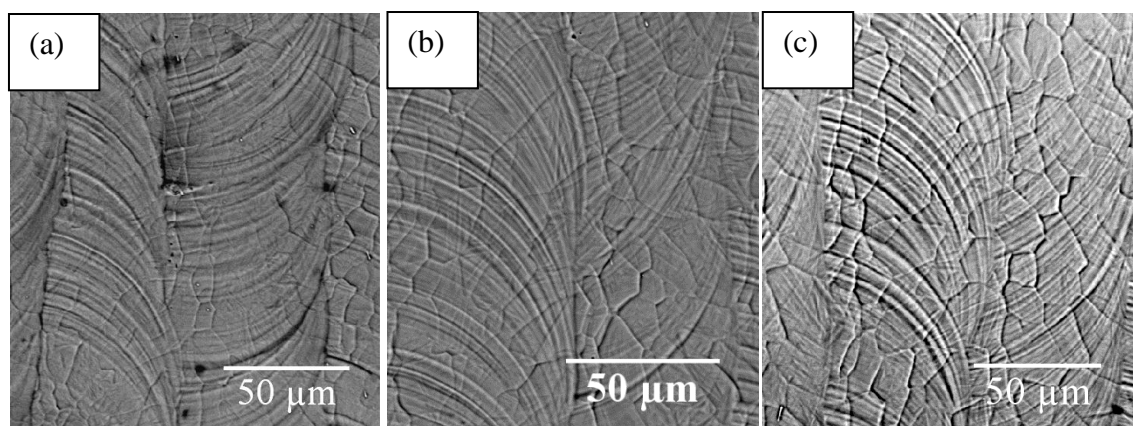


Figure 5-4: Back scatter detector (BSE) surface morphology images of laser surface modified Ti-6Al-4V at a constant residence time of 2.16 ms and three levels of irradiance (a) 15.72, (b) 20.4 and (c) 26.7 kW/mm².

Figure 5-2 shows the morphological structure at the lowest residence time of 1.08 ms and three levels of irradiance (15.72, 20.4 and 26.7 kW/mm²). Increase in irradiance produced a smoother treated region with a more homogeneous melting regime. A similar trend with increased irradiance was observed for samples processed at higher residence times of 1.44 ms (Figure 5-3) and 2.16 ms (Figure 5-4).

Evolution of roughness and rippling effect on the treated surface confirms that the surface was heated to a liquid phase as seen in Figure 5-5. No evidence of ablation is visible on all treated sample due to the careful selection of the laser processing parameters. Grain structure formation is also visible on all topographic micrographs. Figure 5-5 shows the typical grain distribution on laser melted topography. The grains are not homogeneous in size and vary within the treated zone. In Figure 5-5 the dimension of the grains varied from as low as 5 μm to 30 μm. It was not possible to quantitatively determine from these images an average the grain size within a particular treated sample. However, the grains generally increased in size and became more visible with increasing irradiance and residence time. The largest grains are visible in Figure 5-4 (c) where the highest irradiance of 26.7 kW/mm² and residence time of 2.16 ms was applied.

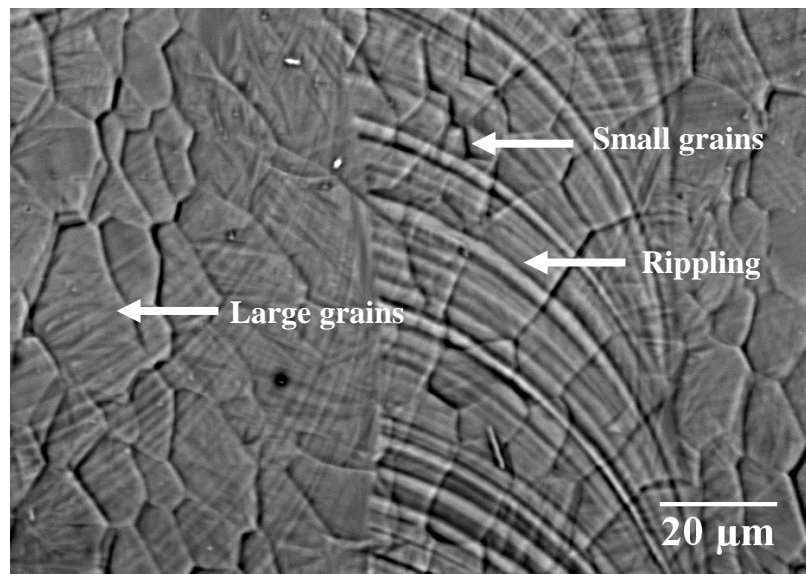


Figure 5-5: Grain distribution on the surface of a sample laser melted at an irradiance of 26 kW/mm² and a residence time of 2.16 ms, imaged in BSE mode.

5.1.2 Cross-sectional microstructure

Figure 5-6 shows the etched cross-sectional microstructure images of the as-received Ti-6Al-4V taken using an optical microscopes, see Figure 5-6 (a), and back scatter electron detector (BSE), see Figure 5-6 (b). The as-received microstructure consists of a fully lamellar microstructure consisting of colonies of alternating laths of α and β phase

as depicted by both the optical and electron microscope in Figure 5-6 (a) and (b) respectively. Optical microscopy shows the α phase as light regions on the micrograph while the β phase are darker regions. BSE micrographs on the other hand show the opposite, with the α phase as dark regions while the lighter regions depict the β phase. To enhance contrast and image clarity a yellow filter was used to take the pictures shown in Figure 5-6 (a) and Figure 5-7 (b).

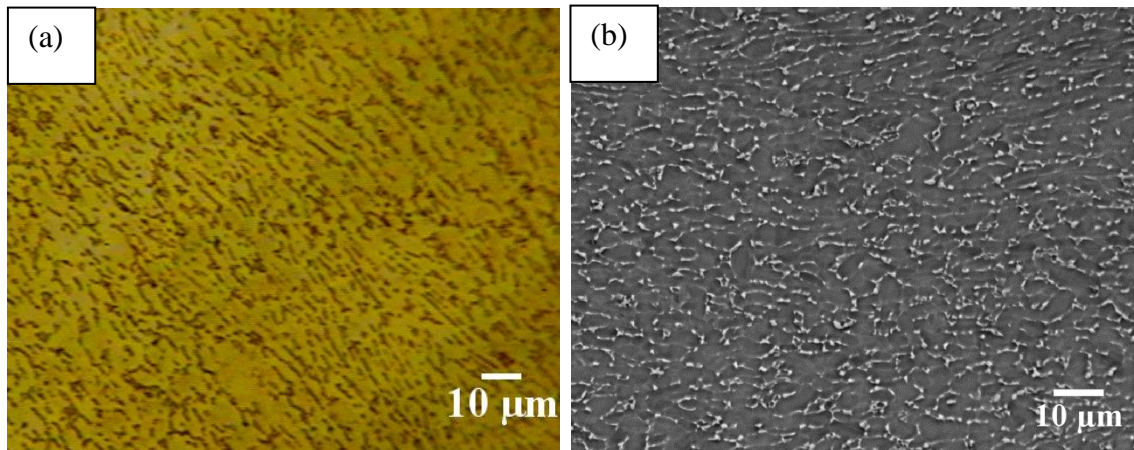


Figure 5-6: Cross-sectional micrographs of the as-received Ti-6Al-4V obtained via (a) optical microscopy and (b) BSE.

High speed laser treatment resulted in the creation of a crack-free modified layer ranging from 20 to 50 μm thick with very different microstructures compared to the bulk alloy. Figure 5-7 reveals a typical crack-free cross sectional microstructure of the laser melted Ti-6Al-4V highlighting also the phase transformation in the modified layer. Following high speed laser melting, the fully lamellar $\alpha+\beta$ microstructure re-crystallised to form a martensite structure with an acicular αTi phase. The extent of the phase transformation is detailed in later sections of the thesis.

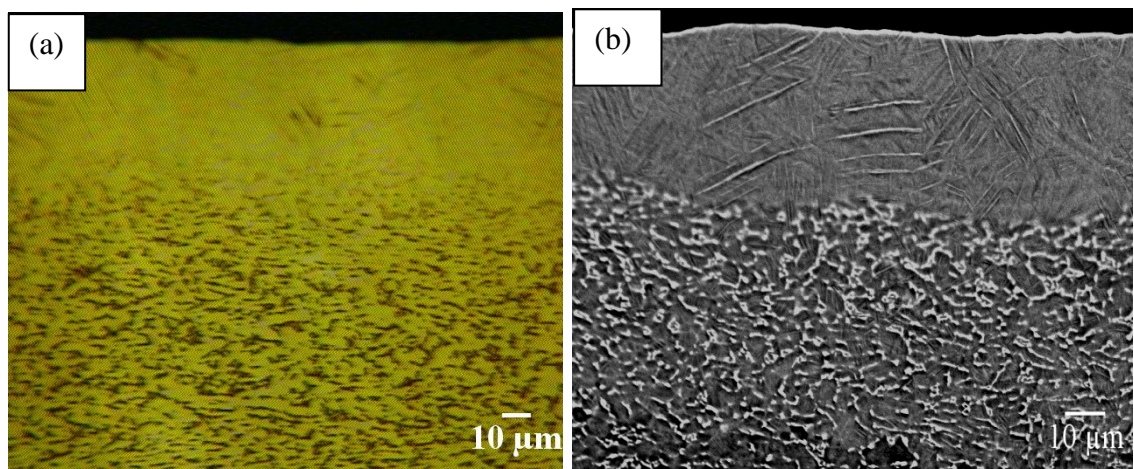


Figure 5-7: Cross sectional BSE micrograph of laser modified Ti-6Al-4V obtained via (a) optical microscopy and (b) BSE.

Figure 5-8 to Figure 5-10 highlight the effects of irradiance and residence time on the cross sectional microstructure of the laser surface modified Ti-6Al-4V. The samples treated at higher irradiances showed a smoother surface finish compared to the samples treated at lower irradiance which had a more wavy surface type. This is particularly noticeable in Figure 5-8 shows a clear increase in depth of processing as the residence time increased. This trend is generally the same at the higher irradiance values in Figure 5-9 and Figure 5-10. More uniform melt pool depths were also created at higher irradiance values and for higher residence times. A relatively homogeneous treated melt pool depth was found in the micrographs for the sample at the highest irradiance of 26.72 kW/mm^2 .

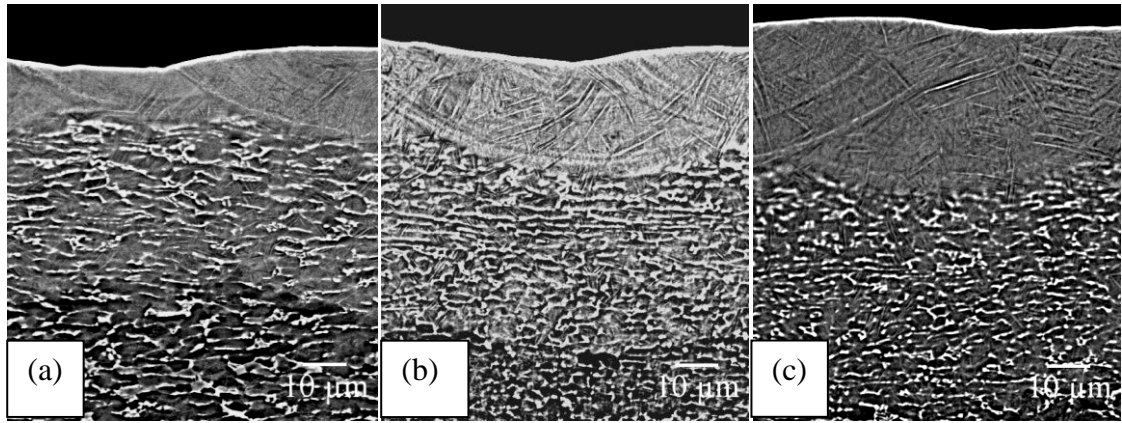


Figure 5-8: Back scatter detector (BSE) surface morphology images of laser surface modified Ti-6Al-4V at a constant level of irradiance 15.72 kW/mm^2 and three levels of irradiance of residence time of (a) 1.08 (b) 1.44 and (c) 2.16 ms.

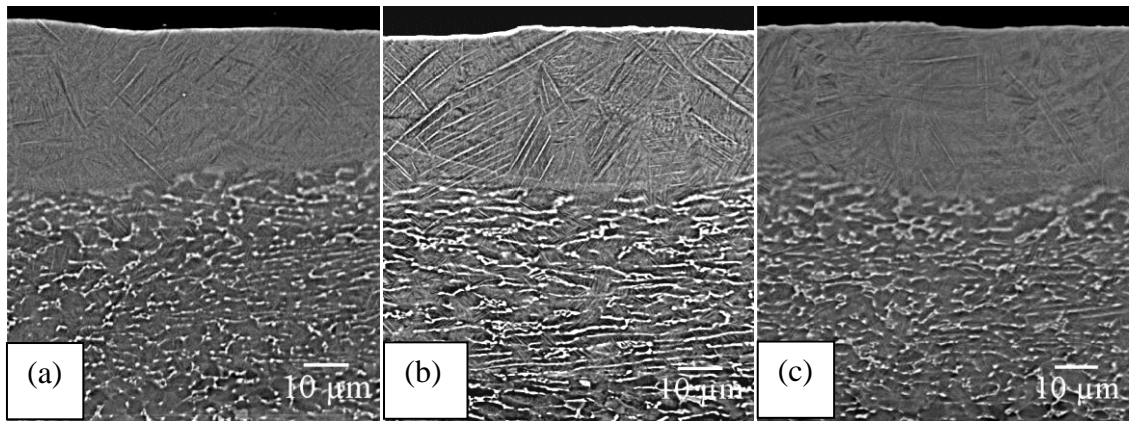


Figure 5-9: Back scatter detector (BSE) surface morphology images of laser surface modified Ti-6Al-4V at a constant level of irradiance 20.4 kW/mm^2 and three levels of irradiance of residence time of (a) 1.08 (b) 1.44 and (c) 2.16 ms.

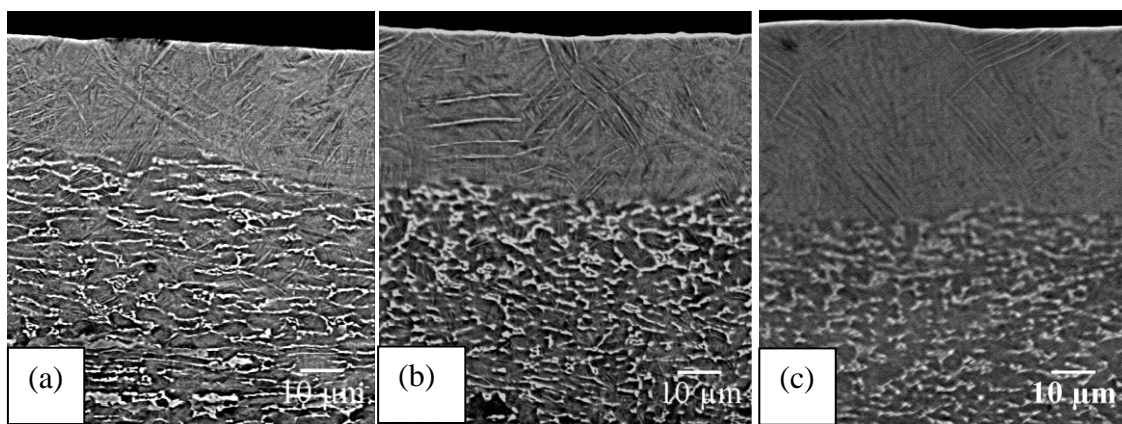


Figure 5-10: Back scatter detector (BSE) surface morphology images of laser surface modified Ti-6Al-4V at a constant level of irradiance 26.72 kW/mm^2 and three levels of irradiance of residence time of (a) 1.08 (b) 1.44 and (c) 2.16 ms.

5.2 Meltpool Profile

Figure 5-8 to Figure 5-10 qualitatively highlighted the changes in microstructure, roughness and meltpool depth of the laser modified regions. These micrographs show that irradiance has an effect on the thickness uniformity of the melted area. Figure 5-11 compares the effects of the lowest and highest irradiance, 15.72 and 26.72 kW/mm² respectively, on the meltpool depth. As the irradiance increased, a more homogeneous meltpool depth with fewer discontinuities was observed. Increase in both irradiance and residence times resulted in an increase in meltpool depth which is quantitatively presented in Figure 5-11.

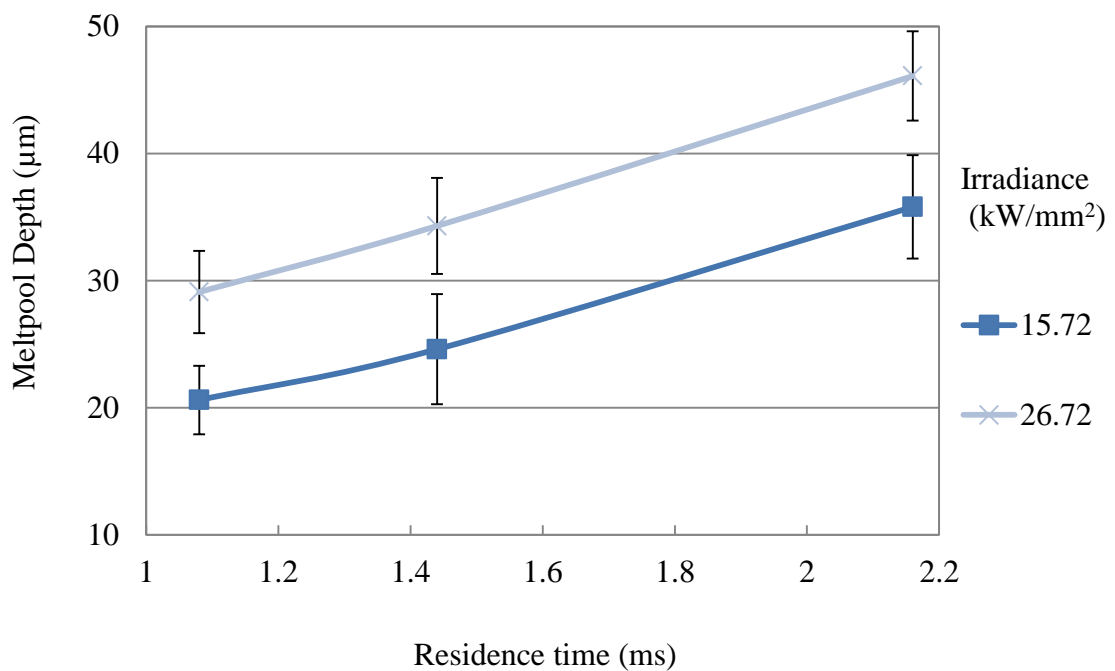


Figure 5-11: Effects of laser irradiance and residence time on meltpool depth for the Ti-6Al-4V samples.

The graph shows the error bars constructed using a 95% confidence t-test from a population of ten samples for each design point. The table in *Appendix G* presents the design points and results obtained from the tests. Figure 5-12 shows a 3D graph simultaneously displaying the effects of irradiance and residence on meltpool depth. The 3D graph was generated, in Design Expert®, using two factor interactions model (2FI). Table 5-1 shows the analysis of variance table generated by the model. The high model F-value of 23.23 implied the model was significant. A p-value of 0.002 suggested that there is a low chance the F-value could occur due to noise. The predicted R² of 0.879 is in reasonable agreement with the adjusted R² of 0.893. There is only 0.014 difference in the R² values, this is significantly smaller than the threshold of 0.2.

High R^2 values suggest there is a statistical significant interaction between the factors. The resulting melt-pool depth can be modelled by the final equation given in Table 5-1.

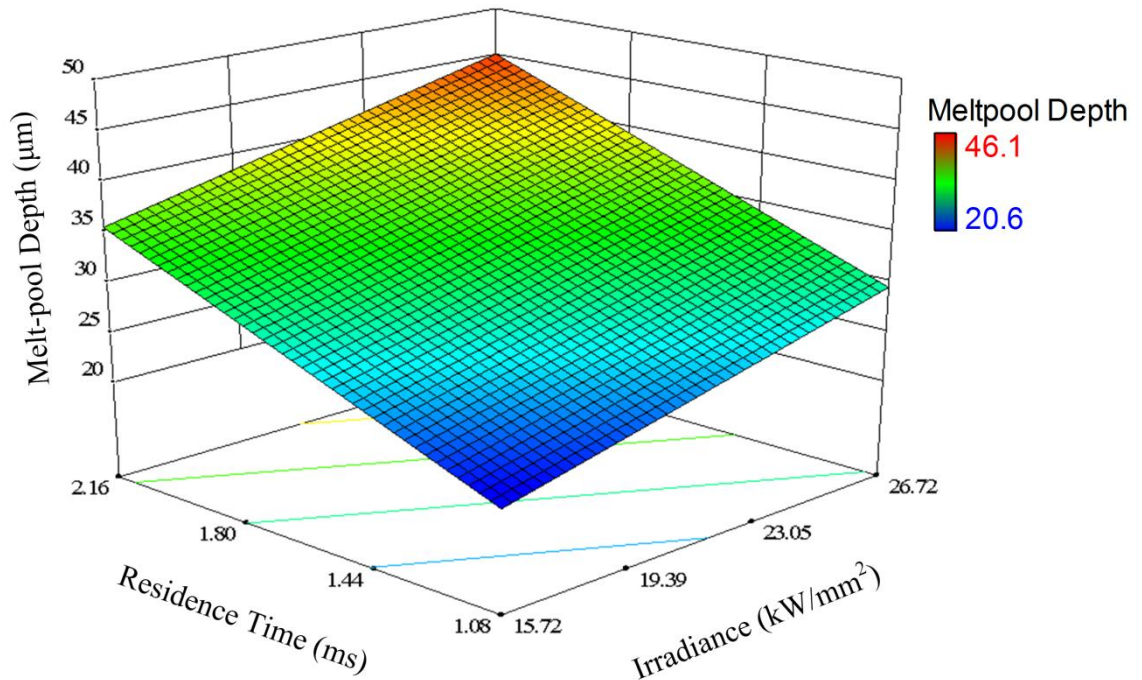


Figure 5-12: Effects of laser irradiance and residence time on melt-pool depth for the Ti-6Al-4V samples.

Table 5-1: Analysis for variance (ANOVA) table for melt-pool depth – 2FI model.

Source	Sum of Squares	Mean Square	F Value	p-value
Model	502.786	167.595	23.268	0.0023
A-Irradiance	135.375	135.375	18.795	0.0075
B-Residence Time	366.601	366.601	50.898	0.0008
AB	0.81	0.81	0.112	0.7510
Residual	36.013	7.202		
Cor Total	538.8			
		<i>Final equation obtained from the model:</i>		
R-Squared	0.933	Microhardness =		
Adj R-Squared	0.893	-3.93448		
Pred R-Squared	0.879	+0.61818 × Irradiance		
Adeq Precision	14.047	+11.26016 × Residence Time		
		+0.15152 × Irradiance × Residence Time		

The ANOVA results show that melt-pool depth was affected by both irradiance (A) and residence time (B). Residence time had the most significant effect on the melt-pool depth

followed by irradiance as highlighted by the F-values 50.898 and 18.795 respectively. The interaction of the factors irradiance and residence time (AB) showed the F-values values highlighting its low significance in resultant meltpool depths. The low effect of the interaction modelled by the 2FI model is further confirmed from the coded factors, Equation (17). The coded factors model equation was derived from the experimental design's low and high coded levels (-1 and 1).

$$\text{Meltpool Depth } (\mu\text{m}) = 32.63 + 4.75A + 7.82B + 0.45AB \quad (17)$$

The predicted meltpool depth values were plotted against the experimental values in Figure 5-13. Meltpool depth values after laser surface treatment were found to be highly predictable, as the values are closely positioned to the best-fit line. The adequate precision, which measures the signal to noise ratio, was found to be 14.047. As this ratio is greater than 4, this indicates an adequate signal, meaning that the model can be used to navigate the design space.

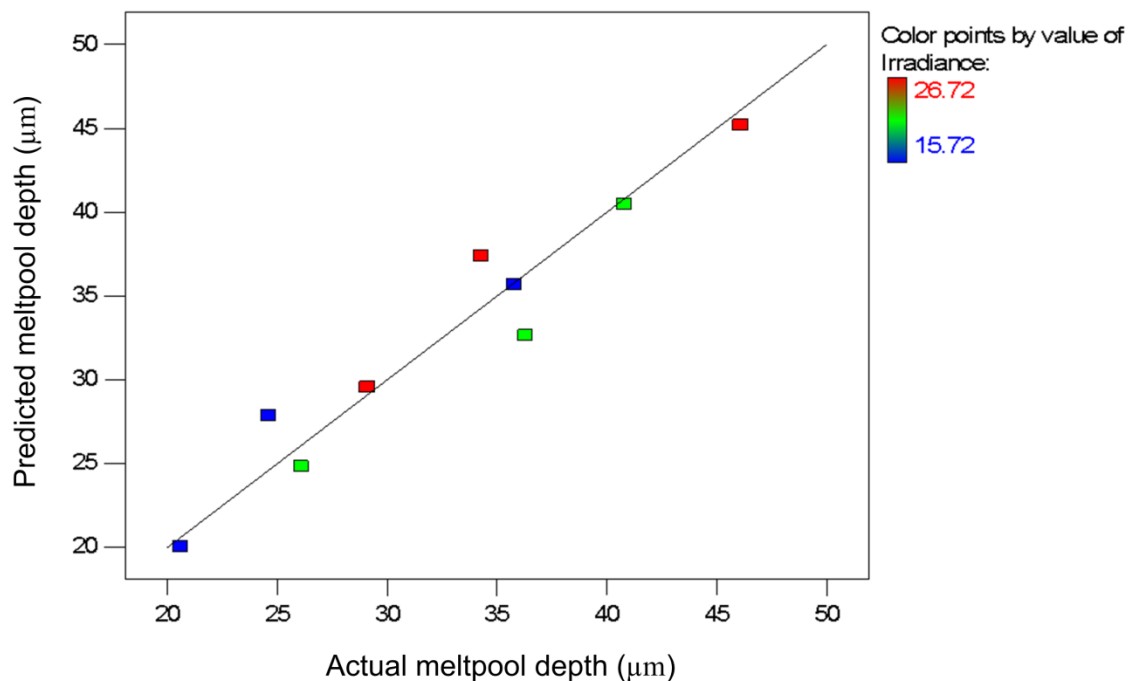


Figure 5-13: A graph of the actual meltpool depth versus the predicted values.

5.3 Roughness

Qualitative analyses of the micrographs in section 5.1 implicitly highlighted smoother surfaces with increased irradiance and residence time. Profilometry measurements showed average roughness of the grit blasted alloy was $0.56 \pm 0.1 \mu\text{m}$. Laser surface melting subsequently produced average roughness values between $1.39 \mu\text{m}$ and $2.73 \mu\text{m}$. Figure 5-14 highlights the effects of irradiance and residence time on roughness. Roughness was found to decrease with increase of irradiance and residence time. The graph shows the error bars constructed using a 95% confidence t-test from a population of five samples for each design point. The table in *Appendix H* lists the design points and results obtained from the tests.

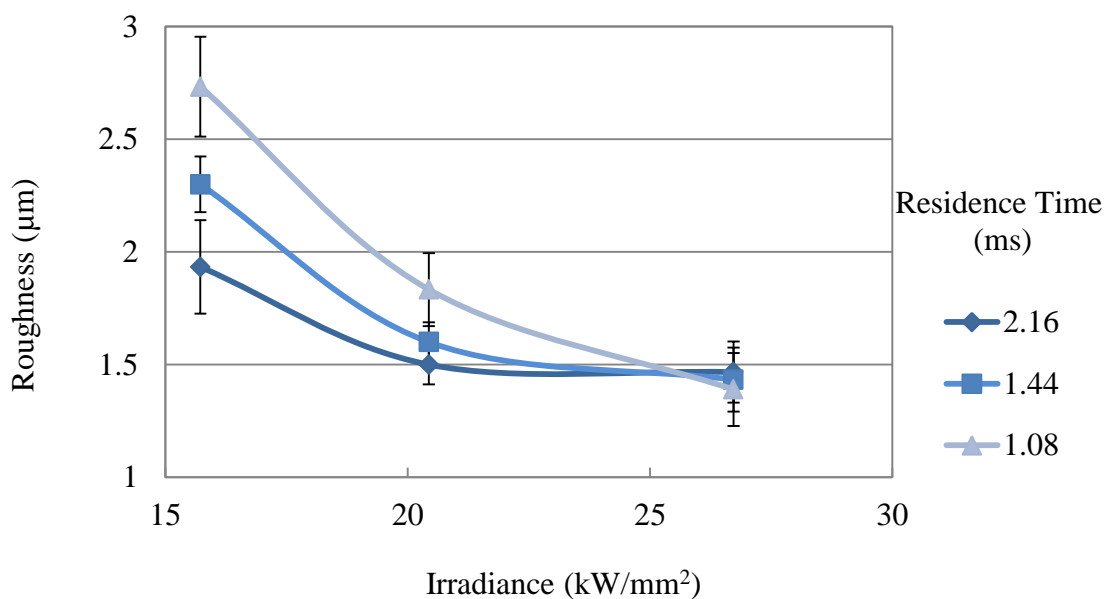


Figure 5-14: Effects of irradiance and residence time on average roughness of the Ti-6Al-4V samples.

Figure 5-15 presents the effects of irradiance and residence time in a response surface plot. Increase in both irradiance and residence time resulted in low average roughness values. The 3D graph was generated using a quadratic model. Table 5-2 shows the analysis of variance (ANOVA) results generated by the model. The Model F-value of 544.86 implied the model was significant. A p-value of 0.0001 suggested that there is a low chance the F-value could occur due to noise in this model. The predicted R^2 of 0.989 is in reasonable agreement with the adjusted R^2 of 0.997. High R^2 values suggest there is a statistical significance between the factors and average roughness subsequent to laser surface melting.

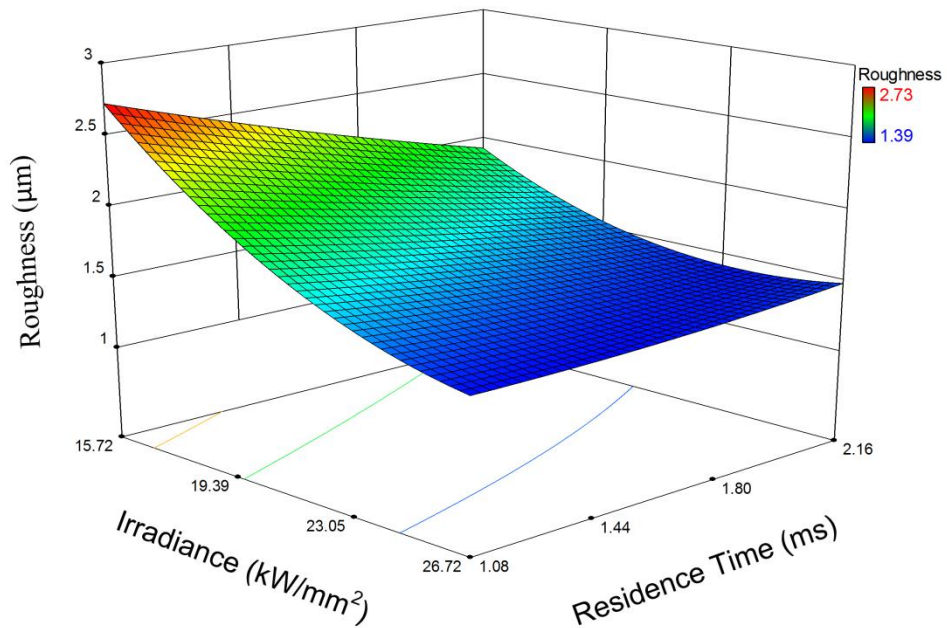


Figure 5-15: Effects of irradiance and residence time on average roughness of the Ti-6Al-4V samples.

Table 5-2: Analysis for variance (ANOVA) table for roughness – quadratic model.

Source	Sum of Squares	Mean Square	F Value	p-value
Model	1.672515	0.334503	544.8589	0.0001
A-Irradiance	1.185482	1.185482	1930.985	< 0.0001
B-Residence Time	0.18375	0.18375	299.3032	0.0004
AB	0.1936	0.1936	315.3475	0.0004
A ²	0.107803	0.107803	175.5957	0.0009
B ²	0.001881	0.001881	3.063707	0.1784
Residual	0.001842	0.000614		
Cor Total	1.674357			
<i>Final equation obtained from the model:</i>				
R-Squared	0.998	$\begin{aligned} \text{Roughness} = & + 10.14118 \\ & - 0.52654 \times \text{Irradiance} \\ & - 2.23667 \times \text{Residence time} \\ & + 0.074074 \times \text{Irradiance} \times \text{Residence time} \\ & + 7.67493 \times 10^{-3} \times \text{Irradiance}^2 \\ & + 0.10517 \times \text{Residence time}^2 \end{aligned}$		
Adj R-Squared	0.997			
Pred R-Squared	0.989			
Adeq Precision	65.692			

The ANOVA table showed p-values less than 0.05 for all model terms except high order residence time (B²). Such low p-values highlight the significance of such these factors and their interactions. The F values from the ANOVA table can be used to rank the influence of factors/interactions on the resultant average roughness. In this case,

irradiance (A) was found to be the most influential with the highest F value of (1930.985). Interaction AB had the second influence followed by residence time (B) and A^2 respectively. B^2 had the least influence as expected with the lowest F-value of just 3.063 – $A \gg AB \gg B \gg A^2 \gg B^2$. The average roughness can therefore be modelled by the final equation produced by the model given in Table 5-2. The coded factors model is presented by Equation (18) again highlighting the influence of each term on the model.

$$Roughness (\mu m) = 1.62 - 0.44A - 0.17B + 0.22AB + 0.23A^2 + 0.031B^2 \quad (18)$$

Average roughness values after laser surface treatment was found to be highly predictable according to the model as seen in Figure 5-16. All roughness values lie on the best-fit line of the predicted results. The adequate precision ratio was found to be 65.692 which is significantly higher than the threshold of 4. This means that the model had very little noise, therefore it can be used to navigate the design space.

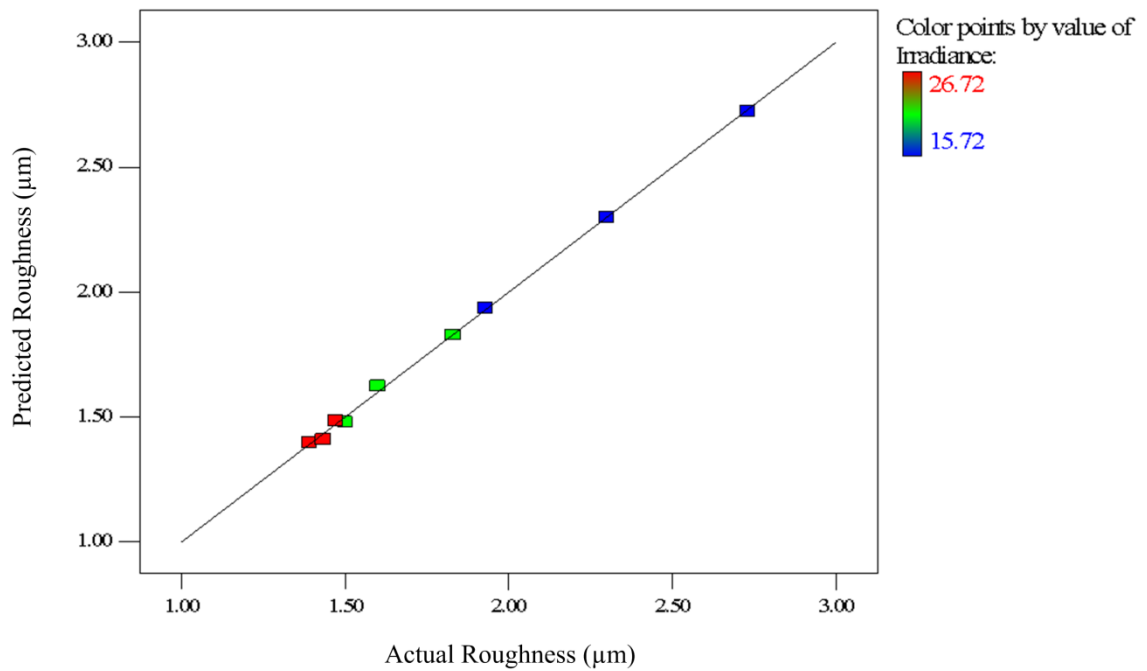


Figure 5-16: A graph of the actual roughness versus the predicted values.

5.4 Microhardness

The average cross-sectional microhardness of untreated as-received Ti-6Al-4V was measured to be 459 HV. Figure 5-17 highlights the effect of laser processing parameters on the resulting microhardness. The 3D surface response plot illustrates microhardness distribution with respect to irradiance and residence time. Laser surface modified samples showed a hardness increase up to 767 HV. This hardness increase was 67% higher than as-received Ti-6Al-4V. The highest microhardness of 767 HV was achieved at the highest level of irradiance (26.72 kW/mm^2) and lowest residence time (1.08 ms).

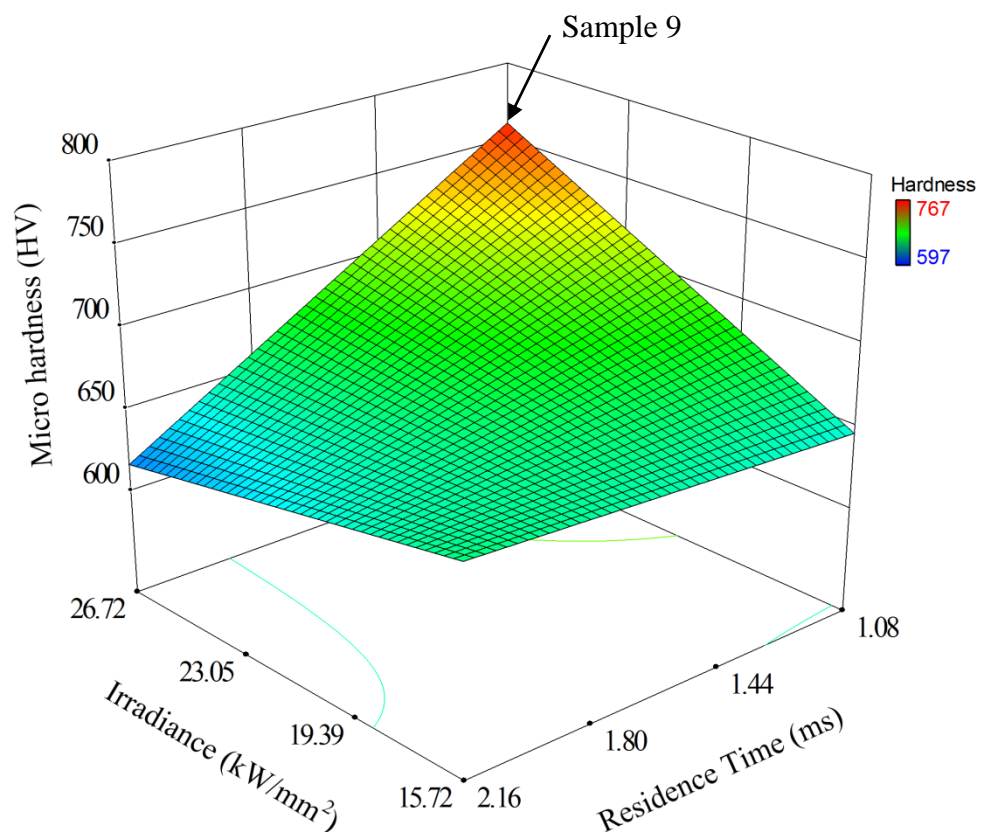


Figure 5-17: Effects of irradiance and residence time on microhardness.

The 3D graph was generated using a two factor interaction model. Table 5-3 shows the analyses of variance generated by the model. The p-value of 0.0198 indicates that the model is significant with a 98% confidence that a high model F-value of 8.719 could be due to noise. The adequate precision was found to be 9.21 indicating an adequate signal. This means that the model can be used to navigate the design space. Resulting microhardness can be modelled by the final equation produced by the model given in Table 5-3. Order of factor influence on microhardness can be established through

analysis of the F-values magnitude as follows: $AB > B > A$. The final equation in terms of the coded factor further confirms the influence of the factors, see Equation (19).

Table 5-3: Analysis for variance (ANOVA) table for microhardness – 2FI model

Source	Sum of Squares	Mean Square	F Value	p-value
Model	14700.39	4900.13	8.719	0.0198
A-Irradiance	1849.06	1849.06	3.290	0.1294
B-Residence Time	6424.89	6424.89	11.432	0.0196
AB	6426.42	6426.42	11.435	0.0196
Residual	2809.93	561.98		
Cor Total	17510.32			
<i>Final equation obtained from the model:</i>				
R-Squared	0.84	$Microhardness =$ $+238.0962$ $+25.055 \times Irradiance$ $+225.7819 \times Residence Time$ $-13.4958 \times Irradiance \times Residence Time$		
Adj R-Squared	0.74			
Pred R-Squared	0.46			
Adeq Precision	9.21			

$$Microhardness (HV) = 671.59 - 17.56A - 32.72B - 40.08AB \quad (19)$$

Figure 5-18 shows a graph of the actual microhardness versus the predicted values.

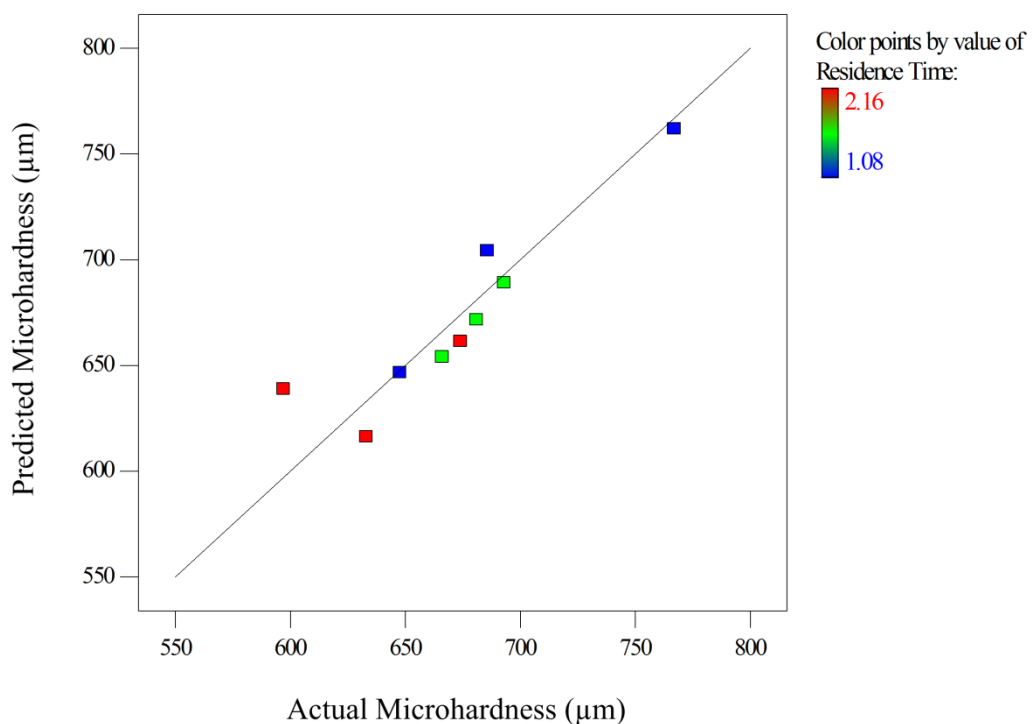


Figure 5-18: A graph of the actual microhardness versus the predicted values.

Microhardness values obtained experimentally lie relatively close to the best-fit line highlighting the adequacy of the model. The slight scatter visible for all design points can be due to the measurement errors due to due to micro-indent placement. Using improved microhardness measurement tools, i.e. nano-indentation, can aid in improving the prediction of the processing parameter effects. The graph also assisted in detecting values that are not easily predicted by the model. There is some moderate scatter for samples treated at high residence times as shown by the graph. Samples treated at high residence times value should therefore be approached cautiously if the model is used for microhardness predictions.

Processing parameters producing the most improved hardness (sample 9; 26.72 kW/mm² and 1.08 ms) were used to illustrate the change in hardness with respect to distance from the surface, see Figure 5-19. Figure 5-19 simultaneously illustrates the microstructure variation as the distance from the surface increases. Within the laser modified region the microhardness was consistently high and dropped at the substrate-laser treated interface. Microhardness values decreased as the distance from the surfaces increased.

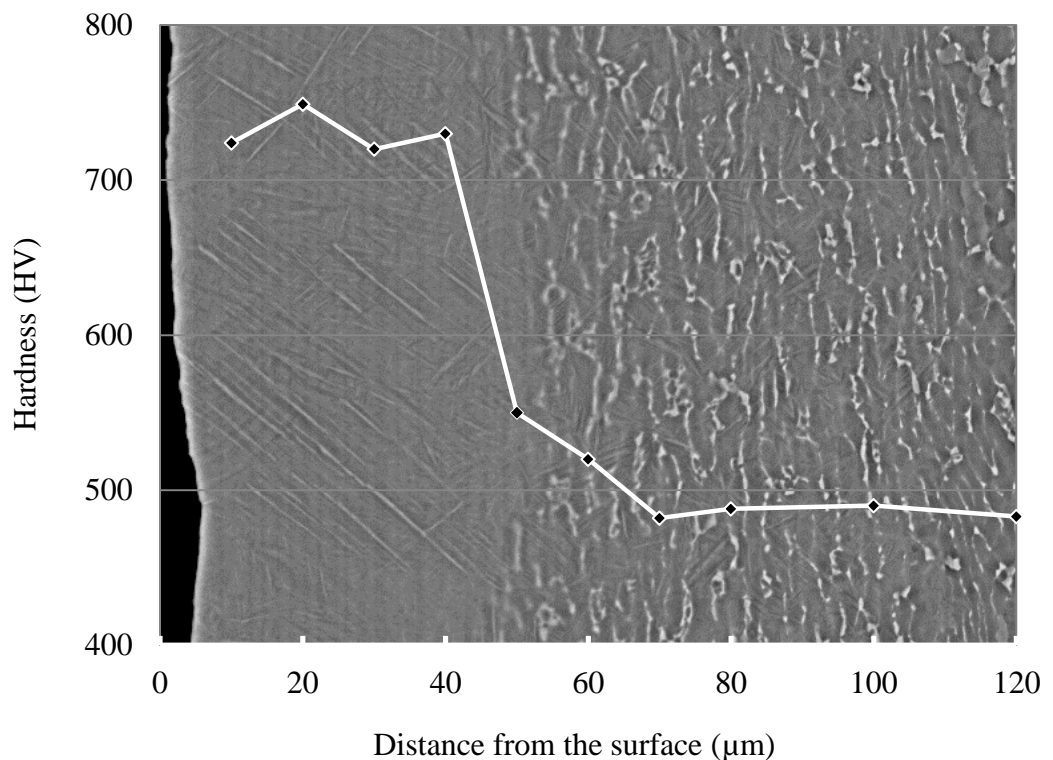


Figure 5-19: Microhardness of laser surface modified Ti-6Al-4V with respect to depth from the surface for sample 9.

5.5 Phase and Chemical Composition Characterisation

5.5.1 X-ray diffraction

X-ray diffraction analysis was used to evaluate the phase transformation and crystallinity changes of Ti-6Al-4V subsequent to laser surface melting. Figure 5-20 demonstrates the x-ray diffraction pattern of untreated Ti-6Al-4V. Figure 5-20 confirms the presents of the $\alpha+\beta$ phase observed by the cross-sectional micrographs in section 5.1.2. Table 5-4 lists the major peaks that were indexed between braggs angle (2-theta) of 20 and 100 degrees. Untreated Ti-6Al-4V is comprised of; the majority α -Ti (100), (101), (102), (110), (112), (201) and (104) at 35.4°, 40.2°, 53.1°, 63.2° and 70.8° respectively; and the minority β -Ti (110) and (211) at 38.4° and 76.5° respectively. The results were found to be in good agreement with reported XRD scans in literature [233].

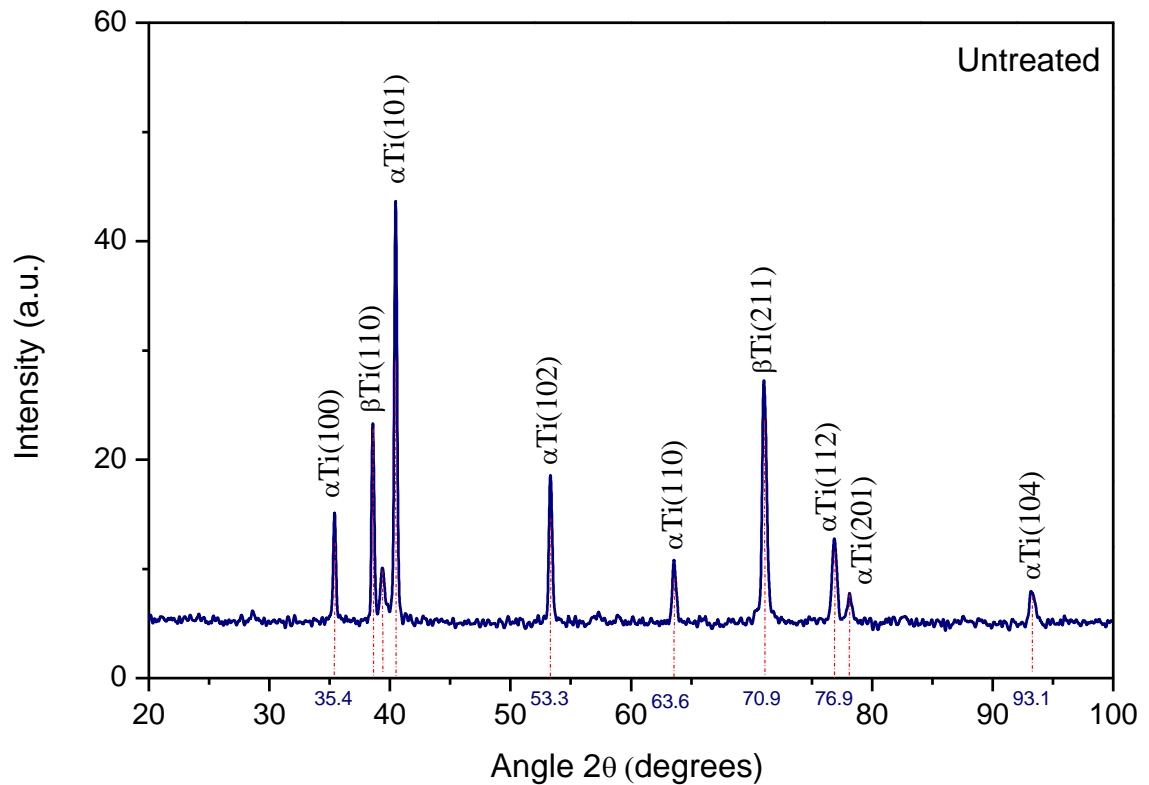


Figure 5-20: X-ray diffraction pattern of untreated Ti-6Al-4V.

Table 5-4: X-ray diffraction data for untreated Ti-6Al-4V.

2θ ($^{\circ}$)	d \AA	<i>Intensity</i>		$hkl-\alpha$	$hkl-\beta$
		<i>Max</i>	$I/I_1(\%)$		
35.407	2.53314	79.8	34.6	100	
38.576	2.33198	124	53.9		110
39.375	2.28652	51.1	22.2	-	-
40.471	2.22705	230	100	101	
53.309	1.71709	96.8	42	102	
63.577	1.46226	56.1	24.4	110	
71.02	1.32617	140	60.7		211
76.86	1.23931	64.6	28.1	112	
78.11	1.22257	40.5	17.6	201	
93.146	1.06065	40.7	17.6	10	

Figure 5-21 show the x-ray diffraction scans of untreated and laser surface modified samples. A reduction in the β -Ti phase is evident in all treated samples. The α -Ti at the 2θ value of 39.375° visible in untreated samples is not visible in any LSM XRD scans.

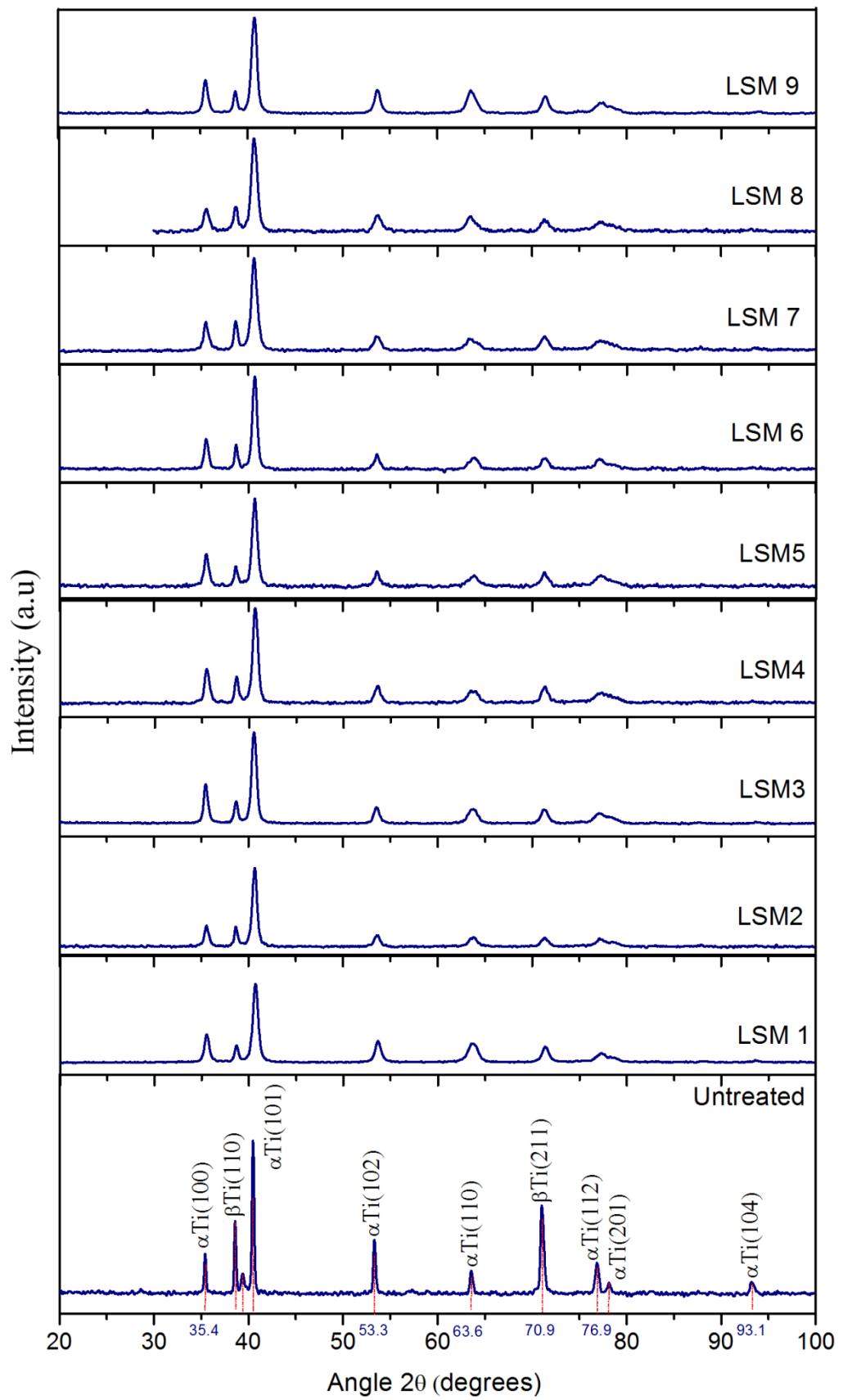


Figure 5-21: XRD pattern of untreated and LSM samples.

Untreated Ti-6Al-4V was calculated to contain 28.6% β -Ti, assuming that the remaining composition is the α phase that means 71.4 % of the material is made up of α -Ti. Figure 5-22 highlights the change in β -Ti phase composition at various levels of irradiance and residence time. Within the treated samples, β -Ti phase was highest at the lowest irradiance and residence time, 15.72 kW/mm² and 1.08 ms respectively. At the lowest residence time (1.08 ms) β -Ti volume fraction decreased with increase in irradiance. At the highest residence time (2.16 ms), β -Ti volume fraction slightly increased with increase in irradiance.

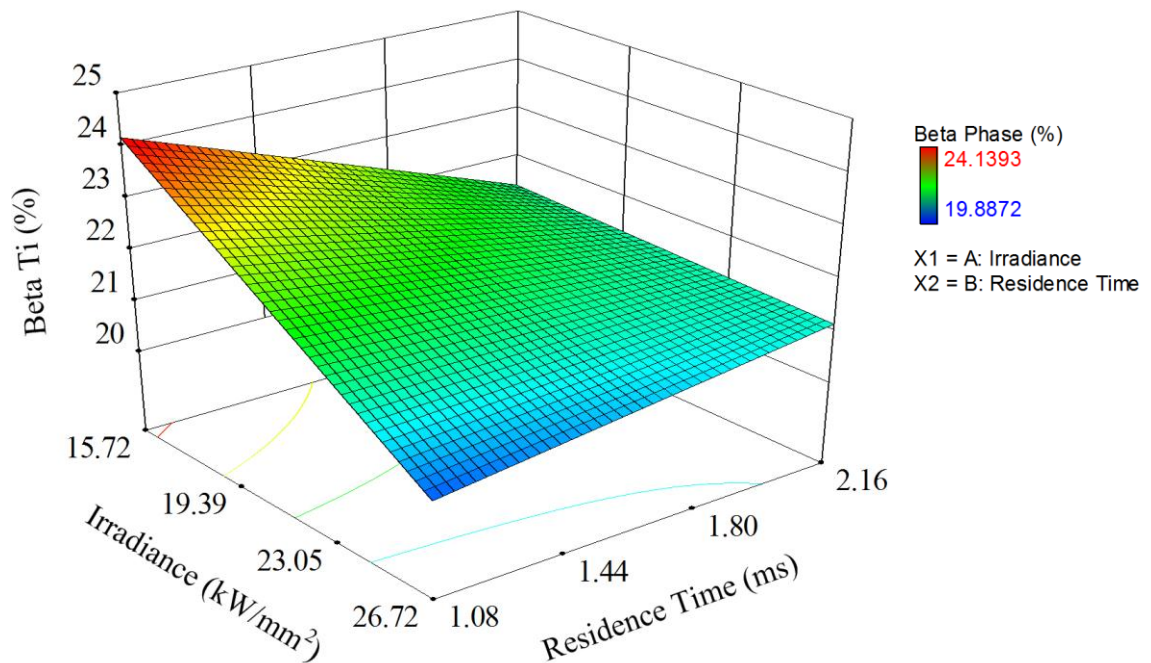


Figure 5-22: Effects of irradiance and residence time on the β -Ti phase.

The 3D graph was generated, in Design Expert®, using two factor interactions model (2FI). Table 5-5 shows the analyses of variance generated by the model. The Model F-value of 17.5 implied the model was significant. A p-value of 0.0044 suggested that there is a low chance the F-value could occur due to noise. High R^2 values suggest there is a statistical significant interaction between the factors. The adequate precision was found to be 12.73 indicating an adequate signal. This means that the model can be used to navigate the design space. Resulting beta Ti phase volume fraction can be modelled by the final equation produced by the model given in Table 5-5. Order of factor influence on microhardness can be established through analysis of the F-values magnitude as follows: A>AB>B. The final equation in terms of the coded factor further confirms the influence of the factors, see Equation (20).

Table 5-5: Analysis for variance (ANOVA) table for β Ti volume fraction– 2FI model

Source	Sum of Squares	Mean Square	F Value	p-value
Model	11.342	3.781	17.500	0.0044
A-Irradiance	6.689	6.689	30.964	0.0026
B-Residence Time	1.244	1.244	5.761	0.0616
AB	3.408	3.408	15.776	0.0106
Residual	1.080	0.216		
Cor Total	12.423			
<i>Final equation obtained from the model:</i>				
R-Squared	0.913	<i>Ti beta phase volume fraction (%) =</i> + 37.870 - 0.695 × Irradiance - 7.438 × Residence Time + 0.310 × Irradiance × Residence Time		
Adj R-Squared	0.860			
Pred R-Squared	0.584			
Adeq Precision	12.773			

$$\beta\text{Ti Volume fraction (\%)} = 21.75 - 1.06A - 0.46B + 0.92AB \quad (20)$$

β -Ti phase volume fraction values after laser surface treatment was found to be highly predictable according to the model as seen in Figure 5-23. All design points are positioned close to the best-fit line of the predicted results.

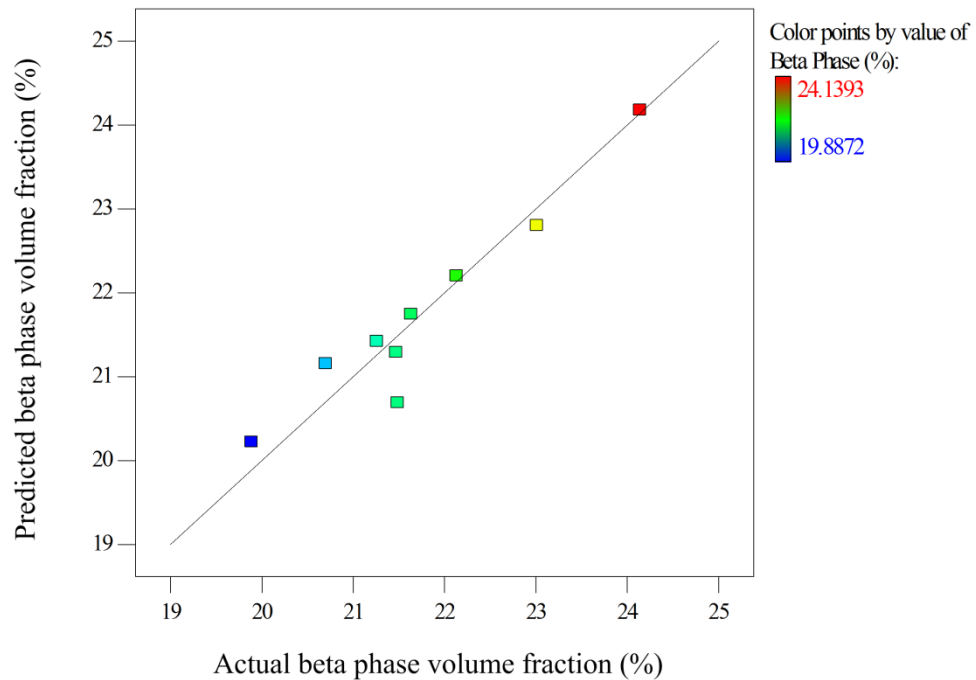


Figure 5-23: A graph of the actual β Ti volume fraction versus the predicted values.

5.5.2 Topographic chemical composition analysis

A comparison of energy dispersive x-ray spectroscopy (EDS) quantitative results was initially carried out to find the most accurate method of analysing the chemical composition of the surface. Figure 5-24 shows the two types of scans used (a) area scan and (b) grid scan.

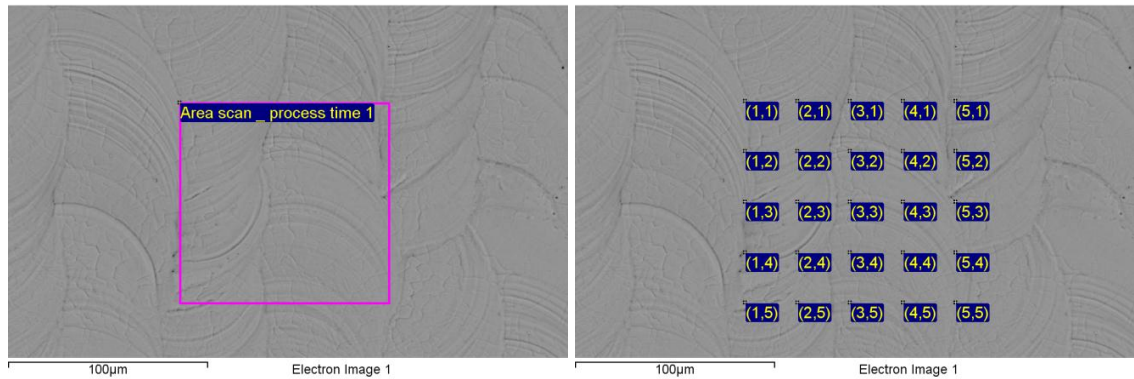


Figure 5-24: EDS analysis of the Ti-6Al-4V topographic surface
(a) area scan and (b) point analysis.

Both methods resulted in relatively similar chemical compositions as illustrated by the weight percentage of the composition in Figure 5-25. The results also suggest a homogeneous chemical composition throughout the surface of the material.

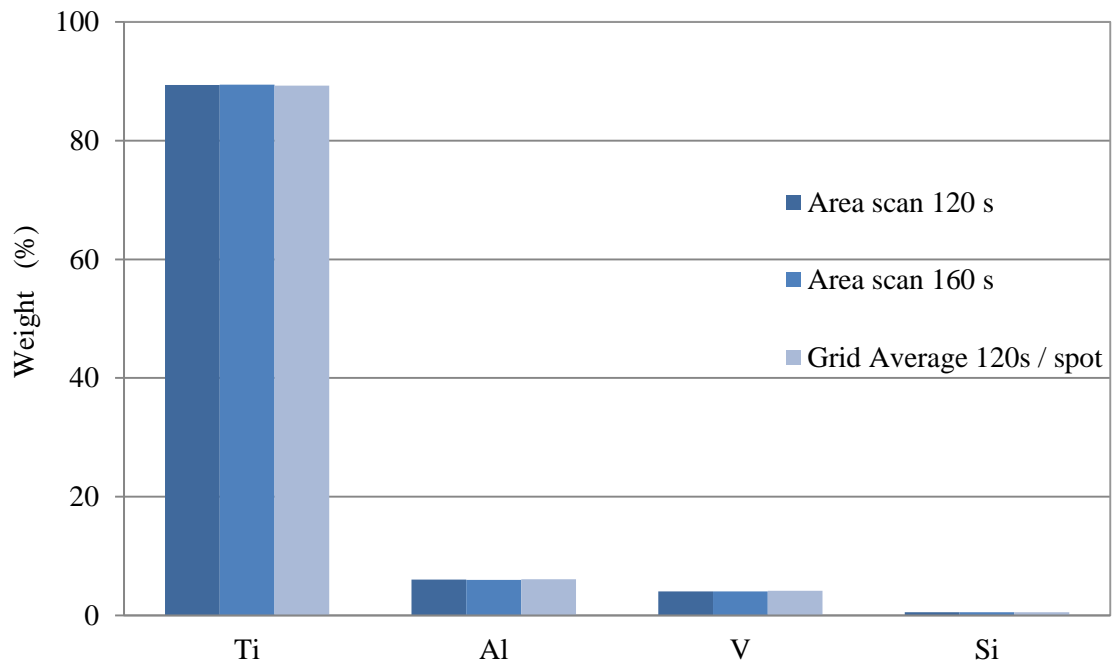


Figure 5-25: Elemental composition using different scan methods and processing times.

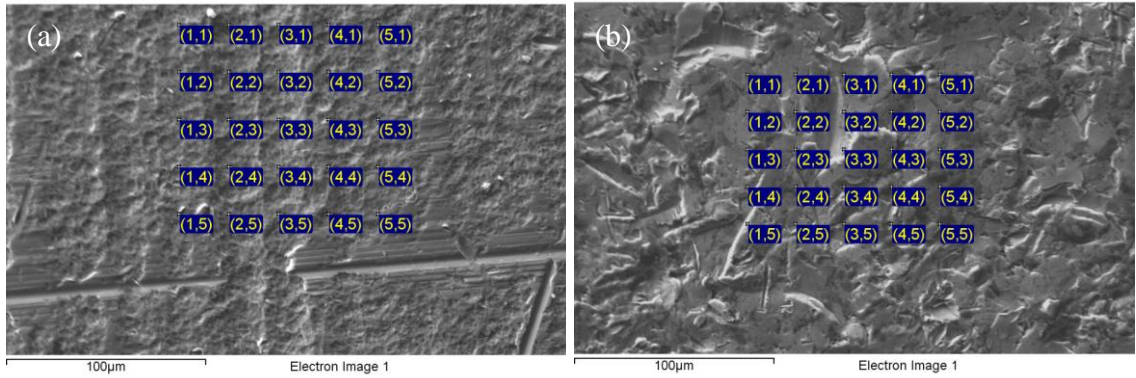


Figure 5-26: Grid scan micrographs of (a) untreated and (b) grit blasted Ti-6Al-4V.

Figure 5-26 shows the micrographs highlighting the scan area for untreated and grit blasted samples. Figure 5-27 to Figure 5-29 shows the EDS spectrum obtained from the untreated, grit blasted and LSM samples. The untreated sample spectrum in Figure 5-27 shows the typical Ti, Al and V elements at the expected electron voltages. However, unexpected minute traces of silicon were observed in grit blasted and some laser treated spectrums, Figure 5-28 and Figure 5-29 respectively. These traces are attributed to the grit blasting process undertaken prior to laser treatment. The chemical composition analysis shows that laser treatment does not result in significant changes in elemental chemical composition of the topography. No evidence of other foreign element contamination was found in the treated zones.

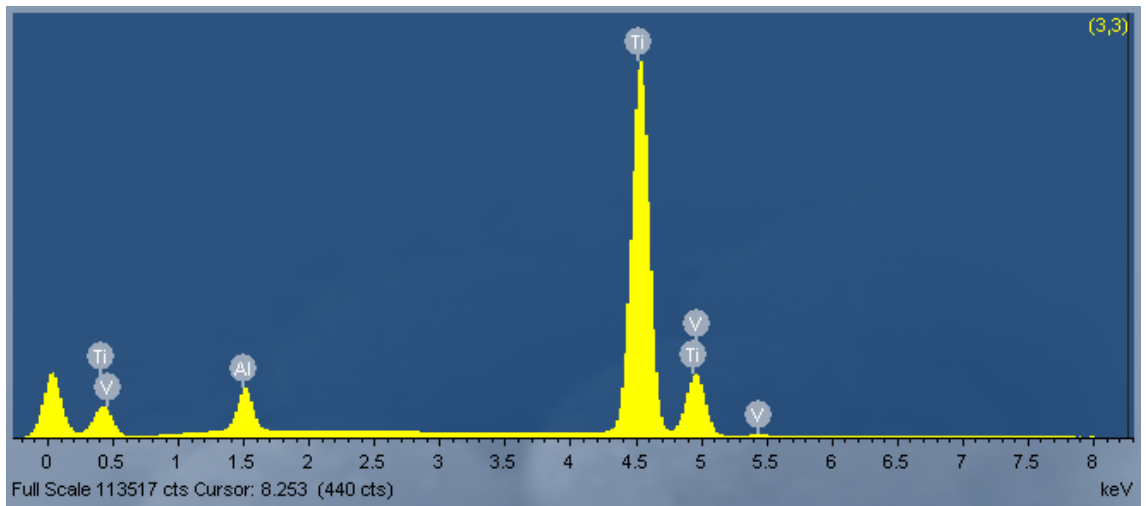


Figure 5-27: EDS spectrum of untreated Ti-6Al-4V.

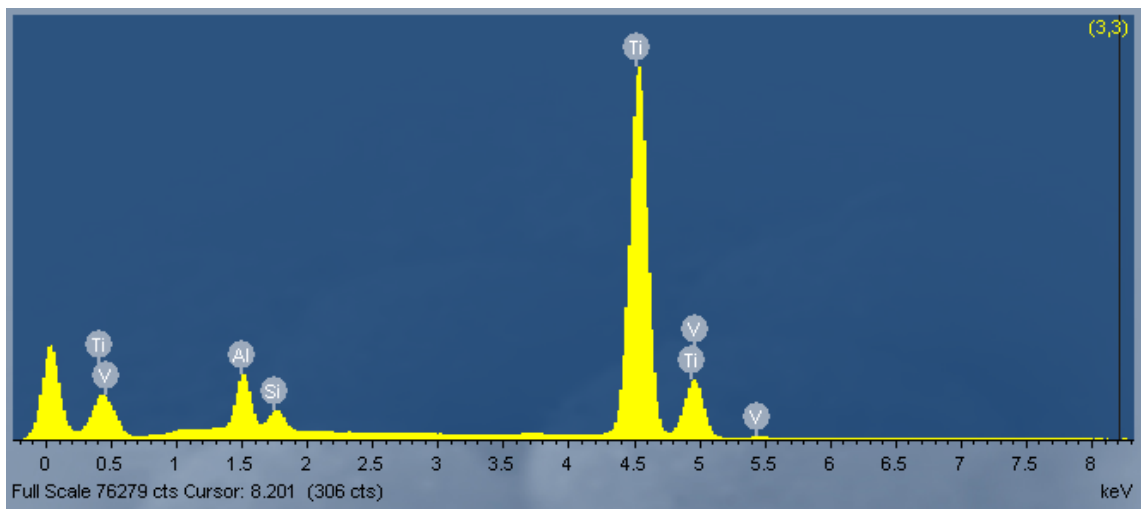


Figure 5-28: EDS spectrum of grit blasted Ti-6Al-4V.

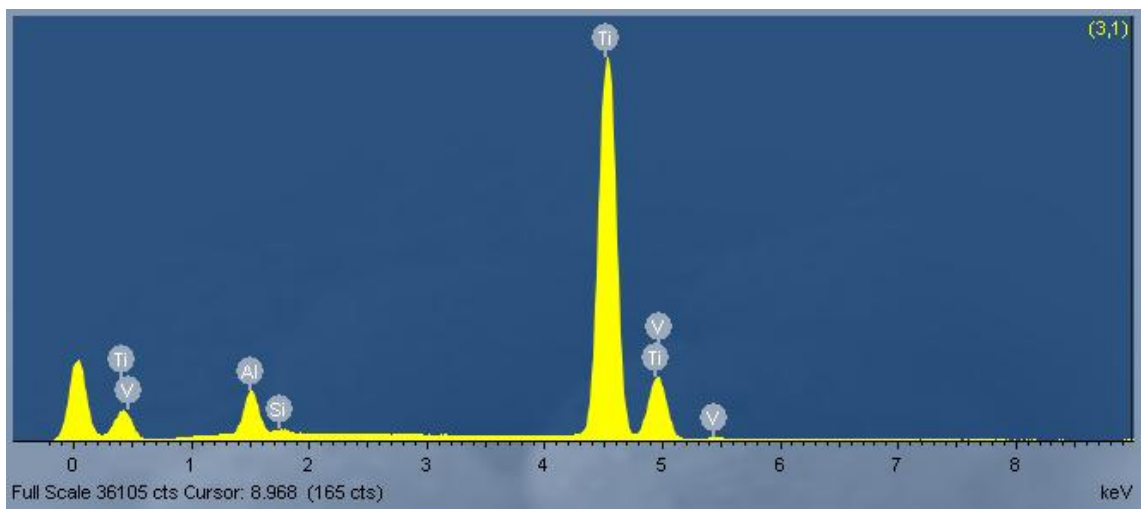


Figure 5-29: EDS spectrum of LSM Ti-6Al-4V.

5.5.3 Cross-sectional chemical composition analysis

A cross-sectional EDS analysis of the laser surface modified samples was carried out at the points as shown in Figure 5-30. Eight spectrum points were analysed beginning at 8 μm from the surface of the material. All points were separated by 8 μm thus giving an analysis range of 64 μm covering both the untreated and laser melted regions.

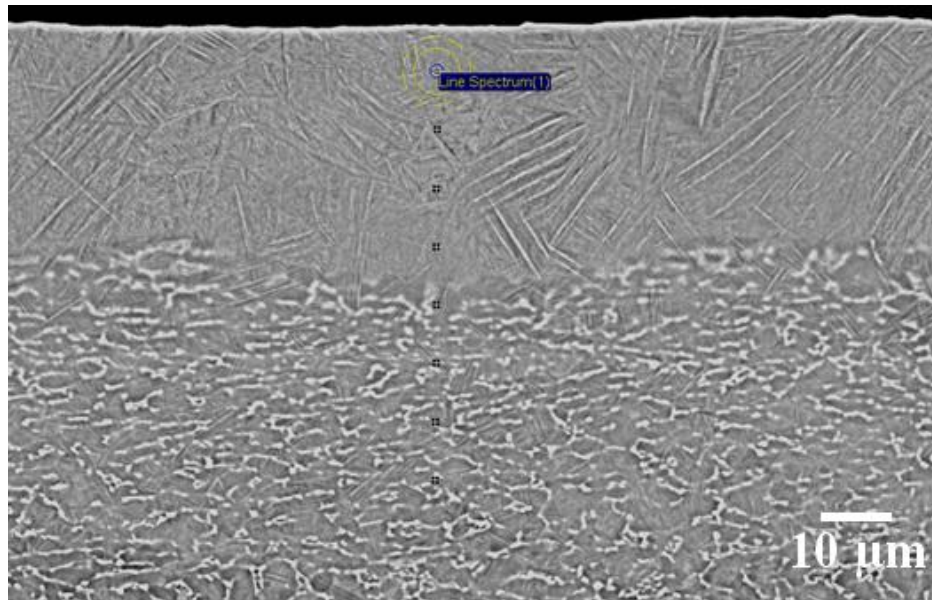


Figure 5-30: Typical EDS analyses of the cross-sectional microstructure perpendicular to the direction of the beam

Figure 5-31 shows variation in weight percent of the Ti element for sample 3, 6 and 9 as the distance from the surface is increased.

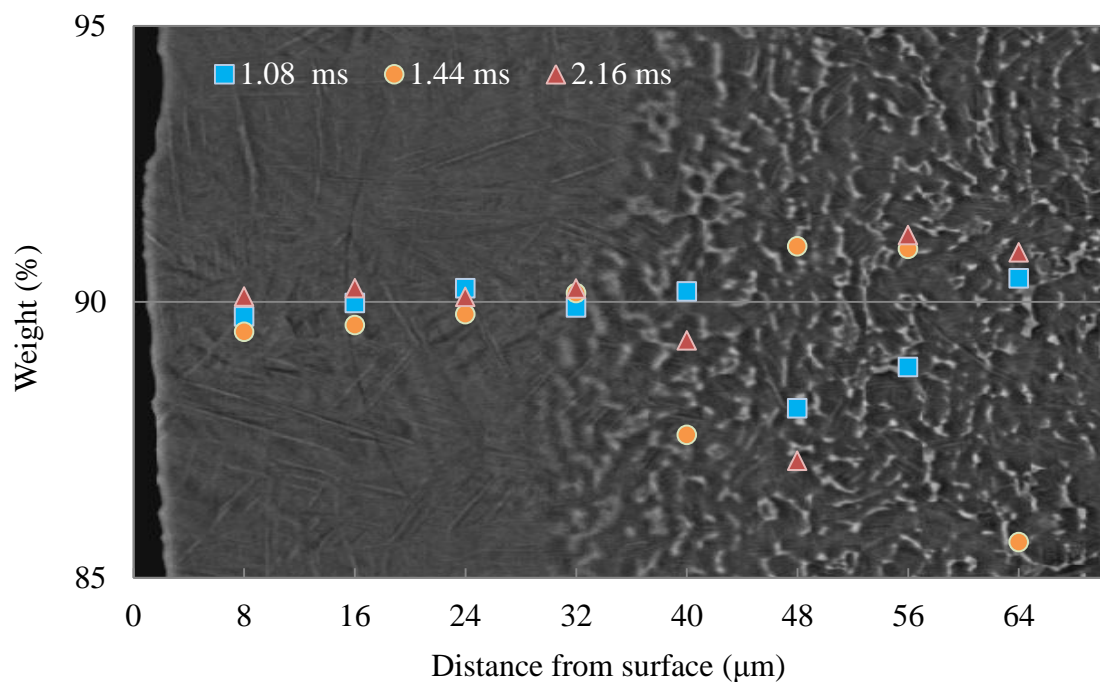


Figure 5-31: EDS analysis of titanium composition distribution in samples 3, 6 and 9.

The graph simultaneously highlights changes in microstructure of a typical laser surface modified sample at the corresponding distances. Within the laser treated region, the titanium element composition is uniform at approximately 90% compared to the relatively non-homogenous titanium distribution within the bulk alloy. The same trend was found for the aluminium alloying elements, see Figure 5-32. The actual cross-sectional micrographs of each sample are given in *Appendix I*.

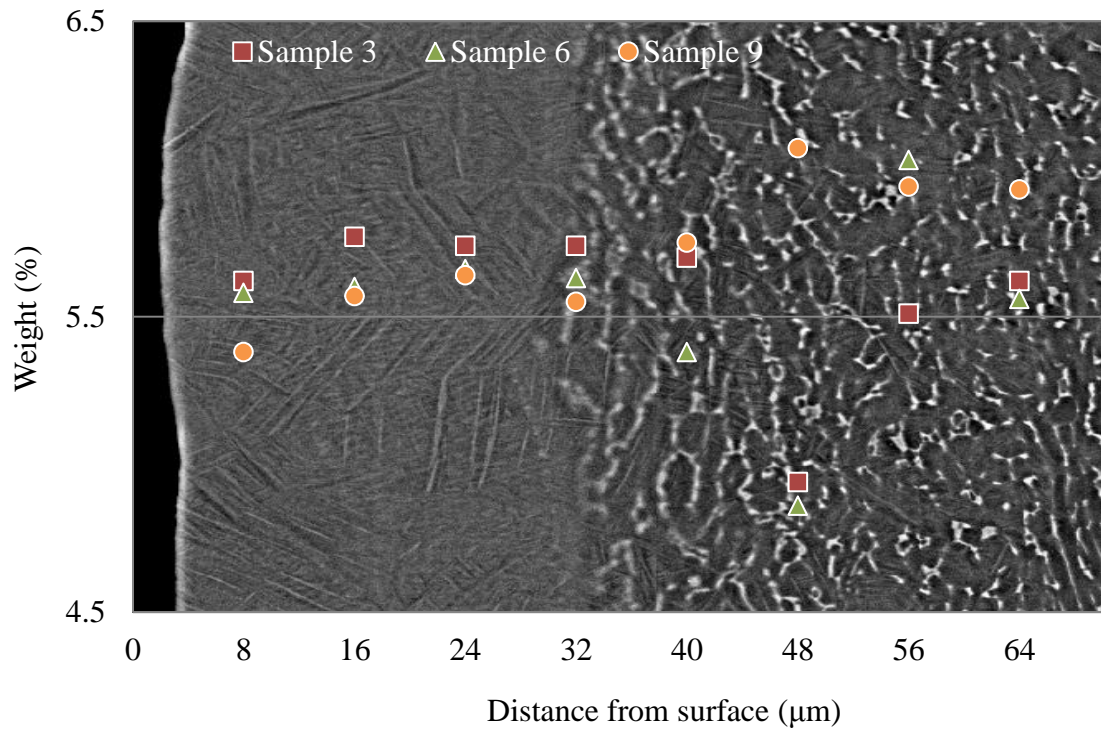


Figure 5-32: EDS analysis of aluminium composition distribution in samples 3, 6 and 9

5.6 Wear Resistance

Initial tests were carried out to distinguish the depth of wear tracks at specific sliding distances. Figure 5-33 shows the relationship between wear track depth and sliding distances of Ti-6Al-4V, characterised via white light interferometry. The wear depth of Ti-6Al-4V was found to increase linearly from 11 to 57 µm when the distance travelled by the pin (sliding distance) was varied between 9.7 and 150 m respectively. The coefficient of determination (R^2) of 0.9966 shows a good fit, representing a good relationship between the depth of wear track and distance travelled by the pin. Two sliding distances, 20 and 150 m, were selected for the remaining study of laser processing parameters influence on the wear characteristics. Figure 5-34 shows 3D wear profiles, of (a) untreated (UT) sample wear tested for 150 m, (b) laser surface modified (LSM) sample wear tested for 150 m and (c) laser surface modified (LSM) samples wear tested for 20 m. The images were obtained via white light interferometry.

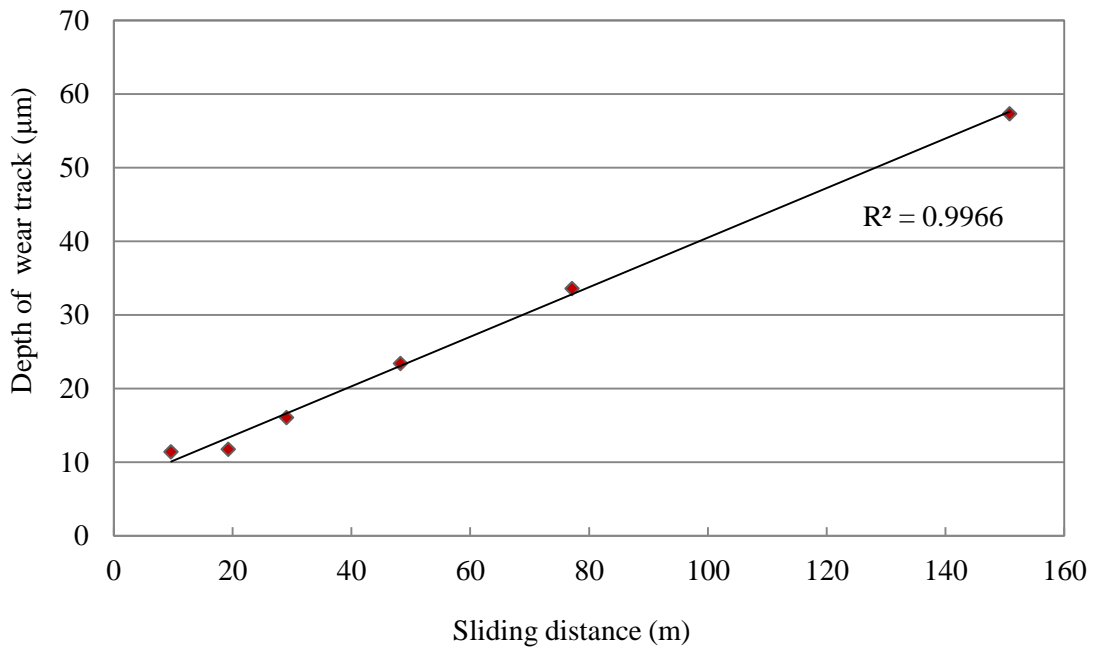


Figure 5-33: Relationship of wear track and distance travelled by the pin.

Untreated wear track profile Figure 5-34 (a), show slightly larger depth and width compared to the LSM profile Figure 5-34 (b). 3D profiles of laser modified samples Figure 5-34 (b) and Figure 5-34 (c) highlight a similar wear track characteristic of ridge formation on the bottom of the tracks. Untreated samples show different wear tracks, highlighting shallower ridge formation on the floor of the wear tracks. These characteristics are the initial evidence indicative of different wear mechanisms between untreated and laser treated samples.

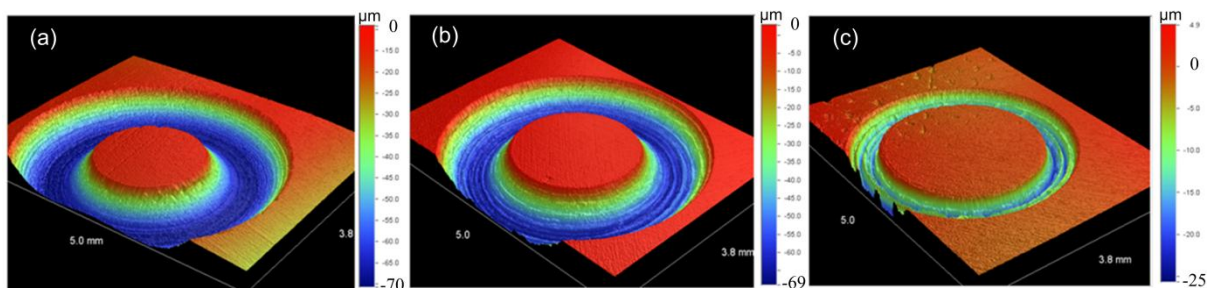


Figure 5-34: 3D wear track profile of (a) untreated Ti-6Al-4V tested for 150 m, (b) LSM Ti-6Al-4V tested for 150 m and (c) LSM Ti-6Al-4V tested for 20 m

5.6.1 Wear Track Micrographs

Figure 5-35 shows the wear track morphology of untreated samples tested for 20 m. Figure 5-35 (b) and Figure 5-35 (c) show magnified micrographs highlighting evidence of abrasive and adhesive wear mechanisms. The wear track of untreated Ti-6Al-4V is

smearred with plastically deformed wear particles. Mass loss detected in the samples was due to disintegration of the wear debris. Figure 5-36 shows the wear track morphology of a typical LSM sample tested for 20 m. The morphology shows a smoother surface with no evidence of smearred wear particles.

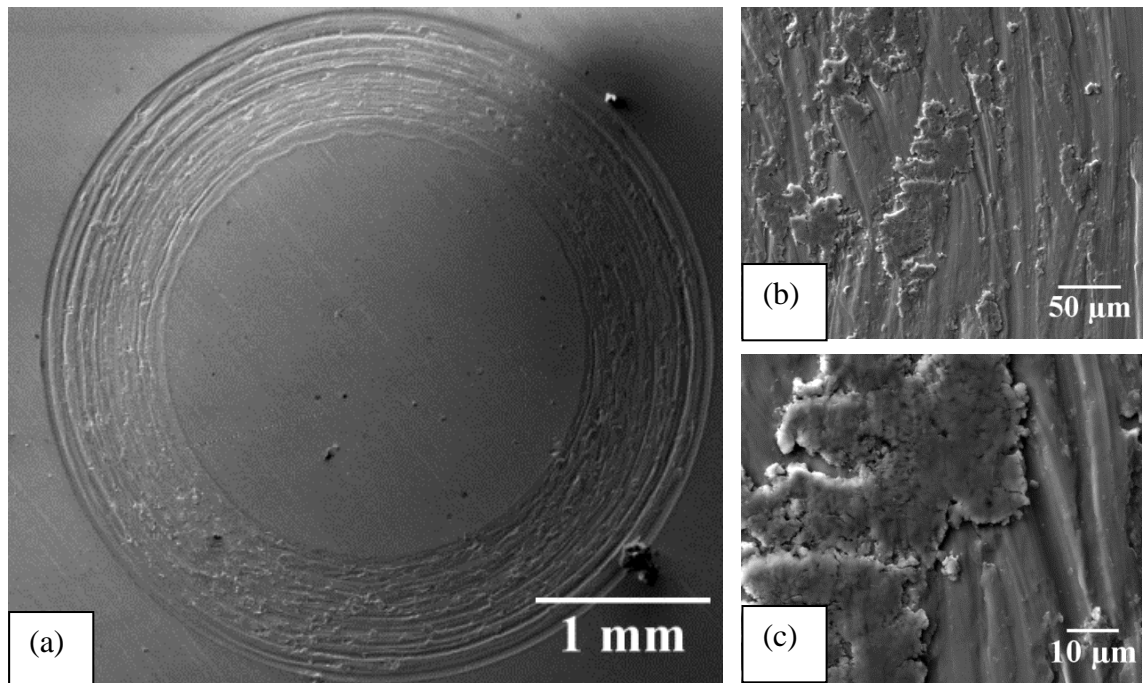


Figure 5-35: Micrographs of untreated Ti-6Al-4V at various magnifications, samples tested for 20 m.

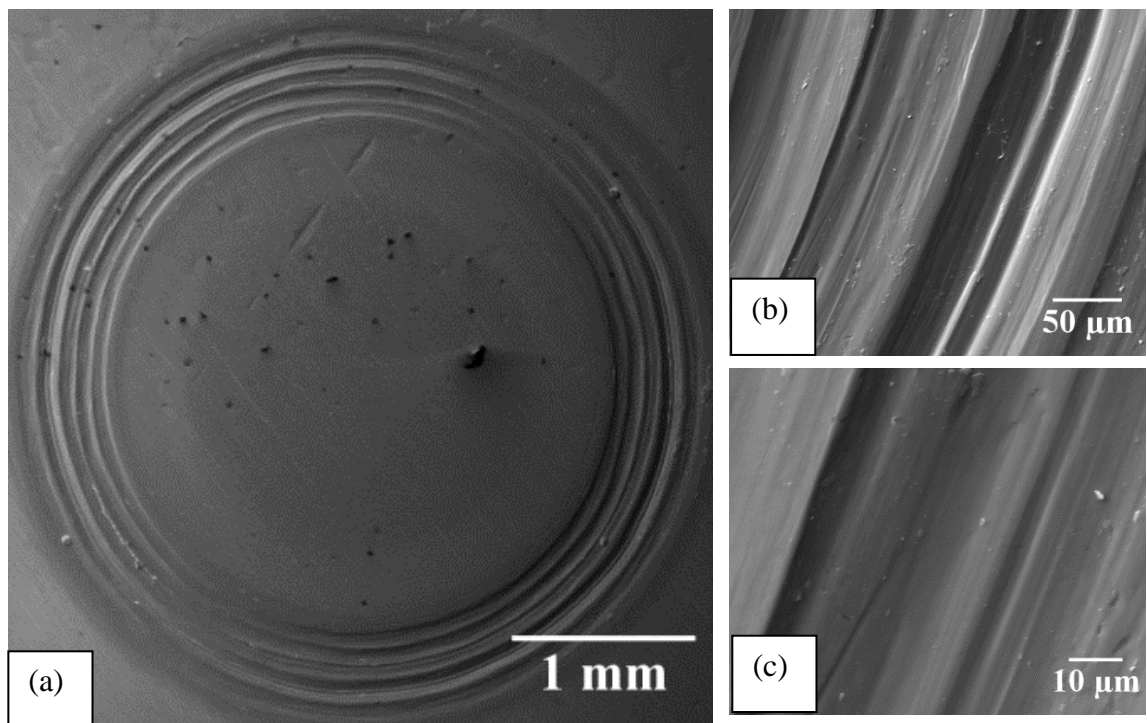


Figure 5-36: Micrographs of LSM 3 (26.72kW/mm^2 and 2.16 ms) at various magnifications, samples tested for 20 m.

Figure 5-37 shows that the wear mechanisms involved for untreated samples tested for 150 m were similar to those observed for samples tested for 20 m. However, LSM samples tested for 150 m also showed worn surfaces due to minor deformation wear mechanism visible in Figure 5-38. Deformation wear mechanism was not observed for samples treated at 20 m.

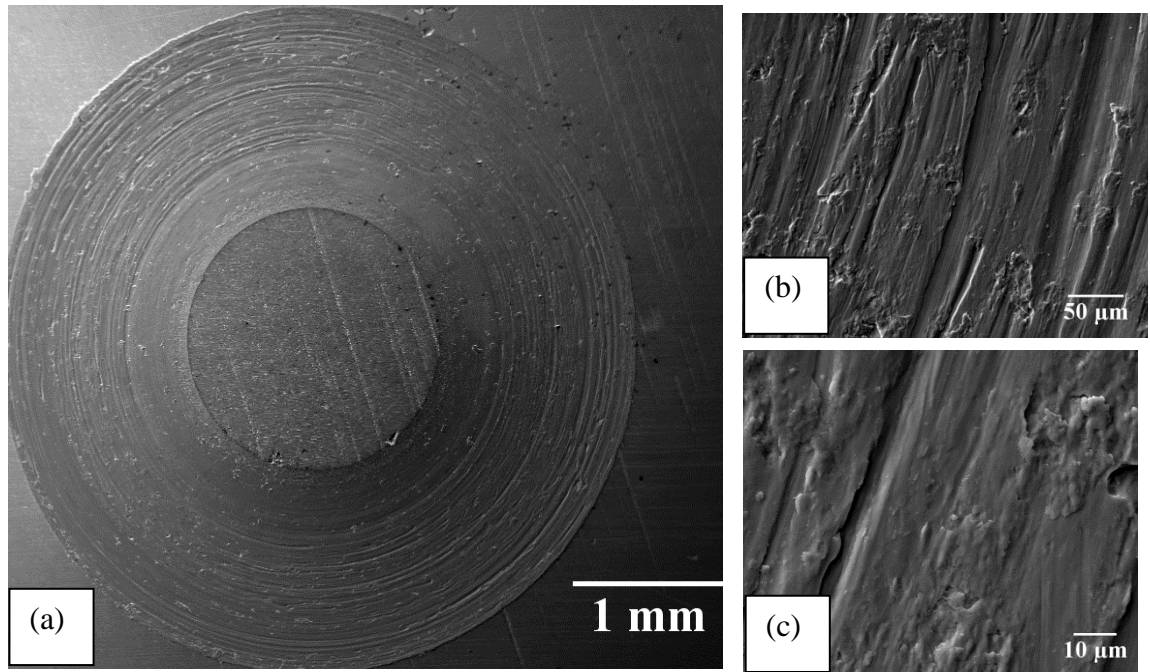


Figure 5-37: Micrographs of untreated Ti-6Al-4V at various magnifications, samples tested for 150 m.

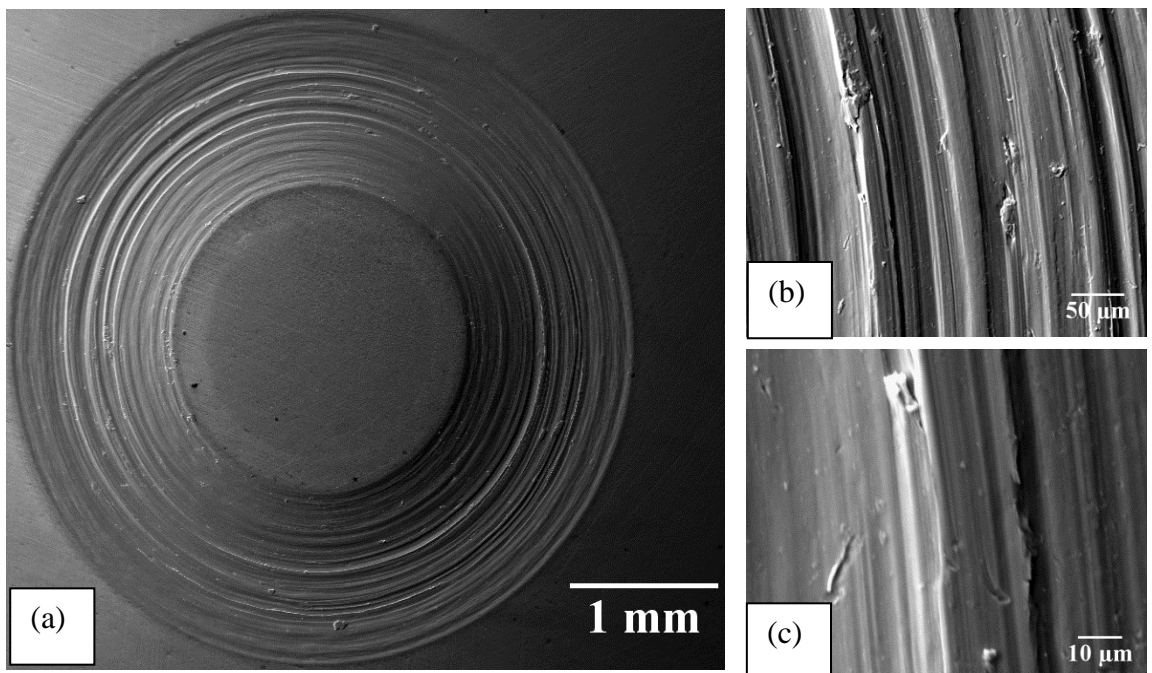


Figure 5-38: Micrographs of LSM 3 (26.72 kW/mm^2 and 2.16 ms) at various magnifications, samples tested for 150 m.

5.6.2 Effects of Laser Processing Parameters on Specific Wear rate

Figure 5-39 shows the specific wear rate of untreated (UT) and laser modified (LSM) samples tested for 20 and 150 m.

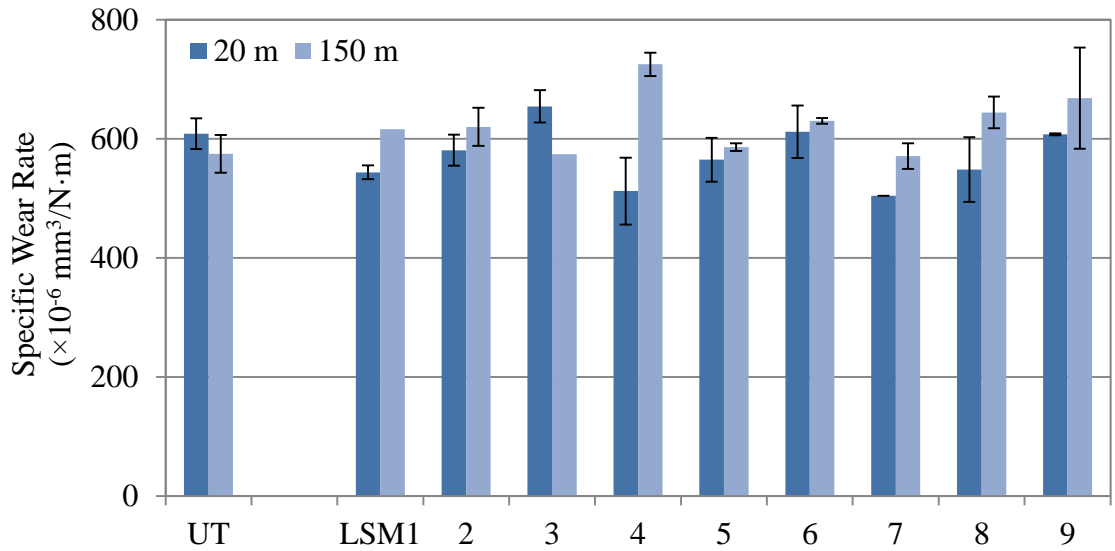


Figure 5-39: Specific wear rates of Ti-6Al-4V at two sliding distances of 20 and 150 m.

When wear testing was conducted for 150 m, specific wear rate of the untreated samples were found to be closely similar to that of the treated samples. No correlation was observed between processing parameters and specific wear rate. However, a strong correlation was found between the specific wear rate and laser modified melt pool depths. Figure 5-40 highlights a linear relationship, R^2 value of 0.7, where samples with higher melt-pool depth produced the least wear.

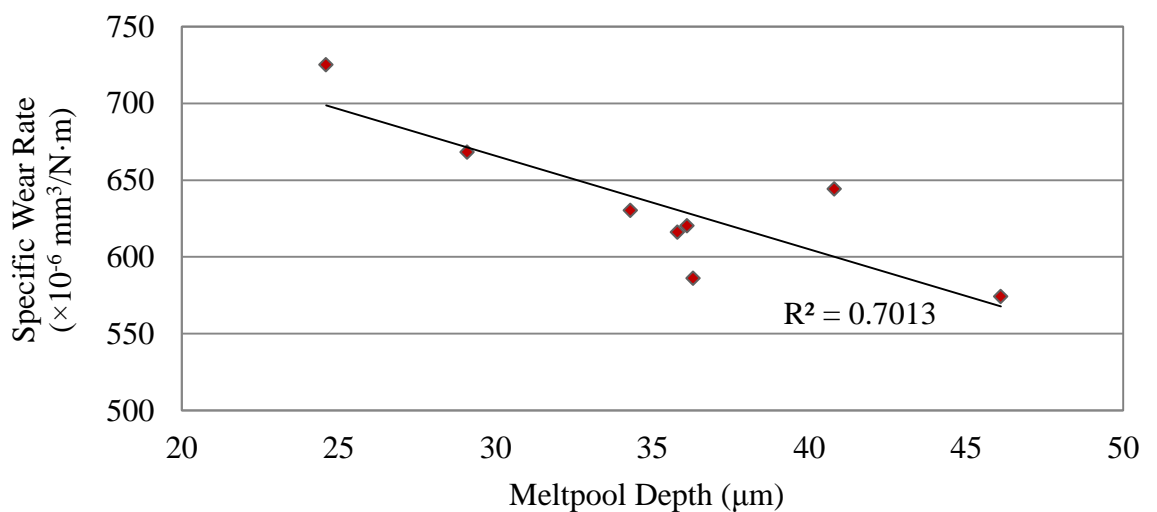


Figure 5-40: Relationship of specific wear rate and melt-pool depth for samples tested for 150 m.

This evidence suggested that the wear track being produced was significantly larger than the melt-pool sizes therefore the tested wear rates combined with the substrate. Samples tested for 20 m showed a relationship between laser processing parameters and the specific wear rate. Figure 5-41 highlights the effects of irradiance time and residence time on specific wear rate for samples tested for 20 m. Increase in both irradiance and residence time resulted in higher specific wear rates.

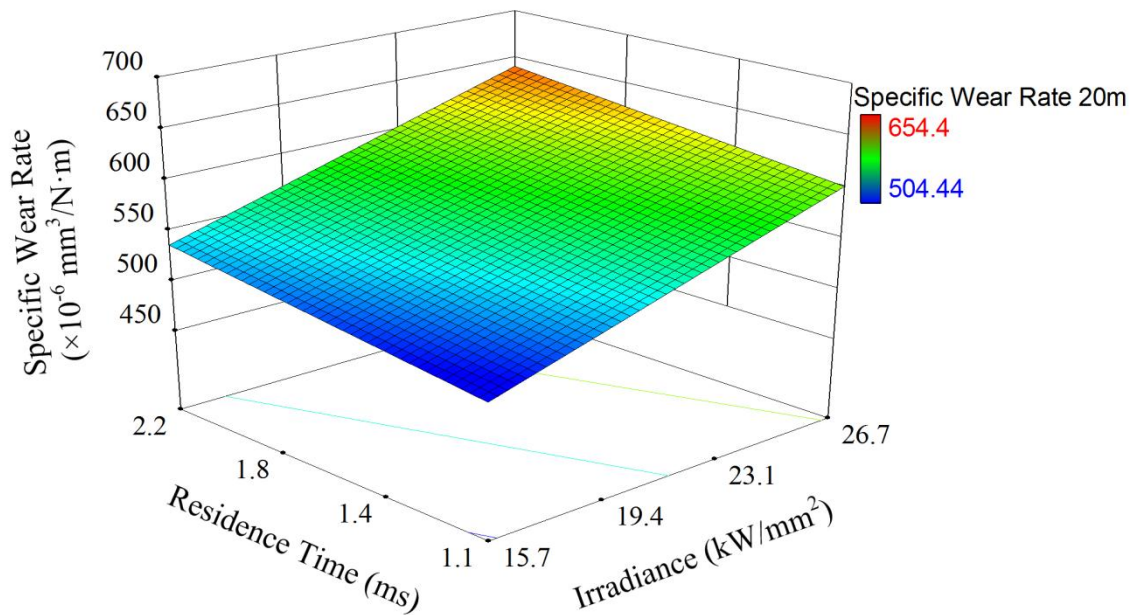


Figure 5-41: Effects of laser processing parameters on specific wear rate over 20 m sliding distance.

The lowest wear rate of $504 \times 10^{-6} \text{ mm}^3/\text{N}\cdot\text{m}$ (17% less than untreated samples) was produced with the minimal irradiance and residence time of $15.7 \text{ kW}/\text{mm}^2$ and 1.08 ms respectively. The 3D graph was generated using a two factor interaction model. Table 5-6 shows the analyses of variance generated by the model. The Model F-value of 62.82 implies the model is significant. A p-value of 0.0002 suggests that there is a low chance the F-value could occur due to noise. The Predicted R^2 of 0.974 is in reasonable agreement with the Adjusted R^2 of 0.9586. High R^2 values suggest there is a statistical significant interaction between the factors. Resulting specific wear rate can be modelled by the final equation produced by the model given in Table 5-6. Order of factor influence on microhardness can be established through analysis of the F-values magnitude as follows: $A \gg B \gg AB$. The final equation in terms of the coded factor further confirms the influence of the factors, see Equation (21).

Table 5-6: Analysis for variance (ANOVA) table for specific wear rate – 2FI model

Source	Sum of Squares	Mean Square	F Value	p-value
Model	18726.17	6242.055	62.819	0.0002
A-Irradiance	16363.66	16363.66	164.683	< 0.0001
B-Residence Time	2347.49	2347.49	23.625	0.0046
AB	15.015	15.015	0.151	0.7135
Residual	496.821	99.36		
Cor Total	19222.99		:	
<i>Final equation obtained from the model</i>				
R-Squared	0.974	<i>Specific Wear Rate 20m =</i> <i>+331.32746</i> <i>+8.43833 × Irradiance</i> <i>+22.78662 × Residence Time</i> <i>+0.65236 × Irradiance × Residence Time</i>		
Adj R-Squared	0.958			
Pred R-Squared	0.832			
Adeq Precision	21.669			

$$\text{Specific wear rate (20m)} = 569.73 + 52.22A + 19.78B + 1.94AB \quad (21)$$

The outcome of wear treated samples has a high predictability factor as presented in Figure 5-42. The specific wear rates values obtained experimentally are positioned close to the best-fit line highlighting the adequacy of the model.

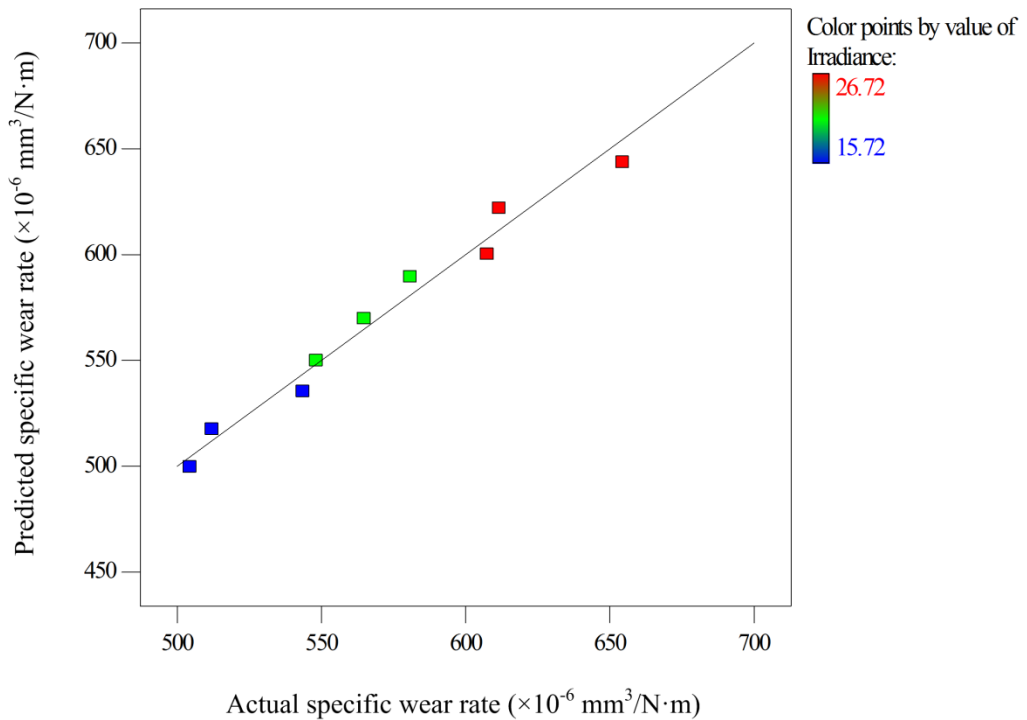


Figure 5-42: Actual specific wear rate values versus the predicted response values

5.7 Corrosion Resistance

Figure 5-43 shows the typical recorded variations of rest potential with time for as-received, grit blasted and LSM 3, 6 and 9 which corresponds to samples treated at the highest irradiance (26.72 kW/mm^2) and decreasing residence time (2.16, 1.44 and 1.08 ms respectively).

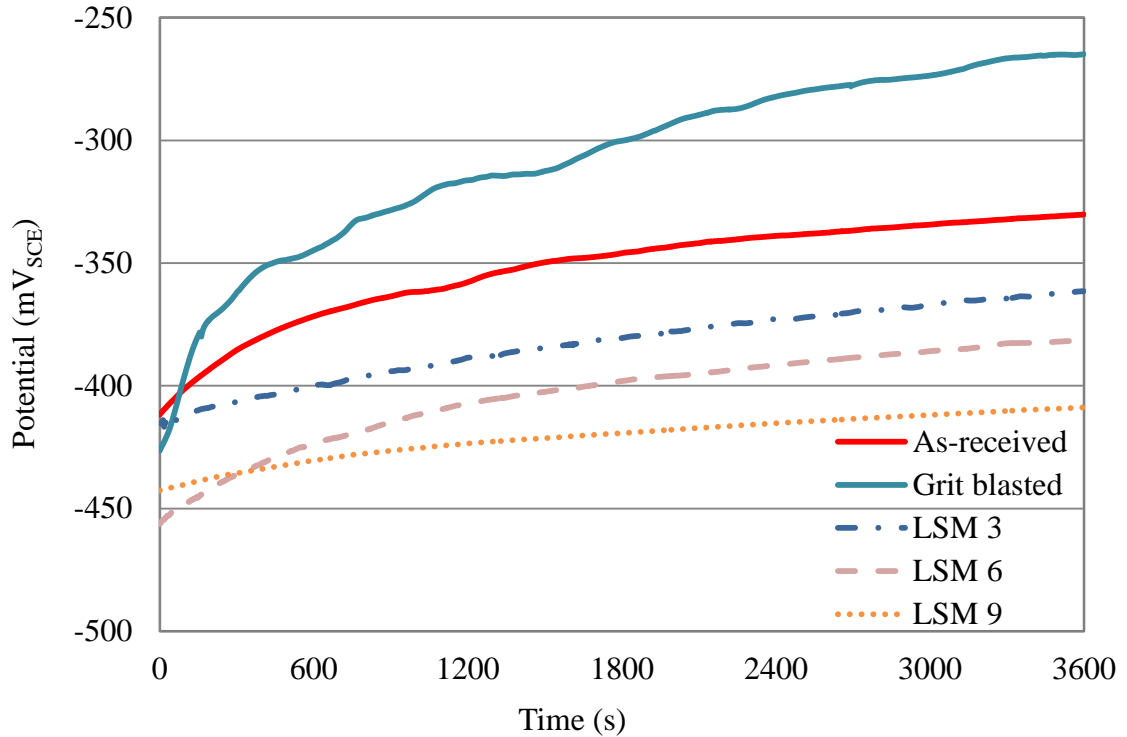


Figure 5-43: OCP variation with time of immersion for as-received, grit blasted and LSM 3,6 and 9 samples during immersion in 0.9 % NaCl at 37°C.

All samples showed potentials moving towards the noble direction signifying improved passivity with increased time. Compared to the laser surface modified (LSM) samples that showed a slow shift in the more noble direction throughout; the untreated samples show a steep increase during the first 1200 seconds. The steep increase indicates the rapid formation of an oxide film on the surface acting as a barrier for metal dissolution thus reducing corrosion rate. Attainment of a steady open circuit potential (OCP) indicates the existence of a steady oxide film. The OCP recorded for the grit blasted sample was the highest at -264 mV, the as received was next at -350 mV and the laser modified samples obtained lower OCP values less than -362 mV. Increase in residence time produced lower OCP samples laser treated at 26.72 kW/mm^2 . Effects of lower irradiances 15.72 and 20.43 kW/mm^2 on OCP is illustrated by Figure 5-44 and Figure 5-45 respectively.

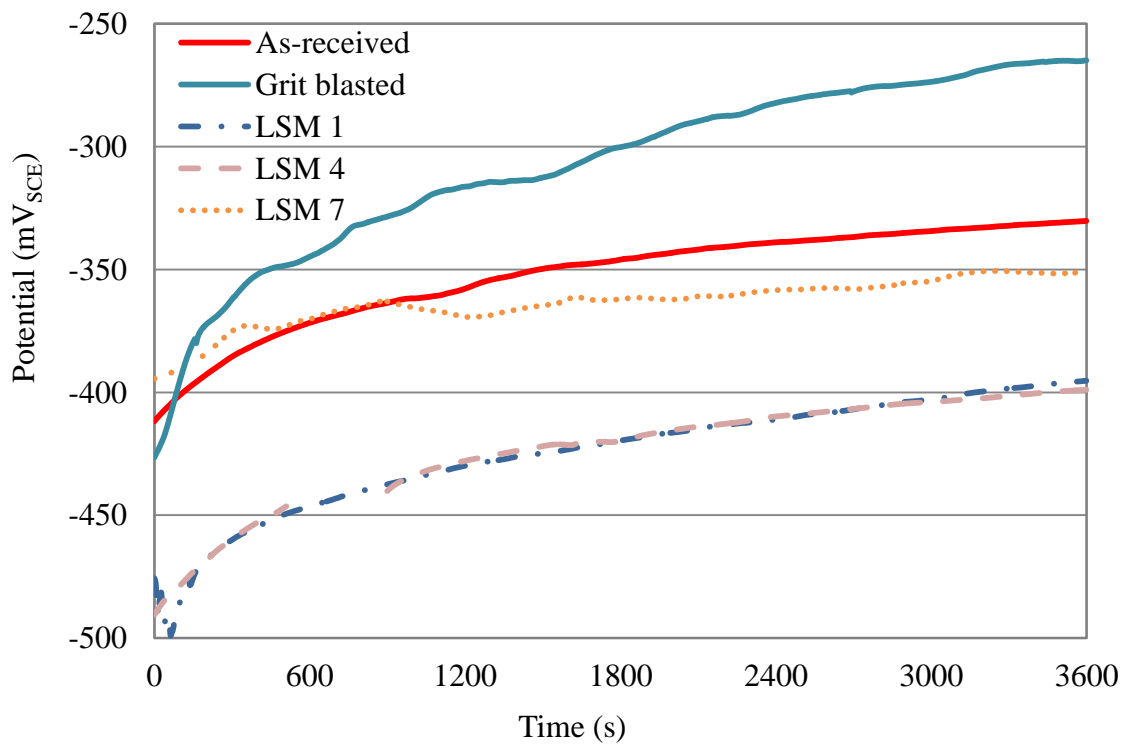


Figure 5-44: OCP variation with time of immersion for as-received, grit blasted and LSM 1,4 and 7 samples during immersion in 0.9 % NaCl at 37°C.

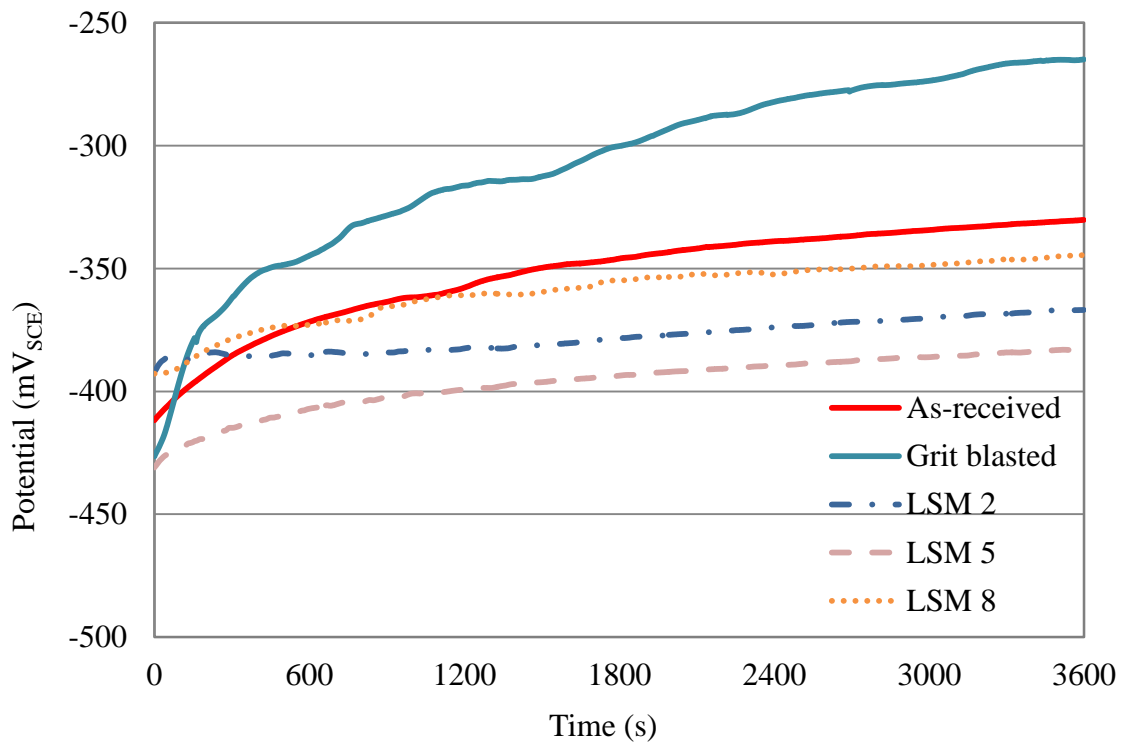


Figure 5-45: OCP variation with time of immersion for as-received, grit blasted and LSM 2,5 and 8 samples during immersion in 0.9 % NaCl at 37°C.

Figure 5-46 shows the potentiodynamic polarisation curve of untreated and selected laser surface modified (LSM) samples swept back before reaching 1000 mV_(SCE). The polarisation curves are broadly similar except for the current density variation with increase in potential. In untreated samples (i.e. grit blasted and as-received samples) a monotonic increase of the potential above about 120 mV_{SCE} was observed, indicative of film/alloy dissolution. The anodic polarisation behaviour of the laser surface modified Ti-6Al-4V samples suggests that a different film type formed on these surfaces compared to the untreated sample surfaces. For laser treated samples a steady current density is maintained with increase in potential. The anodic Tafel slopes of the as received and grit blasted samples ($\beta_a = 345$ to 346 mV dec.⁻¹) were higher compared to the LSM samples 4 and 2 ($\beta_a = 225$ to 281 mV dec.⁻¹), see Figure 5-46.

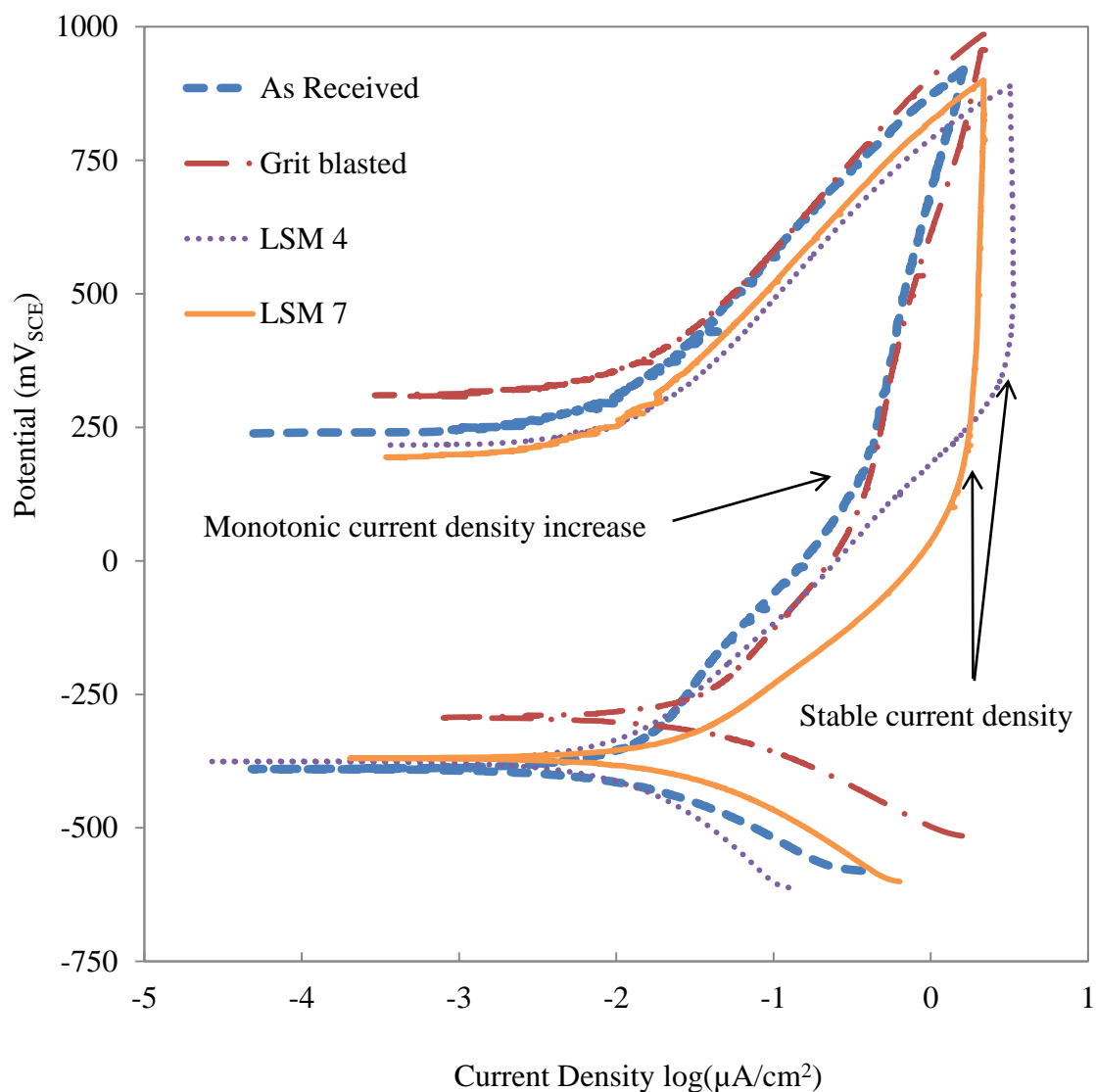


Figure 5-46: Polarisation curves of As-received, grit blasted, LSM 4 and LSM 7 Ti-6Al-4V samples in 0.9% NaCl at 37°C.

Figure 5-47 shows the potentiodynamic polarisation curve of untreated and laser surface melted Ti-6Al-4V where the upscan reached the breakdown potential. Low Tafel slopes in LSM samples are clearly visible. The monotonic increase of untreated samples intersects LSM samples at approximately 1000 mV_(SCE). LSM sample show a stable current density resembling a superior stable passive film compared to untreated samples. Both laser treated and untreated samples showed localised corrosion characteristics, illustrated in Figure 5-47 as the rapid increase in current density at a high potentials. In this case the localised corrosion was found to be pitting corrosion.

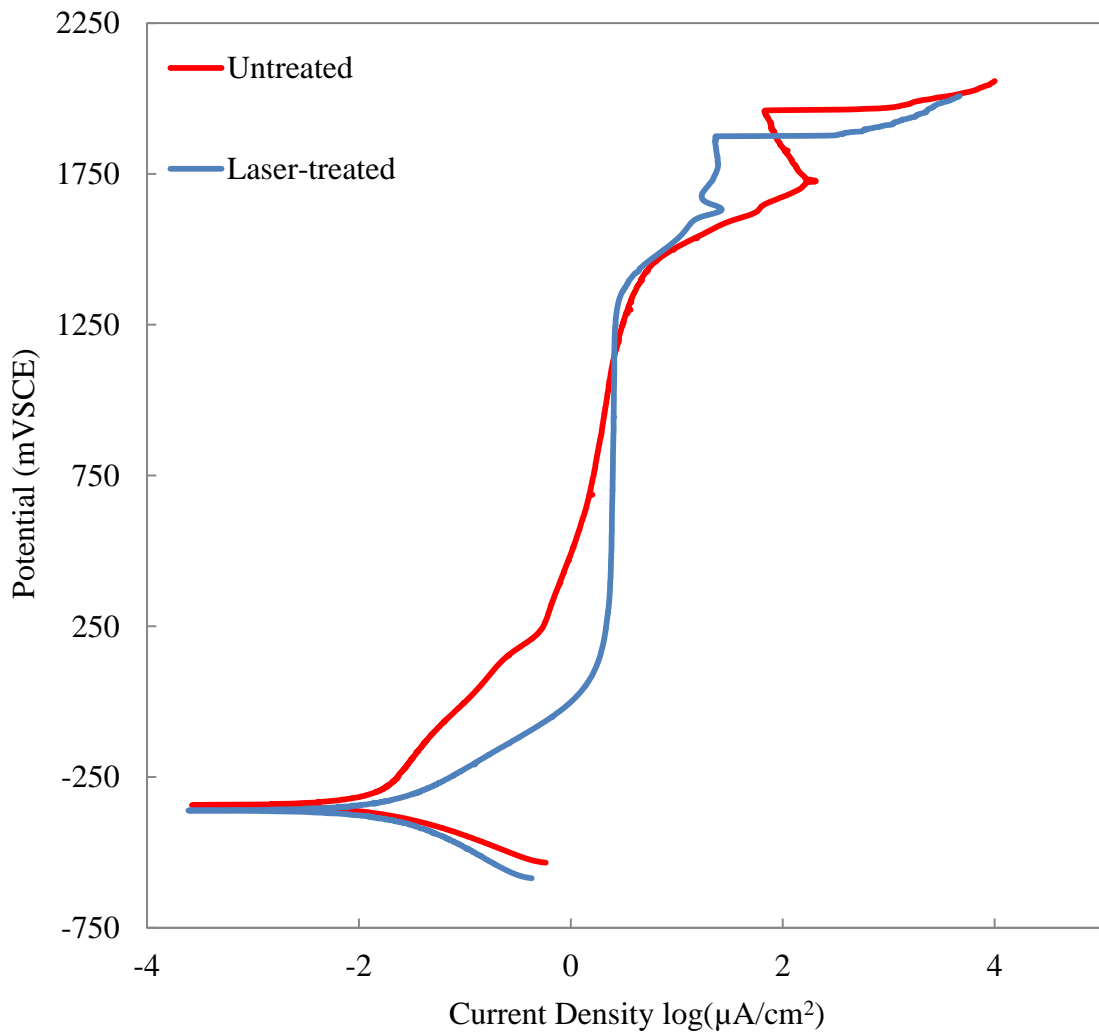


Figure 5-47: potentiodynamic polarisation curves of an untreated and laser treated Ti-6Al-4V

Localised corrosion in the form of pitting is clearly shown for both the untreated and LSM 8 in Figure 5-48. The pit size and shape of the LSM and as-received samples are different highlighting different surface properties on both set of samples. Figure 5-48 (c) shows the appearance of the laser-treated surface layer on the pit. A smoother pitting

surface is produced on the laser modified layer. No pitting was observed in any of these samples kept below $1000 \text{ mV}_{\text{SCE}}$, indicating the existence of stable passive protective films up to approximately $1300 \text{ mV}_{\text{SCE}}$.

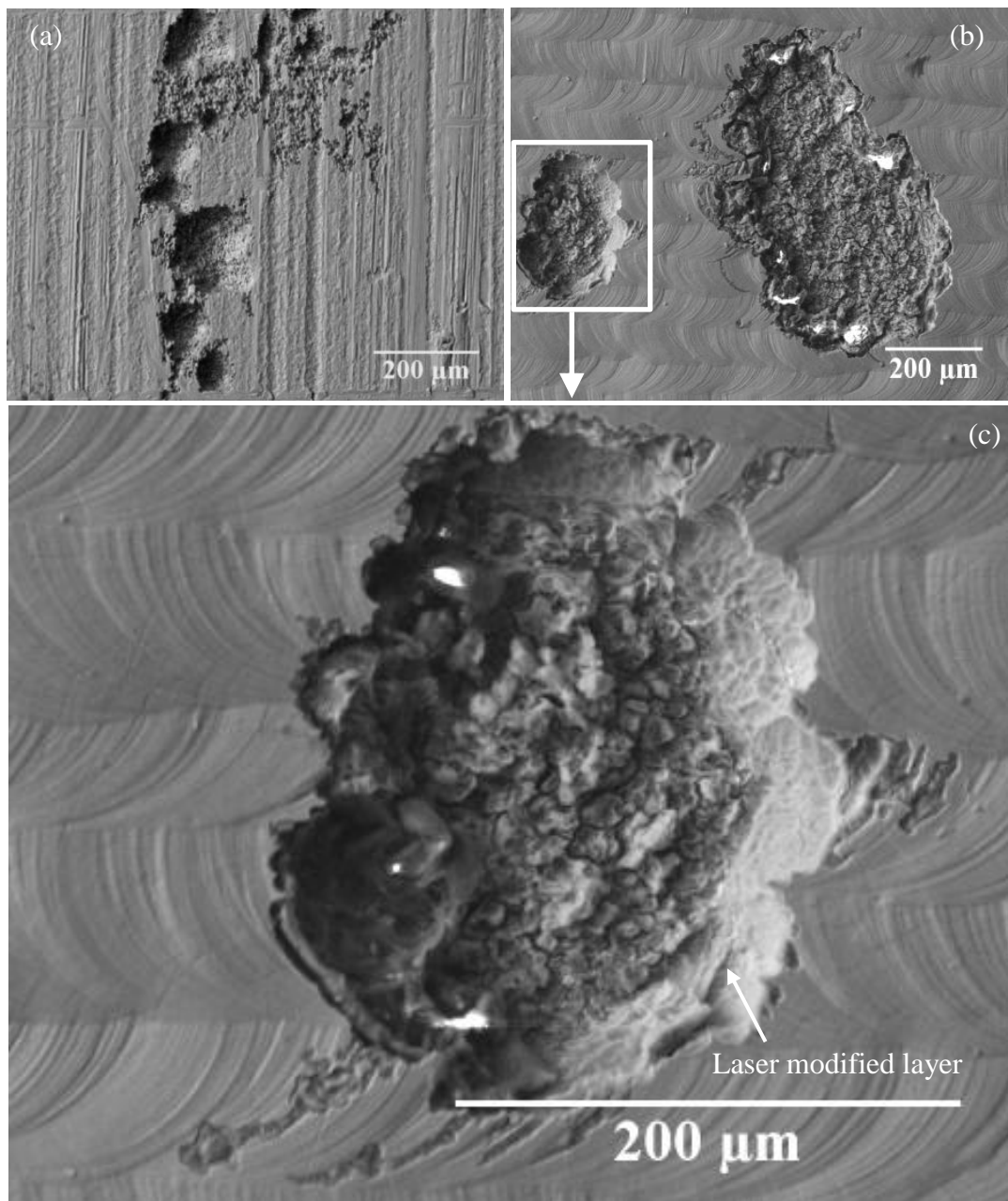


Figure 5-48: Localised corrosion of (a) as-received Ti-6Al-4V, (b) LSM 8 and (c) magnified view of sub-section from (b).

Tafel analysis results obtained using Tafel rulers of the ACM Sequencer software are tabulated in Table 5-7. The corrosion current densities (i_{corr}) were found to be between 10 and 28 nA cm^{-2} . Samples treated at the lowest residence 1.08 and highest irradiance 26.72 kW/mm^2 showed the lowest average corrosion rate of 86 nm yr^{-1} . At a constant residence time of 1.08 ms (lowest residence time implemented), irradiances of 15.72 ,

20.44 and 26.72 kW mm⁻² produced decreasing corrosion rates of 239, 188 and 86 nm yr⁻¹.

Table 5-7: Tafel analysis results of untreated and LSM Ti-6Al-4V in 0.9% NaCl.

Sample ID	β_a (mV/dec.)	β_c (mV/dec.)	i_{corr} (nA /cm ²)	Corr. Rate (nm yr ⁻¹)
As-received	345±4	146±9	12.45	108±8
Grit blasted	346±13	139±3	35.4	309±23
LSM 1	288.11	158.27333	50.66	441±20
LSM 2	193.57	169.26667	28.84	251±16
LSM 3	139.02667	91.55	23.24	202±17
LSM 4	281.23	243.39333	12.27	106±17
LSM 5	199.19667	179.87333	19.04	165±23
LSM 6	217.83	191.66667	14.9	129±10
LSM 7	225±4	179±13	27.48	239±21
LSM 8	207±4	187±5	21.6	188±8
LSM 9	231±2	179±11	10.0	86±5

5.8 Surface Wettability

The final shape taken by a drop of water when it is brought in contact with the flat Ti-6Al-4V depends upon the relative magnitudes of the molecular forces that exist within the liquid (cohesive) and between the liquid and the solid (adhesive). The result of this effect is θ , the angle at which the liquid subtends to the solid. Figure 5-49 shows the typical contact angles of polished and grit blasted Ti-6Al-4V prior to laser treatment.

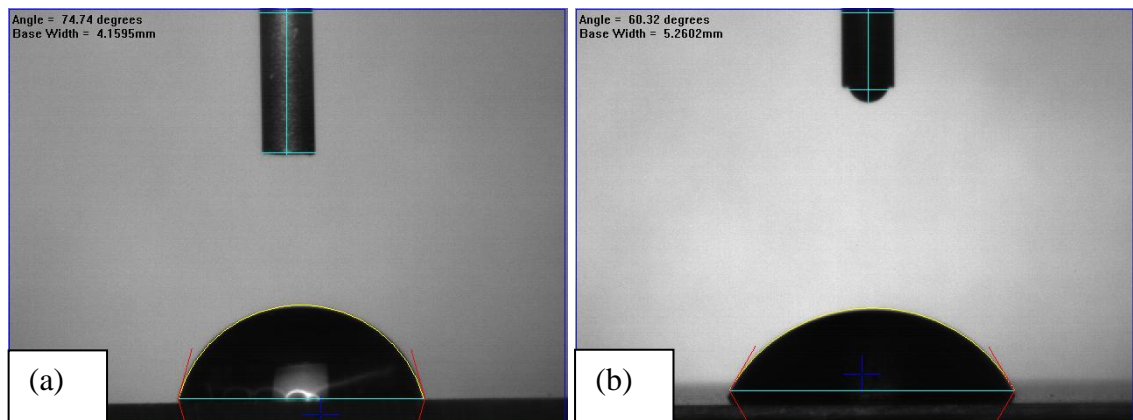


Figure 5-49: Typical contact angles of (a) polished and (b) grit blasted Ti-6Al-4V.

The average contact angles of as-received and polished Ti-6Al-4V were $71.3 \pm 2.5^\circ$ and $73.9 \pm 3.7^\circ$ respectively. The measured contact angle values for as-received and polished samples were within 3° . Grit blasting produced a lower contact angle of $60.6 \pm 1.1^\circ$.

5.8.1 Contact Angles of Unpolished Samples

Subsequent to laser surface modification the average contact angle dropped to a range between approximately 24° and 61° depending on the processing conditions. Optical micrographs of the sessile drops placed on the laser treated surface are shown in Figure 5-50 to Figure 5-52. The optical micrographs also illustrate the effects of irradiance and residence time on contact angles. At the lowest residence time 15.7 kW/mm^2 the contact angle reduced with increase in residence time, see Figure 5-50.

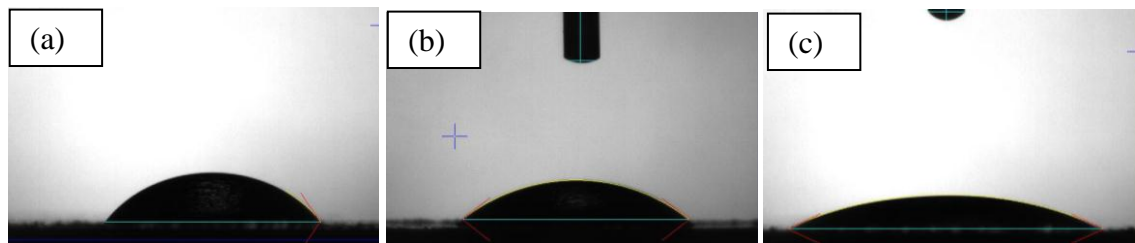


Figure 5-50: Images of contact angles on laser surface modified Ti-6Al-4V at a constant irradiance of 15.72 kW/mm^2 and three levels of residence time (a) 1.08, 1.44 and 2.16ms

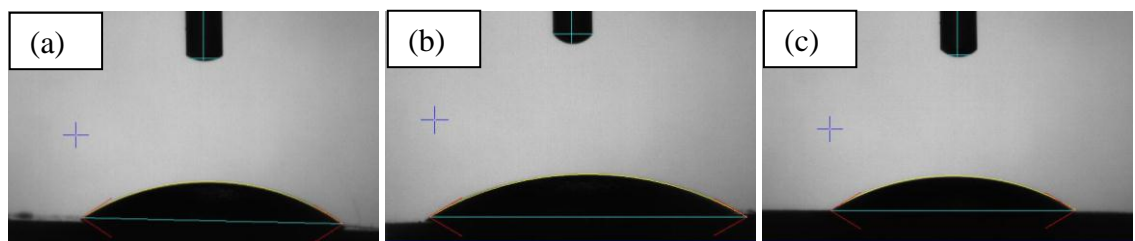


Figure 5-51: Images of contact angles on laser surface modified Ti-6Al-4V at a constant irradiance of 20.43 kW/mm^2 and three levels of residence time (a) 1.08, 1.44 and 2.16ms

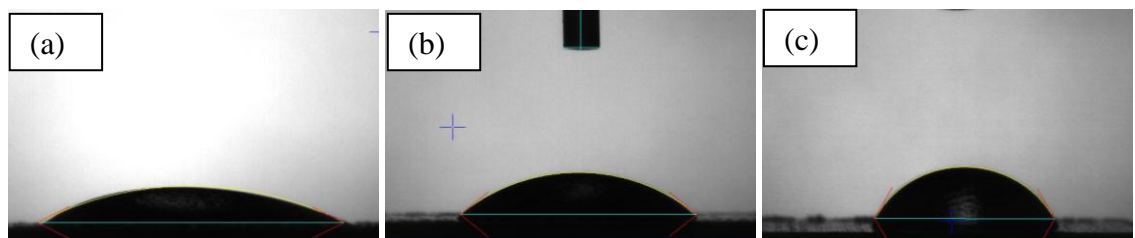


Figure 5-52: Images of contact angles on laser surface modified Ti-6Al-4V at a constant irradiance of 26.72 kW/mm^2 and three levels of residence time (a) 1.08, 1.44 and 2.16ms

Figure 5-53 shows effects of processing parameters on contact angles. A line representing the contact angle of untreated samples was included to highlight reduction in contact angles induced by laser surface melting. At low residence time (1.08 ms), contact angle decreases with increase in irradiance. This opposite happens at high residence times (2.16 ms) where contact angles increase with increase in irradiance. At the mid-range residence time (1.44 ms), the contact angle does not vary significantly. The effect can easily be viewed by the contour plot presented in Figure 5-54.

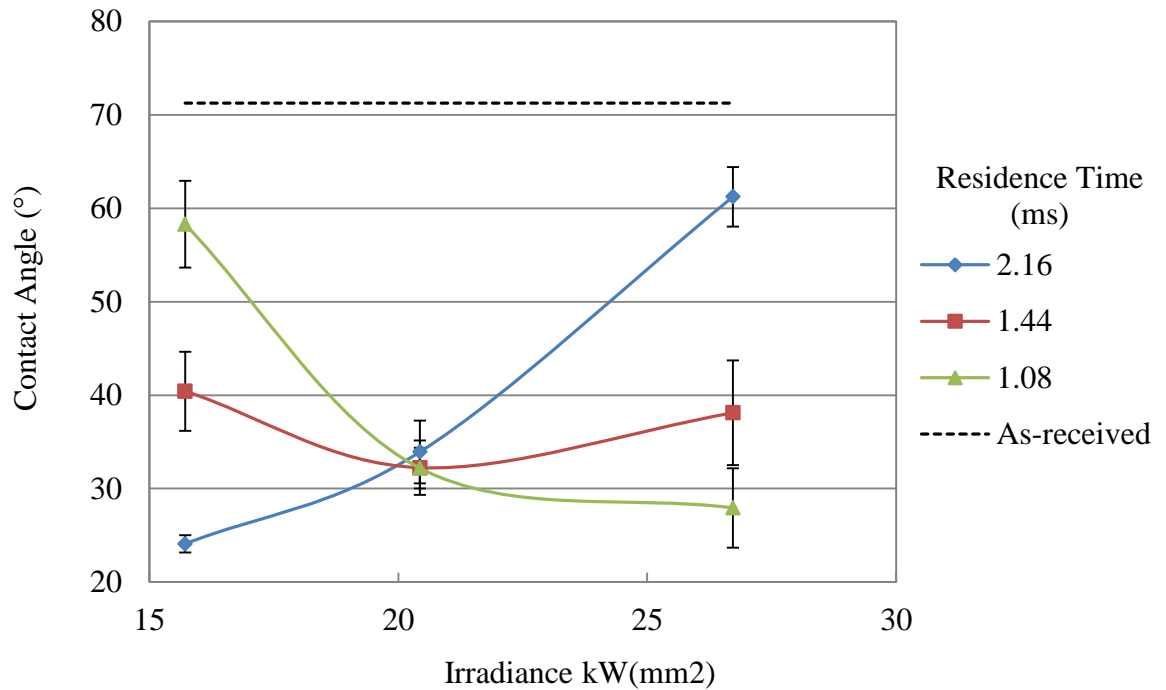


Figure 5-53: Effects of irradiance and residence time on contact angle.

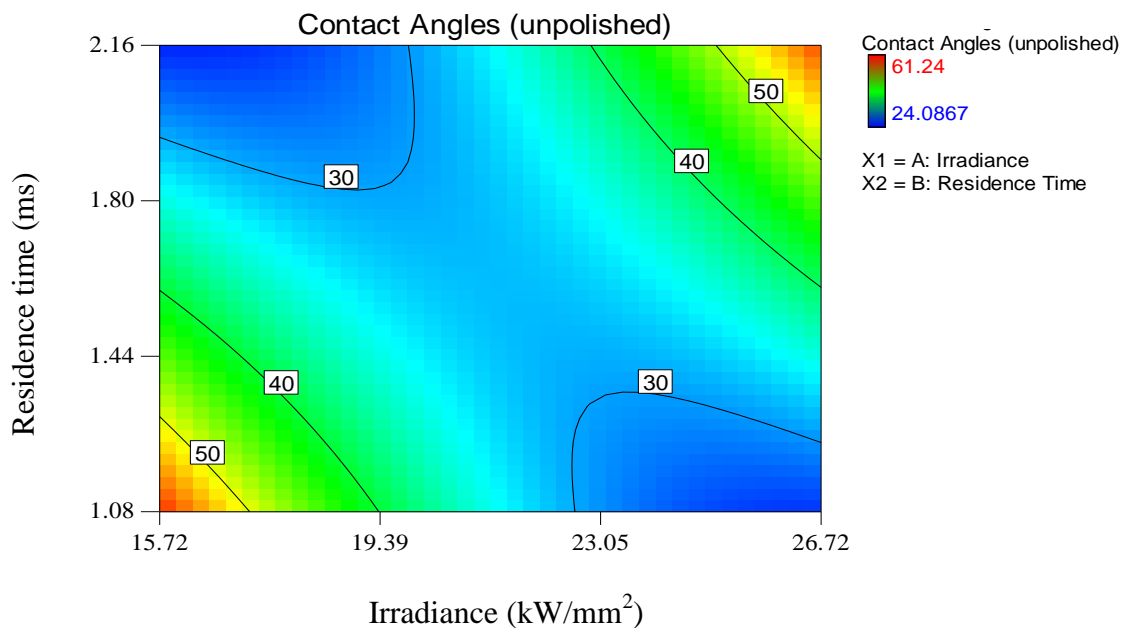


Figure 5-54: Contour plot highlighting the effects of irradiance and residence time on measured contact angles.

The contour plot was generated using a quadratic model. Table 5-8 shows the analysis of variance generated by the model. The high Model F-value of 49.348 implied the model was significant. A p-value of 0.0044 suggested that there was a low chance such a high F-value could occur due to noise. The predicted R^2 of 0.968 is in reasonable agreement with the adjusted R^2 of 0.86. High R^2 values suggest there is a statistical significance between the factors and average contact angles subsequent to laser surface melting. Contact angles of unpolished samples can be modelled by the final equation produced by the model given in Table 5-8. Order of factor influence on contact angles can be established through analysis of the F-values magnitude as follows: $AB \gg A^2 \gg B^2 > A > B$. The final equation in terms of the coded factor further confirms the influence of the factors, see Equation (22).

Table 5-8: Analysis for variance (ANOVA) table for contact angles of unpolished samples - quadratic model

<i>Source</i>	<i>Sum of Squares</i>	<i>Mean Square</i>	<i>F Value</i>	<i>p-value</i>
<i>Model</i>	1315.486	263.097	49.348	0.0044
<i>A-Irradiance</i>	3.3450	3.345	0.627	0.4862
<i>B-Residence Time</i>	0.115	0.115	0.0217	0.8922
<i>AB</i>	1139.288	1139.288	213.694	0.0007
<i>A²</i>	158.301	158.301	29.692	0.0121
<i>B²</i>	14.436	14.4363	2.707	0.1984
<i>Residual</i>	15.994	5.331		
<i>Cor Total</i>	1331.48			
		<i>Final equation obtained from the model:</i>		
<i>R-Squared</i>	0.988	<i>Contact angles of unpolished sample (°)=</i> $+ 379.649$ $+ 21.551 \times \text{Irradiance}$ $- 150.175 \times \text{Residence time}$ $+ 5.683 \times \text{Irradiance} \times \text{Residence time}$ $+ 0.294 \times \text{Irradiance}^2$ $+ 9.214 \times \text{Residence time}^2$		
<i>Adj R-Squared</i>	0.968			
<i>Pred R-Squared</i>	0.866			
<i>Adeq Precision</i>	18.696			

$$\text{Contact angle (unpolished)} \quad (22)$$

$$= 31 + 0.75A + 0.14B + 16.88AB + 8.9A^2 + 2.69B^2$$

Measured contact angles after laser surface treatment was found to be highly predictable according to the model as seen in Figure 5-55. All design points are positioned close to the best-fit line of the predicted results. The adequate precision was found to be 18.696

indicating an adequate signal. This means that the model can be used to navigate the design space.

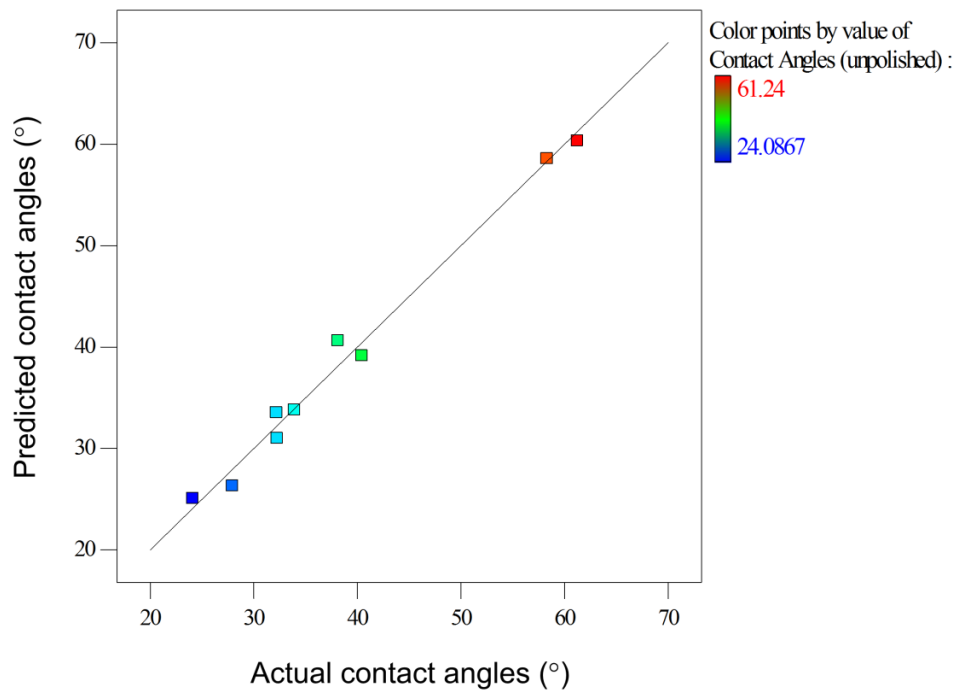


Figure 5-55: A graph of the actual contact angles of unpolished laser treated samples versus the predicted values.

The highest contact angles (approximately 58° and 61°) corresponded to points with the lowest and highest energy density, approximately 17 and 58 J/mm². This evidence suggests a relationship between contact angle and energy density. Figure 5-56 shows the relationship between energy density and contact angle measurements.

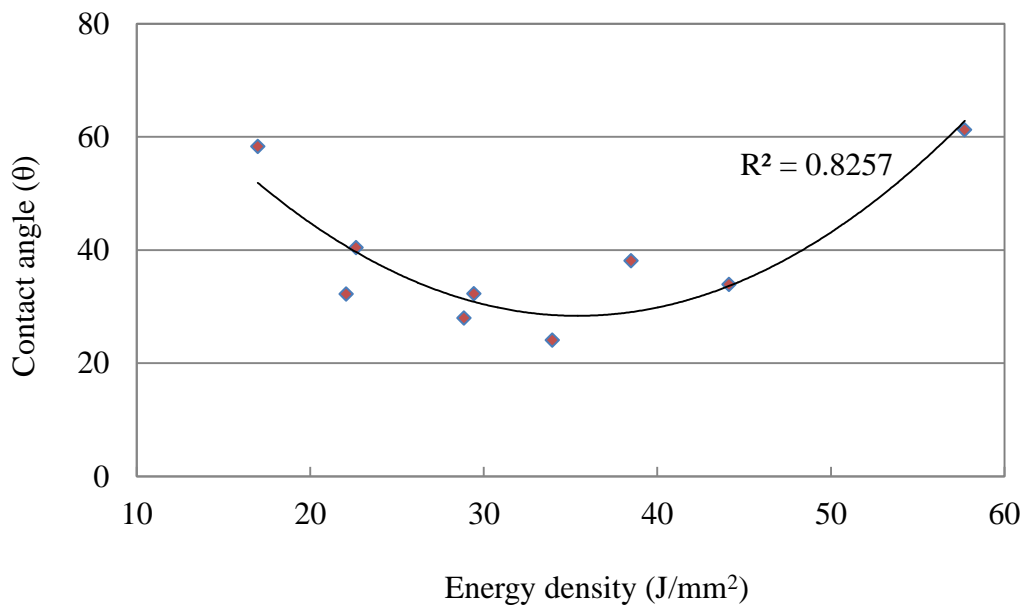


Figure 5-56: Relationship between energy density and contact angles

The R^2 value of 0.826 indicates that the second order polynomial relationship between the parameters is significant. A saddle point was observed at mid-range energy densities, where the lowest contact angles were measured.

5.8.2 Contact Angle of Polished Samples

Figure 5-57 shows the effects of processing parameters on contact angles measure from samples polished subsequent to laser modification. A saddle shape relationship highlighting stationary values at the mid-range residence time was observed. The graph shows a different relationship of effects of processing parameters on contact angles compared to the unpolished samples thus further suggesting significance of roughness in contact angle measurements. The contour plot was produced using Design Expert via a quadratic model. Table 5-9 shows the analyses variance generated by the model. The model F-value of 15.86 implies the model is significant with a 0.0228 chance that this model F value is due to noise. The predicted R^2 of 0.7 is above the minimum threshold and the difference between the adjusted R^2 is also within the minium require 0.2. High R^2 values suggest there is a statical significant interaction between the factors. This interaction can be modelled by the final equation produced by the model given in Table 5-9.

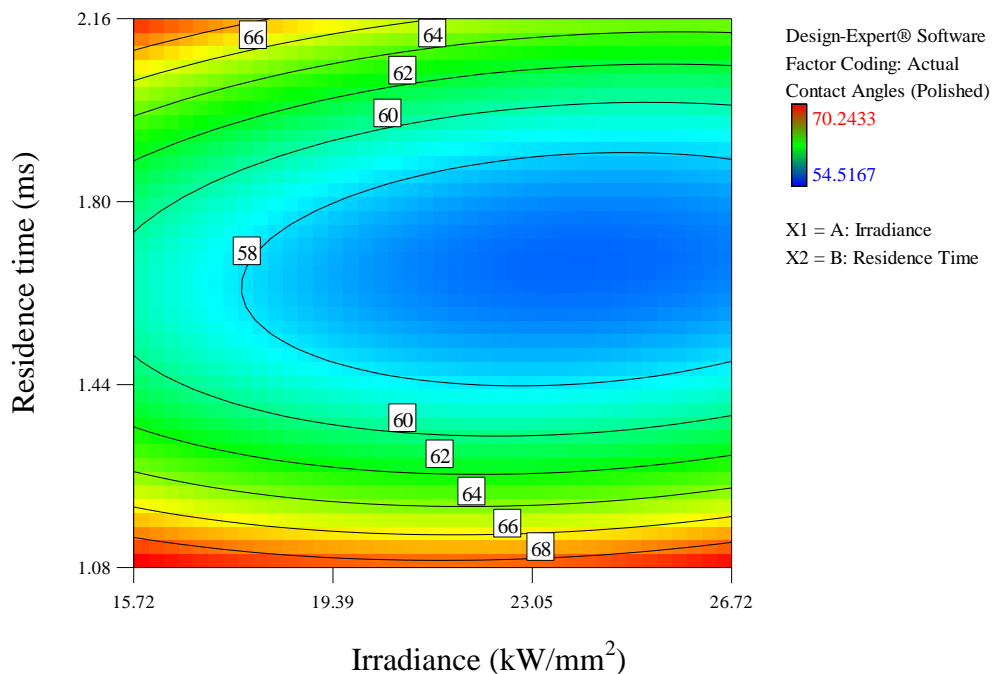


Figure 5-57: Effects of contact angle Irradiance and residence time on contact angles of polished samples.

Table 5-9: Analysis for variance (ANOVA) table for contact angles of polished samples - quadratic model

Source	Sum of Squares	Mean Square	F Value	p-value
Model	269.037	53.807	15.867	0.0228
A-Irradiance	11.454	11.454	3.377	0.1634
B-Residence Time	9.685	9.685	2.856	0.1896
AB	7.049	7.049	2.078	0.2450
A ²	5.137	5.137	1.515	0.3061
B ²	235.710	235.710	69.509	0.0036
Residual	10.173	3.391		
Cor Total	279.210			
		<i>Final equation obtained from the model:</i>		
R-Squared	0.963	<i>Contact Angle (polished) =</i> <i>+171.80192</i> <i>- 1.77578 × Irradiance</i> <i>-113.4916 × Residence Time</i> <i>-0.44697 × Irradiance × Residence Time</i> <i>+0.052987 × Irradiance²</i> <i>+37.22946 × Residence Time²</i>		
Adj R-Squared	0.902			
Pred R-Squared	0.701			
Adeq Precision	9.243			

Order of factor influence on contact angles can be established through analysis of the F-values magnitude as follows: B²>>A>B>AB>A². The final equation in terms of the coded factor further confirms the influence of the factors, see Equation (23).

$$\begin{aligned}
 \text{Contact angle (polished)} & \quad (23) \\
 & = 56.46 - 1.38A - 1.27B - 1.33AB + 1.6A^2 + 10.86B^2
 \end{aligned}$$

5.9 Biocompatibility

5.9.1 Cell Attachment and Metabolic Activity

Figure 5-58 demonstrates the percentage cell attachment of each group with the error bars indicating the standard deviation between groups. One way ANOVA showed that there was no significant difference in cell attachment. This is due to large variation between several groups, illustrated by the error bars in Figure 5-58.

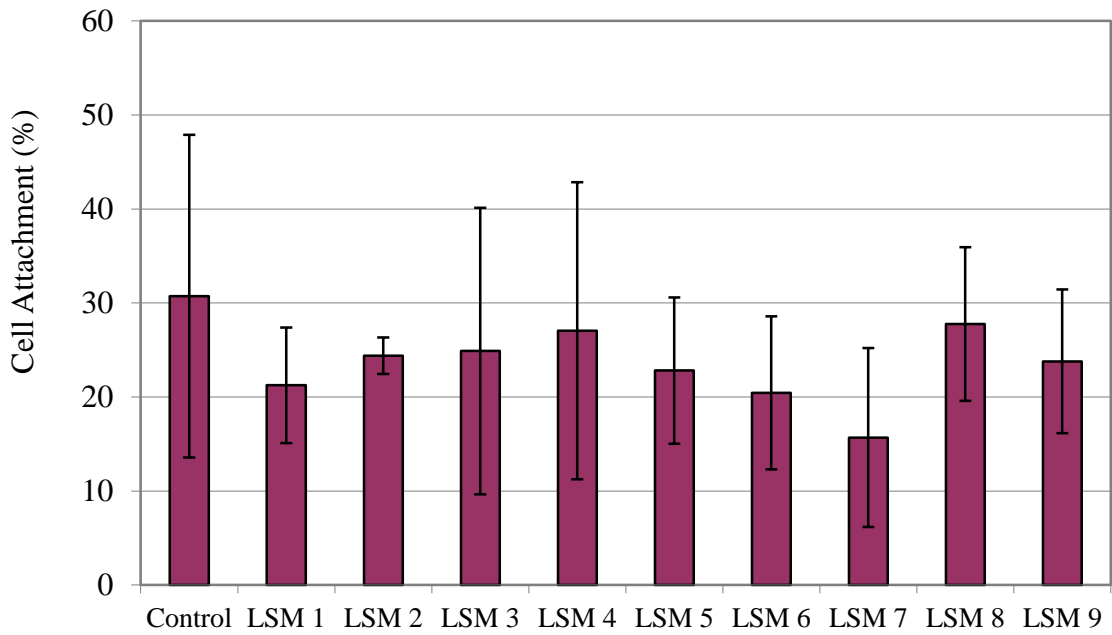


Figure 5-58: Cellular attachment at 2 hours shown as a percentage of the number of cells originally seeded.

Figure 5-59 shows the relationship between cell attachment and measured contact angles. The graph shows that cell attachment percentage generally decreased with an increase in measured contact angles.

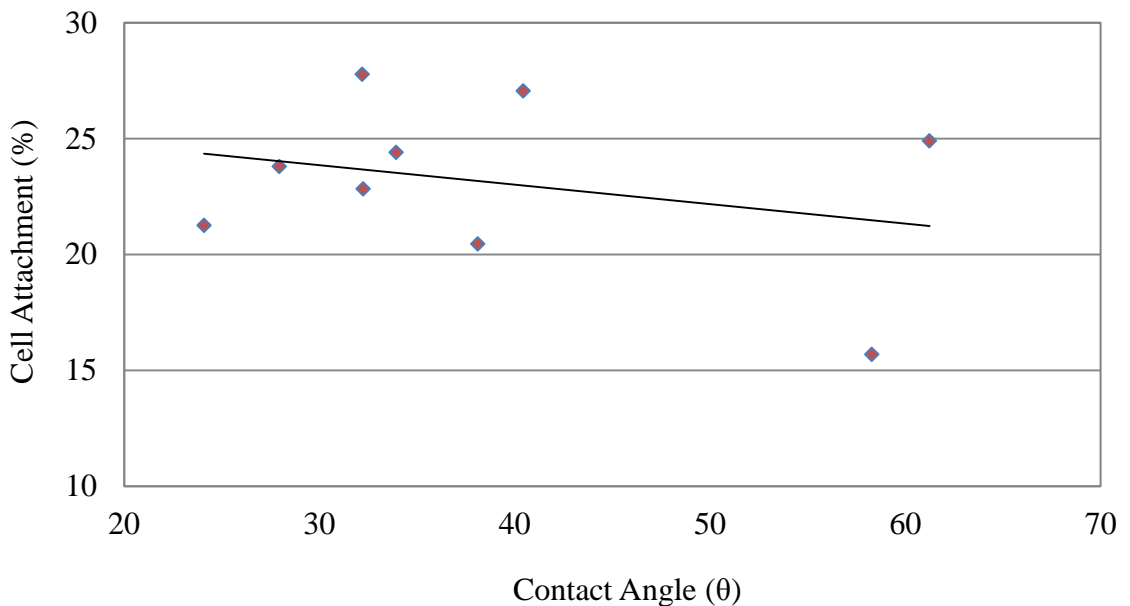


Figure 5-59: Relationship between contact angle of unpolished LSM samples and cell attachment

However, roughness did not have any effects on cell attachment percentage. Figure 5-60 demonstrates that cell attachment is independent of roughness values.

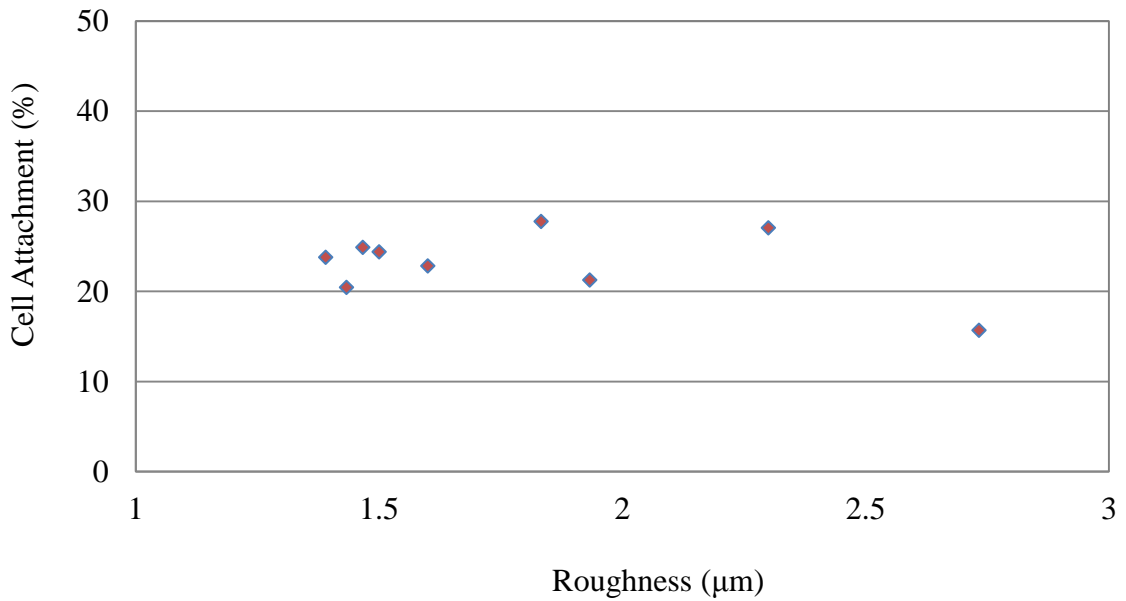


Figure 5-60: Effects of roughness on cell attachment

Figure 5-61 demonstrates the varying levels of proliferation for different samples. One way ANOVA for each set of data demonstrates that there is no significant difference between cell proliferation on laser treated samples.

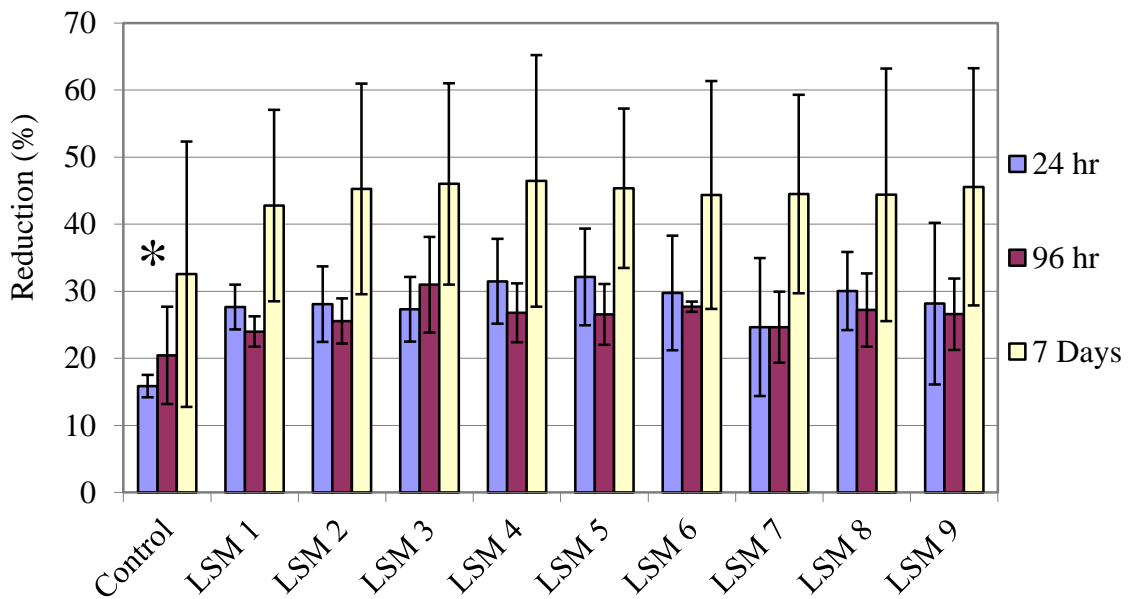


Figure 5-61: Metabolic activity at 24 hr, 96 hr, and 7 days * (p<0.05).

However, the difference between the control (untreated sample) and the laser treated samples was significant (P<0.05). This demonstrates that there was more cell metabolic activity on the laser treated samples and less on the untreated control Ti-6Al-4V samples. Further t-tests showed that there was a significant difference between the untreated control and the treated samples at all-time points, see Figure 5-62.

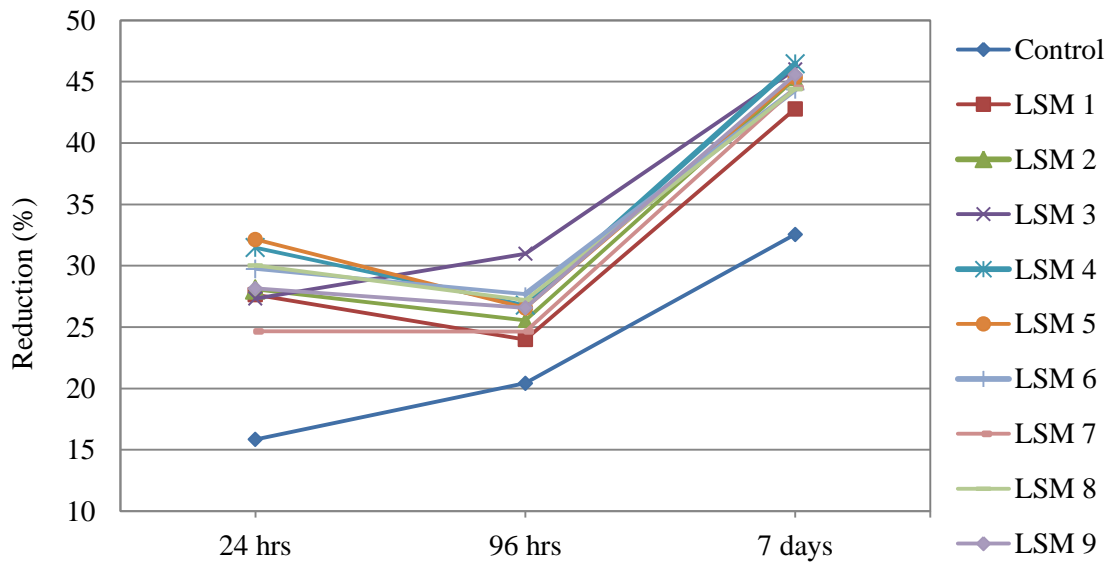


Figure 5-62: Metabolic activity shown as percent reduction.

Figure 5-63 shows the differences in cell number on day 3 and day 7. One way ANOVA for day 3 and day 7 showed that the difference between cell number was not significantly different on day 3, while cell number was significantly higher for all treated samples compared to the untreated controls on day 7 ($p < 0.1$). The difference between the treated samples themselves on day 7 was not significant.

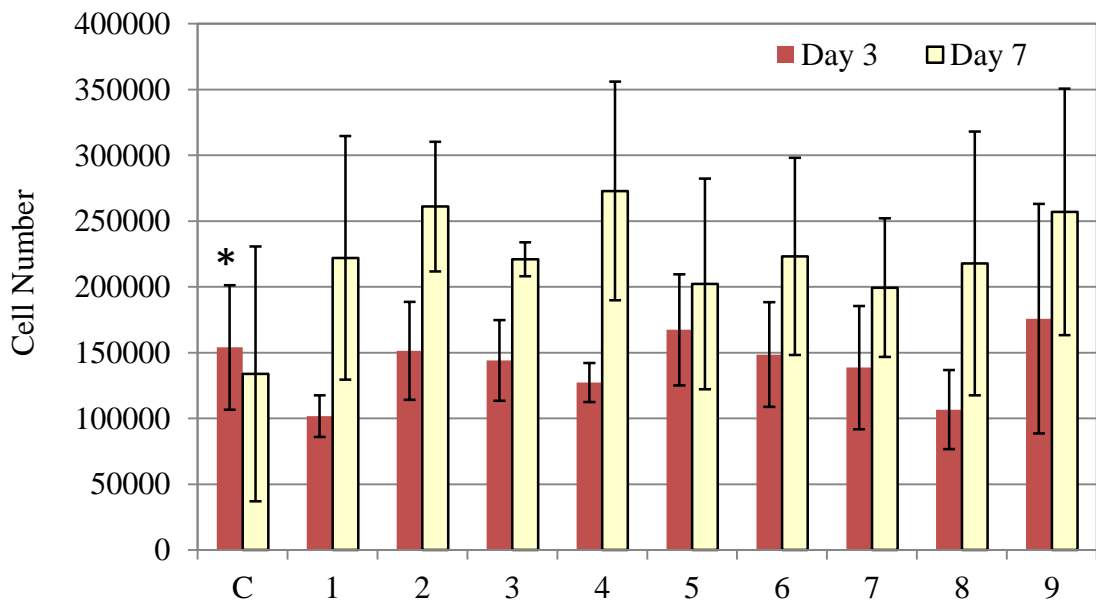


Figure 5-63: Cell number as measured on day 3 and day 7 * ($p < 0.1$).

5.9.2 Cytotoxicity

Direct contact

The results for the MTT viability assessment of NIH/3T3 fibroblast cells following 24 hour exposure to Ti-6Al-4V samples are shown in Figure 5-64. Each column is the mean of three separate experiments where $n = 3 \pm \text{SEM}$, (* denotes a significant difference from the control $* = p < 0.05$). A high degree of reproducibility was achieved as indicated by the relatively small error bars. In general, all samples produced a significant decrease in viability. Samples 6-9 showed a slight but significant ($p < 0.05$) inhibition of formazan production while the untreated sample, reduced the viability values below 50% at 24 h exposure. The results clearly indicate that the treatment (laser) had an impact on the cytotoxic potential of the tested samples. In contrast to results obtained from untreated samples, treated samples showed only slight cytotoxic behaviour.

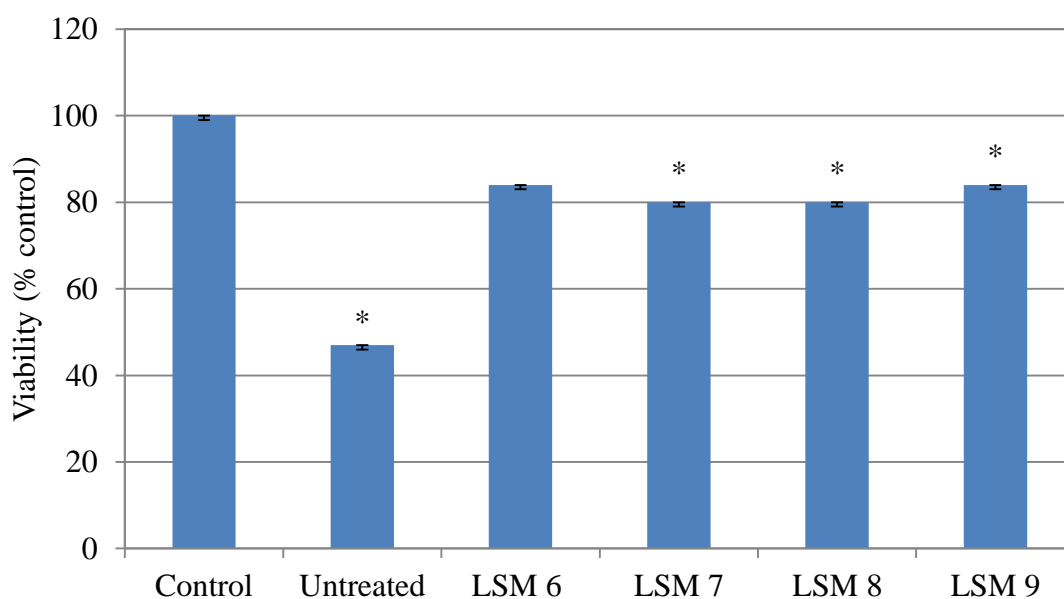


Figure 5-64: Effect of Ti-6Al-4V samples in direct contact with NIH/3T3 fibroblasts for 24 hr using the MTT cell viability assay as a measure of toxicity.

Leachate/Elusion test

Figure 5-65 shows the effect of various concentrations of untreated and laser melted Ti-6Al-4V samples in contact with NIH/3T3 fibroblasts for 24 hr using the MTT cell viability assay as a measure of toxicity. Each data point is the mean of three separate experiments where $n = 18 \pm \text{SEM}$, (* denotes a significant difference from the control $* = p < 0.05$).

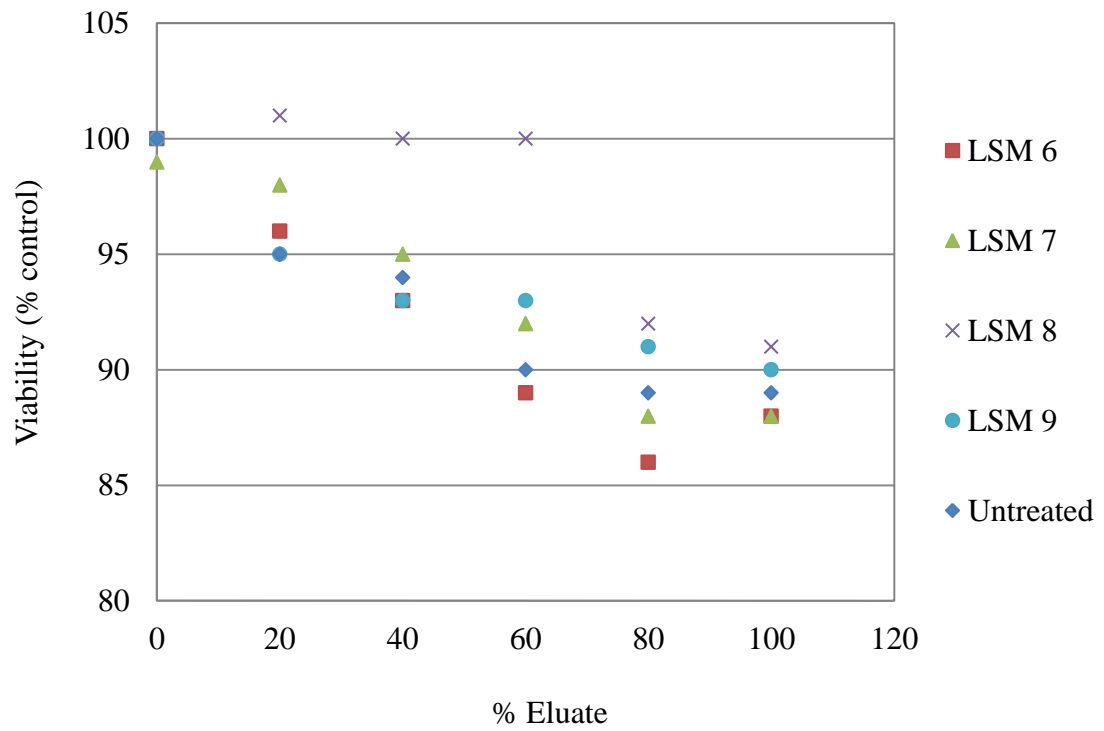


Figure 5-65: Effect of various concentrations of Ti-6Al-4V sample extract in contact with NIH/3T3 fibroblasts for 24 hr using the MTT cell viability assay as a measure of toxicity.

Chapter 6

Discussion: Ti-Al-4V

6.1 Metallography Analysis

6.1.1 Surface Melting and Morphological Features

Laser surface melting produced a typical melting morphology with no voids, inclusions, pits or cracks. Exclusion of such asperities was crucial to establish a consistent and analogous laser treatment of the samples. This also suggested that a non-contaminated laser melting could be achieved at these processing conditions. Processing parameters used in this study were carefully chosen so that energy densities do not exceed levels that induce ablation of surface material. *Appendix J* highlights preliminary tests where high energy densities were implemented resulting in material ejection from the surface. From the preliminary studies, it was established that energy densities greater than 67 J/mm^2 resulted in ablation. At this energy level sample sparking while laser processing began to occur.

The BSE topographic micrographs from the final DOE (Figure 5-2 to Figure 5-10) showed no evidence of ablation of the surface. Lack of ejected material or channel-like features in the BSE images can be evidenced as absence of ablation on the surface. Instead, the surface is melted and rapidly solidifies due to high speed processing. Roughness and ripple-like features visible on the surface of the treated zone is evidence that the material reached a liquid phase. A schematic representation of the formation of the rippling effect is shown in Figure 6-1.

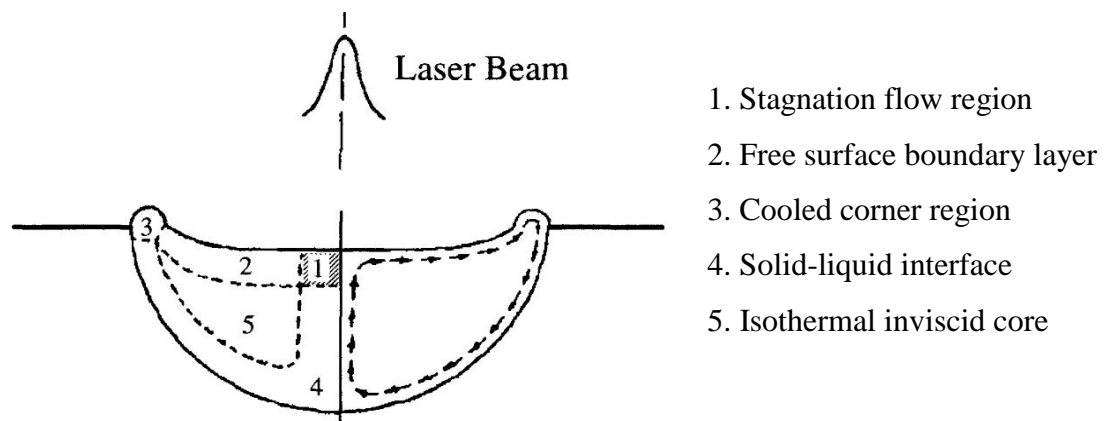


Figure 6-1: Schematic of the laser melted pool perpendicular to the direction of laser beam movement [97].

When the surface is laser melted an immediate depression is formed directly underneath the beam due to liquid movement. Absorbed energy by the surface is altered by the alteration in focal distance and the newly formed liquid phase. This lead to a uniform distribution of surface temperature and altered the driving force. When the depression diminished the reverse occurred thus causing the cyclic nature made obvious in the ripples characterising laser melting.

The width of the tracks, deduced from the ripple-like features, is representative of the laser beam spot size of 90 μm . However, the set overlap of 30% is inadvertently larger, construed to be approximately 50% in all the treated samples. The beam is skewed towards the direction of the linear displacement therefore resulting in a slightly higher overlap than the set 30%. Another effect of this phenomenon can be due to the Gaussian nature of the laser beam and the beam quality of TEM_{00} . TEM Gaussian beam drops from the centre forming a bell shaped curve, resembling a normal distribution. The effects of the beam effect can be demonstrated by Figure 6-2. Diameter of such laser beam qualities is defined by the distance at which the irradiance is $1/e^2$ of the maximum peak irradiance, as illustrated by Figure 6-2 [234]. This means that only 86.5% of the total laser beam power lies within this region since $1/e^2$ is 0.135. The remainder of this energy outside this point is regarded as insignificant to impact the material thus resulting in the reduced overlap percentage.

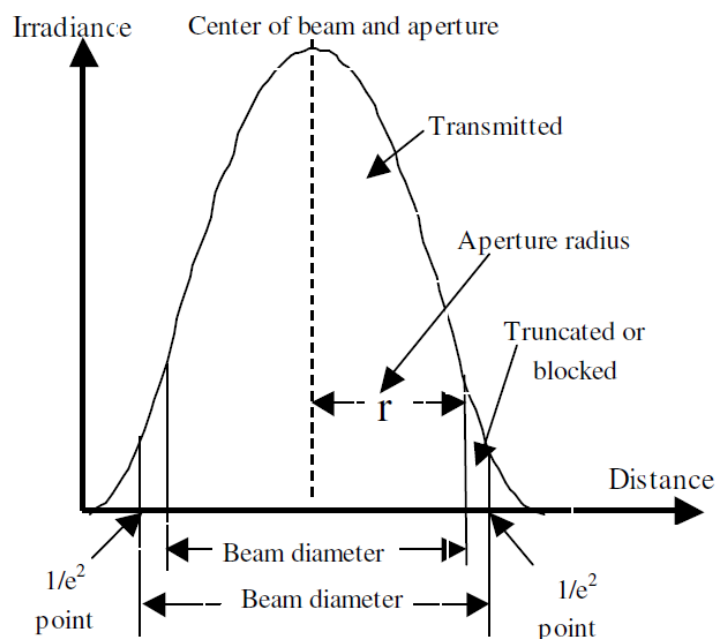


Figure 6-2: Irradiance of the TEM mode as a function of distance across the laser beam [234].

The dimensions of grains observed on the laser processed surface tend to increase with increase in irradiance. This behaviour is related to the low cooling rates induced by high power densities. When the surface is treated at high power density, a much larger instantaneous maximum temperature could be attained thus producing a larger molten volume which took longer to cool therefore produced larger grain sizes compared to samples treated at low power densities. The instantaneous maximum temperature could be calculated using thermal heat energy Equation (9) [16].

6.1.2 Cross-sectional microstructure

Laser treatment transformed the regular lamellar $\alpha+\beta$ phase of Ti-6Al-4V into one that consists of acicular α structures. The transformation resulted in a martensite structure that is significantly different from the substrate. The unetched modified region is brighter than the substrate under an optical microscope and when etched the true nature of the transformation is demonstrated again in Figure 6-3.

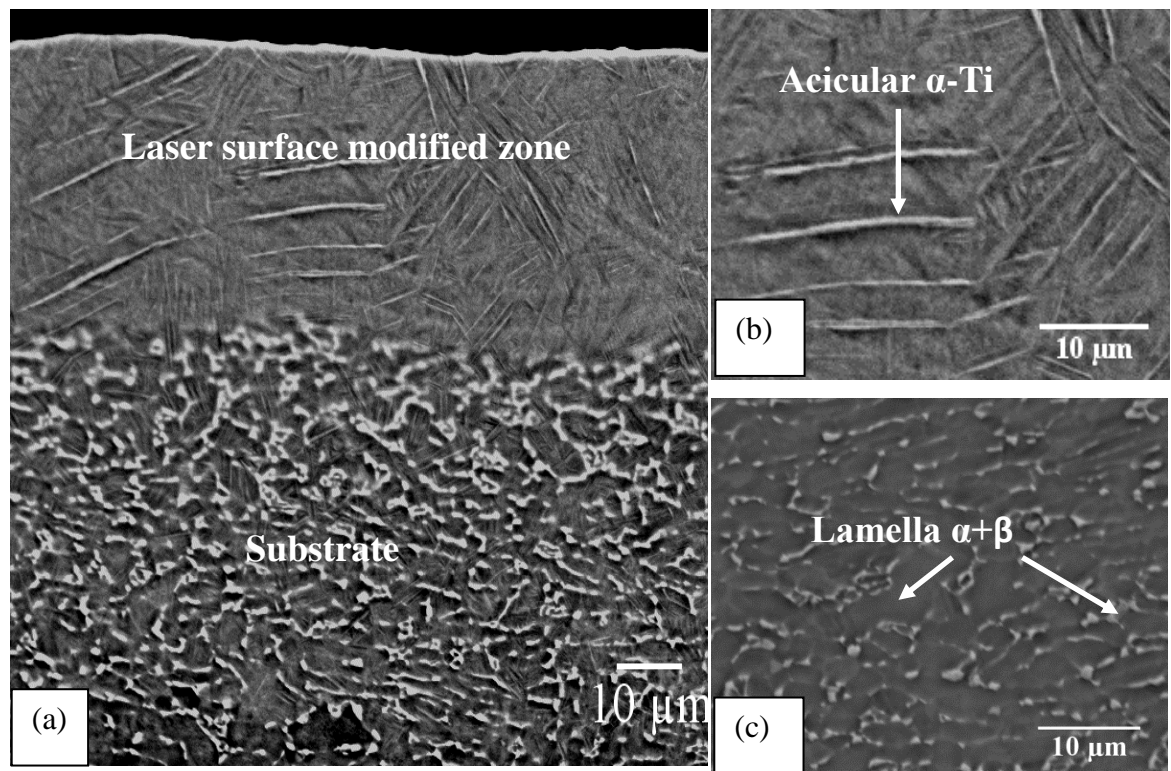


Figure 6-3: (a) Cross sectional BSE micrograph of laser modified Ti-6Al-4V, (b) laser modified layer and (c) substrate microstructure.

Unlike other surface modification techniques that have three distinct regions: modified region, heat affected zone and the bulk alloy; this type of laser treatment does not show a discernible heat affected zone which is prevalent in other laser treatment processes in literature [169]. Formation of this structure was due to the rapid solidification which

thwarted the segregation of the various alloying elements into high and low concentration. Another advantageous trait from the newly formed surface compared to other studies in literature is the absence of cracks [195]. The exclusion of cracks and the lack of a heat affected zone, from the experimental conditions examined in this work, indicate a surface modification technique that can be successfully applied and is well adjacent to the bulk metal. Crack elimination is attributed to the high speed processing, low residence times and corresponding assist gas parameters. These processing characteristics ensure minimal thermal stress is exerted on the surface thus avoiding crack development. Excellent bonding was observed in the modified layers processed in this work which is typical of laser surface processing [169].

6.2 Meltpool Depth Analysis

Meltpool depth is crucial in contact components since the depth of the modified layer is related to the lifetime of the component. Homogeneous, deep and well bonded surface treatments are the optimal requirements for bio-implants. Etching the surface revealed that laser surface modification varied between 20 and 50 μm . BSE micrographs were qualitatively used to analyse meltpool depths. The qualitative analyses showed an increase in depth at higher irradiance and residence times. The cross sectional analysis showed a smoother surface finish on the surface treated at high irradiance compared to those treated at lower irradiances which were rather wavy. This effect is due to thorough melting regime and ideal power densities matching the prescribed overlap. At low irradiance, the beam profile becomes more perceptible in the microstructure. High irradiances resulted in a more homogenous meltpool depth much superior to the meltpool depth produced at low irradiances. Homogeneous treated meltpool depths are preferred in most surface engineering applications. A homogeneous meltpool depth is desirable in bioimplants since uniformity of mechanical properties is attained throughout the implant. This eliminates preferential damages of weak (low depth) points on the newly modified surface. Uniformity in meltpool depths created at high irradiance and residence times are also attributed to thorough melting regime phenomenon.

Figure 5-9 and Figure 5-10 also highlights that there is no significant change in depth of processing between samples irradiated at 20.4 and 26.72 kW/mm^2 ; this is due to insignificant difference in energy densities, 22 and 29 J/mm^2 respectively. However, the significance can be easily demonstrated for samples treated at irradiances of 15.72 and 26.72 kW/mm^2 as seen in Figure 5-11; this is due to a higher difference in energy density. The effect of energy density on meltpool depth is further illustrated by Figure 6-4. The meltpool profile not only depends on energy density but also on the laser beam profile used which was TEM_{00} (Gaussian), thermal conductivity, microstructure, absorption mechanisms and convection of the liquid phase meltpool. Energy density absorbed by the alloy controls the melt pool depth and thus the volume of the molten alloy [152].

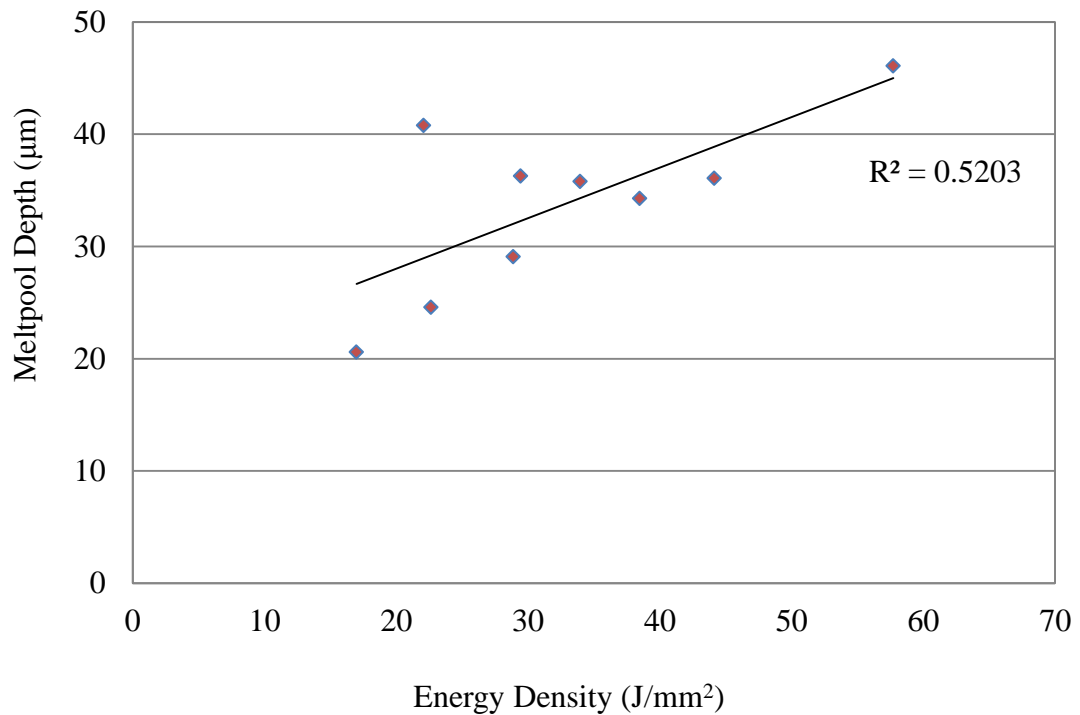


Figure 6-4: Effects of energy density on meltpool depth.

As the irradiance increased, a more homogeneous meltpool depth with fewer discontinuities was observed. However, lower meltpool depths (between 20 and 50 µm) were obtained in this experiment compared to other laser surface modification studies [16, 169]. Lower meltpool depths are attributed to extremely low exposure time used in these experiments. Lower meltpool depths can be advantageous due to their corresponding lower induced thermal stress thus eliminating formation of cracks on the surface.

6.3 Roughness Analysis

Function of bioimplants greatly depends on the surface rugosity. Roughness of laser surface modified layers has received very little attention in literature mainly due to the fact that various applications require machining of the surface before service. The bearing component of the hip implant require polishing (i.e. to reduce friction) while the stem require rougher surfaces (i.e. greater than 3 µm, for improved cell adhesion). It is therefore vital that the resulting roughness can be predicted prior to surface engineering. A combination of low residence time and low irradiance produced the highest roughness due to a more unevenly melted surface produced by the lower energy density. Note that the energy density is the product of irradiance and residence time. Figure 6-5

shows a power regression line highlighting the relationship between roughness and energy density.

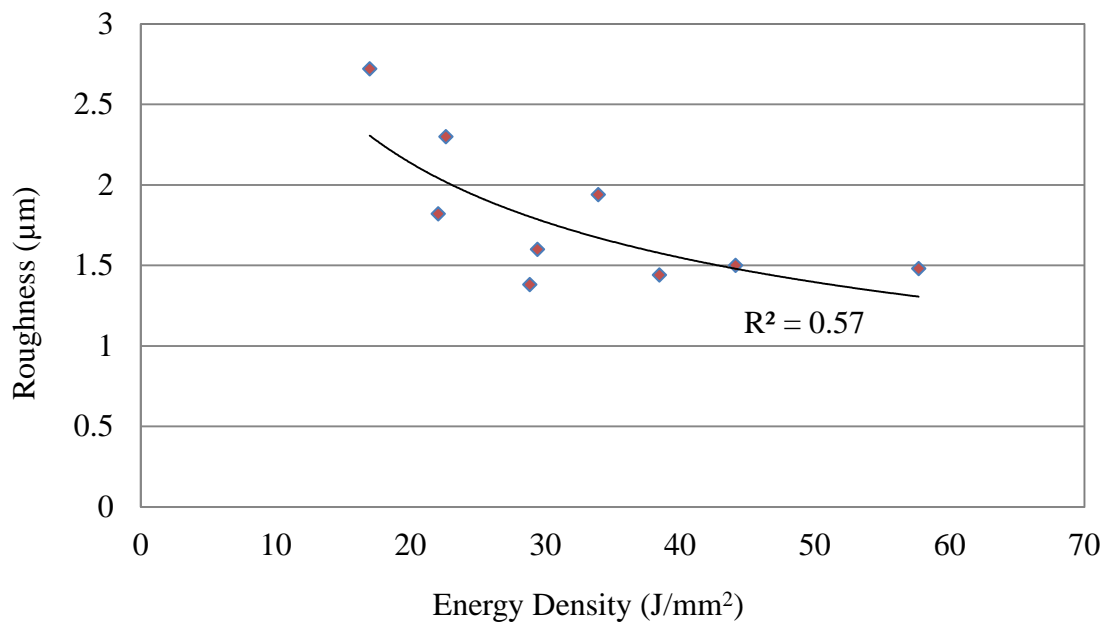


Figure 6-5: Relationship between energy density and roughness.

Effects of irradiance and residence time on surface roughness inferred from Figure 5-2 to Figure 5-4 and Figure 5-14 suggest improved homogeneity and smoothness of the surface with an increase in both irradiance and residence time. However, it should strongly be noted that this analogy applies to this collection of processing parameters, where melting occurs without necessitating ablation. Once ablation initiates, at energy densities over 67 J/mm^2 , an increase in entropy occurs forcing the smooth nature of the surface to collapse. Preliminary experimental design studies found that a further increase in irradiance ($>26.72 \text{ kW/mm}^2$) at high residence times ($>2.16 \text{ ms}$) would result in ablation thus an associated rise in roughness, see *Appendix J*. At lower energy densities that facilitate melting; the smooth surface is replaced by waviness of partially melted regions. The processing parameters used in this study were fully optimised to take advantage of the region where the Ti-6Al-4V “just melts (flux)” thus aiding extremely rapid solidification rates. The decrease in roughness is mainly attributed to a more homogenous melting produced at high irradiance thus producing smoother surfaces. Roughness variation thus depends on energy density. In this experiment an energy density of approximately 29 J/mm^2 (samples 9) produced preeminent homogeneity with the lowest roughness. Development of ridges/ripples, explained in section 6.1.1, is the another cause of roughness evolution in laser surface modified

regions. The waviness observed in low energy density samples is a function of the convectional flow of the melt influenced by the percentage overlap [173].

6.4 Microhardness

Hardness of the material plays a crucial role in the overall wear resistance of the material. Ti-6Al-4V among biomedical alloys is known to have relatively low hardness. By determining the effects which processing parameters have on hardness a process map can be developed in order to predict outcome hardness after laser treatment and also to aid future researchers. All laser melted samples produced hardness values greater than the untreated samples. Increase of hardness in laser treated samples is attributed to microstructure refinement, which is depended on the thermal gradient developed and extremely high cooling rates. Thermal gradient controls the extent of plastic deformation and cooling rates controls the nature and extent of non-equilibrium phases, acicular martensite formation [163]. The fine, acicular martensite has a hexagonal closed packed structure and possesses a high hardness but relatively low ductility and toughness [184, 185].

The highest microhardness was obtained at the highest level of irradiance (26.72 kW/mm^2) and the lowest residence time (1.08 ms). The combination of these parameters gave optimal conditions for hardness improvement since irradiance increases target temperature producing steeper gradients. Similarly low irradiance times (high scanning rates) increase cooling rate thus encouraging transformation into the non-equilibrium phase produced. Hardness relationship with processing parameters obtained in this study is in good agreement with studies in literature [163]. However, the absolute microhardness values recorded cannot be compared to all literature results due to variation in load and loading times implemented. Increase in hardness at low residence time can also be related to the low grain sizes observed in topography images in section 5.1.1. This explanation is in accordance to the Hall-Petch theory which relates increase of hardness and yield strength to reduced grain size [194].

An analysis of hardness distribution with increase in distance from the surface revealed a relatively uniform hardness within the treated region which rapidly reduced at the treated-substrate interface. Uniformly high hardness levels throughout the laser modified region iterate the superiority of the modified regions compared to the bulk alloy. High hardness and uniformity of the modified layer is crucial in biomedical Ti-6Al-4V alloys as it has a significant influence on wear resistance properties [152, 192].

Improved hardness can therefore be beneficial on the femoral head (bearing region) of the hip prosthesis.

6.5 Phase Transformation and Chemical Analysis

6.5.1 X-ray Diffraction Analysis

Backscatter images of the laser treated surfaces provided an ideal starting point for further phase microanalysis by highlighting presence of two phases. The micrographs visually presented the alternating laths of α and β phase present in as-received Ti-6Al-4V. Presence of such phases was confirmed by the XRD patterns obtained using the X-ray diffractometer. The relative volume fraction of β -Ti was lower than that of α -Ti. The characterised Ti-6Al-4V alloy consisted of 28% β phase and the remaining 72% was the α phase. Subsequent to laser processing, the α -Ti phase was transformed into an acicular structure. The microstructure of the treated Ti-6Al-4V revealed that the transformed acicular α -Ti was nested within the aged β matrix. Figure 6-6 is used to properly demonstrate the microstructure and phase transformation within the alloy. Laser treatment also resulted in detection of a new peak, at 29.4° , not observed in untreated samples. The peak is believed to have been induced by phase transformation of the surface. This peak in essence represents the articular phase induced within the martensite structure.

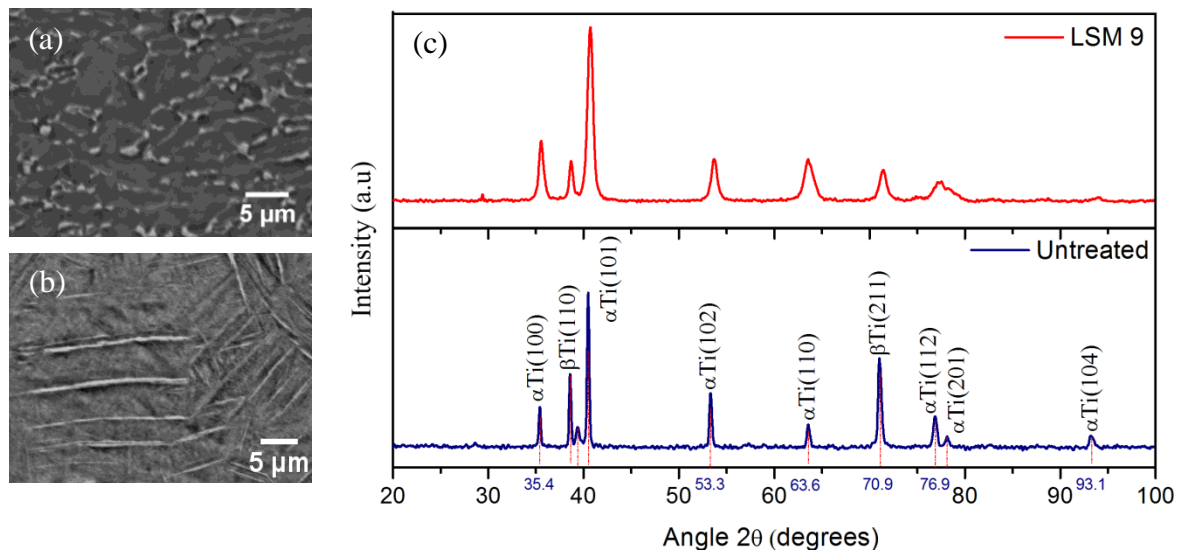


Figure 6-6: BSE microstructural images of (a) untreated and (b) laser treated Ti-6Al-4V; and (c) x-ray diffraction pattern of untreated and laser treated Ti-6Al-4V.

A reduction in volume fraction of β -Ti up to 19% following laser melting was measured. Reduction in volume fraction of β -Ti phase can also be related to the energy density. Figure 6-7 demonstrates that β -Ti volume fraction tends to diminish as the

energy density increases. A dotted line representing the volume fraction of untreated sample was imposed on the data to highlight the reduction of the phase within treated samples. Acicular martensite structure also enhances the materials wear and corrosion resistance.

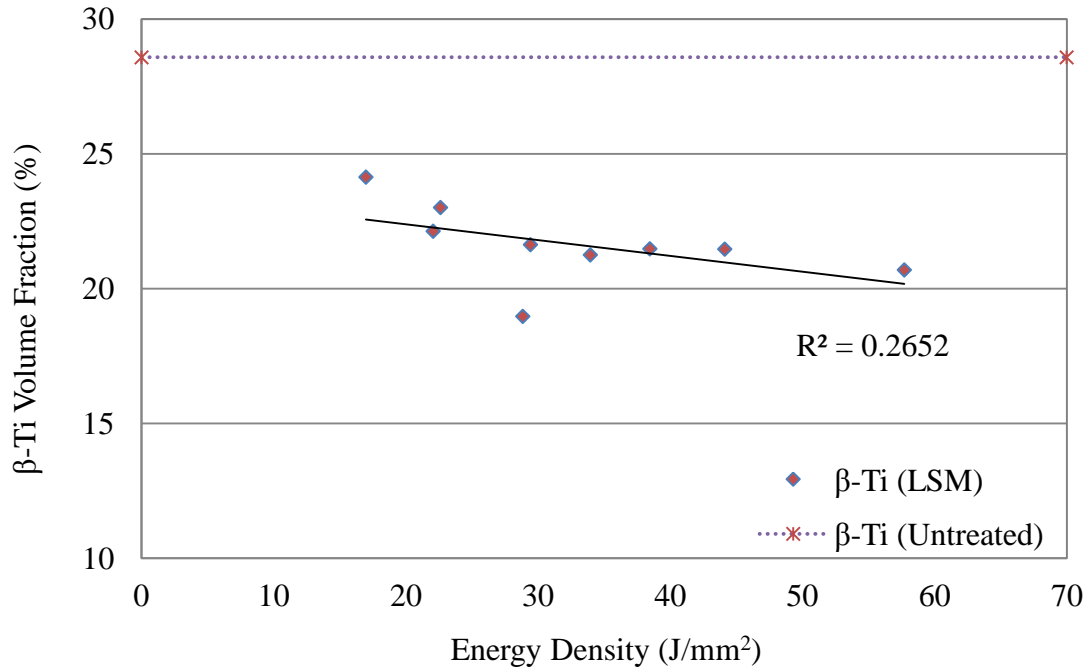


Figure 6-7: Effects of energy density on the volume fraction of the β -Ti phase.

The phase structure transformation from the typical $\alpha + \beta$ structure into a fine martensite structure was due to the low residence times used in the experiments which resulted in high cooling rates. Such high cooling rates force formation of different composition phases but allow very little time for diffusion to produce those phases' equilibrium compositions [184]. A decrease in β phase in the microstructure is known to improve corrosion properties since pitting attacks mainly target the β phase [71]. The volume fraction of the phases is depended on the laser treatment cooling rates. Samples treated at the lowest residence time of 1.08 ms exhibited the lowest β -Ti due to relatively higher cooling rates. The reduction of volume fraction of β -Ti following melting is also attributed to the stabilisation of acicular martensite in the structure during rapid quenching [17]. When the extreme cooling rates were utilised, the microstructure that was single β phase transformed to α phase either by nucleation and growth or α' martensite, which has a HCP crystal structure [71].

The shift in diffraction peaks to a new 2θ position within the laser treated samples, in Figure 6-6 (c), depicts a uniform microstrain within the structure [235]. Laser treatment of Ti-6Al-4V induced uniform strain generated over relatively large distances, thus

changing the lattice plane spacings in the constituent grains from a stress free value to a new value corresponding to the magnitude of stress applied. Micro-strain is induced within the melted zone of the surface treated Ti-6Al-4V samples mainly due to a very high thermal gradient developed and the related quench stress built thereafter.

6.5.2 Chemical Composition

The two types of scans, area and grid, used for chemical composition analysis produced similar results. This highlighted that the topographic chemical composition was homogeneous. Uniform distribution of chemical elements was also observed on the cross-sectional analysis of laser modified samples. Uniform element distribution in the modified region could be due to high speed of convection stream providing intensive stirring of the elements inside the molten pool as well as the high cooling rates prohibiting sufficient time for elemental diffusion and segregation typical under slower cooling conditions. Re-distribution of alloying elements within the treated titanium alloys is also known to improve pitting corrosion resistance due to preferential corrosion attack prevention [130].

6.6 Wear Resistance

A linear relationship, $R^2=0.9966$, between depth wear tracks and distance travelled by the pin suggest good repeatability thus suggesting accurate predictions of wear depth to be derived from known sliding distances. There was no correlation between laser processing parameters and specific wear rates for samples wear tested for 150 m. This was due to the high depth of wear tracks which infringed the substrate and in some cases completely wore the laser modified region. This meant part of substrate material was included in the analysis of specific wear rate thus there was no relationship between processing parameters and specific wear rate. The ratio of the worn substrate and laser modified region was different for all samples and this further impacted the statistical significance. Results from samples tested for 20 m provided an improved insight of the effects of laser processing parameters on specific wear rate. An improved wear rate was achieved by LSM samples. The lowest irradiance (15.72 kW/mm^2) and residence time (1.08 ms) produced the most improved wear rate. Reduction in wear rate of treated samples is attributed to phase transformation inducing martensite microstructure, improved hardness properties and alteration of electrochemical responses of the material. Samples treated with the minimal residence time and irradiance produced highest cooling rates associated with the transformation thus resulting in the lowest wear rates. For the processing parameters used in this study, energy density greatly influence the resultant specific wear rates. Figure 6-8 shows a good relationship between specific wear rate and energy density. Specific wear rate increased with increased energy density. The highest energy density of 57.7 J/mm^2 produced the highest wear rate of $654 \times 10^{-6} \text{ mm}^3/\text{N}\cdot\text{m}$.

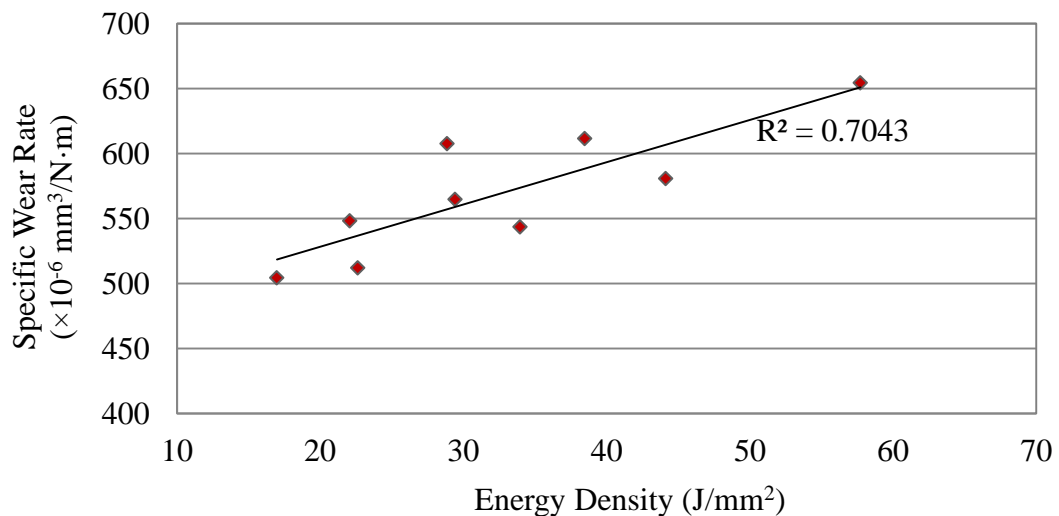


Figure 6-8: Effects of energy density on specific wear rate.

Evidence of both abrasive and adhesion wear mechanisms were visible in untreated samples. Abrasive wear produced micro-cutting features visible on the floor of the wear tracks. Smearing of wear particles on the bottom surface of the wear track was extensive in untreated samples. Higher mass losses observed in untreated samples could also be attributed to micro-fragmentation of the particles adhering to the surface from subsequent sliding of the pin. Micro-cracking is believed to assist the fragmentation allowing for wieldier disintegration. Micro-cracking develops due to thermal and corrosion fatigue brought about by frictional forces of the zirconia pin and the Ti-6Al-4V sample [16]. The evidence from the SEM images also suggests a form of scuffing wear that is associated with local solid-state welding between rubbing surfaces. Scuffing occurs when the boundary lubricant films breakdown due to high friction generated by the rubbing surfaces. Other studies have also attributed features found in untreated wear tracks to be due mild tribochemical wear during sliding caused by tribooxidation and chemical reactions between Ti-6Al-4V, Zirconia and the physiological solution [236-239]. The continuous wear process constantly exposes a fresh surface thus accelerating the tribochemical reactions [239].

Plastic deformation of worn particles was not observed in LSM samples; where abrasive micro-cutting was the prominent wear mechanism. LSM samples produced a smoother and shiny worn track where grooves and scratches were clearly seen. The surface of worn tracks of LSM samples appear to be polished compared to the untreated counterparts. The aforementioned characteristics of the worn tracks are due to a harder surface created during rapid quenching of the laser modified surfaces. LSM samples show high resistance to scuffing due to a tenacious boundary lubricant film formed on the surface. The formed film is crucial in maintaining a stable boundary in the contacting area, conferring to low friction. Laser surface melting effectively results in low adhesion between contacting surfaces thus reducing frictional forces and wear [240].

6.7 Corrosion Resistance

The open circuit measurement produced a steady increase in potential with time. This indicates that there was steady growth of TiO_2 passive films on the surface of the samples, known as spontaneous passivity, and as expected according to the Ti-H₂O Pourbaix diagram [241]. The thickness of the spontaneously formed protective oxide on the surface at open circuit conditions is expected to be within the range of 1 to 4 nm for a buffered aqueous solution at 23°C [242]. Okazaki *et al.* and Ask *et al.* have previously noted from chemical composition analysis of the oxide films formed on Ti-6Al-4V that they are predominantly composed of TiO_2 (rutile) containing small amounts of TiO and Ti_2O_3 near the metal-oxide interface [243, 244].

Untreated Ti-6Al-4V alloys had lower current densities at low potential scans. However at high potentials, displayed in Figure 6-9, the as-received samples do not reach stable passivity and therefore the current density continues to rise with increase in potential and converge with LSM samples at 1000 mV_{SCE}.

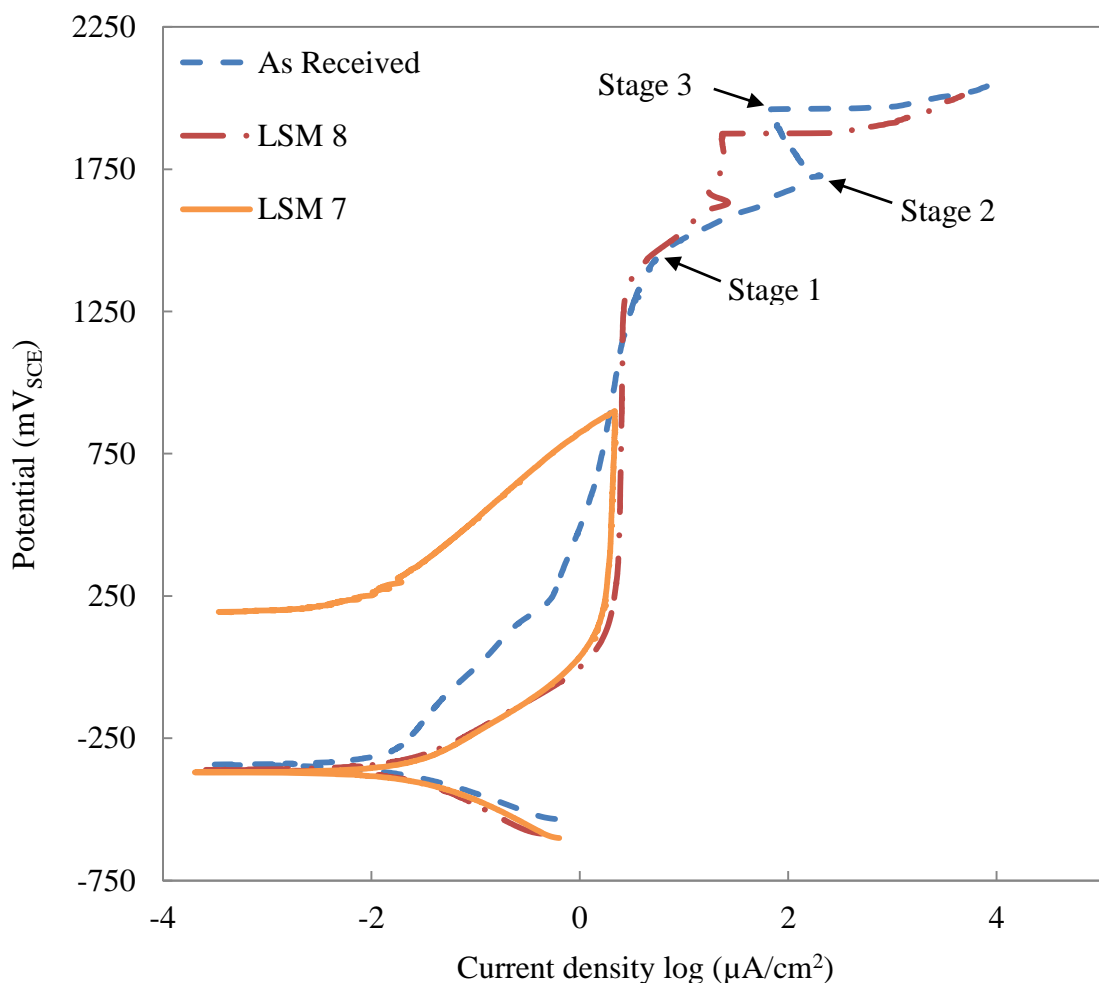


Figure 6-9: Polarisation curves of as-received, LSM 7 and LSM 8 Ti-6Al-4V in 0.9% NaCl at 37°C.

These characteristics displayed by the potentiodynamic scans reveals that the LSM samples have more stable passivity and continue to maintain a constant protective film with increase in potential. LSM samples resemble highly passive corrosive behaviour found in pure Titanium [87]. In Figure 6-9, the potential for LSM 7 was increased up to only 1000 mV_{SCE} and then swept back to illustrate the influence that termination potential have on electrochemical behaviour. When the potential was reversed at 1000 mV_{SCE} before reaching the breakdown potential, a high repassivation potential is noted showing that the protective passive film remains. At the potential upscan of 1350 mV_{SCE} and 1460 mV_{SCE} (breakdown potential, E_b), a transition occurs for both LSM and untreated samples. The transition invokes three separate stages, a rapid increase in current density (stage 1) followed by a decrease (stage 2) then another increase (stage 3) initiates and remains high for the rest of the scan. The transition is caused by the crystallisation and/or formation of new phases from the existing amorphous TiO₂ which slows the localised corrosion until at higher potentials [245]. Stage 2 could indicate some kind of salt film deposition which slows the localised corrosion until at higher potentials, where it accelerates markedly. Stage 3 transition behaviour signifies localised corrosion.

The lower Tafel slopes (i.e. higher current density rate) in the LSM samples is attributed to rougher surfaces in compared to untreated samples. This subsequently results in a thinner oxide films in these samples due to the slower formation of the oxide film on the laser treated surfaces or the formation of TiO₂ and Ti₂O₃ [246, 247]. At 130 mV (1.5 μA/cm²) and 340 mV (2.8 μA/cm²) the current density reaches a steady state for LSM 7 and LSM 4 respectively. This passive current density is higher than that normally reported for titanium polarised in saline solutions, but this is connected with the higher scan rates used in this study compared to potentiostatic or slow scan rates of 0.167mVs normally employed [87]. For potentials beyond these points, the current densities recorded are associated with steady passive films already formed on the LSM samples. On the other hand, the passive films can be seen (lower slope values) to be still forming on the untreated samples at these higher potentials. The stable current densities for the LSM samples indicate that the stable oxide layer prevents further current density increases for increased potential. All samples showed similar response on the reverse sweep. As the potential decreased there was a marked decrease in current until a new steady state formed around 250 mV_{SCE}. The reverse sweep anodic Tafel slopes are similar to those in the forward sweep direction, indicative of the same activation controlled oxidation process.

The lowest corrosion rate of 86 nm/yr was found in the laser surface modified sample. An increase in irradiance produced a decrease in corrosion rates at the lowest residence time of 1.08 ms. LSM samples had a more compact and stable passive film compared to the untreated sample. The difference behaviour between the polarisation curves is mainly attributed to the change in microstructure instigated by rapid melting and solidification of the laser melted region in LSM samples and its effect on the passive film formed on the alloy's surface. Thus the three main factors that contributed to the change in corrosion behaviour for LSM samples are: the martensite structure formation, β Ti phase reduction and homogeneity in elemental chemical composition.

Calculation of current density was done using sample geometric area without taking into account the rugosity on the surface. Therefore, high corrosion rates in some laser treated samples are due to slightly higher roughness in LSM sample.

6.8 Surface Wettability Analysis

Contact angle analysis plays a crucial part in cell adhesion in bio-implants [248]. Hydrophilicity means the fluid can wet the surface corresponding to higher surface adhesion. All laser treated samples exhibited lower contact angles (hydrophilic) compared to untreated sample thus suggesting improved cell adhesion and proliferation properties. Wetting characteristics also influence the interaction characteristics of the treated surfaces with the corrosive species [249]. The main factors that affect the wetting characteristics of a surface are its composition, the content of oxygen, the surface morphology, surface energy and the temperature [250]. However, laser surface treatment by melting does not significantly change the composition and oxygen content, compared with the untreated surface thus roughness becomes the main factor influencing wetting properties (contact angles). The results agree to numerous publications that detail the effects of roughness on wetting characteristics [251-253].

6.8.1 Effects of roughness on contact angle

Figure 6-10 graphs the relationship between contact angles and roughness. A second order polynomial with a R^2 value of 0.416 was achieved. This initial result hints infers that the relationship between the two responses is present but not significant. However when the outlier is ignored the R^2 value becomes 0.8415, see Figure 6-11. This indicates that roughness influence the resultant contact angles.

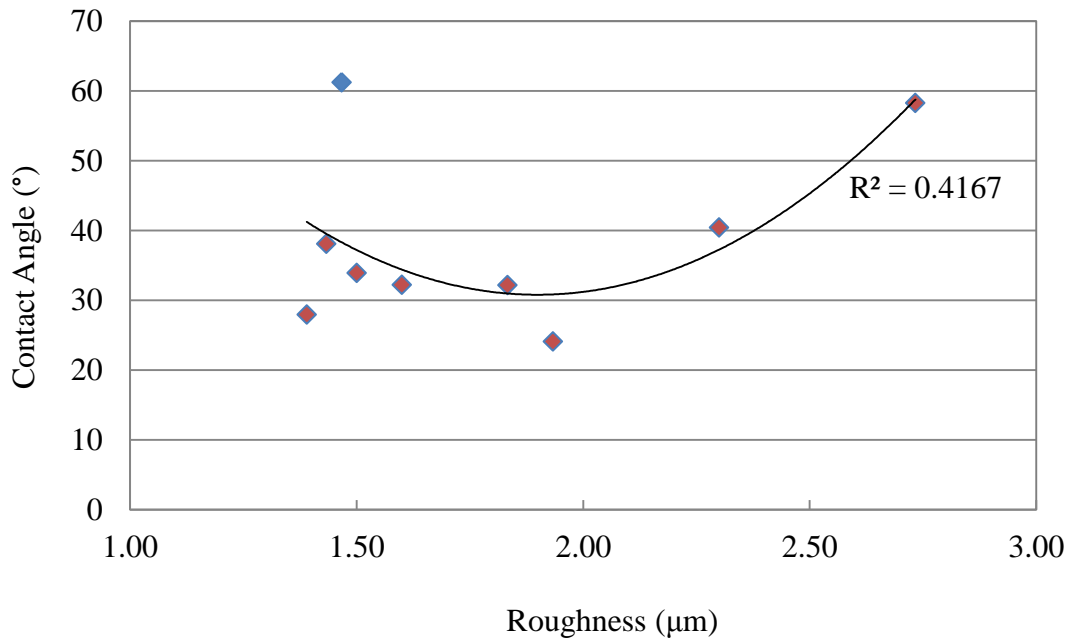


Figure 6-10: Relationship between contact angle and roughness of the LSM samples.

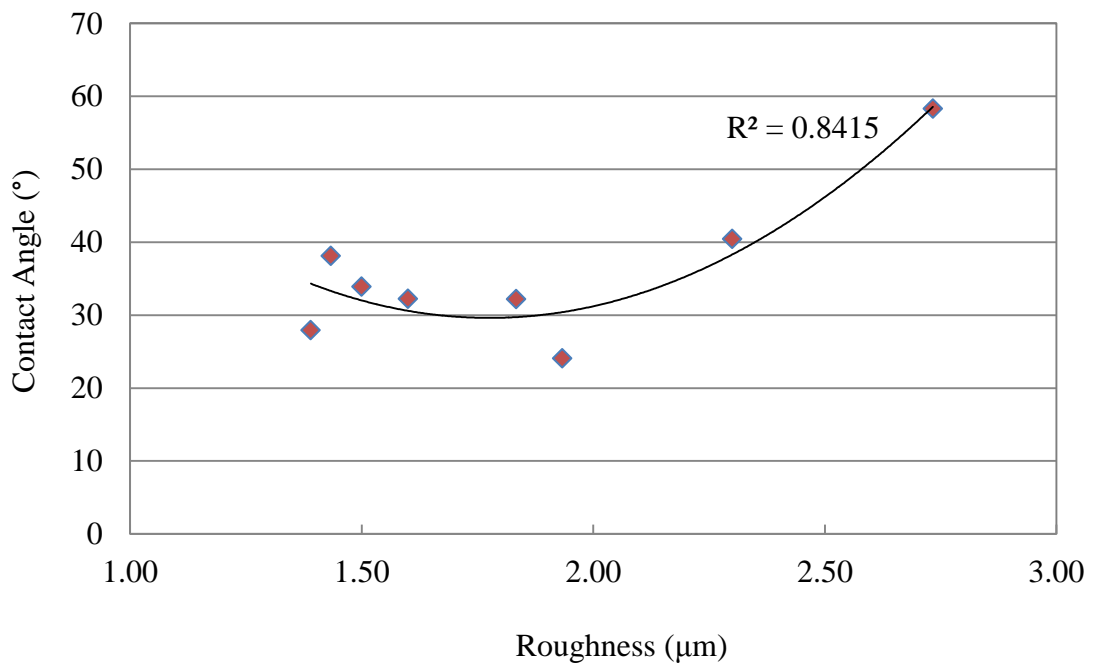


Figure 6-11: Relationship between contact angle and roughness without the outlier.

The effects of processing parameters on contact angles, independent of roughness, were further explored by polishing laser surface modified sample. Polishing was carried out using 1200 grit SiC paper, with water as a lubricant. Figure 6-12 shows the contact angles of unpolished and polished laser surface modified samples. All polished samples produced higher average contact angles ($64.7 \pm 1.9^{\circ}$) compared to the unpolished samples

($38.7\pm 3.5^\circ$). However, the contact angles are still relatively low compared to the polished as received sample. The lowest contact angle recorded was $54.5\pm 1.4^\circ$ obtained at a mid-range energy density of 29.4 J/mm^2 . Contact angles of all polished samples showed relatively low deviation from the mean value thus suggesting more homogenous contact angle values in polished laser surface modified samples. The relatively non uniformity of the wetting characteristics of unpolished LSM samples is due to the inhomogeneous morphology produced by laser surface modification.

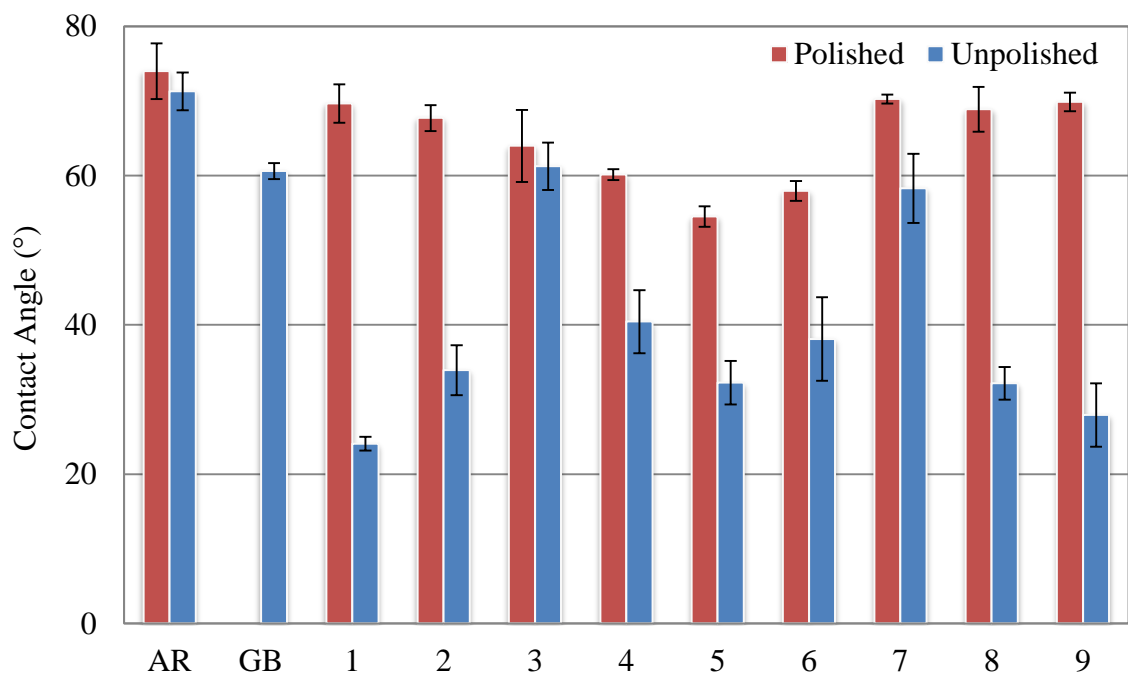


Figure 6-12: Contact angles of polished and unpolished samples, where AR is as-received, GB is grit blasted and 1-9 are laser modified samples.

6.9 Biocompatibility

There was no difference in initial cell attachment between the samples. Laser surface melting did not adversely affect the initial cell attachment. The roughness difference in previous publications that showed differences in cell attachment were much larger, which may explain the lack of a significant difference between cell attachment of relatively similar roughness values [254]. The surface area of the samples, which was constant across all the samples, may have restricted the number of cells that can attach to the surface (approximately 30%). The cells, unable to have contact with the surface of the sample, were possibly subsequently washed away when media was added. Metabolic activity was significantly higher for all the treated samples compared to the untreated controls at all time points. However, there was not a significant difference

between the treated samples. This may have been due to the narrow range of R_a values of the treated samples (1.32-2.72 μm). At this range the roughness may be high enough that the cells grow in roughly the same manner on the surface. The higher metabolic activity may be due to the higher bioactivity of the treated surfaces [90].

There was no significant difference in cell number at day 3, but there were higher numbers of cells at day 7 for all treated samples compared to the untreated controls. At day 3, the slight differences in surface properties may not have led to significantly different rates of cell mitosis, but metabolic activity was higher. The difference in both cell number and metabolism is shown on day 7, where both cell metabolism and cell number were significantly higher. Cell number increased at a higher rate for treated samples, and this was visible at day 7. As the differences between the properties of the treated samples are not large enough to show significant differences in cell metabolism and proliferation, further studies may need to be performed to evaluate cell metabolism and proliferation over a longer time frame (i.e. greater than 7 days).

Direct contact analysis showed improved cytotoxicity behaviour in laser treated sample compared to the untreated ones. Elusion test results showed that all samples produced a dose dependant decrease in viability. High extract concentrations resulted in up to 20% inhibition of formazan production while low concentrations exerted only slight cytotoxic behaviour. Overall the viability of the NIH/3T3 monolayer did not significantly vary from the untreated control monolayer indicating that minimal loss of viability following treatment with extracts prepared from samples 6-8. On the other hand, the highest tested concentration of extracts obtained from sample 9 and untreated samples induced a slight but significant ($p < 0.05$) loss in cell viability which became more pronounced with an increase in concentration indicating the presence of leachates. The results from the biocompatibility analysis are encouraging, showing that laser melted Ti-6Al-4V can potentially be used for bioimplants.

Chapter 7

Conclusions

7.1 316 Stainless steel

High speed laser surface melting was successfully achieved for 316L stainless steel. The novel processing parameters used in the research (Irradiance up to 235 kW/mm² and residence times as low as 50 μs) produced extremely high cooling rates and high thermal gradients capable of eliminating asperities, cracks and inclusions within the treated region. The research successfully process mapped the melting regimes induced by high speed laser processing. In DOE 1, at low energy densities of 5.24 J/mm², localised melting became visible. Low depth of processing was observed with no physical change in grain structure detected. Medium energy density of 10.48 J/mm² produced uniform melting on the surface. In this case, melt pool depth reached approximately 60 μm with visible overlapping induced by increased melting areas larger than the laser spot size and the rotational nature of the laser treatment process. High levels of energy density, exceeding 20.96 J/mm² were characteristic of high melt pool depths (up to 130 μm) and also evidence of ablation became visible on the surface. At such high energy density transformation of the microstructure grain size and orientation and was observed, however this transformation did not impact chemical composition, crystallinity and hardness significantly. On the other hand, a clear correlation between the process parameters (irradiance and residence time) and melt pool depth and surface roughness was noted. As these input parameters were increased, both melt pool depth and roughness increased in a linear fashion.

A similar level of influence of these input parameters on the melt pool depth and surface roughness was found. In particular within DOE 1, going from the low level of irradiance (79 kW/mm²) to the high level (246 kW/mm²) at 100 μs residence time resulted in a 52 μm increase in melt pool depth and a 10.5 μm increase in surface roughness. The lowest roughness from this DOE was noted at 1 μm for a irradiance of 79 kW/mm² and a residence time of 50 μs. Further studies using the surface temperature prediction model for 316L stainless steel revealed that this can be used to aid prediction of the energy density required to melt the surface of the steel.

In DOE 2, at fixed energy densities melt pool depth was largely influenced by surface pre-treatment conditions, irradiance and residence time. An average increase in melt

pool depth of 40 μm was noted from increasing residence time from the lowest (50 μs) to the highest level (167 μs). Etching of the surface prior to laser treatment produced the least effect on melt-pool depth, while machining produced the most pronounced effect. Depth increases of 34, 38 and 43 μm were noted for increased irradiance from the highest level to the lowest level (from 63 to 220 kW/mm^2) for the as received, machined and machined and etched surfaces respectively. At fixed energy densities, the highest melt-pool depth (91 μm) was achieved for machined+etched surfaces laser melted at lowest irradiance (63 kW/mm^2) and highest residence time (167 μs). From this analysis on laser processing of 316L, it is clear that at fixed energy density, that a combination of low to mid levels of irradiance (such as 63, 79 and 127 kW/mm^2) and low to mid levels of residence time (such as 50 μs , 67 and 83 μs) could produce the sought combination of homogeneous melting regime with moderate melt-pool depth (10 to 51 μm) and low roughness (1 to 2.79 μm).

The main contribution of the research study on 316L stainless steel for biomedical applications was creation of a process map that could be used to determine surface properties (i.e. roughness and melt-pool depth) through variation of irradiance and residence time.

7.2 Ti-6Al-4V

High speed laser melting was implemented on Ti-6Al-4V in an inert argon environment which resulted in a well bonded 20 to 50 μm melt-pool free of cracks, inclusion, voids and surface asperities. BSE micrographs and XRD results confirmed that the typical $\alpha+\beta$ microstructure in Ti-6Al-4V was transformed into a martensite structure characterised by acicular α embedded in the β matrix due to high cooling rates experienced. Melt-pool depth was found to increase with increase in both irradiance and residence time. The study found that the resulting melt-pool depth can be estimated from energy density with reasonable accuracy. Higher irradiance levels were found to provide for a more uniform depth of processing which reached a maximum of 50 μm . The high speed laser treatment resulted in an average roughness ranging from 1.39 to 2.73 μm . Roughness in laser melting was influenced by the beam profile and ripple effects due to convection and absorption mechanism of the molten metal. A relationship between irradiance and residence time for roughness was observed, whereby roughness decreased with an increase in irradiance and residence time, see Figure 5-14. Roughness characteristics were closely related to the melting energy density.

X-Ray diffraction results demonstrated an increase of α phase and corresponding decrease of the β Ti phase in Ti-6Al-4V subsequent to laser treatment. The analysis showed that the lowest beta phase was achieved at the lowest residence time and highest irradiance. This point resembles the highest cooling rates and steepest cooling gradients due to extreme nature of residence time and irradiance. Topographic and cross-sectional EDS analysis revealed homogeneous elemental composition in all laser treated samples due to redistribution of elements as a result of rapid solidification. This phenomenon is widely regarded as beneficial as it eliminates preferential corrosion attacks.

Unlike 316L stainless steel, microhardness examination revealed improved microhardness in all laser treated Ti-6Al-4V. Highest irradiance (26.7kW/mm^2) and the lowest residence time (1.08 ms) resulted in a 67% increase in microhardness (767 HV) compared to the untreated region (459 HV). The associated low residence time and rapid cooling rates allowed for novel and apparently useful wear and corrosion properties to be achieved. Laser surface modified samples showed improved wear characteristics compared to untreated samples. Within the laser surface modified samples, low irradiance (15.7 kW/mm^2) and residence time (1.08 ms) produced the least specific wear rate of $504 \times 10^{-6}\text{ mm}^3/\text{N}\cdot\text{m}$. Specific wear rate increased with increase in both irradiance and residence time. A strong relationship between energy density and specific wear rate was observed, whereby specific wear rate increased with increases in energy density. Both adhesive and abrasion wear mechanisms were driving forces in material removal from the untreated samples. Micro-cracking, micro-fragmentation and scuffing were all features involved in mass loss of untreated samples. Laser modified samples showed smoother wear tracks with no evidence of plastically deformed debris embedded on the wear track surfaces as was apparent for the untreated samples. Microstructure transformation from the typical $\alpha+\beta$ Ti-6Al-4V to improved martensite structure due to rapid quenching induced by high speed laser melting which explains the improved wear characteristics noted.

Electrochemical polarisation tests revealed different oxide films formed on the untreated and LSM samples. LSM samples had a more compact and stable passive film compared to the untreated sample. A three stage transition was observed starting at breakdown potential for untreated and LSM samples. The transition indicated crystallisation and/or formation of new phases from amorphous TiO_2 and a salt film deposition which slows the localised corrosion until at higher potentials. The lowest corrosion rate according to comparison of Tafel slopes, which was observed at the lowest irradiance (15.72 kW/mm^2) and lowest residence time (1.08 ms) was found to be 86 nm/yr. An increase in

irradiance produced a decrease in corrosion rates at the lowest residence time of 1.08 ms. Pitting was observed in both untreated and laser modified samples with a more uniform pitting occurring in the treated regions.

High speed laser melting produced hydrophilic surfaces compared to the untreated samples. Contact angles as low as 23° was measured on the laser treated sample, compared to 72° on the untreated sample. The lowest contact angles (23°) were found at the mid energy density (30 J/mm^2). Contact angle was found to be independent of irradiance but strongly dependent on residence time in a non-linear fashion, see Figure 5-56. Roughness was also found to effect wettability in a non-linear fashion. The unpolished laser treated sample produced lower contact angles compared to their polished counterparts. There was no significant difference in cell attachment and metabolic activity between untreated and laser treated samples. Direct contact tests showed improved cytotoxicity in laser modified samples. The results proved that the high speed laser treatments used in this work can potentially be used for bioimplants application. This work established that Ti-6Al-4V could be successfully treated by high speed laser for surface modification. The laser treatments resulted in an improved asperity free surface with a martensitic microstructure which contained reduced β -Ti phase. These treatments were shown to be capable of producing improvements in micro-hardness, chemical composition, surface wettability, biocompatibility, wear and corrosion resistance which are all beneficial factors for biomedical implants.

7.3 Future Work

Further detailed advanced characterisation of the surface could be carried out to study the microstructure transformation process during laser surface modification and its effects on biocompatibility properties. Such characterisation techniques that could be used include nano-indentation, transmission electron microscopy, electrochemical impedance spectroscopy, and *in vivo* biocompatibility testing. Future work should also study high speed laser processing of biomedical alloys for the possibility of achieving semi-crystalline, quasi-crystalline or even an amorphous microstructure. Amorphous structures are known to have excellent wear and corrosion properties. Such a structure could potentially be achieved by cryogenic laser surface treatment. A system could be devised that simultaneously laser melts the surface while enabling rapidly quenching to create such an amorphous layer on the surface. Another crucial area that could be studied is development of polishing techniques that could be used to produce the required surface finish of approximately 25 nm for hip replacement bearings.

References

- [1] M. Long and H. J. Rack, Titanium Alloys in Total Joint Replacement - A Materials Science Perspective, *Biomaterials*, **19** (18), pp. 1621-1639, 1998.
Available: [http://dx.doi.org/10.1016/S0142-9612\(97\)00146-4](http://dx.doi.org/10.1016/S0142-9612(97)00146-4).
- [2] B. Basu, D. S. Katti and A. Kumar, *Advanced Biomaterials: Fundamentals, Processing, and Applications*, Wiley-American Ceramic Society, 2009.
- [3] S. Kurtz, K. Ong, E. Lau, F. Mowat and M. Halpern, Projections of Primary and Revision Hip and Knee Arthroplasty in the United States from 2005 to 2030, *The Journal of Bone and Joint Surgery American Volume*, **89** (4), pp. 780-785, 2007.
- [4] Wrong Diagnosis Website, Statistics by Country for Hip Replacement, 2010
Accessed (3/3/2010)
Available: http://www.wrongdiagnosis.com/h/hip_replacement/stats-country.htm#extrapwarning.
- [5] Frost and Sullivan Ltd, Orthopedics joint replacement markets, market engineering research, Frost and Sullivan, 9 May 2007.
- [6] Americas Academy of Orthopaedic Surgeons, Joint Revision Surgery, [online]
Accessed (06/05/2011), 2011.
Available: <http://orthoinfo.aaos.org/topic.cfm?topic=A00510>.
- [7] M. Borstlap, J. Zant, M. Soesbergen and J. Korst, Effects of Total Hip Replacement on Quality of Life in Patients with Osteoarthritis and in Patients with Rheumatoid Arthritis, *Clinical Rheumatology*, **13** (1), pp. 45-50, 1994.
- [8] A. S. Edelstein and R. C. Cammarata, *Nanomaterials: Synthesis, Properties and Applications* London: Institute of Physics Publishing, 1998.
- [9] H. Malchau, P. Herberts and L. Ahnfelt, Prognosis of Total Hip Replacement in Sweden: Follow-Up of 92,675 Operations Performed 1978–1990, *Acta Orthop*, **64** (5), pp. 497-506, 1993.
- [10] D. C. Hansen, Metal Corrosion in the Human Body: The Ultimate Bio-corrosion Scenario, *Electrochemical Society Interface*, **17** (2), pp. 24-7, 2008.

- [11] D. W. Hoepfner and V. Chandrasekaran, Fretting in Orthopaedic Implants: A Review, *Wear*, **173** (1-2), pp. 189-197, 1994.
- [12] R. Banerjee and N. Soumya, "Laser processing of orthopedic biomaterials" in *Advanced Biomaterials*, 1st ed., Wiley, 2009, pp. 278.
- [13] S. Hiromoto, Corrosion of Metallic Biomaterials in Cell Culture Environments, *Electrochemical Society Interface*, **17** (2), pp. 41, 2008.
- [14] Zimmer Website, Hip Replacement, 2011 [online] Accessed (23/08/2011).
<http://www.zimmer.com/z/ctl/op/global/action/1/id/8140/template/PC/navid/68/>
- [15] L. Hao, J. Lawrence, Y. F. Phua, K. S. Chian, G. C. Lim and H. Y. Zheng, Enhanced Human Osteoblast Cell Adhesion and Proliferation on 316 LS Stainless Steel by Means of CO₂ Laser Surface Treatment, *Journal of Biomedical Materials Research - Part B Applied Biomaterials*, **73** (1), pp. 148-156, 2005. Available: <http://dx.doi.org/10.1002/jbm.b.30194>.
- [16] R. Singh, A. Kurella and N. B. Dahotre, Laser Surface Modification of Ti-6Al-4V: Wear and Corrosion Characterization in Simulated Biofluid, *Journal of Biomaterials Applications*, **21** (1), pp. 49-73, 2006. Available: <http://dx.doi.org/10.1177/0885328206055998>.
- [17] A. Biswas, L. Li, T. K. Maity, U. K. Chatterjee, B. L. Mordike, I. Manna and J. Dutta Majumdar, Laser Surface Treatment of Ti-6Al-4V for Bio-Implant Application, *Lasers in Engineering*, **17** (1-2), pp. 59-73, 2007.
- [18] T. M. Yue, J. K. Yu, Z. Mei and H. C. Man, Excimer Laser Surface Treatment of Ti-6Al-4V Alloy for Corrosion Resistance Enhancement, *Materials Letters*, **52** (3), pp. 206-212, 2002.
- [19] R. Singh, M. Martin and N. B. Dahotre, Influence of Laser Surface Modification on Corrosion Behavior of Stainless Steel 316L and Ti-6Al-4V in Simulated Biofluid, *Surface Engineering*, **21** (4), pp. 297-306, 2005. Available: <http://dx.doi.org/10.1179/174329405X55320>.
- [20] C. Langlade, A. B. Vannes, J. M. Krafft and J. R. Martin, Surface Modification and Tribological Behaviour of Titanium and Titanium Alloys After YAG-Laser Treatments, *Surface and Coatings Technology*, **100-101** pp. 383-387, 1998.
- [21] R. Singh, S. K. Tiwari, S. K. Mishra and N. B. Dahotre, Electrochemical and Mechanical Behavior of Laser Processed Ti-6Al-4V Surface in Ringer's

Physiological Solution, pp. 1-10, 2011. Available:

<http://dx.doi.org/10.1007/s10856-011-4362-z>.

- [22] E. W. Karlson, L. A. Mandl, G. N. Aweh, O. Sangha, M. H. Liang and F. Grodstein, Total Hip Replacement due to Osteoarthritis: The Importance of Age, Obesity, and Other Modifiable Risk Factors, *The American Journal of Medicine*, **114** (2), pp. 93-98, 2003.
- [23] J. C. Schrama, B. Espehaug, G. Hallan, L. B. Engesaeter, O. Furnes, L. I. Havelin and B. S. Fevang, Risk of Revision for Infection in Primary Total Hip and Knee Arthroplasty in Patients with Rheumatoid Arthritis Compared with Osteoarthritis: A Prospective, Population-Based Study on 108,786 Hip and Knee Joint Arthroplasties from the Norwegian Arthroplasty Register, *Arthritis Care & Research*, **62** (4), pp. 473-479, 2010.
- [24] Hip & Knee Advice Website, Total Hip Replacement, 2011 [online] Accessed (05/08/2010), Available: <http://www.hipandkneeadvice.com/index.php/hip-procedures/hip-replacement/>.
- [25] C. R. Wheelless, J. A. Nunley and J. R. Urbaniak, *Wheelless' Textbook of Orthopaedics*, 2011 [online] Accessed (8/16/2011), Available: <http://www.wheellesonline.com/>
- [26] S. L. Smith, D. Dowson and A. A. J. Goldsmith, The Effect of Femoral Head Diameter upon Lubrication and Wear of Metal-on-Metal Total Hip Replacements, *Proceedings of the Institution of Mechanical Engineers, Part H: Journal of Engineering in Medicine* , **215** (2), pp. 161-170, 2001.
- [27] Z. M. Jin, D. Dowson and J. Fisher, Analysis of Fluid Film Lubrication in Artificial Hip Joint Replacements with Surfaces of High Elastic Modulus, *Proceedings of the Institution of Mechanical Engineers, Part H: Journal of Engineering in Medicine* , **211** (3), pp. 247-256, 1997.
- [28] K. Martin, Unpublished thesis: Development of Pneumatic Percussion Tool for Total Hip Replacement and Quality Control Measures in the Medical Device Industry, Dublin City University, 2011.
- [29] P. A. Dearnley, A Review of Metallic, Ceramic and Surface-Treated Metals used for Bearing Surfaces in Human Joint Replacements, *Proceedings of the Institution of Mechanical Engineers -- Part H -- Journal of Engineering in Medicine* , **213** (2), pp. 107-135, 1999.

- [30] A. Shimmin, P. E. Beaulé and P. Campbell, Metal-on-Metal Hip Resurfacing Arthroplasty, *The Journal of Bone and Joint Surgery*, **90** (3), pp. 637, 2008.
- [31] B. D. Ratner and B. D. Ratner, *Biomaterials Science: An Introduction to Materials in Medicine*, 2004. Available:
http://isbndb.com/d/book/biomaterials_science_a01.
- [32] J. D. Bronzino, *The Biomedical Engineering Handbook* Boca Raton, USA: Boca Raton, FL: CRC Press, 2000.
- [33] K. S. Katti, Biomaterials in Total Joint Replacement, *Colloids and Surfaces B: Biointerfaces*, **39** (3), pp. 133-142, 2004.
- [34] BrownMed Website, Saint Gobain Desmarquest Hip Implant, 2011 [online] (05/08/2011), Available:
http://biomed.brown.edu/Courses/BI108/BI108_2007_Groups/group05/pages/saint_gobain_desmarquest.html.
- [35] W. Suchanek and M. Yoshimura, Processing and Properties of Hydroxyapatite-Based Biomaterials for use as Hard Tissue Replacement Implants, *Journal of Materials Research*, **13** (1), pp. 94-117, 1998.
- [36] A. Kurella and N. B. Dahotre, Review Paper: Surface Modification for Bioimplants: The Role of Laser Surface Engineering, *Journal of Biomaterials Applications*, **20** (1), pp. 5-50, 2005. Available:
<http://dx.doi.org/10.1177/0885328205052974>.
- [37] T. R. Green, J. Fisher, M. Stone, B. M. Wroblewski and E. Ingham, Polyethylene Particles of a 'Critical Size' are Necessary for the Induction of Cytokines by Macrophages in Vitro, *Biomaterials*, **19** (24), pp. 2297-2302, 1998.
- [38] P. Campbell, S. Nasser, N. Kossovsky and H. C. Amstutz, Histopathological Effects of Ultrahigh-Molecular-Weight Polyethylene and Metal Wear Debris in Porous and Cemented Surface Replacements, *Presented at: Symposium on Biocompatibility of Particulate Implant Materials, October 31, 1990 - October 31, 1992*, pp. 38-51.
- [39] J. Cawley, J. E. P. Metcalf, A. H. Jones, T. J. Band and D. S. Skupien, A Tribological Study of Cobalt Chromium Molybdenum Alloys used in Metal-on-Metal Resurfacing Hip Arthroplasty, *Wear*, **255** (7-12), pp. 999-1006, 2003.

- [40] W. Pospula, Total Hip Replacement: Past, Present and Future, *Kuwait Medical Journal*, **36** (4), pp. 250-255, 2004.
- [41] J. L. Tipper, P. J. Firkins, E. Ingham, J. Fisher, M. H. Stone and R. Farrar, Quantitative Analysis of the Wear and Wear Debris from Low and High Carbon Content Cobalt Chrome Alloys used in Metal on Metal Total Hip Replacements, *Journal of Materials Science: Materials in Medicine* , **10** (6), pp. 353-362, 1999. Available: <http://dx.doi.org/10.1023/A:1026473723777>.
- [42] M. P. Staiger, A. M. Pietak, J. Huadmai and G. Dias, Magnesium and its Alloys as Orthopedic Biomaterials: A Review, *Biomaterials*, **27** (9), pp. 1728-1734, 2006.
- [43] Disabled-World Website, DePuy ASR Hip Replacement Recall: 12,000 Patients Will Need Revision Surgery, 2011 [online] Accessed (29/08/2011), Available: <http://www.disabled-world.com/medical/recalls/asr-recall.php>.
- [44] S. Hierholzer, G. Hierholzer and K. H. Saucer, Increased Corrosion of Stainless Steel Implants in Infected Plated Fractures, *Archives of Orthopaedic and Traumatic Surgery* , **102** (3), pp. 198, 1984.
- [45] Pwatlas Website, Micrographs: Low Carbon Steel, 2009 (6/22/2009), Available: <http://pwatlas.mt.umist.ac.uk/internetmicroscope//micrographs/microstructures/low-carbon-steel.html>.
- [46] M. Meier, Heat Treatment of Steel, 2010 [online] (16/02/2010), Available: <http://ocw.kfupm.edu.sa/user062/ME2155355/HT-Steel.pdf>.
- [47] W. D. Callister, *Materials Science and Engineering: An Introduction* 2000, Available: http://isbndb.com/d/book/materials_science_and_engineering_a09.
- [48] M. Diaz, P. Sevilla, A. M. Galan, G. Escolar, E. Engel and F. J. Gil, Evaluation of Ion Release, Cytotoxicity, and Platelet Adhesion of Electrochemical Anodized 316 L Stainless Steel Cardiovascular Stents, *Journal of Biomedical Materials Research - Part B Applied Biomaterials* , **87** (2), pp. 555-561, 2008, Available: <http://dx.doi.org/10.1002/jbm.b.31144>.
- [49] J. C. Wataha, C. T. Hanks and R. G. Craig, The *in Vitro* Effects of Metal Cations on Eukaryotic Cell Metabolism, *Journal of Biomedical Materials Research* , **25** (9), pp. 1133-1149, 1991. Available: <http://dx.doi.org/10.1002/jbm.820250907>.

- [50] T. Hanawa, Metal Ion Release from Metal Implants, pp. 745-752, 2004.
Available: <http://dx.doi.org/10.1016/j.msec.2004.08.018>.
- [51] M. Uo, F. Watari, A. Yokoyama, H. Matsuno and T. Kawasaki, Tissue Reaction Around Metal Implants Observed by X-Ray Scanning Analytical Microscopy, *Biomaterials*, **22** (7), pp. 677-85, 2001. Available:
[http://dx.doi.org/10.1016/S0142-9612\(00\)00230-1](http://dx.doi.org/10.1016/S0142-9612(00)00230-1).
- [52] Efunda Inc., Heat Treatments: Hardening: Diffusion Treatments, 2011 [online]
Accessed (1/16/2010) Available:
http://www.efunda.com/processes/heat_treat/hardening/diffusion.cfm
- [53] S. H. Aldajah, O. O. Ajayi, G. R. Fenske and Z. Xu, Effect of Laser Surface Modifications Tribological Performance of 1080 Carbon Steel, *Journal of Tribology*, **127** (3), pp. 596, 2005.
- [54] J. E. G. González and J. C. Mirza-Rosca, Study of the Corrosion Behavior of Titanium and some of its Alloys for Biomedical and Dental Implant Applications, *Journal of Electroanalytical Chemistry*, **471** (2), pp. 109-115, 1999.
- [55] B. Grosogeat, L. Reclaru, M. Lissac and F. Dalard, Measurement and Evaluation of Galvanic Corrosion between titanium/Ti6Al4V Implants and Dental Alloys by Electrochemical Techniques and Auger Spectrometry, *Biomaterials*, **20** (10), pp. 933-941, 1999. Available:
[http://dx.doi.org/10.1016/S0142-9612\(98\)00248-8](http://dx.doi.org/10.1016/S0142-9612(98)00248-8).
- [56] B. F. Lowenberg, S. Lugowski, M. Chipman and J. E. Davies, ASTM-F86 Passivation Increases Trace Element Release from Ti6Al4V into Culture Medium, *Journal of Materials Science: Materials in Medicine*, **5** (6-7), pp. 467-472, 1994. Available: <http://dx.doi.org/10.1007/BF00058985>.
- [57] P. Schmutz, N. Quach-Vu and I. Gerber, Metallic Medical Implants: Electrochemical Characterization of Corrosion Processes, *Electrochemical Society Interface*, **17** (2), pp. 35-40, 2008.
- [58] E. Eisenbarth, D. Velten, M. Müller, R. Thull and J. Breme, Biocompatibility of β -Stabilizing Elements of Titanium Alloys, *Biomaterials*, **25** (26), pp. 5705-5713, 2004.

- [59] B. Kasemo, Biocompatibility of Titanium Implants: Surface Science Aspects, *The Journal of Prosthetic Dentistry*, **49** (6), pp. 832-837, 1983.
- [60] D. Julka, R. Vasishta and K. Gill, Distribution of Aluminum in Different Brain Regions and Body Organs of Rat, *Biological Trace Element Research*, **52** (2), pp. 181-192, 1996. Available: <http://dx.doi.org/10.1007/BF02789460>.
- [61] J. G. Joshi, Aluminum, a Neurotoxin which Affects Diverse Metabolic Reactions, *Biofactors*, **2** (3), pp. 163-9, 1990.
- [62] J. Scales, Black Staining Around Titanium Alloy Prostheses--an Orthopaedic Enigma, *Journal of Bone and Joint Surgery, British Version*, **73-B** (4), pp. 534-536, 1991.
- [63] C. R. F. Azevedo, Failure Analysis of a Commercially Pure Titanium Plate for Osteosynthesis, *Engineering Failure Analysis*, **10** (2), pp. 153-164, 2003.
- [64] J. Black, H. Sherk, J. Bonini, W. Rostoker, F. Schajowicz and J. Galante, Metallosis Associated with a Stable Titanium-Alloy Femoral Component in Total Hip Replacement. A Case Report, *Journal of Bone and Joint Surgery*, **72** (1), pp. 126-130, 1990.
- [65] J. J. Jacobs, A. K. Skipor, L. M. Patterson, N. J. Hallab, W. G. Paprosky, J. Black and J. O. Galante, Metal Release in Patients Who have had a Primary Total Hip Arthroplasty. A Prospective, Controlled, Longitudinal Study, *Journal of Bone and Joint Surgery*, **80** (10), pp. 1447-58, 1998.
- [66] R. M. Urban, J. L. Gilbert and J. J. Jacobs, Corrosion of Modular Titanium Alloy Stems in Cementless Hip Replacement, *Journal of ASTM International*, **2** (10), pp. 357-366, 2005, Available: <http://dx.doi.org/10.1520/JAI12810>.
- [67] O. Matsumoto, M. Konuma and Y. Kanzaki, Nitriding of Titanium in an r.f. Discharge II: Effect of the Addition of Hydrogen to Nitrogen on Nitriding, *Journal of the Less Common Metals*, **84** pp. 157-163, 1982.
- [68] Calphad website, Titanium-Aluminium Phase Diagram, 2012. [online] Accessed (18/01/2012) Available: <http://www.calphad.com/titanium-aluminum.html>
- [69] H. Baker, "Introduction to alloy phase diagrams" in *ASM Handbook Vol.3: Alloy Phase Diagrams*, 3rd ed., H. Baker and H. Okamoto, Eds. Ohio, USA: ASM International, pp. 1-24, 2001.

- [70] G. Lütjering, G. Lötjering and J. S. Williams, *Titanium*, 2007. Available: http://isbndb.com/d/book/titanium_a05.
- [71] M. Atapour, A. Pilchak, G. S. Frankel, J. C. Williams, M. H. Fathi and M. Shamanian, Corrosion Behavior of Ti-6Al-4V with Different Thermomechanical Treatments and Microstructures, *Corrosion* , **66** (6), pp. 1-9, 2010. Available: <http://link.aip.org/link/?COR/66/065004/1>.
- [72] R. W. Schutz and D. E. Thomas, "Corrosion of titanium and titanium alloys" in *ASM Handbook Volume 13* (9th ed.) Anonymous 2003, Available: http://isbndb.com/d/book/asm_handbook_corrosion.
- [73] D. Brabazon, PhD Thesis: Processing and Properties of Rheocast Alloys, University College Dublin, 2001.
- [74] W. Kurz and D. J. Fisher, *Fundamentals of Solidification* 1998, Available: http://isbndb.com/d/book/fundamentals_of_solidification.
- [75] W. M. Steen, J. Mazumder and K. Watkins, *Laser Material Processing* 2010, Available: http://isbndb.com/d/book/laser_material_processing_a04.
- [76] M. Furukawa, Z. Horita, M. Nemoto, R. Z. Valiev and T. G. Langdon, Microhardness Measurements and the Hall-Petch Relationship in an Al-Mg Alloy with Submicrometer Grain Size, *Acta Materialia* , **44** (11), pp. 4619-4629, 1996.
- [77] G. Giavaresi, L. Ambrosio, G. A. Battiston, U. Casellato, R. Gerbasi, M. Finia, N. Aldini, L. Martini, L. Rimondini and R. Giardino, Histomorphometric, Ultrastructural and Microhardness Evaluation of the Osseointegration of a Nanostructured Titanium Oxide Coating by Metal-Organic Chemical Vapour Deposition: An in Vivo Study, *Biomaterials* , **25** (25), pp. 5583-5591, 2004.
- [78] J. R. Goldberg and J. L. Gilbert, The Electrochemical and Mechanical Behavior of Passivated and TiN/AlN-Coated CoCrMo and Ti6Al4V Alloys, *Biomaterials*, **25** (5), pp. 851-864, 2004.
- [79] H. Güleriyüz and H. Çimenoglu, Effect of Thermal Oxidation on Corrosion and corrosion–wear Behaviour of a Ti–6Al–4V Alloy, *Biomaterials*, **25** (16), pp. 3325-3333, 2004.
- [80] J. D. Majumdar and I. Manna, Laser Processing of Materials, *Sadhana*, **28** (3&4), pp. 11/05/2009-495–562. 2003.

- [81] J. Epinette and M. Manley, *Fifteen Years of Clinical Experience with Hydroxyapatite Coatings in Joint Arthroplasty* 2003. Available: http://isbndb.com/d/book/fifteen_years_of_clinical_experience_with_hydroxyapatite_coa.
- [82] J. de Damborenea, Surface Modification of Metals by High Power Lasers, *Surface and Coatings Technology* , **100-101** pp. 377-382, 1998.
- [83] J. J. JACOBS, J. L. GILBERT and R. M. URBAN, Current Concepts Review - Corrosion of Metal Orthopaedic Implants, *Journal of Bone and Joint Surgery* , **80** (2), pp. 268-82, 1998.
- [84] L. L. Hench and E. C. Ethridge, Biomaterials - the Interfacial Problem, *Advances in Biomedical Engineering* , **5**, pp. 35-150, 1975.
- [85] A. W. E. Hodgson, S. Kurz, S. Virtanen, V. Fervel, C. -. A. Olsson and S. Mischler, Passive and Transpassive Behaviour of CoCrMo in Simulated Biological Solutions, *Electrochimica Acta*, **49** (13), pp. 2167-2178, 2004. Available: <http://dx.doi.org/10.1016/j.electacta.2003.12.043>.
- [86] H. J. Mueller and E. H. Greener, Polarization Studies of Surgical Materials in Ringer's Solution, *Journal of Biomedical Materials Research*, **4** (1), pp. 29-41, 1970.
- [87] M. Aziz-Kerrzo, K. G. Conroy, A. M. Fenelon, S. T. Farrell and C. B. Breslin, Electrochemical Studies on the Stability and Corrosion Resistance of Titanium-Based Implant Materials, *Biomaterials* , **22** (12), pp. 1531-1539, 2001. Available: [http://dx.doi.org/10.1016/S0142-9612\(00\)00309-4](http://dx.doi.org/10.1016/S0142-9612(00)00309-4).
- [88] Y. Mu, T. Kobayashi, M. Sumita, A. Yamamoto and T. Hanawa, Metal Ion Release from Titanium with Active Oxygen Species Generated by Rat Macrophages in Vitro, *Journal of Biomedical Materials Research* , **49** (2), pp. 238-243, 2000. Available: [http://dx.doi.org/10.1002/\(SICI\)1097-4636\(200002\)49:2<238::AID-JBM12>3.0.CO;2-J](http://dx.doi.org/10.1002/(SICI)1097-4636(200002)49:2<238::AID-JBM12>3.0.CO;2-J).
- [89] M. Browne and P. J. Gregson, Effect of Mechanical Surface Pretreatment on Metal Ion Release, *Biomaterials*, **21** (4), pp. 385-392, 2000. Available: [http://dx.doi.org/10.1016/S0142-9612\(99\)00200-8](http://dx.doi.org/10.1016/S0142-9612(99)00200-8).
- [90] L. Hao, *Laser Surface Treatment of Bio-Implant Materials* 2005, Available: http://isbndb.com/d/book/laser_surface_treatment_of_bio_implant_materials.

- [91] E. A. Vogler, Structure and Reactivity of Water at Biomaterial Surfaces, *Advances in Colloid and Interface Science*, **74** (1-3), pp. 69-117, 1998.
- [92] J. Lawrence and L. Li, *Laser Modification of the Wettability Characteristics of Engineering Materials (Engineering Research)* 2001. Available: http://isbndb.com/d/book/laser_modification_of_the_wettability_characteristics_of_eng.
- [93] I. Gentle and G. Barnes, *Interfacial Science: An Introduction* 2005. Available: http://isbndb.com/d/book/interfacial_science_a01.
- [94] S. C. Wong, Y. D. Ramkissoon, M. Lopez, K. Page, I. P. Parkin and P. M. Sullivan, Use of Hydroxypropylmethylcellulose 2% for Removing Adherent Silicone Oil from Silicone Intraocular Lenses, *British Journal of Ophthalmology*, **93** (8), pp. 1085-1088, 2009.
- [95] Gelwell Biotech Website, Hydrophilic and Hydrophobic Coatings, 2011 [online] Accessed (23/09/2011), Available: <http://www.gelwell.com/1.htm>.
- [96] Pacific BioLabs, Assessing Biocompatibility, 2009 [online] Accessed (19/01/2009) Available: <http://www.pacificbiolabs.com/downloads/PBL%20biocompatibility%202008%20-final.pdf>.
- [97] J. F. Ready and D. Farson, *LIA Handbook of Laser Materials Processing*, 2001. Available: http://isbndb.com/d/book/lia_handbook_of_laser_materials_processing.
- [98] D. T. A. Matthews, V. Ocelík and J. T. M. de Hosson, Tribological and Mechanical Properties of High Power Laser Surface-Treated Metallic Glasses, *Materials Science and Engineering: A*, **471** (1-2), pp. 155-164, 2007.
- [99] T. Mahank, PhD Thesis: Laser Glazing of Metals and Metallic and Ceramic Coatings, Pennsylvania State University, 2004.
- [100] A. A. Peligrad, E. Zhou, D. Morton and L. Li, A Melt Depth Prediction Model for Quality Control of Laser Surface Glazing of Inhomogeneous Materials, *Optics & Laser Technology*, **33** (1), pp. 7-13, 2001.
- [101] H. L. Tsai and P. C. Tsai, Laser Glazing of Plasma-Sprayed Zirconia Coatings, *Journal of Materials Engineering and Performance*, **7** (2), pp. 258-264, 1998.

- [102] S. N. Aqida, D. Brabazon and S. Naher, H13 Die Steel Modified Surface by Pulse Laser Glazing, AMPT Proceedings, Malaysia, 2009.
- [103] J. C. Ion, *Laser Processing of Engineering Materials: Principles, Procedure and Industrial Application* 2005, Available:
http://isbndb.com/d/book/laser_processing_of_engineering_materials.
- [104] R. J. DiMelfi, P. G. Sanders, B. Hunter, J. A. Eastman, K. J. Sawley, K. H. Leong and J. M. Kramer, Mitigation of Subsurface Crack Propagation in Railroad Rails by Laser Surface Modification, *Surface and Coatings Technology*, **106** (1), pp. 30-43, 1998. Available:
[http://dx.doi.org/10.1016/S0257-8972\(98\)00487-3](http://dx.doi.org/10.1016/S0257-8972(98)00487-3).
- [105] C. Sreedhar, G. Santhanakrishnan, C. V. Gokularathnam and R. Krishnamurthy, Effect of Processing Parameters on the Laser Glazing of Plasma-Sprayed alumina–titania Ceramic, *Journal of Materials Processing Technology* , **114** (3), pp. 246-251, 2001.
- [106] W. Jiang and P. Molian, Nanocrystalline TiC Powder Alloying and Glazing of H13 Steel using a CO2 Laser for Improved Life of Die-Casting Dies, *Surface and Coatings Technology* , **135** (2-3), pp. 139-149, 2001.
- [107] W. L. Johnson, Bulk Metallic Glasses - a New Engineering Material, *Current Opinion in Solid State and Materials Science*, **1** (3), pp. 383-386, 1996.
- [108] W. L. Johnson, Fundamental Aspects of Bulk Metallic Glass Formation in Multicomponent Alloys, *Presented at: ISMANAM-95*, pp. 35-50, 1996.
- [109] B. Lemley, Glassy Metals, *Materials Science: Discover Magazine*, 2008 [online] Accessed (19/11/2008), Available:
http://discovermagazine.com/2004/apr/glassymetals/article_view?b_start:int=1&-C=.
- [110] F. Audebert, R. Colaco, R. Vilar and H. Sirkin, Production of Glassy Metallic Layers by Laser Surface Treatment, *Scripta Materialia* , **48** (3), pp. 281-6, 2003. Available: [http://dx.doi.org/10.1016/S1359-6462\(02\)00382-2](http://dx.doi.org/10.1016/S1359-6462(02)00382-2).
- [111] A. Inoue, Stabilization of Metallic Supercooled Liquid and Bulk Amorphous Alloys, *Acta Materialia*, **48** (1), pp. 279-306, 2000.

- [112] G. Malakondaiah and T. Nicholas, The Influence of Laser Glazing on Fatigue Crack Growth in Ti-24Al-11Nb, *Metallurgical and Materials Transactions A (Physical Metallurgy and Materials Science)*, **25A** (1), pp. 183-92, 1994.
- [113] O. V. Akgun and O. T. Inal, Laser Surface Melting of Ti-6Al-4V Alloy, *Journal of Materials Science*, **27** (5), pp. 1404-1408, 1992, Available: <http://dx.doi.org/10.1007/BF01142062>.
- [114] A. Bandyopadhyay, V. Balla, M. Roy and S. Bose, Laser Surface Modification of Metallic Biomaterials, *JOM Journal of the Minerals, Metals and Materials Society*, **63** (6), pp. 94-99, 2011.
- [115] X. K. Xi, D. Q. Zhao, M. X. Pan, W. H. Wang, Y. Wu and J. J. Lewandowski, Fracture of Brittle Metallic Glasses: Brittleness Or Plasticity, *Physical Review Letters*, **94** (12), pp. 125510, 2005. Available: <http://link.aps.org/doi/10.1103/PhysRevLett.94.125510>.
- [116] C. W. Draper and C. A. Ewing, Laser Surface Alloying: A Bibliography, *Journal of Materials Science*, **19** (12), pp. 3815-3825, 1984.
- [117] S. V. Joshi and G. Sundararajan, "Lasers for metallic and intermetallic coatings" in *Lasers in Surface Engineering*, N. B. Dahotre, Ed. 1998, Available: http://isbndb.com/d/book/lasers_in_surface_engineering.
- [118] H. Chen and Q. Luo, Study on Laser Gas Alloying for Titanium Alloy, *Jiguang Zazhi/Laser Journal*, **18** (3), pp. 32-36, 44, 1997.
- [119] J. Liu, Q. Luo and Z. Zou, Laser Gas Alloying of Titanium Alloy with Nitrogen, *Surface and Coatings Technology*, **57** (2-3), pp. 191-195, 1993. Available: [http://dx.doi.org/10.1016/0257-8972\(93\)90039-Q](http://dx.doi.org/10.1016/0257-8972(93)90039-Q).
- [120] H. Chmelickova, L. Kucharicova and J. Grezl, Powder Alloying of Low-Carbon Steel by CO₂ Laser, *Presented at: Sixth International Workshop on Laser Physics (LPHYS'97)*, pp. 349-51, 1998.
- [121] O. d. Diniz Neto and R. M. C. Vilar, Interaction between the Laser Beam and the Powder Jet in Blown Powder Laser Alloying and Cladding, *Presented at: Proceedings of International Congress on the Applications of Lasers and Electro-Optics*, 1998, pp. 180-8.
- [122] E. Brandl, F. Palm, V. Michailov, B. Viehweger and C. Leyens, Mechanical Properties of Additive Manufactured Titanium (Ti-6Al-4V) Blocks Deposited by

- a Solid-State Laser and Wire, *Materials and Design* , **32** (10), pp. 4665-4675, 2011. Available: <http://dx.doi.org/10.1016/j.matdes.2011.06.062>.
- [123] H. C. Man, M. Bai and F. T. Cheng, Laser Diffusion Nitriding of Ti-6Al-4V for Improving Hardness and Wear Resistance, *Applied Surface Science* , **258** (1), pp. 436-441, 2011, Available: <http://dx.doi.org/10.1016/j.apsusc.2011.08.114>.
- [124] R. Filip, Laser Nitriding of the Surface Layer of Ti6Al4V Titanium Alloy, *Int. Sci. Journal*, **30** (1), pp. 25, 2008. http://www.archivesmse.org/vol30_1/3016.pdf
- [125] A. R. Hamad, J. H. Abboud, F. M. Shuaeib and K. Y. Benyounis, Surface Hardening of Commercially Pure Titanium by Laser Nitriding: Response Surface Analysis, *Advances in Engineering Software*, **41** (4), pp. 674-679, 2010.
- [126] S. Fare, N. Lecis, M. Vedani, G. Vimercati, A. Silipigni, D. Corti and P. Favoino, Ion Nitriding of a Commercially Pure Titanium Alloy and of a Ti-6Al-4V; *Metallurgia Italiana* , **102** (6), pp. 13-18, 2010.
- [127] C. Hu and T. N. Baker, The Importance of Preheat before Laser Nitriding a Ti-6Al-4V Alloy, *Materials Science and Engineering A*, **265** (1-2), pp. 268-275, 1999.
- [128] C. Gerdes, A. Karimi and H. W. Bieler, Water Droplet Erosion and Microstructure of Laser-Nitrided Ti-6Al-4V, *Wear*, **186-187** (Part 2), pp. 368-374, 1995.
- [129] T. I. Khan, A Review of Methods used for Surface Melting and Gaseous Alloying, *Proc. Pakistan Acad. Sci.*, **1** (44), pp. 63, 2006.
- [130] M. Geetha, U. K. Mudali, N. D. Pandey, R. Asokamani and B. Raj, Microstructural and Corrosion Evaluation of Laser Surface Nitrided Ti-13Nb-13Zr Alloy, *Surface Engineering* , **20** (1), pp. 68-74, 2004.
- [131] Y. S. Tian, C. Z. Chen, S. T. Li and Q. H. Huo, Research Progress on Laser Surface Modification of Titanium Alloys, *Applied Surface Science* , **242** (1-2), pp. 177-184, 2005.
- [132] H. O. Pierson, *Handbook of Refractory Carbides and Nitrides: Properties, Characteristics, Processing and Applications*, 1996, Available: http://isbndb.com/d/book/handbook_of_refractory_carbides_and_nitrides.

- [133] S. Ettaqi, V. Hays, J. J. Hantzpergue, G. Saindrenan and J. C. Remy, Mechanical, Structural and Tribological Properties of Titanium Nitrided by a Pulsed Laser, *Surface and Coatings Technology*, **100-101** pp. 428-432, 1998.
- [134] J. C. Mori, P. Serra, E. Martínez, G. Sardin, J. Esteve and J. L. Morenza, Surface Treatment of Titanium by Nd:YAG Laser Irradiation in the Presence of Nitrogen, *Applied Physics A: Materials Science & Processing*, **69** (7), pp. S699, 1999.
- [135] MatWeb Website, Titanium Nitride (TiN) Coating, 2010 [online] Accessed (1/13/2010), Available:
<http://www.matweb.com/search/datasheet.aspx?MatGUID=ffbf753c500949db95e502e043f9a404&ckck=1>.
- [136] [136] P. Jiang, X. L. He, X. X. Li, L. G. Yu and H. M. Wang, Wear Resistance of a Laser Surface Alloyed Ti-6Al-4V Alloy, *Surface and Coatings Technology*, **130** (1), pp. 24-28, 2000.
- [137] E. György, A. Pérez del Pino, P. Serra and J. L. Morenza, Surface Nitridation of Titanium by Pulsed Nd:YAG Laser Irradiation, *Applied Surface Science*, **186** (1-4), pp. 130-134, 2002.
- [138] S. Yerramareddy and S. Bahadur, The Effect of Laser Surface Treatments on the Tribological Behavior of Ti-6Al-4V, *Wear*, **157** (2), pp. 245-262, 1992.
- [139] H. C. Man, Z. D. Cui, T. M. Yue and F. T. Cheng, Cavitation Erosion Behavior of Laser Gas Nitrided Ti and Ti6Al4V Alloy, *Materials Science and Engineering A*, **355** (1-2), pp. 167-173, 2003.
- [140] S. Mridha and T. N. Baker, Crack-Free Hard Surfaces Produced by Laser Nitriding of Commercial Purity Titanium, *Materials Science and Engineering A*, **A188** (1-2), pp. 229-239, 1994.
- [141] R. L. Sun, J. F. Mao and D. Z. Yang, Microstructural Characterization of NiCr1BSiC Laser Clad Layer on Titanium Alloy Substrate, *Surface and Coatings Technology*, **150** (2-3), pp. 199-204, 2002.
- [142] S. Yang, W. Liu and M. Zhong, Microstructure Characteristics and Properties of in-Situ Formed TiC/Ni Based Alloy Composite Coating by Laser Cladding, *Presented at: First International Symposium on High-Power Laser*

Macroprocessing, 2003, pp. 481-6. Available:

<http://dx.doi.org/10.1117/12.497602>.

- [143] M. Qingwu, G. Lin and Z. Zhenzhu, Laser Cladding Ni-Base Composite Coating on Titanium Alloy with Pre-Placed B₄C+NiCoCrAlY, *Presented at: Fifth Pacific Rim International Conference on Advanced Materials and Processing PRICM-5*, 2005, pp. 905-8.
- [144] Y. Wang and H. M. Wang, Wear Resistance of Laser Clad Ti₂Ni₃Si Reinforced Intermetallic Composite Coatings on Titanium Alloy, *Applied Surface Science*, **229** (1-4), pp. 81-86, 2004.
- [145] A. Hirose, T. Ueda and K. F. Kobayashi, Wear and Oxidation Properties of Titanium Aluminides Formed on Titanium Surface by Laser Alloying, *Materials Science and Engineering: A*, **160** (1), pp. 143-153, 1993.
- [146] B. Guo, J. Zhou, S. Zhang, H. Zhou, Y. Pu and J. Chen, Microstructure and Tribological Properties of in Situ Synthesized TiN/Ti₃Al Intermetallic Matrix Composite Coatings on Titanium by Laser Cladding and Laser Nitriding, *Materials Science and Engineering: A*, **480** (1-2), pp. 404-410, 2008.
- [147] Y. Pu, B. Guo, J. Zhou, S. Zhang, H. Zhou and J. Chen, Microstructure and Tribological Properties of in Situ Synthesized TiC, TiN, and SiC Reinforced Ti₃Al Intermetallic Matrix Composite Coatings on Pure Ti by Laser Cladding, *Applied Surface Science*, **255** (5, Part 2), pp. 2697-2703, 2008.
- [148] L. Cai, Y. Zhang and L. Shi, Microstructure and Formation Mechanism of Titanium Matrix Composites Coating on Ti-6Al-4V by Laser Cladding, *Rare Metals*, **26** (4), pp. 342-346, 2007.
- [149] J. Dutta Majumdar, I. Manna, A. Kumar, P. Bhargava and A. K. Nath, Direct Laser Cladding of Co on Ti-6Al-4V with a Compositionally Graded Interface, *Journal of Materials Processing Technology*, **209** (5), pp. 2237-2243, 2009.
- [150] A. Kruusing, Underwater and Water-Assisted Laser Processing: Part 2 - Etching, Cutting and Rarely used Methods, *Optics and Lasers in Engineering*, **41** (2), pp. 329-352, 2004.
- [151] M. Rozmus-Gornikowska, Surface Modifications of a Ti6Al4V Alloy by a Laser Shock Processing, 2010, pp. 808-811.

- [152] T. N. Baker, "Laser surface modification of Ti alloys" in *Surface Engineering of Light Alloys - Aluminium, Magnesium and Titanium Alloys*, H. Dong, Ed. 2009.
- [153] T. M. Yue, T. M. Cheung and H. C. Man, The Effects of Laser Surface Treatment on the Corrosion Properties of Ti-6Al-4V Alloy in Hank's Solution, *Journal of Materials Science Letters* , **19** (3), pp. 205-8, 2000, Available: <http://dx.doi.org/10.1023/A:1006750422831>.
- [154] J. Hyzak and I. Bernstein, The Role of Microstructure on the Strength and Toughness of Fully Pearlitic Steels, *Metallurgical and Materials Transactions A*, **7** (8), pp. 1217-1224, 1976.
- [155] A. Lasalmonie and J. L. Strudel, Influence of Grain Size on the Mechanical Behaviour of some High Strength Materials, *Journal of Materials Science*, **21** (6), pp. 1837-1852, 1986.
- [156] M. Pellizzari and M. G. De Flora, Influence of Laser Hardening on the Tribological Properties of Forged Steel for Hot Rolls, *Wear* , **271** (9-10), pp. 2402-2411, 2011.
- [157] J. C. Ion, Laser transformation hardening, *Surface Engineering*, **18** (1), pp. 14-31, 2002.
- [158] P. A. A. Khan and T. Debroy, Absorption of CO₂ Laser Beam by AISI 4340 Steel, *Metallurgical Transactions B*, **16** (4), pp. 853, 1985.
- [159] Y. Touloukian, *Thermophysical Properties of Matter - Thermal Radiative Properties – Coatings*, 1973, Available: http://isbndb.com/d/book/touloukian_thermophysical_properties_of_matter_thermal_radiative_properties_coatings.
- [160] L. Quintino, A. Costa, R. Miranda, D. Yapp, V. Kumar and C. J. Kong, Welding with High Power Fiber Lasers – A Preliminary Study, *Materials & Design* , **28** (4), pp. 1231-1237, 2007.
- [161] W. M. Steen and K. Watkins, *Laser Material Processing*, 2003, Available: http://isbndb.com/d/book/laser_material_processing_a02.
- [162] D. Bergström, J. Powell and A. F. H. Kaplan, The Absorptance of Steels to Nd:YLF and Nd:YAG Laser Light at Room Temperature, *Applied Surface Science*, **253** (11), pp. 5017-5028, 2007.

- [163] V. C. Kumar, Process Parameters Influencing Melt Profile and Hardness of Pulsed Laser Treated Ti-6Al-4V, *Surface & Coatings Technology* , **201** (6), pp. 3174-80, 2006, Available: <http://dx.doi.org/10.1016/j.surfcoat.2006.06.035>.
- [164] A. N. Samant, B. Du, S. R. Paital, S. Kumar and N. B. Dahotre, Pulsed Laser Surface Treatment of Magnesium Alloy: Correlation between Thermal Model and Experimental Observations, *Journal of Materials Processing Technology* , **209** (11), pp. 5060-5067, 2009.
- [165] A. J. Pinkerton and L. Li, An Investigation of the Effect of Pulse Frequency in Laser Multiple-Layer Cladding of Stainless Steel, *Applied Surface Science*, **208-209** pp. 405-410, 2003.
- [166] A. N. Samant, S. P. Harimkar and N. B. Dahotre, Laser Beam Operation Mode Dependent Grain Morphology of Alumina, *Journal of Applied Physics* , **102** (12), 2007, Available: <http://dx.doi.org/10.1063/1.2825403>.
- [167] J. T. Black, "Machining" in *ASM Handbook, 9th Edition*, ASM-International, Ohio USA, 1997.
- [168] N. Zaveri, M. Mahapatra, A. Deceuster, Y. Peng, L. Li and A. Zhou, Corrosion Resistance of Pulsed Laser-Treated Ti-6Al-4V Implant in Simulated Biofluids, *Electrochimica Acta* , **53** (15), pp. 5022-5032, 2008. Available: <http://dx.doi.org/10.1016/j.electacta.2008.01.086>.
- [169] Z. Sun, I. Annergren, D. Pan and T. A. Mai, Effect of Laser Surface Remelting on the Corrosion Behavior of Commercially Pure Titanium Sheet, *Materials Science & Engineering A (Structural Materials: Properties, Microstructure and Processing)* , **A345** (1-2), pp. 293-300, 2003, Available: [http://dx.doi.org/10.1016/S0921-5093\(02\)00477-X](http://dx.doi.org/10.1016/S0921-5093(02)00477-X).
- [170] A. Issa, PhD Thesis: Computational Control of Laser Systems for Micro-Machining, Dublin City University, 2007.
- [171] W. W. Duley, *Laser Processing and Analysis of Materials* 1983. Available: http://isbndb.com/d/book/laser_processing_and_analysis_of_materials.
- [172] E. V. Bordatchev and S. K. Nikumb, Effect of Focus Position on Informational Properties of Acoustic Emission Generated by laser-material Interactions, *Applied Surface Science* , **253** (3), pp. 1122-1129, 2006.

- [173] P. H. Morton, T. Bell, A. Weisheit, J. Kroll, B. L. Mordike and K. Sagoo, "Laser gas nitriding of titanium and titanium alloys" in *Surface Modification Technologies V*, T. S. Sudarshan and J. Braza, Eds. 1992.
- [174] H. Xin, S. Mridha and T. N. Baker, The Effect of Laser Surface Nitriding with a Spinning Laser Beam on the Wear Resistance of Commercial Purity Titanium, *Journal of Materials Science* , **31** (1), pp. 22-30, 1996.
- [175] C. Hu and T. Baker, Overlapping Laser Tracks to Produce a Continuous Nitrided Layer in Ti-6Al-4V Alloy, *Journal of Materials Science*, **32** (11), pp. 2821-2826, 1997.
- [176] F. Laroudie, C. Tassin and M. Pons, Laser Surface Alloying of 316L Stainless Steel: Different Hardening Routes and Related Microstructures, *Journal De Physique*, **4** (4), pp. 77-80, 1994.
- [177] G. Manivasagam, D. Dhinasekaran and A. Rajamanickam, Biomedical Implants: Corrosion and its Prevention - A Review~, *Recent Patents on Corrosion Science*, **2** (1), pp. 40, 2010.
- [178] U. Mudali, M. Pujar and R. Dayal, Effects of Laser Surface Melting on the Pitting Resistance of Sensitized Nitrogen-Bearing Type 316L Stainless Steel, *Journal of Materials Engineering and Performance* , **7** (2), pp. 214-220, 1998. Available: <http://dx.doi.org/10.1361/105994998770347945>.
- [179] M. Sivakumar and S. Rajeswari, Investigation of Failures in Stainless Steel Orthopaedic Implant Devices: Pit-Induced Stress Corrosion Cracking, *Journal of Materials Science Letters*, **11** (15), pp. 1039-42, 1992.
- [180] O. V. Akgun and O. T. Inal, Laser Surface Melting and Alloying of Type 304L Stainless Steel, *Journal of Materials Science* , **30** (23), pp. 6105-6112, 1995, Available: <http://dx.doi.org/10.1007/BF01151534>.
- [181] N. Parvathavarthini, R. V. Subbarao, S. Kumar, R. K. Dayal and H. S. Khatak, Elimination of Intergranular Corrosion Susceptibility of Cold-Worked and Sensitized AISI 316 SS by Laser Surface Melting, *Journal of Materials Engineering and Performance* , **10** (1), pp. 5-13, 2001, Available: <http://dx.doi.org/10.1361/105994901770345277>.

- [182] A. Ossowska and A. Zieliński, Properties of Surface Layers of Titanium Alloy Ti6AL4V After Laser Melting Processes, *Advances in Materials Sciences* , (4), pp. 63, 2010.
- [183] L. Lavisse, D. Grevey, C. Langlade and B. Vannes, The Early Stage of the Laser-Induced Oxidation of Titanium Substrates, *Applied Surface Science*, **186** (1-4), pp. 150-155, 2002.
- [184] R. R. Boyer, "ASM handbook volume 09: Metallography and microstructures." in *Vander Voort, G.*; ASM Handbook Volume 09: Metallography and Microstructures, Ed. 2004, pp. 458-475.
- [185] K. Ferjutz and J. R. Davis, "Welding, brazing, and soldering" in *ASM Handbook*, 1990, Available: http://isbndb.com/d/book/asm_handbook_a09.
- [186] W. Liu and J. N. DuPont, Effects of Melt-Pool Geometry on Crystal Growth and Microstructure Development in Laser Surface-Melted Superalloy Single Crystals: Mathematical Modelling of Single-Crystal Growth in a Melt Pool (Part I), *Acta Materialia* , **52** (16), pp. 4833-4847, 2004.
- [187] K. Farooq and A. Kar, Effects of Laser Mode and Scanning Direction on Melt Pool Shape, *Journal of Applied Physics* , **85** (9), pp. 6415-20, 1999, Available: <http://dx.doi.org/10.1063/1.370145>.
- [188] L. Han, F. W. Liou and S. Musti, Thermal Behavior and Geometry Model of Melt Pool in Laser Material Process, *Journal of Heat Transfer* , **127** (9), pp. 1005-1014, 2005, Available: <http://dx.doi.org/10.1115/1.2005275>.
- [189] C. L. Chan, J. Mazumder and M. M. Chen, Effect of Surface Tension Gradient Driven Convection in a Laser Melt Pool: Three-dimensional Perturbation Model, *Journal of Applied Physics*, **64** (11), pp. 6166-6174, 1988.
- [190] M. Bamberger, "Rapid melting kinetics" in *Handbook of Laser Materials Processing*, J. F. Ready, Ed. Library of congress control, 2001.
- [191] H. Li, S. Costil, V. Barnier, R. Oltra, O. Heintz and C. Coddet, Surface Modifications Induced by Nanosecond Pulsed Nd:YAG Laser Irradiation of Metallic Substrates, *Surface and Coatings Technology* , **201**, (3-4), pp. 1383-1392, 2006.

- [192] N. Axén, S. Jacobson and S. Hogmark, Influence of Hardness of the Counterbody in Three-Body Abrasive Wear - an Overlooked Hardness Effect, *Tribology International* , **27** (4), pp. 233-241, 1994.
- [193] Y. S. Tian, C. Z. Chen, D. Y. Wang and T. Q. Lei, Laser Surface Modification of Titanium Alloys - a Review, *Surface Review and Letters* , **12** (1), pp. 123-30, 2005, Available: <http://dx.doi.org/10.1142/S0218625X0500686X>.
- [194] G. Gray, S. Chen and K. Vecchio, Influence of Grain Size on the Constitutive Response and Substructure Evolution of MONEL 400, *Metallurgical and Materials Transactions A*, **30** (5), pp. 1235-1247, 1999.
- [195] A. Biswas, T. K. Maity, U. K. Chatterjee, I. Manna, L. Li and J. Dutta Majumdar, Laser Surface Nitriding of Ti-6Al-4V for Bio-Implant Application, *Trends in Biomaterials and Artificial Organs* , **20** (1), pp. 68-71, 2006.
- [196] K. Miyoshi and D. H. Buckley, Adhesion and Friction of Transition Metals in Contact with Non-Metallic Hard Materials, *Wear* , **77** (2), pp. 253-264, 1982.
- [197] F. M. Kustas and M. S. Misra, "Friction and wear of titanium alloys" in *ASM Handbook Volume 18, Friction, Lubrication, and Wear Technology*, ASM International, Ohio USA, 2001.
- [198] A. Biswas, I. Manna, U. K. Chatterjee, U. Bhattacharyya and J. D. Majumdar, Evaluation of Electrochemical Properties of Thermally Oxidised Ti-6Al-4V for Bioimplant Application, *Surface Engineering* , **25** (2), pp. 141-145, 2009. Available: <http://dx.doi.org/10.1179/174329409X379264>.
- [199] S. Meassick and H. Champaign, Noble Metal Cathodic Arc Implantation for Corrosion Control of Ti-6Al-4V, *Surface and Coatings Technology* , **93** (2-3), pp. 292-296, 1997.
- [200] J. L. - Gilbert, C. A. - Buckley and J. J. - Jacobs, In Vivo Corrosion of Modular Hip Prosthesis Components in Mixed and Similar Metal Combinations: the Effect of Crevice, Stress, Motion, and Alloy Coupling, - *Journal of Biomedical Materials Research*, - **27** (- 12), pp. - 1533-- 1544, - 1993.
- [201] A. Gaggl, G. Schultes, W. D. Muller and H. Karcher, Scanning Electron Microscopical Analysis of Laser-Treated Titanium Implant Surfaces-a Comparative Study, *Biomaterials* , **21** (10), pp. 1067-73, 2000. Available: [http://dx.doi.org/10.1016/S0142-9612\(00\)00002-8](http://dx.doi.org/10.1016/S0142-9612(00)00002-8).

- [202] N. Mirhosseini, P. L. Crouse, M. J. J. Schmidh, L. Li and D. Garrod, Laser Surface Micro-Texturing of Ti-6Al-4V Substrates for Improved Cell Integration, *Applied Surface Science* , **253** (19), pp. 7738-43, 2007. Available: <http://dx.doi.org/10.1016/j.apsusc.2007.02.168>.
- [203] X. Liu, P. K. Chu and C. Ding, Surface Modification of Titanium, Titanium Alloys, and Related Materials for Biomedical Applications, *Materials Science and Engineering: R: Reports* , **47** (3-4), pp. 49-121, 2004.
- [204] A. Göransson, E. Jansson, P. Tengvall and A. Wennerberg, Bone Formation After 4 Weeks Around Blood-Plasma-Modified Titanium Implants with Varying Surface Topographies: An in Vivo Study, *Biomaterials* , **24** (2), pp. 197-205, 2003.
- [205] T. M. Lee, E. Chang and C. Y. Yang, Attachment and Proliferation of Neonatal Rat Calvarial Osteoblasts on Ti6Al4V: Effect of Surface Chemistries of the Alloy, *Biomaterials*, **25** (1), pp. 23-32, 2004.
- [206] A. Bagno and C. Di Bello, Surface Treatments and Roughness Properties of Ti-Based Biomaterials, *Journal of Materials Science: Materials in Medicine*, **15** (9), pp. 935-949, 2004.
- [207] L. Hao, J. Lawrence and L. Li, Manipulation of the Osteoblast Response to a Ti-6Al-4V Titanium Alloy using a High Power Diode Laser, *Applied Surface Science* , **247** (1-4), pp. 602-606, 2005.
- [208] J. Chen, J. P. Ulerich, E. Abelev, A. Fasasi, C. B. Arnold and W. O. Soboyejo, An Investigation of the Initial Attachment and Orientation of Osteoblast-Like Cells on Laser Grooved Ti-6Al-4V Surfaces, *Materials Science and Engineering: C* , **29** (4), pp. 1442-1452, 2009.
- [209] C. Hallgren, H. Reimers, D. Chakarov, J. Gold and A. Wennerberg, An in Vivo Study of Bone Response to Implants Topographically Modified by Laser Micromachining, *Biomaterials* , **24** (5), pp. 701-10, 2003, Available: [http://dx.doi.org/10.1016/S0142-9612\(02\)00266-1](http://dx.doi.org/10.1016/S0142-9612(02)00266-1).
- [210] K. Anselme and M. Bigerelle, Topography Effects of Pure Titanium Substrates on Human Osteoblast Long-Term Adhesion, *Acta Biomaterialia* , **1** (2), pp. 211-222, 2005.

- [211] T. Chung, D. Liu, S. Wang and S. Wang, Enhancement of the Growth of Human Endothelial Cells by Surface Roughness at Nanometer Scale, *Biomaterials*, **24** (25), pp. 4655-4661, 2003.
- [212] D. Sowden and J. P. Schmitz, AO Self-Drilling and Self-Tapping Screws in Rat Calvarial Bone: An Ultrastructural Study of the Implant Interface, *Journal of Oral and Maxillofacial Surgery*, **60** (3), pp. 294-299, 2002.
- [213] J. Vlacic-Zischke, S. M. Hamlet, T. Friis, M. S. Tonetti and S. Ivanovski, The Influence of Surface Microroughness and Hydrophilicity of Titanium on the Up-Regulation of TGF β /BMP Signalling in Osteoblasts. *Biomaterials*, **32** (3), pp. 665-671, 2011.
- [214] Guyson Website, Blast Media, 2010 [online] Accessed (6/23/2010), Available: <http://www.guyson.co.uk/consumables/media.html>.
- [215] N. Blackstone, Fundamentals of ultrasonic cleaning, *Process Cleaning Magazine*, 2000 Available: www.blackstone-ney.com/pdfs/T_Fundametals.htm.
- [216] D. R. Whitehouse, Understanding CO² Lasers, 2010 [Online] Accessed (2/21/2010), Available: <http://www.laserk.com/newsletters/whiteCO.html>.
- [217] M.B Bever, "Metallurgical Techniques and Microstructures" in ASM Handbook: *Metallography and Microstructures*", **9**, ASM International, pp. 163. 2003.
- [218] Metallography Website, Metallographic Cleaning, 2010 [online] Accessed (3/9/2010), Available: <http://www.metallographic.com/Technical/Etching.htm>.
- [219] G. F. Vander Voort, Materials Characterization & Testing: Microstructure of Titanium and its Alloys, *International Journal of Thermal Technology*, 2006.
- [220] J. S. Selvan, G. Soundararajan and K. Subramanian, Laser Alloying of Aluminium with Electrodeposited Nickel: Optimisation of Plating Thickness and Processing Parameters, *Surface and Coatings Technology*, **124** (2-3), pp. 117-127, 2000.
- [221] A to Z of Material Website, Stainless Steel - Grade 316L - Properties, Fabrication and Applications, 2008 [online] Accessed (12/12/2008), Available: <http://www.azom.com/details.asp?ArticleID=2382>.
- [222] W. H. Walton, Feret's Statistical Diameter as a Measure of Particle Size, *Nature*, **162** (4113), pp. 329, 1948.

- [223] X. D. Hou, Study of the Interaction between the Indentation Size Effect and Hall–Petch Effect with Spherical Indenters on Annealed Polycrystalline Copper, *Journal of Physics D: Applied Physics*, **41** (7), 074006, 2008. Available: <http://stacks.iop.org/0022-3727/41/i=7/a=074006>.
- [224] B. D. Cullity, *Elements of x-Ray Diffraction* USA: Reading, Addison-Wesley P, 2001.
- [225] S. J. B. Reed, *Electron Microprobe Analysis* 1993, Available: http://isbndb.com/d/book/electron_microprobe_analysis_a02.
- [226] M. P. Gispert, A. P. Serro, R. Colaço and B. Saramago, Friction and Wear Mechanisms in Hip Prosthesis: Comparison of Joint Materials Behaviour in several Lubricants, *Wear*, **260** (1-2), pp. 149-158, 2006.
- [227] M. G. Fontana, *Corrosion Engineering* 1986, Available: http://isbndb.com/d/book/corrosion_engineering.
- [228] ASTM International, "ASTM G102 – 89 (2010) standard practice for calculation of corrosion rates and related information from electrochemical measurements" in *Corrosion Standards and Wear Standards*: ASTM International, pp. 422, 2010.
- [229] First Ten Angstroms, FTA 200 operating manual, 2006 [online] Available: <http://www.firsttenangstroms.com/products/fta200/fta200.html>
- [230] HPACC Website, Health Protection Agency Culture Collection: Cell Counting using a Haemocytometer, 2011 [online] Accessed (08/05/2011) Available: <http://www.hpacultures.org.uk/technical/ccp/cellcounting.jsp>.
- [231] G. R. Speich, "Martensitic structures" in *ASM Handbook Vol 9: Metallography and Microstructures*, G. F. Vander Voort, Ed. Ohio, USA: ASM International, 2001.
- [232] S. N. Aqida, PhD Thesis: Laser Surface Modification of Steel, Dublin City University, 2011.
- [233] S. L. R. da Silva, L. O. Kerber, L. Amaral and C. A. dos Santos, X-Ray Diffraction Measurements of Plasma-Nitrided Ti–6Al–4V, *Surface and Coatings Technology*, **116-119** (0), pp. 342-346, 1999.
- [234] Y. A. Alsultanny, Laser Beam Analysis using Image Processing, *Journal of Computer Science*, **2**, pp. 109-113, 2006.

- [235] B. D. Cullity and S. H. Stock, *Elements of x-Ray Diffraction* 2001, Available: http://isbndb.com/d/book/elements_of_x_ray_diffraction.
- [236] H. Dong and T. Bell, Tribological Behaviour of Alumina Sliding Against Ti6Al4V in Unlubricated Contact, *Wear*, **225-229**, Part 2 (0), pp. 874-884, 1999.
- [237] M. Long and H. J. Rack, Friction and Surface Behavior of Selected Titanium Alloys during Reciprocating-Sliding Motion, *Wear*, **249** (1-2), pp. 157-167, 2001.
- [238] A. Molinari, G. Straffelini, B. Tesi and T. Bacci, Dry Sliding Wear Mechanisms of the Ti6Al4V Alloy, *Wear*, **208** (1-2), pp. 105-112, 1997.
- [239] J. Qu, P. J. Blau, T. R. Watkins, O. B. Cavin and N. S. Kulkarni, Friction and Wear of Titanium Alloys Sliding Against Metal, Polymer, and Ceramic Counterfaces, *Wear*, **258** (9), pp. 1348-56, 2005. Available: <http://dx.doi.org/10.1016/j.wear.2004.09.062>.
- [240] A. Bloyce, P. -. Qi, H. Dong and T. Bell, Surface Modification of Titanium Alloys for Combined Improvements in Corrosion and Wear Resistance, *Surface and Coatings Technology*, **107** (2-3), pp. 125-32, 1998, Available: [http://dx.doi.org/10.1016/S0257-8972\(98\)00580-5](http://dx.doi.org/10.1016/S0257-8972(98)00580-5).
- [241] M. Pourbaix, *Atlas of Electrochemical Equilibrium in Aqueous Solutions*, 1974. Available: http://isbndb.com/d/book/atlas_of_electrochemical_equilibria_in_aqueous_solutions.
- [242] C. E. B. Marino, E. M. d. Oliveira, R. C. Rocha-Filho and S. R. Biaggio, On the Stability of Thin-Anodic-Oxide Films of Titanium in Acid Phosphoric Media, *Corrosion Science*, **43** (8), pp. 1465-1476, 2001.
- [243] Y. Okazaki, M. Ohota, Y. Ito and T. Tateishi, Corrosion Resistance of Implant Alloys in Pseudo Physiological Solution and Role of Alloying Elements in Passive Films, *Journal of the Japan Institute of Metals*, **59** (2), pp. 229-36, 1995, .
- [244] M. Ask, J. Lausmaa and B. Kasemo, Preparation and Surface Spectroscopic Characterization of Oxide Films on Ti6Al4V, *Applied Surface Science*, **35** (3), pp. 283-301, 1989. Available: [http://dx.doi.org/10.1016/0169-4332\(89\)90013-5](http://dx.doi.org/10.1016/0169-4332(89)90013-5).

- [245] M. Metikos-Hukovic, A. Kwokal and J. Piljac, The Influence of Niobium and Vanadium on Passivity of Titanium-Based Implants in Physiological Solution, *Biomaterials*, **24** (21), pp. 3765-3775, 2003.
- [246] I. Cvijovic-Alagic, Z. Cvijovic, S. Mitrovic, V. Panic and M. Rakin, Wear and Corrosion Behaviour of Ti-13Nb-13Zr and Ti-6Al-4V Alloys in Simulated Physiological Solution, *Corrosion Science*, **53** (2), pp. 796-808, 2011.
- [247] S. Y. Yu and J. R. Scully, Corrosion and Passivity of Ti-13% Nb-13% Zr in Comparison to Other Biomedical Implant Alloys, *Corrosion*, **53** (12), pp. 965-976, 1997, Available: <http://link.aip.org/link/?COR/53/965/1>.
- [248] D. P. Dowling, I. S. Miller, M. Ardhaoui and W. M. Gallagher, Effect of Surface Wettability and Topography on the Adhesion of Osteosarcoma Cells on Plasma-Modified Polystyrene, *Journal of Biomaterials Applications*, 2010.
- [249] D. Triantafyllidis, L. Li and F. H. Stott, The Effects of Laser-Induced Modification of Surface Roughness of Al₂O₃-Based Ceramics on Fluid Contact Angle, *Materials Science and Engineering: A*, **390** (1-2), pp. 271-277, 2005.
- [250] L. J, Identification of the Principal Elements Governing the Wettability Characteristics of Ordinary Portland Cement Following High Power Diode Laser Surface Treatment, *Materials Science and Engineering: A*, **356** (1-2), pp. 162-172, 2003.
- [251] J. Bico, U. Thiele and D. Quéré, Wetting of Textured Surfaces, *Colloids and Surfaces A: Physicochemical and Engineering Aspects*, **206** (1-3), pp. 41-46, 2002.
- [252] A. Feng, B. J. McCoy, Z. A. Munir and D. Cagliostro, Wettability of Transition Metal Oxide Surfaces, *Materials Science and Engineering: A*, **242** (1-2), pp. 50-56, 1998.
- [253] J. Chen, S. Mwenifumbo, C. Langhammer, J. - McGovern, M. Li, A. Beye and W. O. Soboyejo, Cell/surface Interactions and Adhesion on Ti-6Al-4V: Effects of Surface Texture, *Journal of Biomedical Materials Research Part B: Applied Biomaterials*, **82B** (2), pp. 360-373, 2007.
- [254] M. Jayaraman, U. Meyer, M. Bühner, U. Joos and H. Wiesmann, Influence of Titanium Surfaces on Attachment of Osteoblast-Like Cells in Vitro, *Biomaterials*, **25** (4), pp. 625-631, 2004.

Appendices

A. Material Certificates from the Suppliers

316L stainless steel produced by Acciaierie

Acciaierie Valbruna S.p.A.



36100 VICENZA (Italia) - Viale della scienza, 25 z.l.
Stab.: 39100 BOLZANO (Italia) - Via A. Volta, 4
Cliente / Besteller/Purchaser/Client

Avviso di Spedizione: D-VI08012297
Lieferanzeige/Packing list/B.L.

K443
CERTIFICATO DI COLLAUDO
ABNAHMEPRUEFZEUGNIS
INSPECTION CERTIFICATE
CERTIFICAT DE RECEPTION
EN 10204 (2005) , 3.1

Produttore: ACCIAIERIE VALBRUNA S.P.A.
Hersteller/Werks/Usine producer

Ordine nr: 709026695 STOCK
Bestell/Your order/Commande

Certificato nr: MEST623195/2008/
Prüfung/Test/Essai

Conferma ordine nr: EI07006261
Werks/Our Order/Ref nr.

Marchio di Fabbrica:
Zeichen des Lieferwerkes
Trade mark
Sigle de l'usine productrice



Oggetto Prove: - Annealed Cold Drawn
Prüfgegenstand/Item Inspected/Finissage

Tipo di Elaborazione: E+AOD
Erweichungsart/Welting process/Mode d'elaboration

Punzone del Collaudatore:
Stempel des Werksachverständigen
Inspector's stamp/Pointon de l'essayeur

Specifiche:

Anforderungen / Requirements / Exigences
VAL STOCK 2005 1.4404/316L A,CF
ASME SA276 2007 S31600 A,CF 0
ASME SA479 2007 S31603 A 3
ASTM A276 2006 S31603 A,CF
EN 10088-3 2005 1.4401 A,CF
EN 10272 2000 1.4404 A,CF
(0) SEC.II PT.A 2007 EDITION
(2) SEC.II PT.A 2007 EDITION

AISI 316
ASME SA276 2007 S31603 A,CF 1
ASTM A262 2002A PRACTICE E
ASTM A479 2006A S31600 A
EN 10088-3 2005 1.4404 A,CF

AISI 316L
ASME SA479 2007 S31600 A (2)
ASTM A276 2006 S31600 A,CF
ASTM A479 2006A S31603 A
EN 10272 2000 1.4401 A,CF

1SEC.II PT.A 2007 EDITION
3SEC.II PT.A 2007 EDITION

Qualità: 1.4404/316/316L
Werkstoff/Grade/Qualité

Marca: MVAPML MAXIVAL
Markenbezeichnung/Brand/ Marque

Punzonatura: 1.4404/316/316L
Kernzeichnung/Marking/ Marquage

Pos. nr. Büh nr. No. de pièce	Oggetto Gegenstand Product description Descr. du produit	Dimensioni - mm Abmessungen Dimension Dimension	Tolleranza Tolérance Allowance Tolerance	Lunghezza - mm Länge Length Longueur	Colata Schmelze Heat Coulée	Pezzi Stückzahl Pieces Pièces	Peso - KG Gewicht Weight Poids	Lotto nr. Losn. Lot nr. Lot nr.
0020	Round	10,000	h9	2900 / 3030	243504		1244,0	632901120

Sino state soddisfatte tutte le condizioni richieste
Die gestellten Anforderungen sind erfüllt.
The material has been furnished in accordance with the requirements.
Le matériel a été trouvé conforme aux exigences

Controllo antimescolanza: OK
Verwechslungsprüfung: spektroskopisch durchgeführt
Antimixing testing performed: OK
Contrôle antimélange fait: r.a.s.

Controllo visivo o dimensionale: soddisfatta le esigenze:
Besichtigung und Ausmessung: ohne Beanstandung
Visual inspection and dimensional check satisfactory
Contrôle visuel et dimension: satisfaisant

TEST	Provetta/Probe Specimen/Eprouvette Längs Stab, Stiele Diam. 0,025 Wahl Diam. 0,025 Läng. diam. 0,025 mm	°C	Posiz. Saggio Position Position	Snervamento Yield Stress Limite élastique Rp 0,2% N/mm2	Snervamento Yield Stress Limite élastique Rp 1% N/mm2	Resistenza Tensile strength festibilté à traction Rm N/mm2	Allungamento Elongation Allongement		Strizione Elongation Reduction of area Striction		Resilienza Kerbschlagarbeit Impact Value Resilience	Durezza Härte Dureté HB
							A5 %	E 4d %	Z %	RA		
	Valori richiesti / Auforderungen/Required values Valeurs demandées	min max		310	235	620 900	20	30	-	40	-	-
A	10	20	L	598	674	732	34	37	68	68		254

Grain size for ASTM E112 : 5

1/L=longitudinale/längs, O=transversale/quer, T=Transversale/Querseitig

Analisi chimica

Chemische Zusammensetzung/Chemical Analysis/Analyse chimique

Colata /Heat Schmelze/Coulée	min - max 0,030	1,00	2,00	16,50 18,50	2,00 2,50	10,00 13,00	-	0,045	0,030	0,100	-	-	-	-	-
	C %	Si %	Mn %	Cr %	Mo %	Ni %	Co %	P %	S %	N %					
243504	0,020	0,55	1,51	16,82	2,03	10,14	0,080	0,030	0,030	0,061					

Intergranular corrosion test per ASTM A262 pract. E: ok.

I.Korrosion nach EN ISO 3651-2A Sensibilisierung : T1 : OK

Corrosion test per EN ISO 3651-2A sensitized T1 : OK

Melted and manufactured in Italy No welding or weld repair Material free from Mercury or radio-activity contamination

The Quality Management System is Certified acc. Pressure Equipment Directive (97/23/EC) Annex 1, s. 4.3 by TUEV and LLOYD'S

Vicenza, 29/04/08 vcc008 (Mod. MCEB)	Il collaudatore di stabilimento / der Werkssachverständige / Works Inspector / L'agent d'usine <i>M. Rizzotto</i>	Pagina - 1 di 1
--	--	-----------------

Ti-6Al-4V supplied by Supper Alloys



SUPER ALLOYS
INTERNATIONAL LIMITED

1 Java Park Brgdbourne Drive Tilbrook Milton Keynes MK7 8AT
T: 01908 275700 F: 01908 275701
W: www.superalloys.co.uk E: sales@superalloys.co.uk

No: SUP 116389

Certificate of Conformity

P/O No 300117027
Rel
S/O No SUP 86277-002
B/L No SUP 85967-002 Shp 07Apr10
Inv No Inv

Sold To: (2371)
DUBLIN CITY UNIVERSITY
FINANCE OFFICE
DUBLIN CITY UNIVERSITY
GLASNEVIN
DUBLIN 9
IRELAND
Tel: 017005000 Fax: 018360830

Ship To: (000)
MICHAEL MAY (sb13a)
SCHOOL OF MECHANICAL ENGINEERING
DUBLIN CITY UNIVERSITY
GLASNEVIN
DUBLIN 9
IRELAND

CERTIFICATE of ANALYSIS and TESTS

Cert. No: SUP 116389
07Apr10

Part No
TITANIUM PLATE 6AL4V AMS4911
4.76MM THICK X 360.00mm X 360.00mm

Pcs	Wgt
1	3

Heat Number
8-45-3314-2

Tag No
77294

Pcs	Wgt
1	3

0.2%=(Mpa 890)/MAX=(Mpa 1042)/ELONG=(12)

*** Release/Condition of Material ***

ANNEALED	AMS 4911	AMS 4928
WL 3.7164	BS 2TA11	BS TA56
MIL-T-9046	MIL-T-9047	ASTM B265

Heat Number
8-45-3314-2

*** Chemical Analysis ***

Al=(6.18) V=(3.80) O=(0.164) Fe=(0.14) C=(0.005) N=(0.007)
H=(0.002) Y=(Lt.005) *(O2+N2-0.17) Each=(Lt.10) Total=(0.110)
Ti=(Balance)

attachment
VSMPO MILL CERTIFICATE NO 03064Y04
NO PAGES 2

RELEASED IN ACCORDANCE WITH EN10204 2004 3.1

Number 1 for titanium and specialist alloys

Certified that the whole of the materials detailed hereon conform in all respects to the standards/specifications and requirements of the order applicable thereto and with the conditions as follows:

- Our own inspection procedures to conform to AS EN 9100, AS EN 9120 & BS EN ISO 9001 : 2000 NQA Refs. 6045 & 6045/1.
- Messier-Dowty Ltd. Approval No. QA119.
- Our own inspection organisation as authorised by Rolls Royce under the terms of their Quality Control requirements for supplies to Rolls Royce (RR9000:SABRe) Approval No. 89730.
- British Aerospace Approval Number BAE/AG/20203/MAA. BAE Systems Regional Aircraft requirements RAL0A/00318/2
- GKN Westland Helicopters Ltd approval SQA50 Approval No. ML/AWP/4302.
- Smiths Aerospace Actuation Systems-Cheltenham. Approval Number. RMS02602H

Conditions applicable a b c d e f

Signed

For and on behalf of

Super Alloys International Limited



PART NO.

Attn:



Verkhnyaya Salda Metallurgical
Production Association

1, Parkovaya St., Verkhnyaya Salda,
Sverdlovsk reg., 624600, RUSSIA
Phone (34345) 2-38-32, 2-17-66
Fax (34345) 2-47-36, 2-05-00
Telex 348176, 348177 "SEVER"

APPROVED CERTIFICATE



18082
**INSPECTION
CERTIFICATE**

CAA approval Ref No AI/9635/98

EN 10204-3 1.8 ISO 9002 CQC 103 CERT. No 09 100 95260

CERTIFICATE No 03064Y04

date 31.03.2004

Purchaser:

Quality/alloy 6Al4V

Condition of delivery Annealed

Contract / order: 7020421TEE Annex 1 / P.O. SAIL-16696

Tag 39961



Item No	Units	Weight, (kg)	Object		Dimensions (mm) or Drawing No	Heat No	Lot No				
2	205		PLATE		4,76 x 1219,2 x 3657,6	8-45-3314-2	4124				
Chemical Composition, %											
Requirement: AMS 4911J, MIL-T 9046J, ASTM B265, BS 2TA11, TA56, WL3.7164.1, LN 9207, 4928Q, MILT-9047G											
	Al	V	O ₂	Fe	C	N ₂	H ₂	Y	O ₂ +N ₂	Residuals, max, %	
	5,50-6,75	3,5-4,5	max 0,20	max 0,30	max 0,08	max 0,05	max 0,0125	max 0,005	max 0,25	each	total
TOP	6,18	3,80	0,164	0,14	0,005	0,007	0,0020	<0,005	0,171	0,10	0,40
BOTTOM	6,23	4,09	0,167	0,13	0,005	0,007	0,0020	<0,005	0,174	<0,10	0,103

Requirement	0,20% proof stress	Tensile strength	Elongation	Reduction	Hardness HBW	In the Part, % H ₂	Heat treatment T°, C time
AMS 4911J, AMS 4928Q WL 3.7164.1	MPa	MPa	%	%			
BS 2TA11, BS TA56	min 830	900-1160	min 10,0				
MIL-T-9047G	Longitudinal						
MIL-T-9046J AB-1	9 890	1042	12,0			0,007	780° 40 min air cooling
ASTM B 265, AMS 923-18-001	11 897	1035	11,2			0,003	
	Transverse						
	9 963	1061	14,2				
	11 972	1068	14,2				

Macrostructure testing

Microstructure testing

As per AMS 4911J par. 3.5.3.2, 3.5.4.2; AMS4928Q par. 3.5.1.2.1, 3.5.1.3; MIL-T-9046J par. 3.8; 3.11; WL 3.7164.1 par. 3.2.3.3 (HV_{0,2} ≤ 450); ASTM E 112 par. 30, 34 (grain size # 10,0), 74 (Free from alpha-case); Fig. 3T10, 3T12; ETTG 4 Fig.P10, P12; MIL-T-9047G par. 3.6; 3.9; BS 2TA11 par. 1.3.2.

Ultrasonic inspection

As per AMS 2631B Cl. A1, MIL-STD 2154 (1982) Cl. A. Longitudinal wave. Immersion method. Focused transducer

Certified that, unless otherwise stated above, the whole of the above-mentioned materials have been manufactured, tested and inspected in accordance with the terms of contract/order applicable thereto and conform fully to the standards/specification quoted hereon and the requirements of the Civil Aviation Authority.

"Surface is free from any oxygen-rich layer, such as alpha-case, or other surface contamination".

Dimension tolerances to AMS 2242 F

Prepared by Kashina I.S.
Name Mitrokhina O.K.

signature

stamp



THIS IS A TRUE COPY
 OF THE ORIGINAL MILL
 TEST CERTIFICATE
 SIZED. AvSno 7/4/10
 FOR INFO ON RETRIEVAL

Traveler(s) Heat# Ingot#
83529 A K88E

CERTIFICATE OF TEST

Page 1 of 6

ATI Allvac
4374 Lancaster Highway
Richburg, SC 29729
Phone (803) 789-3595

VIA-ALLVAC LTD
DISTRIBUTION

Prof 3 Rev 0

Customer Name
SUPER ALLOYS INTERNATIONAL
1 Java Park Bradbourne Drive
Milton Keynes GB

Purchase Order
SUP-33198

Size Alloy
10 MM Rd. 6A4V

PCS 362 Weight 1158

Tina Coletti

Date: 03/20/2009 Quality Auditor: Tina Coletti

CONDITION SHIPPED

SURFACE: Centerless Ground

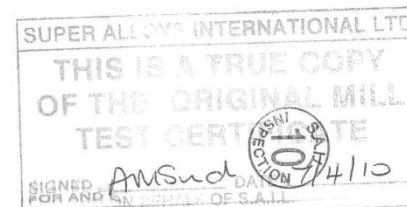
HEAT TREATMENT: 1300 F (704 C), 2 hrs, AC

SPECIFICATIONS

SAIL/WI/16 3

HEADER REMARKS

This material was produced under a BAE Systems (Air Systems) approved quality management system per ISO 9001/AS9100.



Traveler(s)
83529 A

Heat #
K88E

Ingot#

ATI Allvac 4374 Lancaster Highway

Richburg, SC 29729

Phone (803) 789-3595

Page 2 of 6

HEADER REMARKS

- ✓ AIR 9183 ALLOY 6-4, 11/21/66 (Capable of) / AMS 4928R
- ✓ AMS 2631B CLASS A
- ✓ ASTM B-348 2008A, GRADE 5
- ✓ BS 2 TAl1 1974
- ✓ BS 7252 5/1/97 PART 3, ALLOY 6-4
- ✓ DMS 1570C
- ✓ DMS 1570C SPEC098-009A
- ✓ ISO 9001 12/15/00
- ✓ ISO 5832-3 REV. 3 ALLOY 6-4
- ✓ MIL-STD-2154 09/30/82 TYPE I CLASS AA
- ✓ MIL-T-9047G, AM. 2, COND. A, COMP. 6-4
- ✓ RRES90000A
- ✓ MSRR8652 ISSUE 15
- ✓ ASNA3307 REV. K (CAPABLE OF)
- ✓ BAE/AG/SCI PART 3
- ✓ BS 2 TAl2 05/30/74
- ✓ DMD 0776-24 G
- ✓ DMS 1570C SPEC096-062, 01/16/97 AS 9100B
- ✓ M000151 REV. K
- ✓ RPS 707 ISSUE 6
- ✓ RR9000:SABRE 10/2008
- ✓ MSRR8614 ISSUE 13
- ✓ WL 3.7164.1 11/01/1990 Teil 2, Code 3.7164.1
- ✓ SQA 50 ISSUE 11

	CHEMISTRY									
	C	Si	Mn	Mo	Ti	Al	Ti+Al	V	Fe	Cu
TOP	.014	<.01	<.01	<.01	89.48	6.36	-	3.97	.16	<.01
BOT	.015	<.01	<.01	<.01	89.37	6.47	-	3.96	.16	<.01

	CHEMISTRY									
	B	Zr	Y	O	N	Sn	Cr	Cb	Ta	Ni
TOP	<.0010	<.01	<.001	.17	.008	<.01	.01	-	-	.01
BOT	<.0010	<.01	<.001	.17	.004	<.01	.01	-	-	.02

	H
Product	.0025
Product	.0024

CHEMISTRY METHOD

CS-C-ONLY
XRF-TI(TIBAL)-CU

ELEMENTS TESTED BY METHOD

C
MO,SN,CR,NI,FE,ZR,MN,V,AL,SI,TI

Traveler(s) Heat # Ingot#
 83529 A K88E ATI Allvac 4374 Lancaster Highway Richburg, SC 29729 Phone (803) 789-3595

GAS-O/N O,N
 WET-Y Y
 WET-B B
 WET-CU CU
 GAS-H H

CHEMISTRY REMARKS

Chemistry tested at ATI ALLVAC unless otherwise noted.

CHEMISTRY ANALYTICAL METHODS

CS = Combustion/IR Detection

GAS = Inert Gas Fusion

OES = Spark Optical Emission

XRF = X-Ray Fluorescence

WET = Flame Atomic Absorption and/or Graphite Furnace Atomic Absorption and/or Inductively Coupled Plasma Emission and/or Mass Spectroscopy

Operation	Ingot	Heat Treat Code	Test Dir	Temp F	As Shipped			Tensile Test				Tensile Diameter	Tested At	
					UTS ksi	2% Yield ksi	.02% Yield ksi	%EL	%RA	Gage Length				
								4D	5D		4D	5D		
SUPER		1300B	L	ROOM	151.8	125.9		18.0		48.0	0.998		0.2525	ALLVAC MONROE
SUPER		1300B	L	ROOM	152.0	126.5		17.5		47.7	0.998		0.253	ALLVAC MONROE
SUPER		1300B	L	ROOM	153.4	127.6		17.3	48.1		1.107		0.222	ALLVAC MONROE

Test Dir: L = Longitudinal, T = Transverse, ST = Short Transverse, LT = Long Transverse,
 TC = Transverse Center At Size, TM = Transverse Mid-Radius At Size,
 PC = Pancake, DB = Drawbar, PD = Paddle, TT = Top Transverse At Size,
 BT = Bottom Transverse At Size, LC = Long Center, TX = Top Transverse Mid-Radius At Size,
 LM = Longitudinal Mid Radius, LS = Longitudinal Surface, TS = Transverse Surface
 Operation: SUPER = Crosshead Sep Rate of .10 inches/minute

Traveler(s)
83529

Heat #
K88E

Ingot#

ATI Allvac 4374 Lancaster Highway

Richburg, SC 29729

Phone (803) 789-3585

Page 4 of 6

As Shipped Tensile Test

Operation	Ingot#	Heat Treat Code	Test Dir	Temp C	UTS Mpa	2% Yield Mpa	.02% Yield Mpa	%EL			Gage Length		Tensile Diameter	Tested At
								4D	5D	%RA	4D	5D		
SUPER		1300B	L	ROOM	1046.5	868.0		18.0		48.0	0.998	0.2525	ALLVAC MONROE	
SUPER		1300B	L	ROOM	1048.3	872.2		17.5		47.7	0.998	0.253	ALLVAC MONROE	
SUPER		1300B	L	ROOM	1058.0	879.8			17.3	48.1		1.107	0.222	ALLVAC MONROE

Test Dir: L = Longitudinal, T = Transverse, ST = Short Transverse, LT = Long Transverse,
 TC = Transverse (Center At Size), TM = Transverse Mid-Radius At Size,
 PC = Pancake, DB = Drawbar, PD = Paddle, TT = Top Transverse At Size,
 BT = Bottom Transverse At Size, LC = Long Center, TX = Top Transverse Mid-Radius At Size,
 LM = Longitudinal Mid Radius, LS = Longitudinal Surface, TS = Transverse Surface
 Operation: SUPER = Crosshead Sep Rate of .10 inches/minute

AS SHIPPED HARDNESS

Ingot	Heat Treat Code	Hardness Val	Hardness Type	Tested At
	1300B	35	ERC	ALLVAC MONROE

TENSILE/STRESS RUPTURE HEAT TREATMENT

HT Code: 1300B

Location	Temp		Furnace Cool Rate Per Hrs (F)	Cool Code
	F	Hours Mins		
PLANT	1300	2		AC

TENSILE/STRESS RUPTURE HEAT TREATMENT

HT Code: 1300B

Location	Temp		Furnace Cool Rate Per Hour (C)	Cool Code
	C	Hours Mins		
PLANT	704	2		AC

Traveler(s)
83529 A

Heat #
K88E

Ingot#

ATI Allvac 4374 Lancaster Highway

Richburg, SC 29729

Phone (803) 789-3595

Page 5 of 6

METALLOGRAPHY

BETA TRANSUS DETERMINED BY DTA: Top - 1830 F, Bottom - 1830 F

Material guaranteed to be free of alpha case.

Microstructure evaluated and found acceptable to ETTC2 Fig A1 & A2 , DMS 1570 Fig 4A, and for general structure.

Tested at Allvac Monroe

SONIC

Material ultrasonically inspected and found acceptable to the requirements of AMS 2631 Class A, MIL-STD-2154 Type I Class AA, RPS 707 Class AAR. Tested at Shalmet

MACRO

Material macro evaluated and found acceptable. Tested at Allvac Monroe

REMARKS

Material has been produced, sampled, inspected, and tested in accordance with the customer purchase order and referenced specifications and conforms to the requirements unless otherwise noted in this certificate of test.

Any deviations to specification or customer purchase order requirements relative to testing, test values, hot working fixed practices, have been resolved in writing with customer prior to shipment.

The recording of false, fictitious, or fraudulent statements or entries on this document may violate Federal statutes, including but not limited to Title 18, Chapter 47 of the United States Code, and may be punishable as a felony.

If customer purchase order does not specifically reference a revision to a specification, Allvac will work to the latest revision on file and in effect at time of order placement.

Test methods are per the latest ASTM Standards, currently recognized industry practices; or as agreed upon between Allvac and customer.

Any chemical elements analyzed and found to have values below the actual limits of detection may be reported as < less than or reported at the detection level.

When values are reported to the significant places called for in the specifications, rounding will be done in accordance with ASTM E-29.

Traveler(s) Heat # Ingot#
83529 A K88E ATI Allvac 4374 Lancaster Highway Richburg, SC 29729 Phone (803) 789-3595 Page 6 of 6

This is to certify that during manufacturing, handling, testing and inspection, this material did not come in direct contact with mercury or any device employing a single boundary of containment.

This Certificate of Test shall not be reproduced except in full, without the written approval of Allvac Quality.

No weld repair has been performed on this material.

Material Safety Data Sheets (MSDS) - View or print from our site: www.allvac.com. Printed copies available on request from the Allvac Sales Department.

Allvac products have not come in contact with radioactive, fertile or fissionable materials during manufacturing or processing.

Melt source in compliance with DFAR 252.225-7014, Alternate 1.

SPECIAL REMARKS

Melt method: Double VAR

Material melted and manufactured in the United States.

Material has been 100% alloy type tested.

TEST METHODS: C = ASTM E1941 (2004); O/N = ASTM E1409 (2005); H = ASTM E1447 (2005); Plasma Emission = ASTM E2371 (2004), ASTM E1097 (2007 Wah Chang only); XRF = ASTM E539 (2007); RIT = ASTM E8 (2008); ETT = ASTM E21 (2005); Creep = ASTM E139 (2006); Fracture Toughness = ASTM E399 (2006*1); Rockwell Hardness = ASTM E18 (2007); Brinell Hardness = ASTM E10 (2007*1); Grain Size = ASTM E112 (1996/2004*1)

B. Linear stage displacement of laser stage

A high speed camera was set up to determine the acceleration and velocity of the X and Y direction of the laser stage. Figure B-1 graphs the velocities of all runs, plotted against their respective displacements. The data was derived from the high-speed footage by tracking a particular point from frame to frame. In this case the left edge of the white line that was positioned on the moving table. The high-speed footage was processed using a LabVIEW VI, please see screen shot as in Figure B-2 The graph represented the 8 degree polynomial trend line that was fitted to the raw displacement data to smooth out the 'blockiness' associated with the camera's pixel resolution (displacement accuracy was ± 0.806 mm and ± 0.693 mm for the 320 mm run and the 115 mm run respectively). The polynomial trend line had an excellent fit for the raw displacement data. This polynomial was then differentiated to obtain the velocity. The graph clearly show that at the highest velocity a lead way of approximately 55 mm needs to be accounted for to achieve uniform velocities during laser processing.

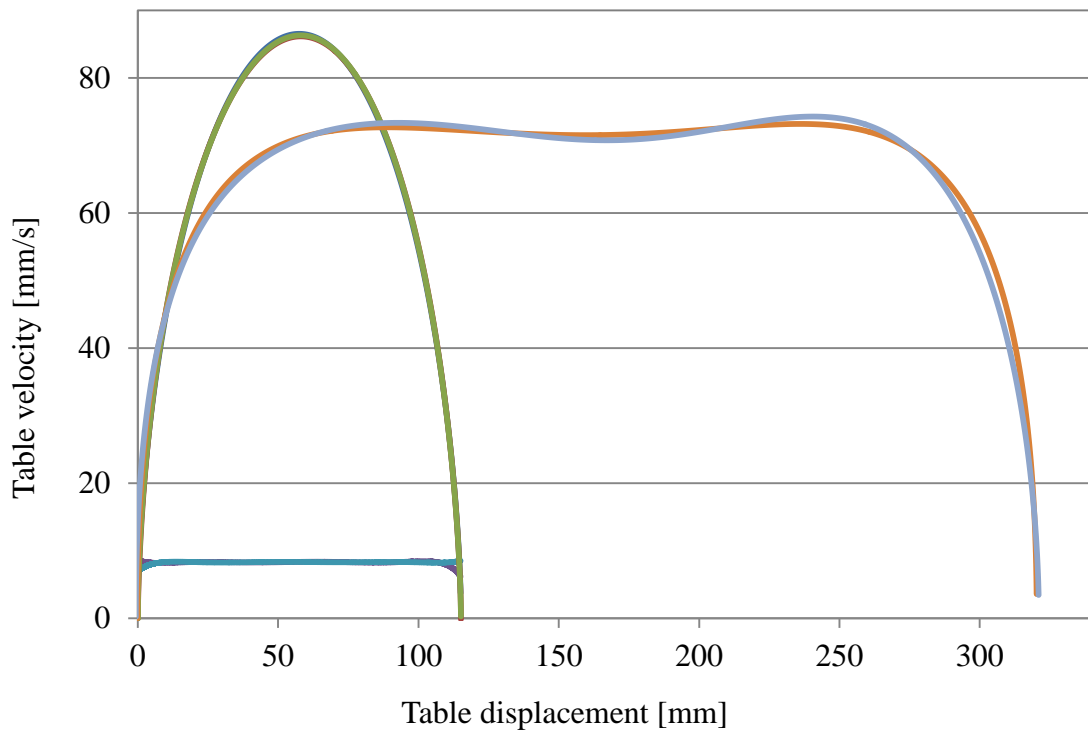


Figure B-1: Velocity profile of laser table in the Y direction

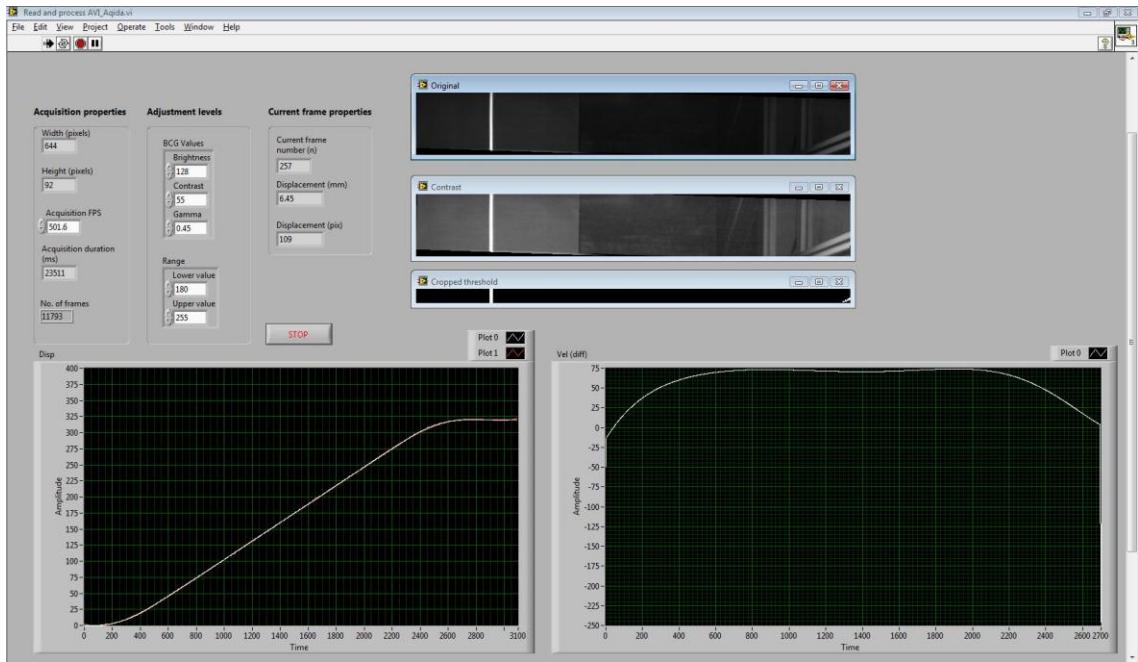


Figure B-2: LabVIEW data acquisition of frames from the high speed camera

C. Preliminary DOE for 316L

Design of experiments

A 3^3 DOE was implemented. Three processing parameters were varied at three levels irradiance (10.5, 23.9 and 38.2 kW/mm²) residence time (265, 382 and 478 μ s) and overlap (0, 10 and 30%), see Table C-1.

Table C-1: Processing parameter for the initial DOE.

<i>ID</i>	<i>Peak Power</i> (W)	<i>Irradiance</i> (kW/mm ²)	<i>Tangential Speed</i> (mm/s)	<i>Residence Time</i> μ s	<i>Overlap</i> (%)
1	330	10.5	419	265	0
2	750	23.9			
3	1200	38.2			
4	330	10.5	524	382	
5	750	23.9			
6	1200	38.2			
7	330	10.5	754	478	
8	750	23.9			
9	1200	38.2			
10	330	10.5	419	265	10
11	750	23.9			
12	1200	38.2			
13	330	10.5	524	382	
14	750	23.9			
15	1200	38.2			
16	330	10.5	754	478	
17	750	23.9			
18	1200	38.2			
19	330	10.5	419	265	30
20	750	23.9			
21	1200	38.2			
22	330	10.5	524	382	
23	750	23.9			
24	1200	38.2			
25	330	10.5	754	478	
26	750	23.9			
27	1200	38.2			

Preliminary DOE Results

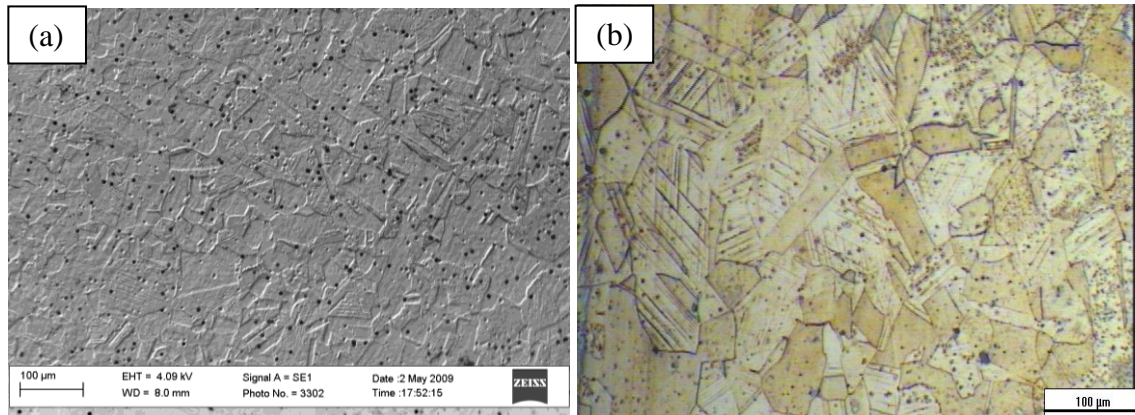


Figure C-1: Optical micrographs of as received 316L Stainless Steel
(a) SE image and (b) optical micrograph.

Low irradiance

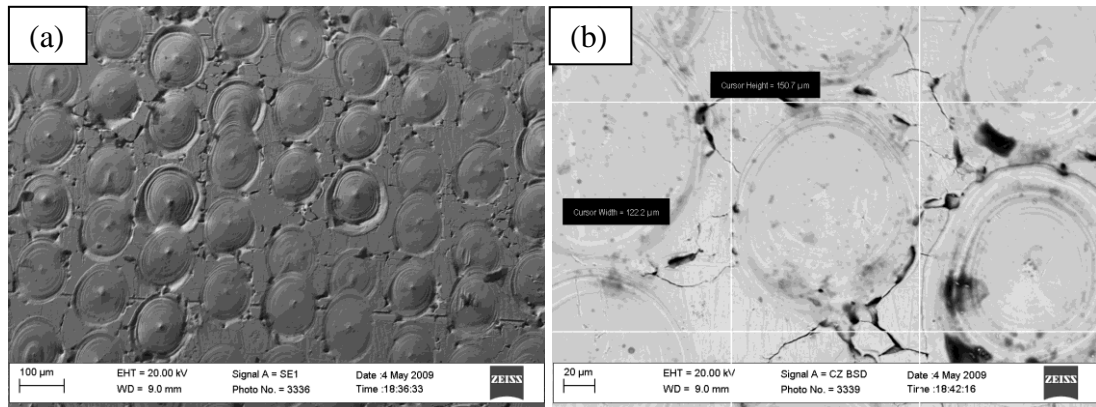


Figure C-2: Optical micrographs processed at low irradiance 10.5 kW/mm^2

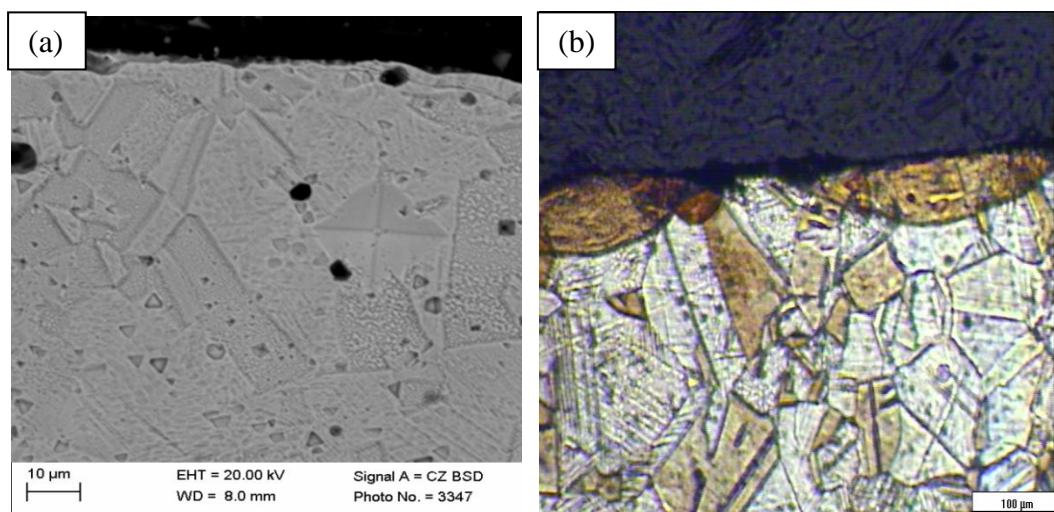


Figure C-3: Optical micrographs of cross-sectional view of 316L SS
corresponding to Figure C-2.

At low irradiance marking effect were observed. The pulse energy was too low to penetrate the surface. Only localised surface melting occurred. The overlap was set at 10% but in the micrograph no evidence of overlap were visible these images. This may be due to two reasons. First reason was may be the speed of rotation was not constant due to the drill used as rotational mechanism. The other reason was due to the beam intensity. CO₂ laser do not have perfect Gaussian beam. Power intensity was concentrated on the middle section of the beam. This could be verified by measurements taken using the SEM. The diameter of the spot seems to be ~ 150 μ but the laser was set to output a 200 μ diameter beam.

High Irradiance

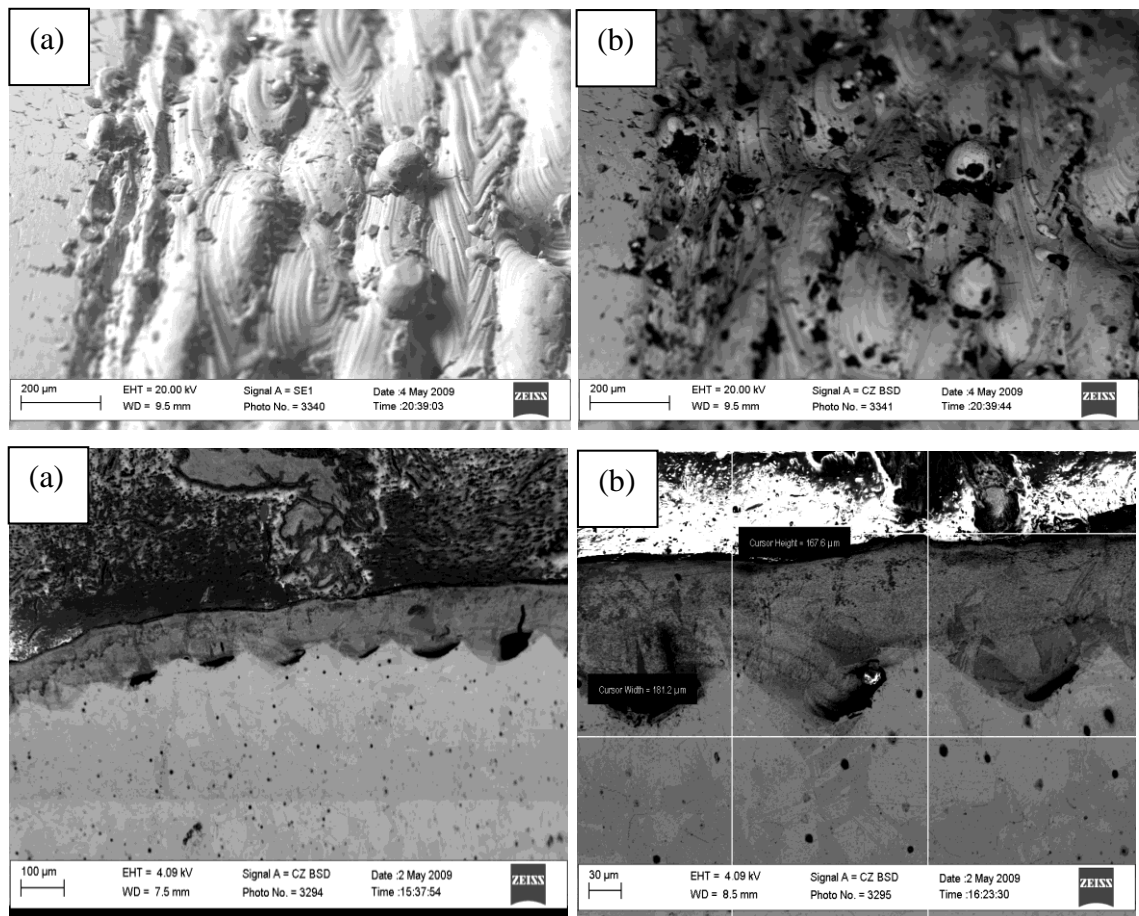


Figure C-4: Optical micrograph of samples processed at high irradiance (38.2 kW/mm^2) at various magnifications.

As compared to samples processed at low irradiance, the surface of the samples processed at high irradiance had full melting effect. The surfaces in Figure C-4 showed a rougher morphology attributed to low cooling rates. Cracks were not visible due to the melting and re-solidification. At a higher irradiance u can clearly observe the melt

pools. Significant grain structure change is observed but due to low cooling rates and high exposure times the surface had lower hardness compared to substrate

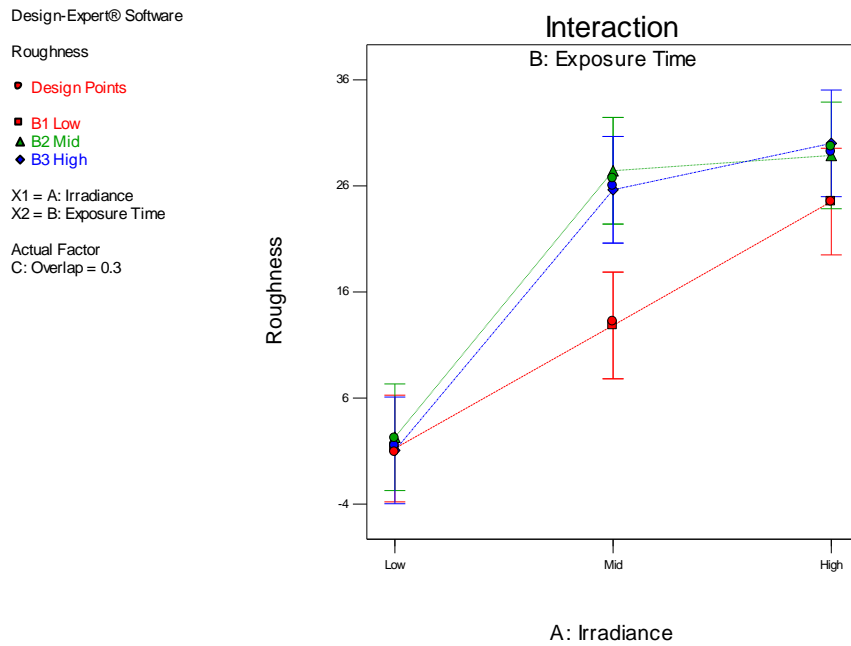


Figure C-5: Effects of irradiance and residence time on roughness

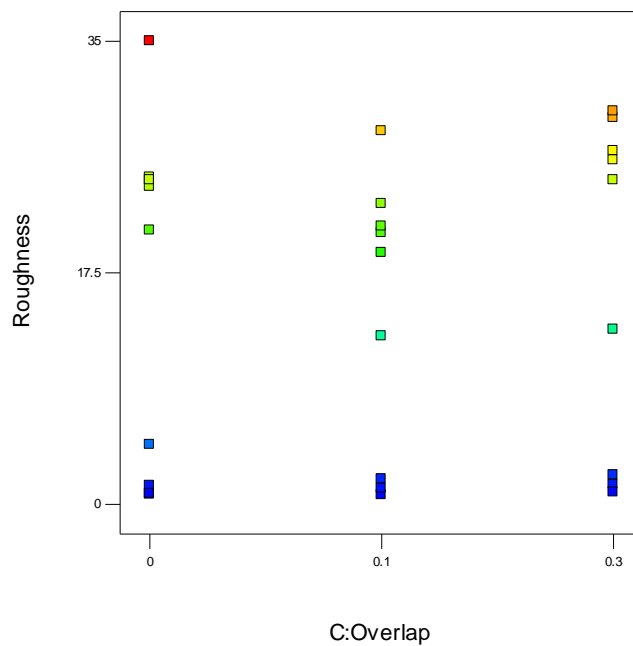


Figure C-6: Effect of overlap on roughness

The DOE showed that the overlap had no real effect on the surface roughness or any other measured properties for that matter. This was attributed to the rotational mechanism and Gaussian beam discussed. The contour plot verified that the least roughness was observed at low irradiance. This was due to low structure change. Low

irradiance did not produce melting. Therefore it was be insignificant for this study. High irradiance proved to produce excessive energy with the melting producing uneven surfaces.

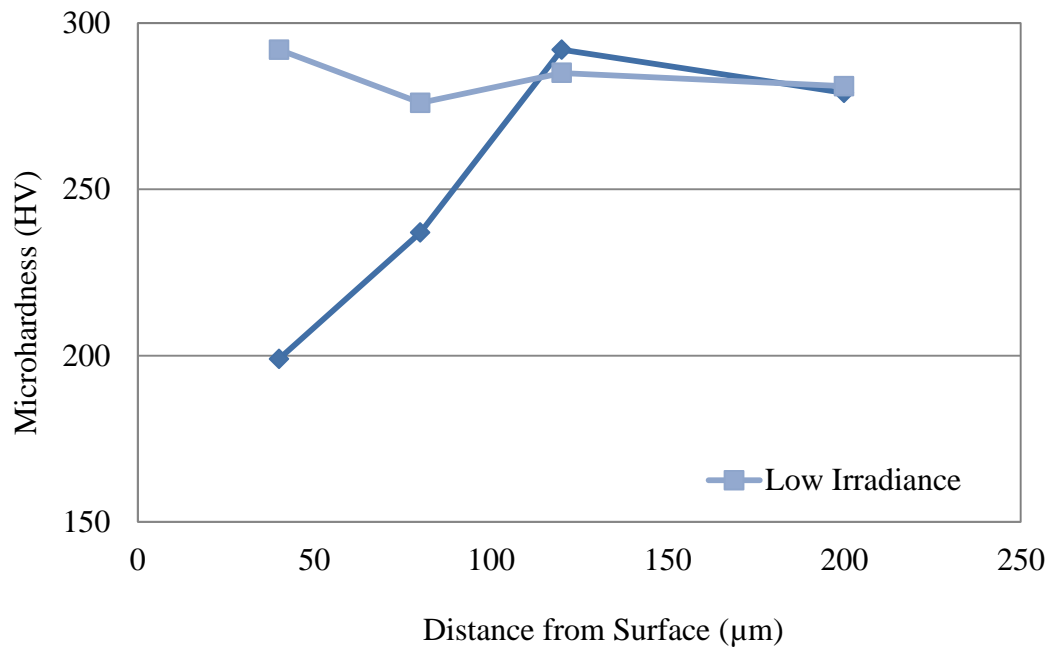


Figure C-7: Effects of low irradiance and high irradiance on microhardness

Figure C-8 to figure C-13 present EDS analysis of a laser treated samples.

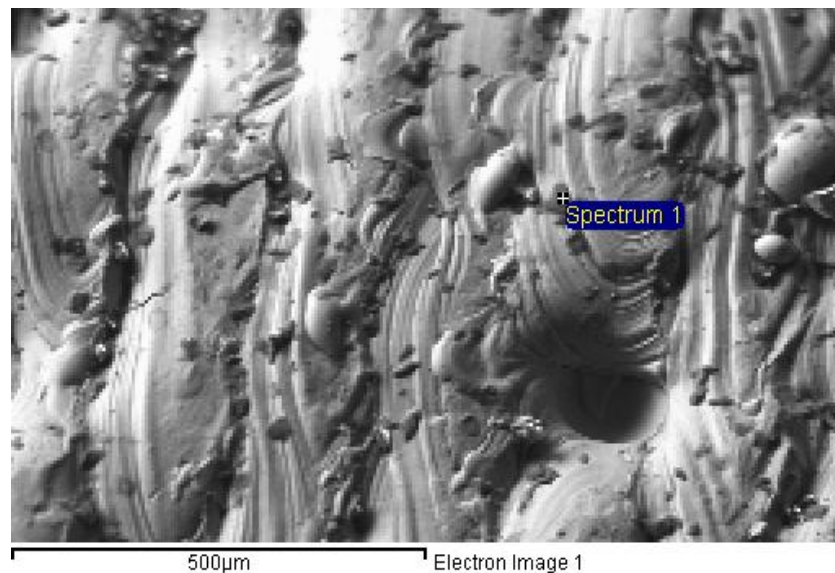


Figure C-8: Micrograph of spectrum 1.

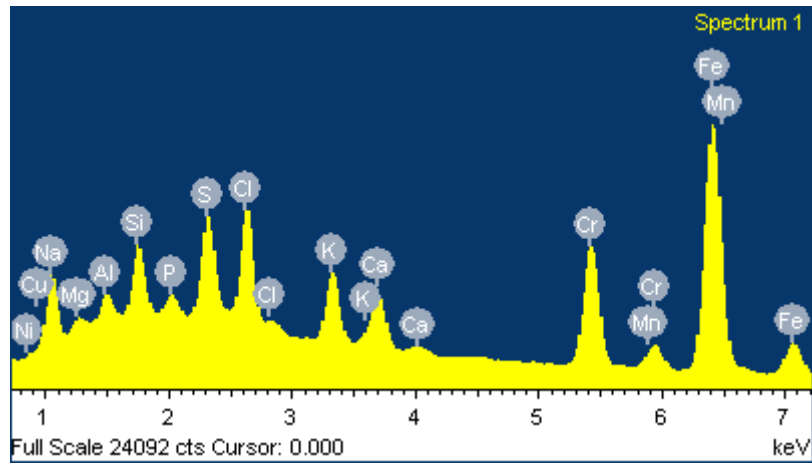


Figure C-9: Spectrum 1 analysis of the slag.

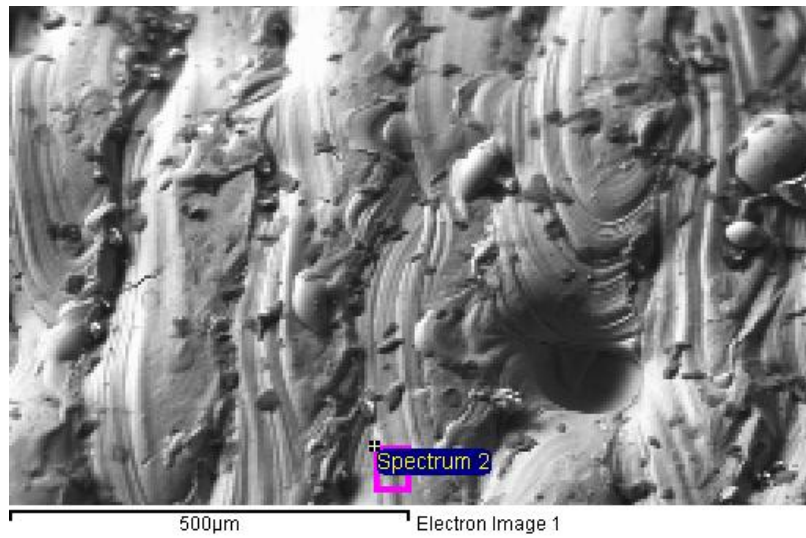


Figure C-10: Micrograph of spectrum 2 of laser treated region

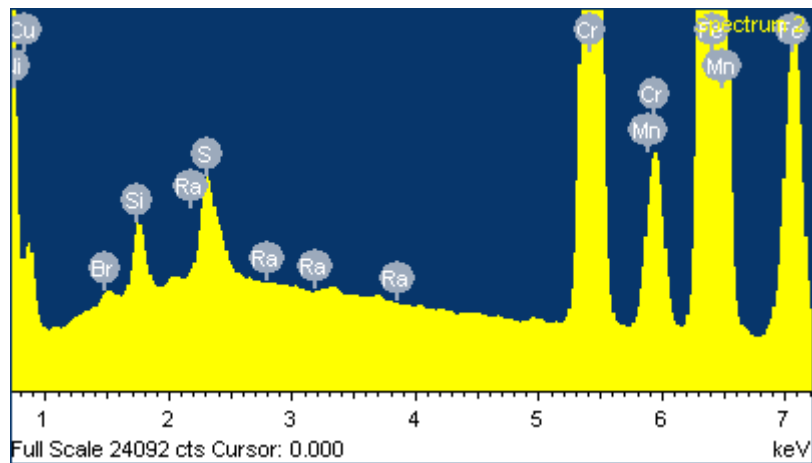


Figure C-11: Spectrum 1 analysis of the slag – laser treated region

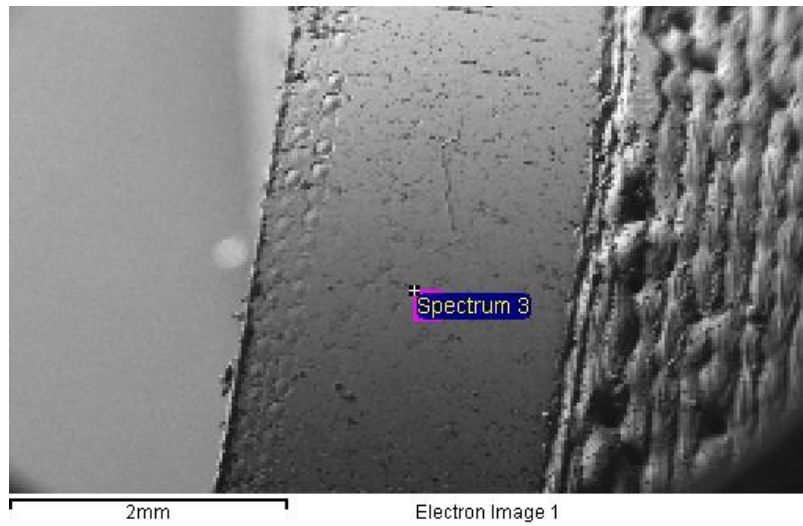


Figure C-12: Micrograph of spectrum 3 - untreated region

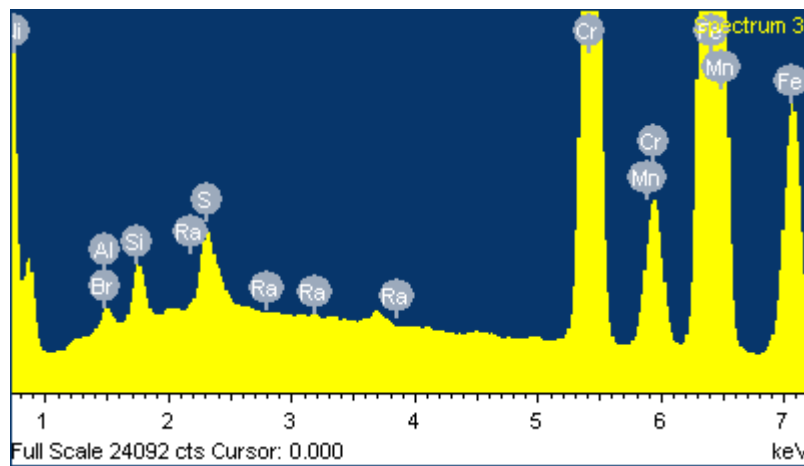


Figure C-13: Spectrum 3 analysis of untreated region

Table C-2: Comparison of Spectrums 1, 2 and 3

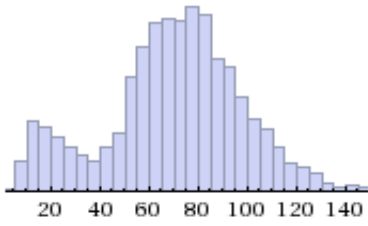
	<i>Untreated region</i>	<i>Laser treated region</i>	<i>Slag</i>
C K	15.52	18.39	71.10
O K	2.22	11.18	10.35
Al K	0.17	-	0.20
Si K	0.61	0.46	0.54
S K	0.60	0.48	0.90
Cr K	14.67	12.79	2.88
Mn K	1.31	0.97	0.27
Fe K	56.65	48.08	8.58
Ni K	8.10	6.97	0.98
Cu K	-	0.49	0.20
Br L	0.18	0.18	
Ra M	-0.04	0.02	
Na K			1.02
Mg K			0.12
P K			0.21
Cl K			1.20
K K			0.80
Ca K			0.66

D. Recommended cut-off lengths for roughness measurements

Table D-1: ISO 4288 recommended cut-off lengths for roughness measurements

Non-Periodic Profile		Periodic Profiles	Measuring conditions according to DIN EN ISO 4288 and DIN EN ISO 3274				
Grinding, honing, lapping, eroding ↓ or ↓		Turning, milling, planing	λ_c =cutoff filter				
			λ_c / l_n =Cut off / Evaluation Length				
			R_{tip} =Maximum radius of the stylus				
			l_n =Evaluation length				
			l =Sampling length				
Rz (μm)	Ra (μm)	RSm (mm)	λ_c (mm)	l_n (mm)	λ_c / l_n	l (mm)	R_{tip} (μm)
>0.025 to 0.1	>0.006 to 0.02	>0.013 to 0.04	0.08	0.4	0.2	0.08	2
>0.1 to 0.5	>0.02 to 0.1	>0.04 to 0.13	0.25	1.25	0.2	0.25	2
>0.5 to 10	>0.1 to 2	>0.13 to 0.4	0.8	4	0.2	0.8	2*
>10 to 50	>2 to 10	>0.4 to 1.3	2.5	12.5	0.2	2.5	5
>50 to 200	>10 to 80	>1.3 to 4	8	40	0.2	8	10

E. Calculation of load for pin on disk wear testing

90% reference range	(24 to 105) kg
95% reference range	(11 to 125) kg
99% reference range	(6.8 to 156) kg
$\pm 1\sigma$ range	(41 to 100) kg
$\pm 2\sigma$ range	(12 to 129) kg
distribution	
median	72 kg
mean	70 kg
data sample size	9847 people

(data from NHANES 2006 study, weighted for USA demographics)

Figure E-1: Diagram highlight weight distribution for humans sourced from Wolfram Alpha

Assuming three times the mass of human body to be 210 kg = 2060 N

Average femoral head diameter = 28 mm

Wear testing ball diameter = 5 mm

Contact area of femoral head (hemi-spherical surface area) = $2\pi \times r^2 = 392\pi$

Contact area of wear testing ball (since disk is flat) = $\pi \times r^2 = \pi \times 1^2 = \pi$

(Approx. 1mm diameter contact area was assessed from examination of scaled engineering drawings, see Figure E2 below)

In order to get a reasonable value for the load that should be used in the wear test, the ratio of the contact area of contact between the pin and disk divided by the contact area of the femoral head was multiplied by expected load during running which is known to be three times body weight and is calculated above as 2060 N.

$$\therefore \text{Load used in the experiment} = \frac{\pi}{392\pi} \times 2060 = 5.25 = \text{rounded to } 5 \text{ N} \quad (24)$$

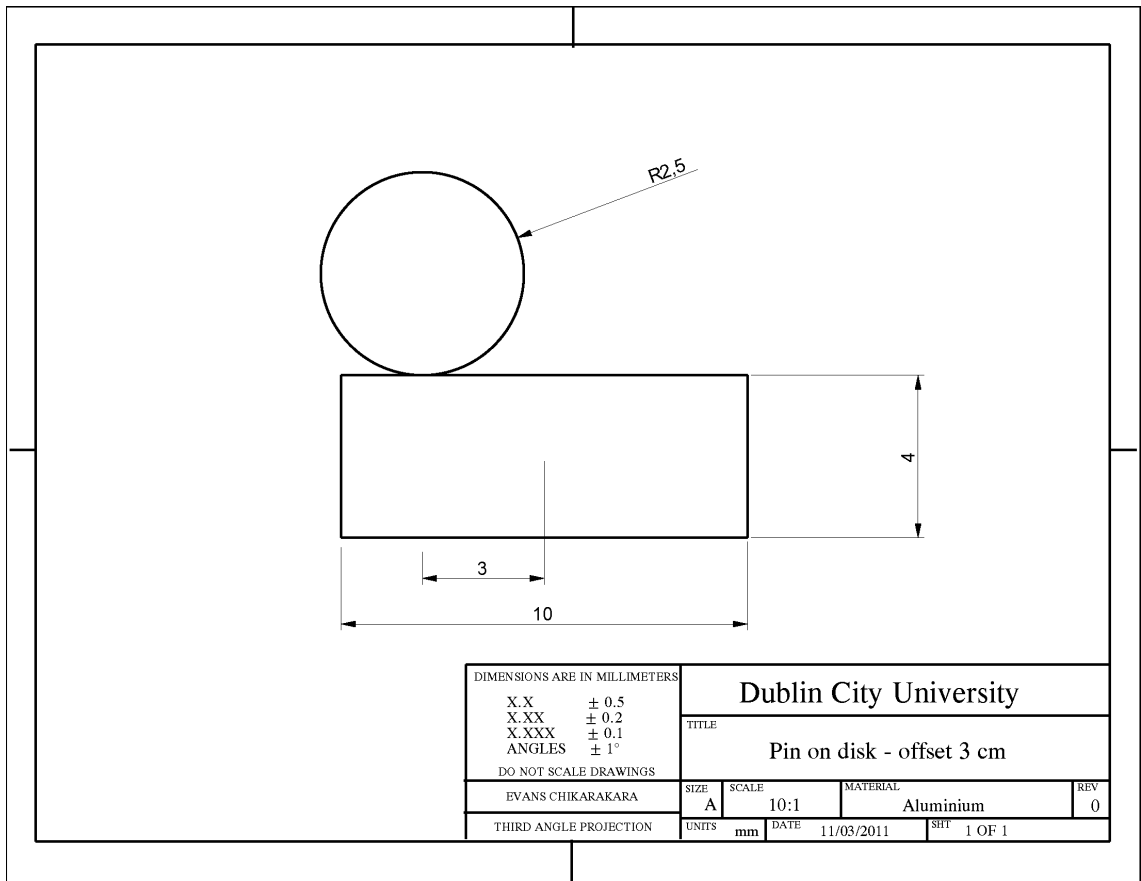


Figure E-2: Illustration of pin on disk contact point.

F. Additional Results for 316L stainless steel DOE

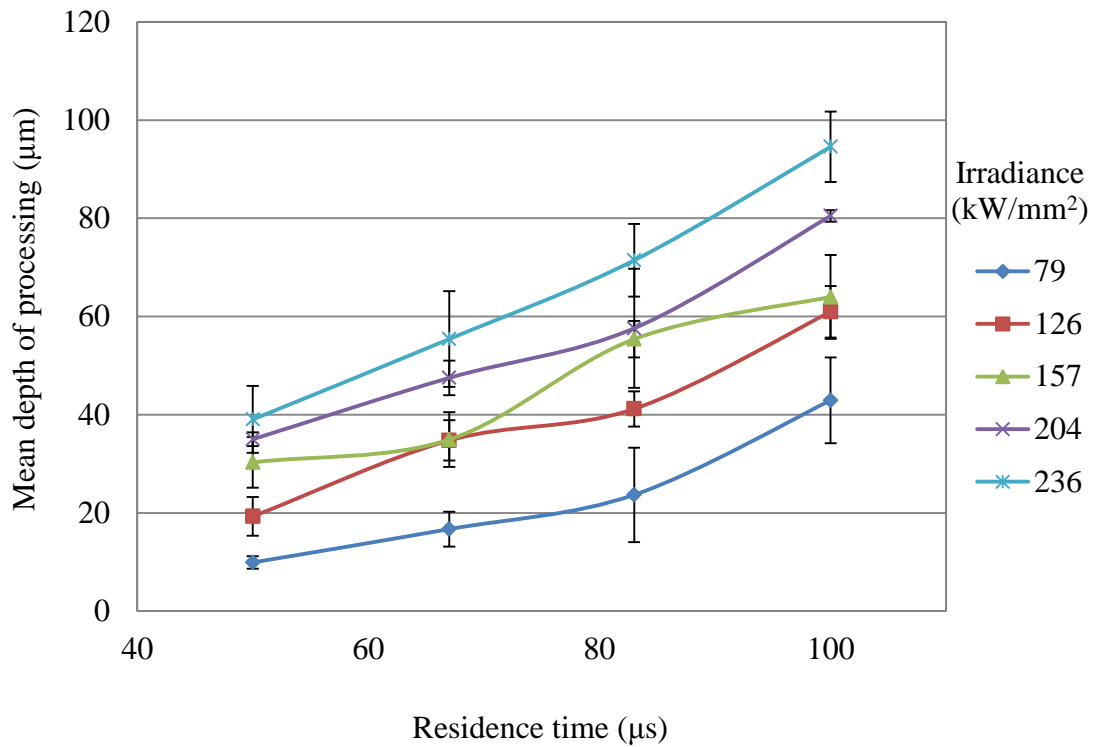


Figure F-1: Effects of irradiance and residence time on meltpool depth

Effects of pre-treatments on roughness

An analysis of the effects of laser processing parameters on average roughness of the sample was carried out. Figure F-2 (a) shows the roughness produced by the laser irradiation when the sample had been subjected to different pre-treatments.

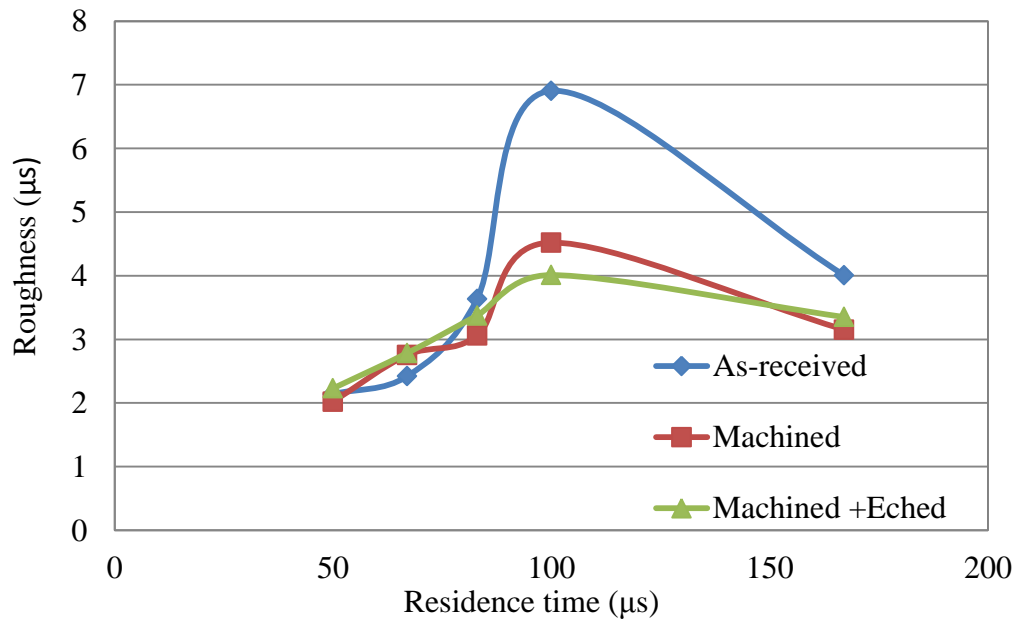


Figure F-2: Effects of surface pre-treatment and power

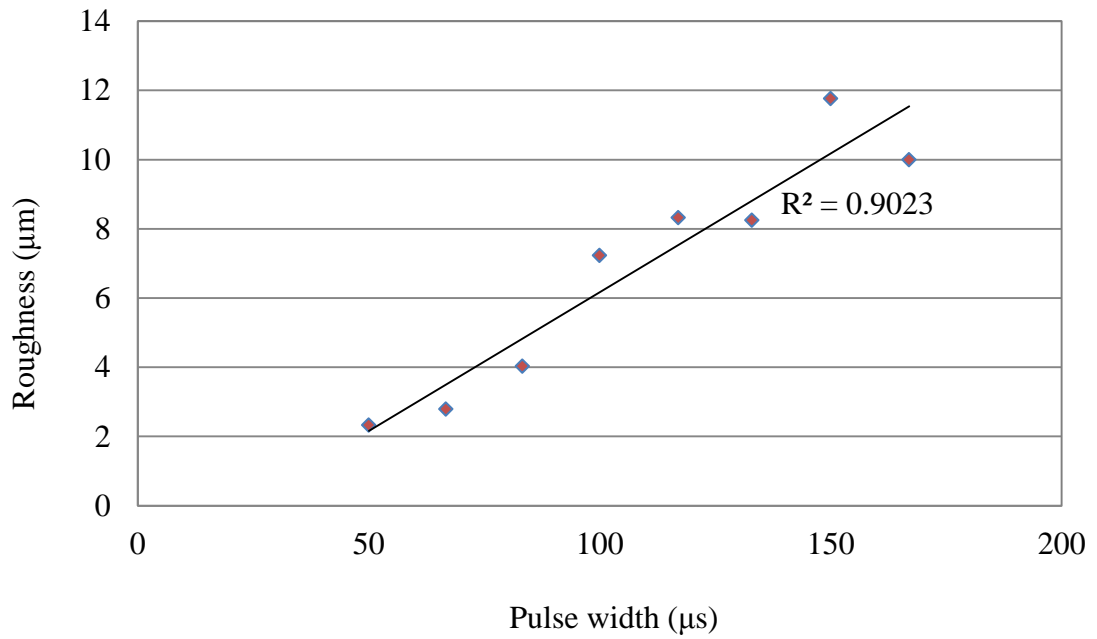


Figure F-3: Effects of (a) surface pre-treatment and power;
 (b) pulse width on roughness

Pre-treated samples produced higher roughness measurements, up to 14 μm mainly due to the machining done prior to laser processing. Low roughness results below 600W were caused by insufficient melting of the surface. Resulting roughness of the samples can be correlated to the pulse width as shown in Figure F-2 (b). Figure F-2 (b) shows an increase in roughness as the pulse width is increased. Increase in pulse width periods results in longer interaction between laser and surface of material. This intensifies melting of the surface and delays the cooling rate consequently resulting in rougher steel surfaces.

G. Meltpool Data

Table G-1: Raw data for meltpool measurements for Ti-6Al-4V DOE 1

<i>Parameter</i>	<i>Units</i>	<i>Data</i>								
<i>DOE ID</i>		<i>1</i>	<i>4</i>	<i>7</i>	<i>2</i>	<i>5</i>	<i>8</i>	<i>3</i>	<i>6</i>	<i>9</i>
<i>Residence Time</i>	<i>ms</i>	2.16	1.44	1.08	2.16	1.44	1.08	2.16	1.44	1.08
<i>Irradiance</i>	<i>kW/mm²</i>	15.72			20.43			26.72		
<i>Meltpool Depth</i>	<i>(μm)</i>	35	20	19	40	29	29	49	36	20
		31	31	17	37	28	29	44	39	28
		35	39	22	36	35	24	44	35	27
		30	25	26	38	35	27	49	33	26
		33	22	20	44	39	25	55	28	35
		41	25	26	35	39	24	50	31	32
		43	21	24	49	45	25	41	28	33
		27	22	15	50	38	28	39	30	34
		40	21	19	40	34	27	42	44	27
		43	20	18	39	41	23	48	39	29
<i>Mean</i>	<i>(μm)</i>	35.80	24.60	20.60	40.80	36.30	26.1	46.10	34.30	29.10
<i>StdDev</i>	<i>(μm)</i>	5.69	6.06	3.78	5.22	5.23	2.09	4.91	5.29	4.53
<i>Error</i>	<i>%</i>	0.159	0.246	0.183	0.128	0.144	0.083	0.106	0.154	0.156
<i>Confidence</i>	<i>%</i>	95								
<i>t-value</i>		2.262157								
<i>Lower Error</i>		4.07	4.33	2.70	3.74	3.74	2.14	3.51	3.79	3.24
<i>Upper Error</i>		4.07	4.33	2.70	3.74	3.74	2.14	3.51	3.79	3.24

H. Roughness Data

Table H-1: Raw data for average roughness measurements for Ti-6Al-4V DOE 1

Parameter	Units	Data								
DOE ID		1	2	3	4	5	9	7	8	9
Irradiance	kW/mm^2	15.72	20.43	26.72	15.72	20.43	26.72	15.72	20.43	26.72
Residence Time	ms	2.16			1.44			1.08		
Average Roughness	(μm)	2	2	2	2	2	1	2.7	1.7	1.3
		2	1	1	2	2	2	2.5	1.9	1.2
		2	1.6	1.4	2.2	1.6	1.4	2.9	1.8	1.4
		1.8	1.5	1.6	2.3	1.5	1.4	2.6	1.7	1.5
		2.2	1.5	1.4	2.4	1.7	1.6	2.9	2	1.5
Mean	(μm)	1.93	1.50	1.47	2.30	1.60	1.43	2.73	1.83	1.39
StdDev	(μm)	0.17	0.07	0.11	0.10	0.07	0.11	0.18	0.13	0.13
Error	%	0.09	0.05	0.07	0.04	0.04	0.08	0.07	0.07	0.09
Confidence	%	95								
Critical T		2.776445								
Lower Error		0.208	0.088	0.136	0.124	0.088	0.142	0.222	0.162	0.162
Upper Error		0.208	0.088	0.136	0.124	0.088	0.142	0.222	0.162	0.162

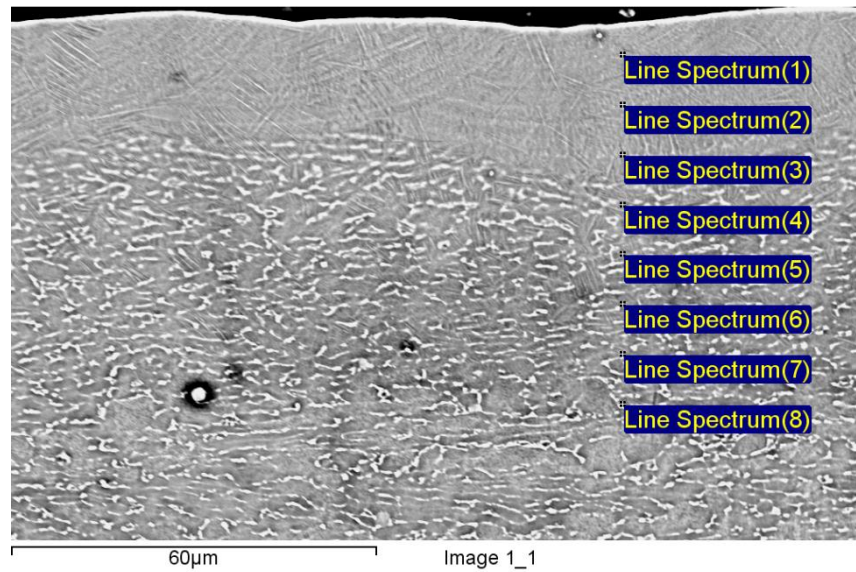
I. Energy Dispersive X-ray Spectroscopy Raw Data

Table I-1: Elemental composition using two different scan methods and processing times

Spectrum	Ti	Al	V	Si	Total
Area scan _ process time 6	89.35	6.03	4.06	0.56	100.00
Area scan _ process time 1	89.42	5.98	4.06	0.54	100.00
(1,1)	89.92	5.46	4.18	0.44	100.00
(2,1)	90.30	5.48	4.22		100.00
(3,1)	89.13	6.39	3.91	0.57	100.00
(4,1)	89.36	6.03	4.28	0.33	100.00
(5,1)	88.34	6.86	4.31	0.49	100.00
(1,2)	89.93	5.38	4.10	0.60	100.00
(2,2)	89.88	5.50	4.13	0.48	100.00
(3,2)	89.58	6.28	4.14		100.00
(4,2)	89.52	6.01	4.10	0.37	100.00
(5,2)	87.85	7.31	4.34	0.50	100.00
(1,3)	89.30	6.09	4.08	0.52	100.00
(2,3)	89.20	5.27	4.52	1.01	100.00
(3,3)	89.59	6.18	4.23		100.00
(4,3)	89.90	5.66	4.14	0.30	100.00
(5,3)	88.88	6.34	4.18	0.59	100.00
(1,4)	87.50	7.74	3.83	0.93	100.00
(2,4)	89.22	5.86	4.07	0.85	100.00
(3,4)	89.06	6.42	4.12	0.40	100.00
(4,4)	89.13	6.29	4.14	0.43	100.00
(5,4)	89.75	5.47	4.28	0.50	100.00
(1,5)	88.51	6.43	4.03	1.03	100.00
(2,5)	89.57	5.74	4.21	0.47	100.00
(3,5)	89.06	6.49	4.05	0.41	100.00
(4,5)	88.75	6.65	4.25	0.35	100.00
(5,5)	90.10	5.07	4.20	0.62	100.00
Max.	90.30	7.74	4.52	1.03	
Min.	87.50	5.07	3.83	0.30	

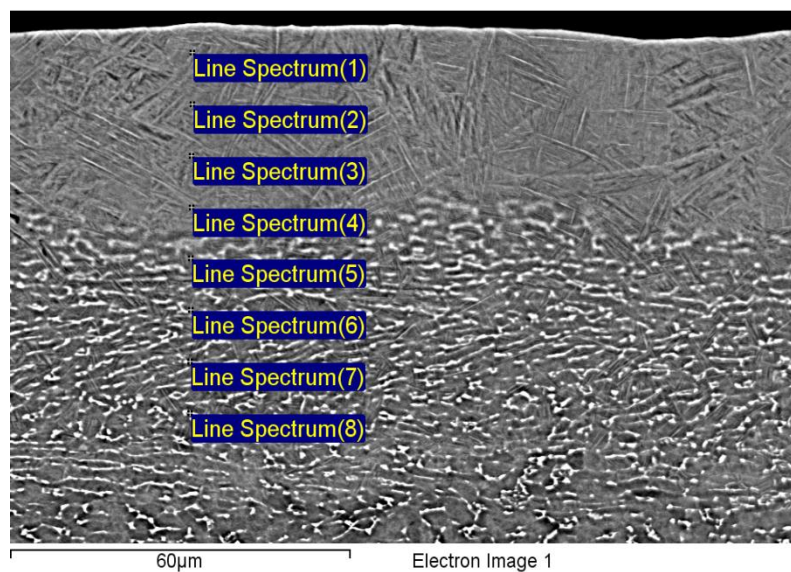
Cross-sectional Analysis

Sample 1



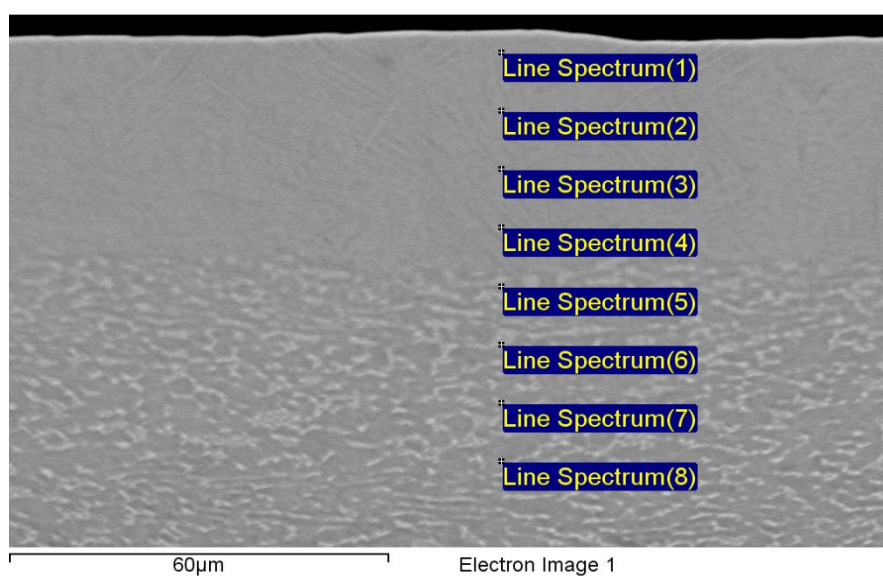
Spectrum	Ti	Al	V	C	Si	Total
1	80.38	5.49	3.53	10.23	0.38	100.00
2	84.76	4.87	4.23	5.65	0.50	100.00
3	86.80	5.33	3.41	4.46		100.00
4	84.14	4.59	5.81	5.45		100.00
5	80.39	4.39	7.79	7.43		100.00
6	84.71	5.00	3.97	6.32		100.00
7	86.21	4.94	3.32	5.53		100.00
8	86.22	5.11	3.75	4.92		100.00
Max.	86.80	5.49	7.79	10.23	0.50	
Min.	80.38	4.39	3.32	4.46	0.38	

Sample 2



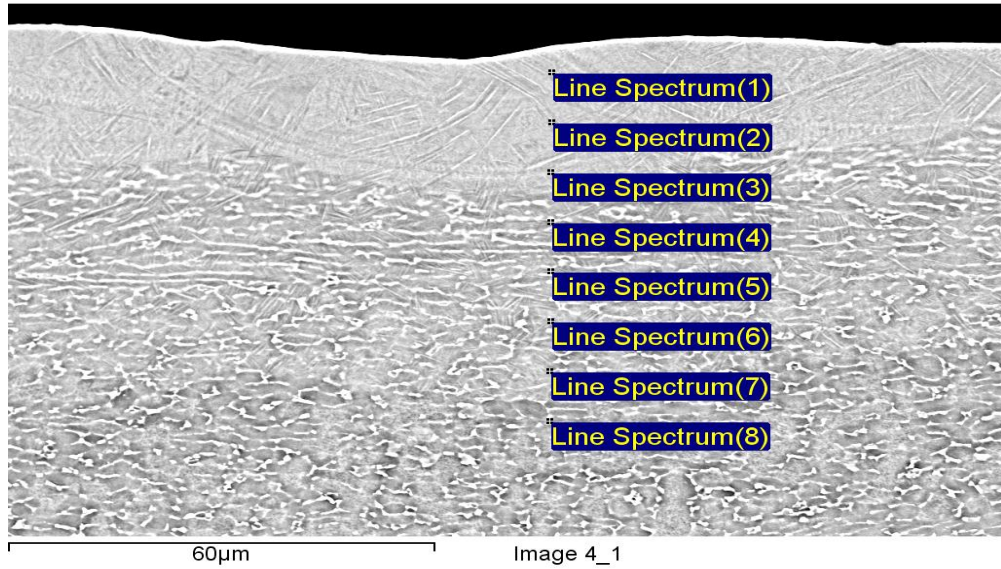
Spectrum	Ti	Al	V	Si	Ca	Total
1	89.71	5.67	4.09	0.27	0.27	100.00
2	90.33	5.52	3.85	0.30		100.00
3	90.02	5.68	4.07	0.23		100.00
4	89.77	5.71	4.28	0.23		100.00
5	91.12	6.09	2.79			100.00
6	88.65	5.23	6.12			100.00
7	89.74	5.47	4.79			100.00
8	90.13	5.69	4.18			100.00
Max.	91.12	6.09	6.12	0.30	0.27	
Min.	88.65	5.23	2.79	0.23	0.27	

Sample 3



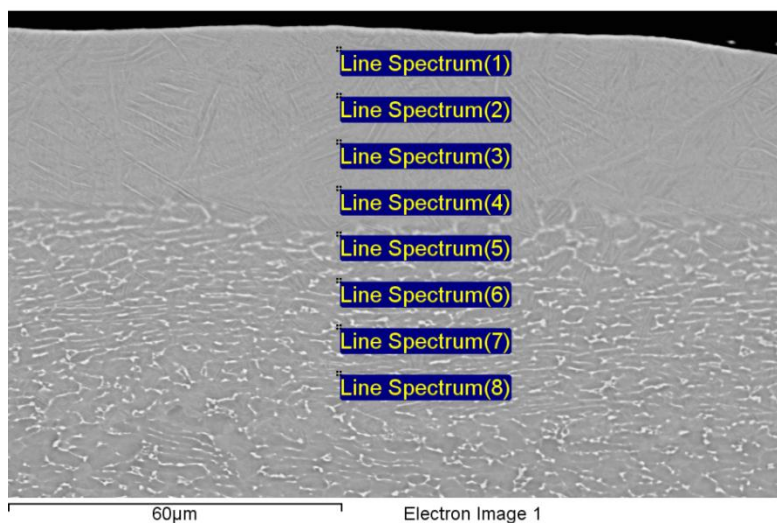
Spectrum	Ti	Al	V	Si	Ca	Total
1	89.74	5.62	4.10	0.27	0.27	100
2	89.98	5.77	4.01	0.24		100
3	90.25	5.74	4.01			100
4	89.90	5.74	4.10	0.26		100
5	90.19	5.70	4.12			100
6	88.07	4.94	6.68			100
7	88.82	5.51	5.67			100
8	90.43	5.62	3.95			100
Max.	90.43	5.77	6.68	0.27	0.27	
Min.	88.07	4.94	3.95	0.24	0.27	

Sample 4



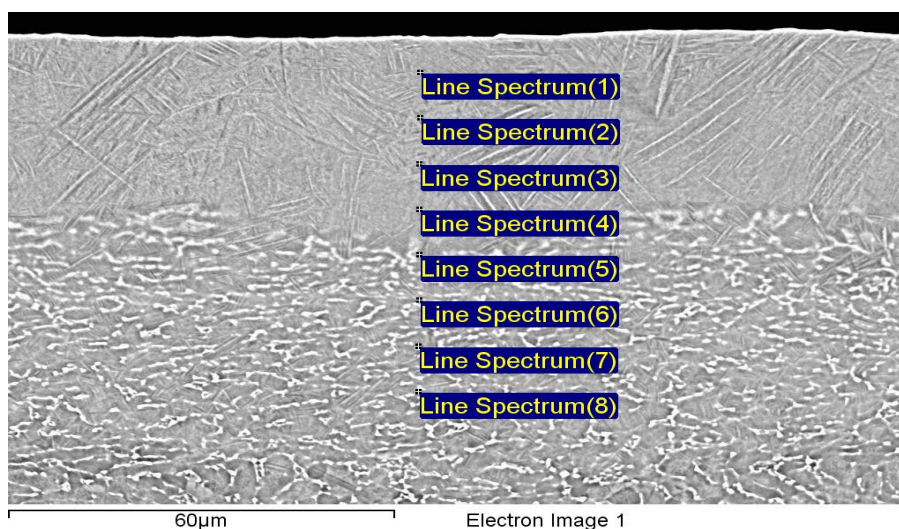
Spectrum	Ti	Al	V	Si	Ca	Fe	Total
1	89.46	5.94	3.99	0.34	0.28		100.00
2	89.58	5.97	4.09	0.35			100.00
3	89.78	5.87	4.03	0.31			100.00
4	90.16	6.57	2.96	0.31			100.00
5	87.59	5.79	6.31			0.31	100.00
6	91.01	6.36	2.63				100.00
7	90.96	6.29	2.76				100.00
8	85.65	5.35	8.33			0.66	100.00
Max.	91.01	6.57	8.33	0.35	0.28	0.66	
Min.	85.65	5.35	2.63	0.31	0.28	0.31	

Sample 5



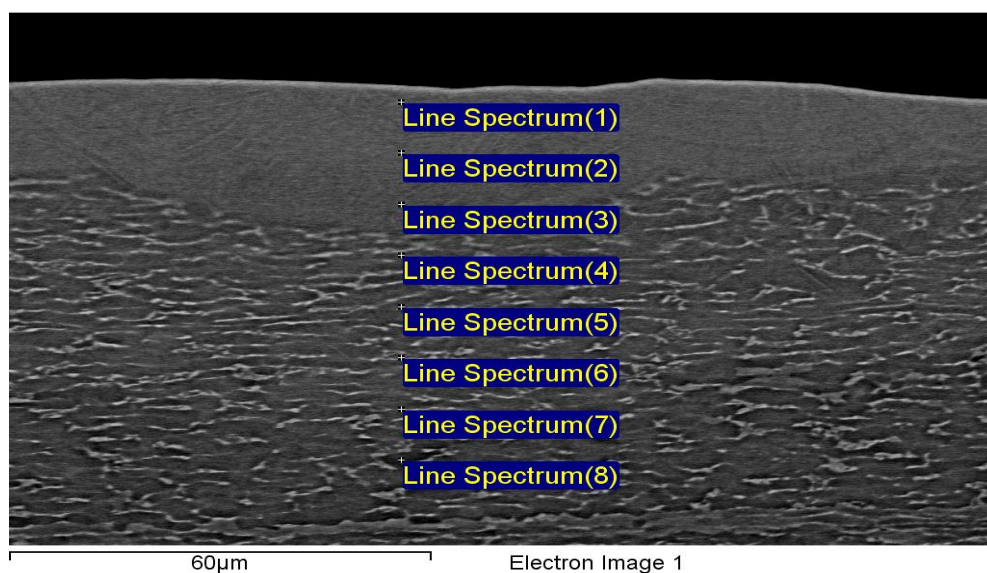
Spectrum	Ti	Al	V	Si	Ca	Fe	Total
1	89.62	5.89	3.90	0.32	0.27		100.00
2	89.90	5.75	3.99	0.36			100.00
3	89.61	5.87	4.15	0.38			100.00
4	89.79	5.90	4.00	0.32			100.00
5	88.89	5.33	5.50			0.28	100.00
6	90.50	6.02	3.48				100.00
7	87.46	5.20	7.06			0.27	100.00
8	90.25	5.87	3.89				100.00
Max.	90.50	6.02	7.06	0.38	0.27	0.28	
Min.	87.46	5.20	3.48	0.32	0.27	0.27	

Sample 6



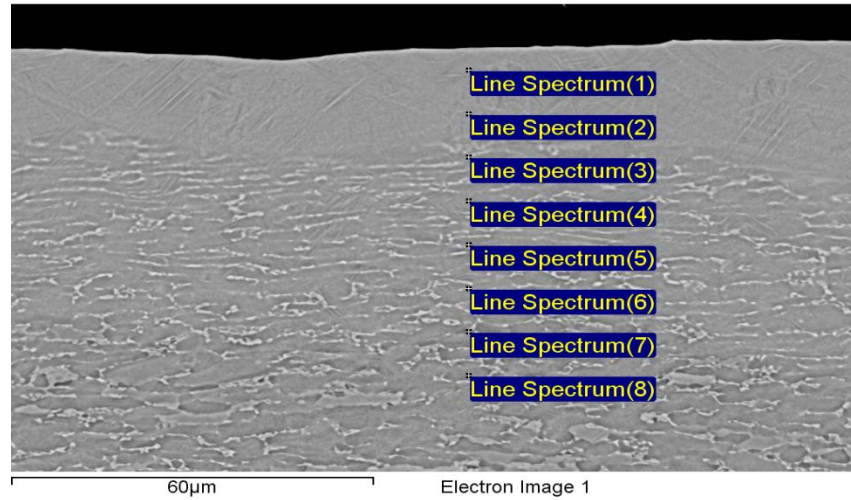
Spectrum	Ti	Al	V	Ca	C	Fe	Total
1	90.10	5.58	4.10	0.21			100.00
2	90.25	5.60	4.15				100.00
3	90.09	5.66	4.25				100.00
4	90.24	5.63	4.14				100.00
5	89.30	5.38	3.55		1.77		100.00
6	87.12	4.86	7.61			0.40	100.00
7	91.21	6.03	2.77				100.00
8	90.90	5.56	3.55				100.00
Max.	91.21	6.03	7.61	0.21	1.77	0.40	
Min.	87.12	4.86	2.77	0.21	1.77	0.40	

Sample 7



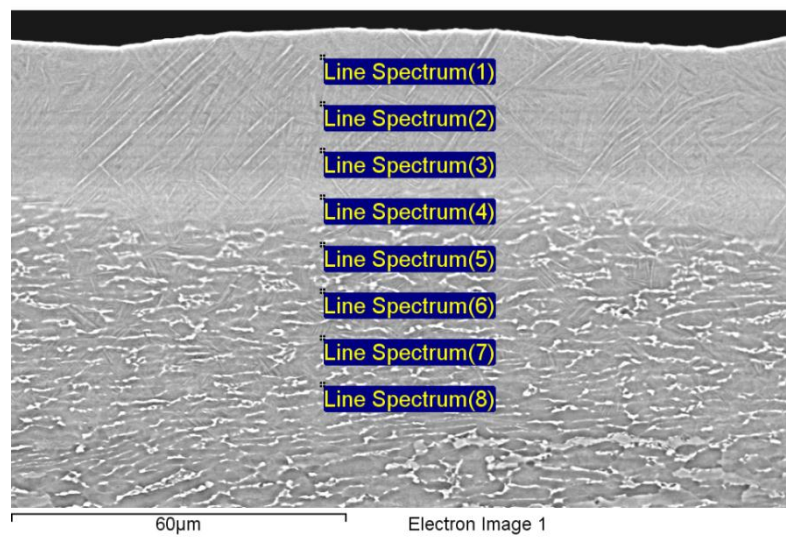
Spectrum	Ti	Al	V	Si	Ca	Fe	Total
1	89.76	5.56	3.98	0.34	0.35		100.00
2	89.75	5.62	4.26	0.36			100.00
3	89.79	5.72	4.11	0.37			100.00
4	91.04	5.84	3.12				100.00
5	90.23	5.59	4.18				100.00
6	87.74	4.81	7.00			0.44	100.00
7	90.27	6.00	3.73				100.00
8	91.20	6.22	2.58				100.00
Max.	91.20	6.22	7.00	0.37	0.35	0.44	
Min.	87.74	4.81	2.58	0.34	0.35	0.44	

Sample 8



Spectrum	Ti	Al	V	Si	Ca	Pt	Total
1	89.34	6.11	3.98	0.34	0.23		100.00
2	89.61	5.99	4.04	0.37			100.00
3	89.64	6.22	4.13			0.01	100.00
4	90.36	6.27	3.36			0.01	100.00
5	90.80	6.07	3.13				100.00
6	90.00	5.88	4.12				100.00
7	89.47	6.65	3.82			0.06	100.00
8	90.83	6.43	2.74				100.00
Max.	90.83	6.65	4.13	0.37	0.23	0.06	
Min.	89.34	5.88	2.74	0.34	0.23	0.01	

Sample 9



Spectrum	Ti	Al	V	C	Si	Total
1	88.32	5.38	4.01	1.98	0.31	100
2	90.12	5.57	3.93		0.39	100
3	90.09	5.64	3.99		0.28	100
4	90.27	5.55	4.18			100
5	89.83	5.75	4.42			100
6	90.51	6.07	3.42			100
7	90.78	5.94	3.28			100
8	89.14	5.93	2.96	1.97		100
Max.	90.78	6.07	4.42	1.98	0.39	
Min.	88.32	5.38	2.96	1.97	0.28	

J. Ablation Effects

The images below highlight ablation of Ti-6Al-4V caused by extremely high energy densities.

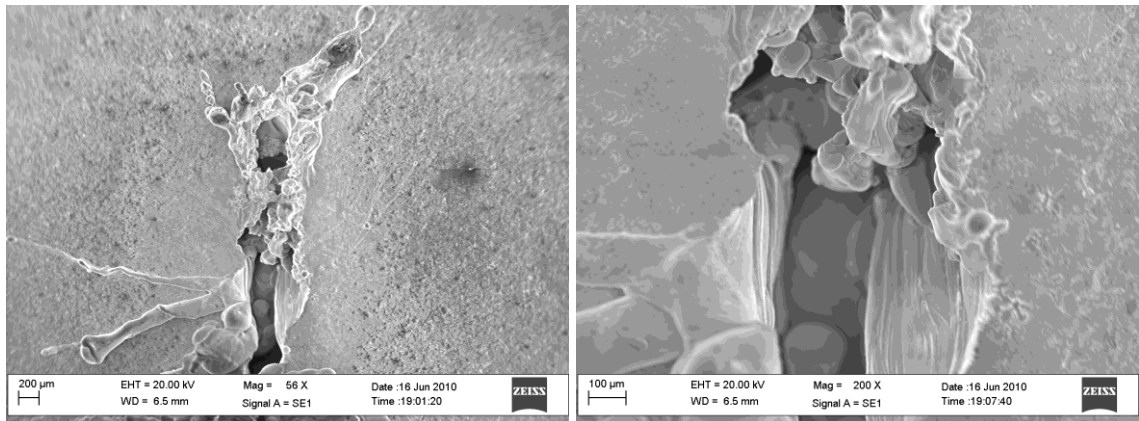


Figure J-1: Ablation at an energy density of 1.6 kJ/mm^2

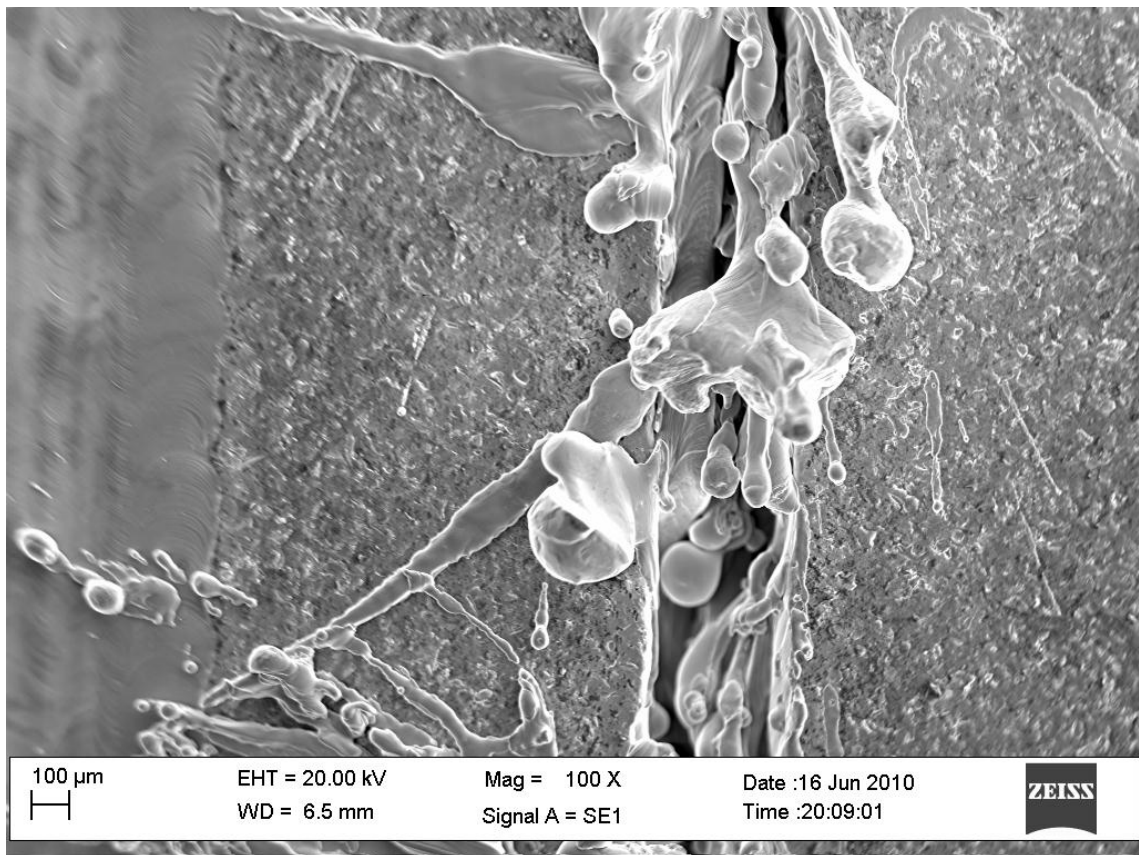


Figure J-2: Ablation at an energy density of 772 J/mm^2

K. Raw Data Material Properties Measured for Ti-6Al-4V

Table K-1: Mean melt-pool depth value (μm)

Melt-pool Depth (μm)		Irradiance (kW/mm^2)		
		15.72	20.43	26.72
Residence Time (ms)	1.08	20.6	26.1	29.1
	1.44	24.9	36.3	34.3
	2.16	35.80	40.8	46.1

Table K-2: Mean roughness (μm)

Roughness (μm)		Irradiance (kW/mm^2)		
		15.72	20.43	26.72
Residence Time (ms)	1.08	2.733	1.833	1.390
	1.44	2.300	1.600	1.433
	2.16	1.933	1.500	1.467

Table K-3: Mean microhardness (HV)

Hardness (HV)		Irradiance (kW/mm^2)		
		15.72	20.43	26.72
Residence Time (ms)	1.08	647.67	685.67	767.00
	1.44	666.00	681.00	693.33
	2.16	674.00	597.33	633.33

Table K-4: Mean β -Ti volume fraction (%)

β -Ti Volume Fraction (%)		Irradiance (kW/mm ²)		
		15.72	20.43	26.72
Residence Time (ms)	1.08	24.139	22.132	18.974
	1.44	23.010	21.632	21.486
	2.16	21.258	21.470	20.698

Table K-5: Mean specific wear rate (mm/N·m) for samples tested for 20 m.

Wear rate (x10 ⁻⁶ mm/N·m)		Irradiance (kW/mm ²)		
		15.72	20.43	26.72
Residence Time (ms)	1.08	504.44	548.24	607.48
	1.44	512.11	564.83	611.62
	2.16	543.61	580.83	654.40

Table K-6: Mean specific wear rate (mm/N·m) for samples tested for 150 m.

Wear rate (x10 ⁻⁶ mm/N·m)		Irradiance (kW/mm ²)		
		15.72	20.43	26.72
Residence Time (ms)	1.08	571.13	644.14	668.15
	1.44	725.16	586.13	630.14
	2.16	616.14	620.14	574.13

Table K-7: Mean corrosion rate nm/yr.

Corrosion Rate (nm/yr)		Irradiance (kW/mm ²)		
		15.72	20.43	26.72
Residence Time (ms)	1.08	239.42	188.35	86.618
	1.44	106.89	165.88	289.39
	2.16	441.31	101.09	202.45-

Table K-8: Mean contact angles (°) of unpolished samples.

Contact Angles unpolished (°)		Irradiance (kW/mm ²)		
		15.72	20.43	26.72
Residence Time (ms)	1.08	58.29	32.19	27.94
	1.44	40.43	32.24	38.11
	2.16	24.09	33.93	61.24

Table K-9: Mean contact angles (°) of polished samples.

Contact Angles polished (°)		Irradiance (kW/mm ²)		
		15.72	20.43	26.72
Residence Time (ms)	1.08	70.24	68.87	69.86
	1.44	60.14	54.52	57.93
	2.16	69.67	67.71	63.97

Table K-10: Mean cell attachment (%).

Cell Attachment (%)		Irradiance (kW/mm ²)		
		15.72	20.43	26.72
Residence Time (ms)	1.08	15.69	27.77	23.79
	1.44	27.05	22.82	20.45
	2.16	21.25	24.40	24.89

Table K-11: Mean cell numbers after 3 days.

Cell Numbers Day 3		Irradiance (kW/mm ²)		
		15.72	20.43	26.72
Residence Time (ms)	1.08	138.6E+3	106.7E+3	175.8E+3
	1.44	127.3E+3	167.3E+3	148.5E+3
	2.16	101.7E+3	151.4E+3	144.1E+3

Table K-12: Mean cell numbers after 7 days.

Cell Numbers Day 7		Irradiance (kW/mm ²)		
		15.72	20.43	26.72
Residence Time (ms)	1.08	199.4E+3	217.9E+3	256.9E+3
	1.44	272.9E+3	202.2E+3	223.2E+3
	2.16	222.0E+3	261.1E+3	221.0E+3

Table K-13: Mean metabolic activity at 24 hrs.

Metabolic Activity 24 hrs (%reduction)		Irradiance (kW/mm ²)		
		15.72	20.43	26.72
Residence Time (ms)	1.08	24.65	30.03	28.15
	1.44	31.48	32.14	29.74
	2.16	27.65	28.08	27.33

Table K-14: Mean metabolic activity at 96 hrs.

Metabolic Activity 96 hrs (%reduction)		Irradiance (kW/mm ²)		
		15.72	20.43	26.72
Residence Time (ms)	1.08	24.64	27.20	26.58
	1.44	26.78	26.56	27.70
	2.16	23.99	25.55	30.98

Table K-15: Mean metabolic activity at 7 days.

Metabolic Activity 7 days (%reduction)		Irradiance (kW/mm ²)		
		15.72	20.43	26.72
Residence Time (ms)	1.08	44.50	44.38	45.56
	1.44	46.46	45.35	44.36
	2.16	42.79	45.25	46.01